

Lecture Notes and Essays in Astrophysics

I

September, 2004
Spain

Editors
A. Ulla and M. Manteiga

Sponsored by the Spanish Ministry of Science and Technology
and by the Royal Spanish Physical Society

FOREWORD

This volume entitled “Lecture Notes and Essays in Astrophysics” is the first of a series containing the invited reviews and lectures presented during the biannual meetings of the Astrophysics Group of the Royal Spanish Physical Society (“Real Sociedad Española de Física”; RSEF). In particular, it includes the conferences and reviews presented during the Astrophysics Symposium held in Madrid (Spain) in July, 2003, during the First Centennial of the RSEF.

Our aim is to offer to the specialized public, and particularly to graduate and postgraduate astrophysics students, a number of selected comprehensive reviews on current topics presented by expert speakers (“Lecture Notes”). These are complemented by a set of chapters on more specific topics (“Essays”).

This first volume gathers a set of lectures that we are very pleased to present. In the first one, Rafael Rebolo describes the Very Small Array (VSA) experiment and reviews the expected recent results on the angular power spectrum of the Cosmic Microwave Background that set constraints on cosmological parameters.

White Dwarfs are the final remnants of low and intermediate mass stars. Their evolution is essentially a cooling process that lasts for ~ 10 Gyr and allows us to obtain information about the age of the Galaxy, setting a clear lower limit on the age of the Universe. Jordi Isern and Enrique García-Berro describe the state of the art of the White Dwarf cooling theory and discuss the uncertainties still remaining.

John Beckman and coauthors give a brief, historically based, survey of kinematic observations, essentially of rotation curves of spiral galaxies, produced as techniques have advanced and new wavelength ranges have been opened to observation, and of the Physics which can be derived.

Agustín Sánchez Lavega and coauthors review our current understanding of the general circulation at cloud top levels in the atmospheres of the giant planets Jupiter and Saturn. The interest in these planets has grown strongly in recent years in view of their similarities with the recently discovered giant extrasolar planets.

The final years of the 20th century and the initial years of the 21st century are witnessing a revolution in the construction of large telescopes. This has been possible thanks to the availability of both thin mirror technologies and growing computing power. Astronomy is clearly benefiting from this. Indeed the turn of the century has been rich with new discoveries, from the detections of Extrasolar Planets to the discovery of the farthest galaxies ever seen or the detection of acceleration in the expansion of the Universe. Spain is leaving her imprint on the telescope making revolution and is promoting the construction of a 10 meter class telescope at the “El Roque de Los Muchachos” observatory, on the Island of La Palma, Spain. The Gran Telescopio Canarias (GTC) is currently at an advanced stage of construction, with science operation expected to start early in 2006. José Miguel Rodríguez Espinosa introduces us to first hand technical considerations on the development and

construction of new-generation telescopes and astronomical instrumentation.

Recent results on Cool Stars, Hot Subdwarfs or Fullerenes in the Interstellar Medium, among several subjects covered, can also be found in the Essays of this book which we hope will provide an interesting insight into selected topics of modern Astrophysics.

The editors are indebted to the Spanish Ministry of Science and Technology (project AYA2001-1657) and to the Royal Spanish Physical Society for financial support.

Minia Manteiga and Ana Ulla
President and Secretary of the Astrophysics Group
Real Sociedad Española de Física

CONTENTS

Foreword	iii
----------	-----

Lecture Notes

Interferometry of the Cosmic Microwave Background <i>Rafael Rebolo et al.</i>	1
White Dwarfs and the Age of the Universe <i>Jordi Isern and Enrique García-Berro</i>	23
Kinematic Measurements of Gas and Stars in Spiral Galaxies <i>John E. Beckman et al.</i>	43
Observations and Models of the General Circulation of Jupiter and Saturn <i>Agustín Sánchez Lavega et al.</i>	63
Astronomical Telescopes at the Turn of the Century <i>José Miguel Rodríguez Espinosa</i>	87

Essays

Fullerenes and Buckyonions in the Interstellar Medium <i>Susana Iglesias Groth</i>	105
Cool Stars: Chromospheric Activity, Rotation, Kinematic and Age <i>David Montes et al.</i>	119
Asteroseismology of Hot Subdwarf Stars <i>Raquel Oreiro Rey et al.</i>	133
Helium Cataclysmic Variables <i>Ricardo Moreno and Ana Ulla</i>	143
Automatic Classification of Stellar Spectra <i>Iciar Carricajo et al.</i>	153

Geomagnetic Storms: Their Sources and a Model to Forecast the DST Index	165
<i>Yolanda Cerrato et al.</i>	
Detection of Energetic Particle Events with SOHO Space Observatory	177
<i>Dolores Rodríguez Frías et al.</i>	
The Role of Laboratory in Astrophysics: Laboratory Experiments on Ices and Astrophysical Applications	187
<i>Miguel Ángel Satorre et al.</i>	
On the Future of Ultraviolet (UV) Astronomy	197
<i>Ana I. Gómez de Castro and Willem Wamsteker</i>	
New Generation Near Infrared Spectrographs in 3.5 m to 10 m Class Telescopes	209
<i>Arturo Manchado</i>	
Author Index	215
Subject Index	217
Astrophysics Symposium Photos	221

INTERFEROMETRY OF THE COSMIC MICROWAVE BACKGROUND

RAFAEL REBOLO ^{1,2} and the VSA consortium^{1,3,4}

1 Instituto de Astrofísica de Canarias, E-38200 La Laguna, Tenerife, SPAIN

2 Consejo Superior de Investigaciones Científicas, SPAIN

3 Astrophysics Group, Cavendish Laboratory, University of Cambridge, Madingley Road, CB3 OHE, UK

4 Jodrell Bank Observatory, University of Manchester, Macclesfield, Cheshire, SK11 9DL, UK

Abstract: We describe the Very Small Array (VSA) and review the recent results on the angular power spectrum of the Cosmic Microwave Background (CMB) obtained in the Ka-band ($\nu \approx 33$ GHz) with this instrument. This array has covered an ℓ -range of 150 to 1500 with a relatively high resolution in ℓ compared to previous measurements at $\ell \geq 1000$; this is achieved by using mosaiced observations in 7 regions covering a total of approximately 82 sq. degrees. Our resolution of $\Delta\ell \approx 60$ between $\ell = 300$ and $\ell = 1500$ allows the first 3 acoustic peaks to be identified. Contamination by extragalactic radiosources brighter than 20 mJy has been taken into account by simultaneously monitoring identified sources with a high resolution interferometer. In addition, it has been performed a statistical correction for the small residual contribution from weaker sources that are below this flux limit. There is good agreement between the VSA power spectrum and that obtained by WMAP and other higher resolution experiments like ACBAR and CBI.

We have set constraints on cosmological parameters using VSA data and combinations with other CMB data and external priors. Within the flat Λ CDM model, the combined VSA+WMAP data without external priors gives $\Omega_b h^2 = 0.0234^{+0.0012}_{-0.0014}$, $\Omega_{dm} h^2 = 0.111^{+0.014}_{-0.016}$, $h = 0.73^{+0.09}_{-0.05}$, $n_s = 0.97^{+0.06}_{-0.03}$, $10^{10} A_S = 23^{+7}_{-3}$ and $\tau = 0.14^{+0.14}_{-0.07}$. We also find evidence for a running spectral index of density fluctuations, $n_{run} = -0.069 \pm 0.032$ at a level of more than 95% confidence. However, inclusion of prior information from the 2dF galaxy redshift survey reduces the significance of the result. When a general cosmological model with 12 parameters is considered we find consistency with other analyses available in the literature. The evidence for $n_{run} < 0$ is only marginal within this model. The fraction of dark matter in neutrinos is constrained to $f_\nu < 0.087$ (95% confidence limit) which implies that $m_\nu < 0.32$ eV if all the three neutrino species have the same mass.

1 Introduction

The CMB is a relic of the primitive Universe observed today as a largely isotropic radiation with Planckian spectral energy distribution of temperature $T_0 = 2.726 \pm 0.004$ K (95 % C.L.) [1]. It carries the imprint of the primordial density fluctuations that originated the large scale structure of the Universe providing extremely valuable information on the physical conditions of the very hot and dense early Universe. Peaks in the CMB angular power spectrum are a consequence of the evolution of pressure waves in the primordial plasma before the recombination epoch [2, 3]. These peaks provide information about the primordial density fluctuations, geometry, matter and radiation content and ionization history of the Universe. Their amplitudes and positions are sensitive to many of the most important cosmological parameters.

Following the detection of large angular scale fluctuations in the CMB temperature distribution by the Differential Microwave Radiometer on board the Cosmic Background Explorer (COBE) satellite [4], a major effort has been devoted to measure the angular power spectrum of primordial anisotropies. Several experiments have consistently detected acoustic peaks in the power spectrum in the ℓ -range 100 – 1000 [5, 6, 7, 8, 9, 10] and a fall-off in power at high- ℓ from the damping tail [11, 12, 13]. The Wilkinson Microwave Anisotropy Probe, henceforth *WMAP*, has provided the highest sensitivity measurements [14, 15] over the ℓ -range 2 – 700. The resulting power spectrum is cosmic variance limited up to $\ell = 350$ and delineates the first 2 peaks (at $\ell \sim 220$ and 550) with excellent signal-to-noise. These recent CMB measurements have brought impressive detailed cosmological information on a wide range of parameters [16], but *WMAP* is limited in angular resolution and hence has not measured the power spectrum above $\ell \sim 800$ with good signal-to-noise. Additional observations at high angular resolution (angular scales and multipoles are related according to the expression $\theta \sim \frac{120^\circ}{\ell}$) are still required to break some of the degeneracies inherent in the CMB power spectrum. Here, we review the recent measurements obtained by VSA out to a multipole of $\ell = 1500$ [17] and discuss their cosmological implications.

2 Interferometry and basic CMB formalism

The temperature fluctuations of the CMB on the sky $\frac{\Delta T}{T_0}(\vec{n}) \equiv \frac{T(\vec{n}) - T_0}{T_0}$ are usually expressed in terms of an expansion into spherical harmonics

$$\frac{\Delta T}{T_0}(\vec{n}) = \sum_{\ell=1}^{\infty} \sum_{m=-\ell}^{\ell} a_{\ell m} Y_{\ell m}(\vec{n}) \quad (1)$$

where \vec{n} is a unity vector that indicates the line of sight. Most of the models predict the temperature field to be gaussian. In that case, the statistical properties are

completely characterized by the angular correlation function: the expectation value of the product of temperatures at pairs of points separated by an angle θ

$$C(\theta) = \left\langle \frac{\Delta T}{T_0}(\vec{n}_1) \frac{\Delta T}{T_0}(\vec{n}_2) \right\rangle = \sum_{\ell} \frac{(2\ell+1)}{4\pi} C_{\ell} P_{\ell}(\cos \theta) \quad (2)$$

where $\cos \theta = \vec{n}_1 \cdot \vec{n}_2$, and P_{ℓ} is the Legendre polynomial of order ℓ .

The angular power spectrum is defined as the set of C_{ℓ} that verify:

$$\langle a_{\ell m} a_{\ell' m'}^* \rangle = C_{\ell} \delta_{\ell \ell'} \delta_{m m'} \quad (3)$$

where $*$ indicates the conjugate.

Experiments measure the $a_{\ell m}$ corresponding to the last scattering surface seen from our position in the Universe. However, the ergodicity property of gaussian fields, allow to determine the angular power spectrum by averaging over the last scattering surface:

$$\langle |a_{\ell m}|^2 \rangle \approx \frac{\sum_m |a_{\ell m}|^2}{2\ell + 1} \quad (4)$$

The power at each ℓ is $(2\ell+1)C_{\ell}/4\pi$. The observing strategy and resolution of each instrument limit the range of angular scales which can be measured as described by the window function [20]:

$$W_{\ell}(\vec{n}_1, \vec{n}_2) \equiv \int d\vec{m}_1 \int d\vec{m}_2 A(\vec{n}_1, \vec{m}_1) A(\vec{n}_2, \vec{m}_2) P_{\ell}(\vec{m}_1 \cdot \vec{m}_2) \quad (5)$$

where $A(\vec{n}_1, \vec{m}_1)$ is the instrument response function to signals coming from direction \vec{n}_1 when pointing towards direction \vec{m}_1 . The particular case $W_{\ell}(\vec{n}_1, \vec{n}_1)$ is frequently referred as window function. The variance of the observed temperature field, or correlation at zero lag ($\theta = 0$), results

$$\langle (\frac{\Delta T}{T_0})^2 \rangle = \sum_{\ell} \frac{(2\ell+1)}{4\pi} C_{\ell} W_{\ell} \quad (6)$$

where the window function is denoted as W_{ℓ} .

An interferometer provides a direct measurement of the Fourier transform of the intensity distribution on the sky and hence, a determination of the C_{ℓ} . For a baseline d , the interferometer is sensitive to CMB structure with multipole $\ell = 2\pi d/\lambda$, where λ is the wavelength of observations. The instantaneous field of view is determined by the primary beam of the antennas. Comprehensive descriptions of the analysis techniques involved in interferometric observations can be found in the literature (see e.g. [18]). Interferometers with different number of dishes/horns, bandwidths, size of primary beam and approximate multipole range have been used in the search for CMB

anisotropies from various locations [19]. These instruments are rather insensitive to atmospheric distortion of the microwave signals (see e.g. [21, 22]).

In the early 90s, the Jodrell Bank-IAC 33 GHz interferometer, a pioneer two-element instrument installed at Teide Observatory clearly demonstrated the feasibility of high-sensitivity interferometric measurements of the CMB anisotropy from this site. This precursor of VSA measured CMB fluctuations with amplitude $\Delta T_\ell = 43 \pm 13 \mu K$ and $63 \pm 7 \mu K$ at $\ell = 109$ and 208 , respectively [23, 24]. A new generation of CMB interferometers has started operation very recently: the Cosmic Background Imager (CBI, [25]) in the Atacama desert, the Degree Angular Scale Interferometer (DASI, [8]) in Antarctic and the Very Small Array (VSA, [26]) in Tenerife have achieved very sensitive measurements of the angular power spectrum in the range $200 \leq \ell \leq 4000$.

3 The VSA

The VSA is a purpose-built 14-element radio interferometer (see Figure 1) that has measured the CMB angular power spectrum between $\ell = 150$ and 900 in a compact array configuration [10] and more recently up to $\ell = 1400$ in an extended array configuration [12]. It is located at Teide Observatory (Tenerife) at an altitude of 2340 m. It can operate in the Ka-band (26 – 36 GHz), however, to minimize the contribution of foregrounds to the signal recorded it was decided to operate with a bandwidth of 1.5 GHz at the higher end of the band (~ 33 GHz). Each antenna consists of a conical corrugated horn feeding a paraboloidal mirror and is placed on a 4-m \times 3-m tip-tilt table surrounded by a metal enclosure to suppress as much as possible ground emission. The VSA can observe any sky region between declination -5° and $+60^\circ$. It has been used in two major modes: in the compact configuration, the mirrors were 143-mm in diameter giving a primary beam of $4^\circ.6$ FWHM; in the extended one, the 322-mm diameter apertures allow longer baselines and therefore higher resolutions to be obtained, with a primary beam of 2° FWHM. This configuration has a total of 91 baselines with lengths ranging from 0.6 m to 2.5 m, although the maximum possible baseline length, set by the size of the main tip-tilt table, is ~ 4 m. The synthesized beam of a typical VSA field has FWHM ~ 11 arcmin over the primary beam.

Combining all 91 baselines the VSA point source sensitivity is ~ 6 Jy s $^{1/2}$. This corresponds to a temperature sensitivity, over a synthesized beam area ($\Omega_{\text{synth}} \approx 1 \times 10^{-5}$ sr) of ~ 15 mK s $^{1/2}$. The exact value depends on the beam area and on the u, v coverage which in turns depends on the declination and the flagging/filtering of the visibility data.

An important feature of the VSA is the ability to subtract radio sources which contaminate CMB data with a dedicated facility. Combined with map-making capabilities, this makes the VSA ideal for making precise CMB measurements, particularly



Figure 1: The VSA at Teide Observatory.

at higher ℓ -values.

4 Observations

The observations with the compact configuration [27] and the initial three regions observed in the extended configuration [12] are already published. During the period 2001–July 2003 VSA conducted observations of 33 additional pointings with the extended configuration. These pointings conform three 7-field mosaics and four 3-field mosaics giving a total area coverage of 82 sq. degrees. The new observations extend the initial regions with a further 4 pointings per region and incorporate a further 4 new regions each with 3 pointings. This corresponds to a factor of ~ 4 in the amount of extended array data and a significant increase in sensitivity over the previous results. Furthermore, the increase in sky-coverage and mosaicing in each field allows an improvement in ℓ -resolution, or reduced bin-bin correlations, using mosaicing techniques. The total effective integration time is ≈ 6000 hours (250 days) after filtering and flagging of the data. About ~ 30 per cent of data was flagged.

The fields were chosen to avoid as much as possible contamination from Galactic and extragalactic emission. High Galactic latitude ($|b| \geq 27^\circ$) fields with low emission as predicted from maps of synchrotron, free-free and dust emission were chosen to minimize Galactic contamination. Fields with bright galaxy clusters were excluded based on existing catalogues [28, 29]. Similarly, fields with bright radio sources (≥ 500 mJy) in the NVSS 1.4 GHz survey [30] and GB6 survey at 4.85 GHz [31] were discarded. Avoiding galaxy clusters is important due to the potential for Sunyaev-Zeldovich Effect (SZE) decrements to contaminate VSA data.

5 Data reduction and calibration

The VSA data reduction and calibration procedures are described for the compact and extended configuration in several papers [27, 12]. In [17] full details are given about the reduction of the new extended data. Fourier filtering is used to remove the majority of local undesired signals. The filtering removes typically 10 – 20 per cent of the data. The same fringe-rate filtering technique is also applied to the Sun and Moon. Data are filtered if the Sun and Moon are within 27° and 18° respectively, while if the Sun or Moon are within 9° of the field centre then the entire observation is flagged. No residual Sun or Moon contamination was detected after stacking the data typically integrated over 50 – 100 days. The data are then further smoothed by a factor of 4 to give 64 sec samples and a correction is applied for the atmospheric contribution to the system noise.

Noise figures vary significantly between baselines, so the final step for each observation is the re-weighting of the data based on the r.m.s. noise of each baseline. This is essential to achieve the optimum overall noise level. The data are then stacked together either in hour angle or in the u, v plane. The final data for each field contains $\sim 10^6$ visibilities, each of 64 sec integration, which are used directly to make maps. For power spectrum estimation, the data are binned in the u, v plane to reduce the number of data points. Each visibility has an associated weight calculated by the reduction pipeline.

The first important step in the calibration of the VSA data is to obtain a precise geometric description of the instrument, i.e. to know the positions for each horn with a precision better than 1/10 the wavelength of observation. This also requires the calculation of corrections for amplitudes, phases and the observing frequency. A maximum-likelihood method [32] is used to solve simultaneously all these parameters. Typically, data from an intense radiosource (like Tau-A) are collected for this purpose. The results are checked via observations of other bright radio sources. Amplitude and phase corrections are usually calculated from a single calibrator for each of the 91 baselines. An unresolved, non-variable bright radio source allows the measured fringes to be corrected for amplitude and phase.

The absolute flux calibration of VSA is made using observations of Jupiter. In the first years of observations we assumed for this planet a brightness temperature $T_{\text{Jup}} = 152 \pm 5$ K (3 per cent accuracy in temperature) at 32 GHz [33]. However, data from WMAP gives a more precise determination of the brightness temperature for Jupiter of $T_{\text{Jup}} = 146.6 \pm 2.0$ K at 33.0 GHz [34] corresponding to an accuracy of 1.5 per cent in temperature terms, or equivalently 3 per cent in the CMB power spectrum (ΔT^2). We have adopted this WMAP temperature for Jupiter in the calibration of the new extended array data, and consistently scaled our earlier measurements of the power spectrum.

A number of data checks are systematically applied to the data (stacking data in

various ways, splitting in different subsets, non-Gaussian tests to search for residual systematics, etc.), but more importantly, a parallel independent reduction for the majority of the data is performed by the three institutions in the VSA collaboration. The comparison of this independent data reduction showed good agreement for both maps and power spectrum measurements.

6 Foregrounds

Radiosources in the fields observed by VSA are first surveyed with the Ryle Telescope at 15 GHz to a limiting flux density of ~ 10 mJy [35]. Then these sources are followed with the Source Subtractor (SS), a two-element interferometer located next to the VSA main array operating at the same frequency. It consists of two 3.7 m dishes with a baseline of 9 m providing a resolution of ~ 3 arcmin. The observations are conducted simultaneously with VSA, so each source is observed many times during the period of time dedicated to each VSA field. The SS data are calibrated using the flux of the planetary nebula NGC7027, assuming a flux density of (5.45 ± 0.20) Jy at 32.0 GHz and a flat spectral index $\alpha = 0.1 \pm 0.1$ [33]. The SS flux densities of the sources in the VSA fields are subtracted from the visibility data down to a level of 20 mJy ($\sim 8 \mu\text{K}$ over the synthesized beam area). The complete source survey is presented by [70]. These source counts are also used to re-scale the 30 GHz differential source count model [36] and to make an estimate of the contribution from faint sources below the source subtraction limit of 20 mJy. The residual source power spectrum ($\sim 210 \mu\text{K}^2$ at $\ell = 1000$) is subtracted from the VSA band-power estimates as an uncorrelated statistical correction.

6.1 Galactic foregrounds

At the frequency and high angular resolution of the VSA observations it is not expected a significant contribution of the diffuse Galactic foregrounds: synchrotron emission, free-free emission from ionized gas and vibrational dust emission. The power spectrum of these well known foregrounds decreases with increasing ℓ [37] and the VSA fields have been selected in regions of high galactic latitude in order to minimize these potential contaminants. Estimates for these foregrounds in the VSA fields have been obtained using three template maps: the 408 MHz all-sky map for synchrotron [38], the H α data from the Wisconsin H-Alpha Mapper (WHAM, [39]) for free-free emission and the 100 μm map [40] for dust-correlated emission. Similar considerations as in previous work [27] lead to synchrotron and free-free r.m.s. power values for the VSA extended fields of less than $(10 \mu\text{K}^2)$ compared to the CMB fluctuations ($\gtrsim 1000 \mu\text{K}^2$).

In addition, we have to consider a more controversial foreground, the so called

“foreground X” [41], which appears to be correlated with far infrared dust emission. The characteristics of this foreground have not been fully established yet. Some models [42] predict that spinning dust particles may be the carrier with maximum emission in the range 20-30 GHz. For the dust-correlated component, we smoothed the [40] 100 μm map to 22 arcmin ($\ell \sim 1000$) and assumed a nominal coupling coefficient between brightness temperature at 33 GHz and the 100 μm intensity of $T_b/I_{100} = 10 \mu\text{K}/(\text{MJy sr}^{-1})$. This is a nominal value averaged for the high latitude sky. The r.m.s. power fluctuations estimates for the VSA fields range between 1 and 90 μK^2 at $\ell = 1000$, typically $\lesssim 10 \mu\text{K}^2$ while the CMB fluctuations are $\Delta T_{\text{rms}}^2 \sim 1000 \mu\text{K}^2$ thus, for most of the VSA regions, the Galactic emission is essentially negligible.

6.2 SZ clusters

The VSA fields are selected to avoid known galaxy clusters and minimize any contribution to the CMB temperature from inverse Compton scattering of hot electrons in the intracluster medium, the Sunyaev-Zeldovich (SZ) effect [43, 3]. At the frequency of VSA observations, the SZ effect, produces temperature decrements in the line of sight of the galaxy clusters. The confusion noise produced by a Poisson distribution of unknown high redshift clusters has been estimated using available models [44]. If we adopt $\sigma_8 = 0.9$, we obtain a contribution of $\approx 1 \text{ mJy beam}^{-1}$, approximately six times lower than the noise level in typical VSA maps.

7 Results

7.1 Maps

The maps are produced using a maximum entropy method (MEM) [45]. The binned visibility data used for deriving the power spectrum are also the starting point for map making. First, the Fourier modes in the u, v -plane are reconstructed, then these are Fourier transformed to obtain the maps. The MEM algorithm assumed a flat sky as prior. The signal-to-noise ratio of the maps is in the range $\text{SNR} \sim 1 - 3$, the change being primarily due to the varying integration times after flagging and filtering of the data [17]. The sensitivity of the mosaiced maps is slightly higher than this, due to the overlapping of the individual fields.

The VSA maps allow a comparison to be made with other CMB data. The recent WMAP data release [14] has provided 5 all-sky maps at frequencies centred at 22.8 (K-band), 33 (Ka-band), 40.7 (Q-band), 60.8 (V-band) and 93.5 GHz (W-band) with resolutions ranging from 49.2 arcmin (K-band) to 12.6 arcmin (W-band). The signal-to-noise ratio of WMAP data at the VSA resolution is ~ 1 and hence much of the CMB signal is lost in the noise. The actual noise level in the WMAP data depends on

position due to the scanning strategy of the WMAP satellite. For the 1-year WMAP data release, the noise is $\sim 100 - 200 \mu\text{K}$ per 12.6 arcmin pixel in the VSA regions, compared to $\sim 20 \mu\text{K} \text{ beam}^{-1}$ in the VSA mosaiced maps.

7.2 Power spectrum

The final visibility data are binned into u, v square cells, each 9 wavelengths on a side, to oversample the data. This reduces the number of data points by a factor of $\gtrsim 1000$. Sources are subtracted using position and flux density information from the Source Subtractor. For each VSA pointing there is a final visibility file with $\sim 10^3$ data points.

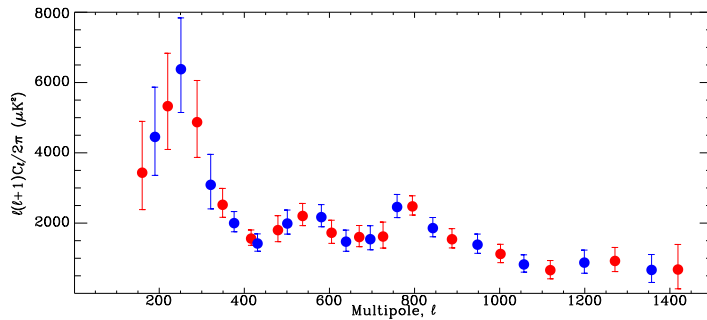


Figure 2: The CMB power spectrum as measured by the VSA by combining the data from all 7 VSA regions [17]. The first 3 bins are included from earlier VSA data in a compact array. The errors represent 1σ limits. Two alternate binnings (grey and black) are displayed. Absolute calibration is accurate to 3 per cent and is not included in the errors.

The binned visibilities form the basic input to the maximum likelihood analysis for the CMB power spectrum. We used the Microwave Anisotropy Dataset Computational sOftWare (MADCOW) [46] which can deal with mosaiced observations and variable bin-widths. The band powers calculated from the complete VSA data set, both the compact and extended arrays are available at the following URL:

http://www.jb.man.ac.uk/research/vsa/vsa_results.html.

The extended array data have little sensitivity at $\ell \lesssim 300$. The 3 bins at $\ell < 300$ are therefore dominated by data from the compact array [10]. The error bars were calculated from the probability likelihood functions by enclosing 68 per cent of the area centred on ℓ_h , the median ℓ value for each bin. Calibration uncertainty (≈ 3 per cent) is not included. Sample variance is included in the error estimates. The

VSA power spectrum (Figure 2) clearly shows the existence of the first three acoustic peaks and the fall-off in power towards higher ℓ .

8 Cosmological implications

We first consider the standard six-parameter flat Λ CDM model, and then include extra parameters as in the approach adopted by the WMAP team [16, 47, 48]. In the case where we do not impose external priors on the CMB data (WMAP+VSA), we find that there is significant evidence ($> 2\sigma$) for negative running; something which is not implied by the WMAP data alone. The significance of this result is sensitive to the inclusion of external priors, the relative calibration of WMAP and VSA, and possible source/cluster contamination of the measured power spectrum. Second, we consider a 12-parameter model fit to WMAP, WMAP+VSA and all available CMB data beyond $\ell > 1000$, illustrating the effects of external priors on the estimated parameters.

8.1 Methodology

Cosmological model

The Λ CDM model assumes that the Universe is flat and dominated by cold dark matter (CDM), baryons and a cosmological constant, Λ . The densities of these components relative to critical are denoted Ω_{dm} , Ω_b and Ω_Λ respectively and we define $\Omega_m = \Omega_{dm} + \Omega_b$ to be the overall matter density (CDM and baryons) in the same units. The expansion rate is quantified in terms of the Hubble constant $H_0 = 100h \text{ km sec}^{-1} \text{ Mpc}^{-1}$ and we allow for instantaneous reionization at some epoch $z_{re}(< 30)$ which can also be quantified in terms of an optical depth τ . The so-called physical densities of the CDM and baryons are defined as $\omega_{dm} = \Omega_{dm}h^2$ and $\omega_b = \Omega_bh^2$. We will consider only adiabatic models and parameterize the initial fluctuation spectrum of this model by

$$P(k) = A_S \left(\frac{k}{k_c} \right)^{n_S}, \quad (7)$$

where $k_c = 0.05 \text{ Mpc}^{-1}$ is the arbitrarily chosen pivot point of the spectrum, n_S is the spectral index and A_S is the scalar power spectrum normalization.

We will also consider a model with a running spectral index,

$$P(k) = A_S \left(\frac{k}{k_c} \right)^{n_S + \frac{1}{2} n_{run} \log(k/k_c)}, \quad (8)$$

so that the overall spectral index of fluctuations is a function of scale, $n_S(k)$, given by

$$n_S(k) = \frac{d(\log P)}{d(\log k)} == n_S + n_{\text{run}} \log \left(\frac{k}{k_c} \right), \quad (9)$$

where n_{run} is known as the running of the spectral index. For slow roll inflation to be well defined, one requires that $|n_{\text{run}}| \ll |1 - n_S|/2$ [49]. Under certain choices of priors we find that there is some evidence that this inequality is violated by the preferred fits to the data.

The other parameters which we will consider in our analyses are: $f_\nu = \Omega_\nu/\Omega_{\text{dm}}$, the fraction of the dark matter which is massive neutrinos; $\Omega_k = 1 - \Omega_{\text{tot}}$ ($\Omega_{\text{tot}} = \Omega_{\text{dm}} + \Omega_b + \Omega_\nu + \Omega_\Lambda$), the curvature in units of the critical density; $w = P_Q/\rho_Q$, the equation-of-state parameter for a dark energy component modelled as a slowly rolling scalar field; n_T the spectral index of tensor fluctuations specified at the pivot point $k_c = 0.002 \text{ Mpc}^{-1}$; $R = A_T/A_S$, the ratio of the amplitude of the scalar fluctuations, A_S , evaluated at $k_c = 0.05 \text{ Mpc}^{-1}$, and that of the tensor fluctuations evaluated at $k_c = 0.002 \text{ Mpc}^{-1}$. In addition to these parameters, for which we fit, we will also comment on various derived quantities: t_0 , the age of the universe; σ_8 , the amplitude of density fluctuations in the spheres of $8h^{-1} \text{ Mpc}$.

8.2 CMB data

Four different combinations of CMB data have been considered.

- The first data set, denoted COBE+VSA contains the VSA data as described in the previous sections [17] combined with the COBE data [4, 50].
- The second data set, denoted WMAP contains only the WMAP temperature (TT) data [15] and temperature-polarization cross-correlation (TE) data [51].
- The third data set contains WMAP data and the new VSA data and is referred to as WMAP+VSA. This allows to illustrate the relevance of measurements of the power spectrum on small angular scales.
- Finally, we combine the previous two with all important CMB experiments providing measurements in the region of the second peak of the spectrum and beyond, namely CBI, ACBAR, Boomerang, Maxima, DASI [11, 13, 7, 52, 8]. This last data set is hereafter referred to as ALLCMB.

External priors

In addition to the CMB data sets described above, we consider the effects of other cosmological data, not only to break the degeneracies, but also to see how the mea-

sured CMB power spectrum fits in the wider cosmological context. The external priors used are:

- The constraint on the expansion rate of the Universe from the Hubble Space Telescope (HST) Key project value of $H_0 = 72 \pm 8 \text{ km sec}^{-1} \text{ Mpc}^{-1}$ [53]. The error-bar includes both statistical and systematic uncertainty.
- Constraints on large scale structure from the 2dF Galaxy Redshift Survey [54, 55, 56], which provides measurements on scales $0.02 < k/(h \text{ Mpc}^{-1}) < 0.15$.
- Constraints from Type Ia Supernovae (SNeIa) [57, 58].
- Constraints from the gas fraction (f_{gas}) in dynamically relaxed clusters of galaxies [59] and from the observed local X-ray luminosity function (XLF) of galaxy clusters [60].
- Constraints from cosmic shear (CS) measurements [61].

Parameter estimation

The parameter estimation has been performed using the COSMOMC software package [62]. The calculations were performed on LAM clusters with a total of 42 CPUs at the IAC in La Laguna, Tenerife and the COSMOS supercomputer facility at the University of Cambridge. The COSMOMC software uses the Markov Chain Monte Carlo (MCMC) algorithm to explore the hypercube of parameters on which we impose flat priors. These priors are listed in Table 8.2. Additionally, the software automatically imposes the physical prior $\Omega_\Lambda > 0$, which can significantly affect the marginalized probability distributions (see [63] for further discussion).

8.3 Flat Λ CDM models

Standard six-parameter model

We begin our discussion in the context of the standard flat Λ CDM model with six free parameters ($\omega_b, \omega_{\text{dm}}, h, n_s, A_s, \tau$) with no external priors.

The constraints derived for the parameters are tabulated in Table 8.3. The values for WMAP alone can be compared with those in [16]. Noting that they present $\omega_m = \Omega_m h^2$, instead of ω_{dm} , there are only minor discrepancies in the central values, although some of the limits appear to be somewhat larger. The preferred value of the redshift of reionization is $z_{\text{re}} = 17^{+8}_{-6}$. The inclusion of the high-resolution data from the VSA modifies the limits on each of the parameters and these are most significant for n_s , whose best fitting value reduces from 1.00 to 0.97. The result for n_s will be central to our subsequent discussion of the primordial power

Basic Parameter	Prior
ω_b	(0.005,0.10)
ω_{dm}	(0.01, 0.99)
h	(0.4,1.0)
n_S, n_1, n_2	(0.5,1.5)
z_{re}	(4,30)
$10^{10} A_S$	(10,100)
n_{run}	(-0.15,0.15)
$A_X/(\mu\text{K})^2$	(-500,500)
f_ν	(0,0.2)
Ω_k	(-0.25,0.25)
w	(-1.5,0)
R	(0,2)
n_T	(-1.5,3)

Table 1: Priors used on each cosmological parameter when it is allowed to vary. The notation (a, b) for parameter x denotes a top-hat prior in the range $a \leq x \leq b$.

Parameter	COBE+VSA	WMAP	WMAP+VSA
ω_b	$0.0328^{+0.0073}_{-0.0071}$	$0.0240^{+0.0027}_{-0.0016}$	$0.0234^{+0.0019}_{-0.0014}$
ω_{dm}	$0.125^{+0.031}_{-0.027}$	$0.117^{+0.018}_{-0.018}$	$0.111^{+0.014}_{-0.016}$
h	$0.77^{+0.15}_{-0.17}$	$0.73^{+0.10}_{-0.06}$	$0.73^{+0.09}_{-0.05}$
n_S	$1.05^{+0.12}_{-0.08}$	$1.00^{+0.09}_{-0.04}$	$0.97^{+0.06}_{-0.03}$
$10^{10} A_S$	25^{+11}_{-6}	27^{+9}_{-5}	23^{+7}_{-3}
τ	Unconstrained	$0.18^{+0.16}_{-0.08}$	$0.14^{+0.14}_{-0.07}$

Table 2: Parameter estimates and 68% confidence limits for the standard six-parameter flat Λ CDM model.

CMB	External	n_s	n_{run}
COBE+VSA	None	$0.93^{+0.13}_{-0.12}$	$-0.081^{+0.049}_{-0.049}$
WMAP	None	$0.94^{+0.07}_{-0.06}$	$-0.060^{+0.037}_{-0.036}$
WMAP+VSA	None	$0.96^{+0.07}_{-0.07}$	$-0.069^{+0.032}_{-0.032}$
COBE+VSA	HST	$0.92^{+0.11}_{-0.12}$	$-0.081^{+0.048}_{-0.048}$
WMAP	HST	$0.95^{+0.06}_{-0.07}$	$-0.060^{+0.037}_{-0.037}$
WMAP+VSA	HST	$0.93^{+0.06}_{-0.05}$	$-0.069^{+0.036}_{-0.036}$
COBE+VSA	2dF	$1.00^{+0.12}_{-0.13}$	$-0.044^{+0.058}_{-0.061}$
WMAP	2dF	$0.95^{+0.05}_{-0.06}$	$-0.038^{+0.025}_{-0.037}$
WMAP+VSA	2dF	$0.93^{+0.05}_{-0.05}$	$-0.049^{+0.035}_{-0.034}$

Table 3: Limits on n_s and n_{run} in the flat Λ CDM model with a running spectral index for different CMB data sets and external priors.

spectrum. The results from WMAP+VSA are very similar to those presented in [16] for WMAP+ACBAR+CBI. We also find a larger value for ω_b than suggested by WMAP, WMAP+VSA and standard Big Bang Nucleosynthesis, $\omega_b = 0.020 \pm 0.002$, [64].

Running spectral index models

In the previous section we saw that the inclusion of the VSA data to that of WMAP shifts the derived limits on the spectral index. Standard, slow-roll models of inflation predict that the spectral index will be a function of scale, albeit at a very low level, and it seems a sensible parameter to allow as the first beyond the standard model. The analysis of [16, 48] provided evidence for a non-zero value of $n_{\text{run}} (= -0.031^{+0.016}_{-0.017})$ when using CMB data from WMAP, ACBAR and CBI, along with large-scale structure data

from the 2dF galaxy redshift survey and the Lyman- α forest.

We will start our discussion by considering the same model as in the previous section with no external priors, but with n_{run} allowed to vary. The derived limits on n_S and n_{run} are presented in the first three rows of Table 8.3 for COBE+VSA, WMAP and WMAP+VSA. The derived limits on ω_b , ω_{dm} and h are not changed appreciably and the other parameters, A_S and τ (or z_{re}) are strongly degenerate and z_{re} will feature in our discussion below.

The values of n_S and n_{run} are not particularly well constrained by COBE+VSA, but it is worth noting that even in this case there is a definite preference for a value of $n_{\text{run}} < 0$. The results have been included for completeness and provide a useful cross-check. The results for WMAP are somewhat different to those presented in [16]. In particular we find that $n_{\text{run}} = -0.060^{+0.037}_{-0.036}$, a 1.6σ preference for $n_{\text{run}} < 0$, as opposed to $n_{\text{run}} = -0.047 \pm 0.04$ from Spergel et al. [16]. The significance of this result is improved to 2.2σ by the inclusion of the high resolution data from the VSA. We remark that this result comes from CMB data alone.

We have tested the sensitivity of this apparently result to the inclusion of external priors from the HST and 2dF galaxy redshift survey, and the results are also presented in Table 8.3. We see that the effect of the HST prior is to relax marginally the constraint on n_{run} , although there is a significant change in the derived limit on n_S . We note that the results for WMAP alone are very similar with and without the HST prior. The inclusion of 2dF does significantly affect our results. Using just WMAP we find that there is only a marginal preference for $n_{\text{run}} < 0$ and the inclusion of VSA only yields a 1.4σ result. We note that this is a shift in the derived value and the error bars do not change significantly.

We have also considered the effects of including other CMB information from the two other high resolution experiments ACBAR and CBI. We find that the inclusion of their results does not appear to be as significant as the VSA in preferring a value of $n_{\text{run}} < 0$ and that the result of considering WMAP+ACBAR+CBI+VSA is very similar to just WMAP+VSA. We note that the ACBAR and CBI experiments quote large global calibration uncertainties (20% and 10% in power), which we believe is at least as responsible for this result as their errors on the individual power spectrum band powers.

Neutrino fraction

As a final extension to our flat Λ CDM model, it is of interest to include the fraction f_ν of dark matter in the form of neutrinos. Evidence for a neutrino oscillation, and hence for the existence of massive neutrinos, has been found by solar neutrino and atmospheric neutrino experiments [65, 66, 67, 68]. Further evidence for a non-zero value of the neutrino mass has recently been claimed from cosmological data [69].

In addition to obtaining constraints on f_ν , the inclusion of this parameter will

inevitably lead to some broadening of the marginalized distributions for the other parameters. Of particular interest is whether the constraints on the running spectral index derived above are robust to the inclusion of f_ν . We therefore include f_ν , with the top-hat prior given in Table 8.2, into the running spectral index model. In the analysis of this model, we include the 2dF external prior, since current CMB alone provide only a weak constraint on f_ν .

We find that the 95% upper limit provided by the COBE+VSA data set, $f_\nu < 0.132$, is only marginally larger than that obtained using WMAP data, $f_\nu < 0.090$. The combination WMAP+VSA gives similar limits to WMAP, namely $f_\nu < 0.087$, which corresponds to neutrino mass of $m_\nu < 0.32\text{eV}$ when the neutrino masses are degenerate.

For the parameters n_S and n_{run} , the marginalized distributions have indeed been shifted and broadened by the inclusion of f_ν , although the effects are not very strong. In particular, we note that our earlier finding of a preference for a non-zero value of n_{run} has been weakened somewhat. A non-zero n_{run} is still preferred, but at reduced significance. For the WMAP+VSA data set, we obtain $n_S = 0.94^{+0.06}_{-0.06}$ and $n_{\text{run}} = -0.041^{+0.037}_{-0.036}$ with 68% confidence limits.

In the above analysis we used only 2dF as an external prior. It is of interest to investigate the effect of including different combinations of the additional external priors listed in Table 8.2. The effect of these additional priors has been calculated by importance sampling our previous results. We also investigate the effect of including all recent CMB data into our analysis. In Figure 3, we plot confidence limits on all the model parameters for each of our four CMB data sets, each of which, in turn, includes four different combinations of external priors: 2dF, 2dF+ f_{gas} , 2dF+ $f_{\text{gas}}+\text{XLF}$, 2dF+HST and 2dF+CS. The points indicate the median of the corresponding marginalized distribution, and the error bars show the 68% central confidence limit. If the distribution peaks at zero, the point is placed on the axis and the 95% upper limit is shown.

We see that the inclusion of the f_{gas} and XLF external priors significantly reduces the error bars on all parameters. The most profound effect is obtained from the XLF prior for the parameters f_ν , σ_8 and z_{re} , as might be expected from [69]. Indeed, it is only with the inclusion of the XLF prior that a non-zero value of f_ν is preferred and only then at limited significance. For each of the CMB data set combinations, the best-fitting value in this case is $f_\nu \approx 0.05$, which corresponds to neutrino mass of $m_\nu \approx 0.18\text{eV}$ when the neutrino masses are degenerate, with a zero value excluded at around 96% confidence. For σ_8 the inclusion of the XLF prior significantly reduces the best-fit value and the error bars for all CMB data set combinations. A similar, but less pronounced, effect is seen for z_{re} .

	WMAP	WMAP+VSA	ALLCMB
$\Omega_b h^2$	$0.025^{+0.003}_{-0.003}$	$0.024^{+0.003}_{-0.002}$	$0.023^{+0.002}_{-0.002}$
$\Omega_{dm} h^2$	$0.108^{+0.022}_{-0.021}$	$0.111^{+0.021}_{-0.019}$	$0.113^{+0.017}_{-0.017}$
h	$0.66^{+0.07}_{-0.06}$	$0.66^{+0.06}_{-0.06}$	$0.65^{+0.07}_{-0.07}$
z_{re}	18^{+7}_{-7}	19^{+7}_{-7}	17^{+7}_{-8}
Ω_k	$-0.02^{+0.03}_{-0.03}$	$-0.01^{+0.03}_{-0.03}$	$-0.02^{+0.03}_{-0.03}$
f_ν	< 0.093	< 0.083	< 0.083
w	$-1.00^{+0.24}_{-0.27}$	$-0.99^{+0.24}_{-0.27}$	$-1.06^{+0.24}_{-0.25}$
n_S	$1.04^{+0.12}_{-0.11}$	$0.99^{+0.09}_{-0.09}$	$0.96^{+0.07}_{-0.07}$
n_T	$0.26^{+0.53}_{-0.60}$	$0.13^{+0.49}_{-0.51}$	$0.12^{+0.48}_{-0.51}$
n_{run}	$-0.02^{+0.07}_{-0.05}$	$-0.04^{+0.05}_{-0.04}$	$-0.04^{+0.04}_{-0.05}$
$10^{10} A_S$	27^{+8}_{-5}	26^{+9}_{-5}	25^{+6}_{-5}
R	< 0.78	< 0.77	< 0.68
Ω_Λ	$0.71^{+0.07}_{-0.09}$	$0.70^{+0.06}_{-0.08}$	$0.69^{+0.07}_{-0.09}$
t_0	$14.1^{+1.4}_{-1.1}$	$14.1^{+1.3}_{-1.2}$	$14.4^{+1.4}_{-1.3}$
Ω_m	$0.31^{+0.09}_{-0.07}$	$0.31^{+0.08}_{-0.06}$	$0.33^{+0.10}_{-0.07}$
σ_8	$0.76^{+0.14}_{-0.14}$	$0.77^{+0.13}_{-0.13}$	$0.76^{+0.11}_{-0.12}$
τ	$0.20^{+0.13}_{-0.11}$	$0.20^{+0.15}_{-0.10}$	$0.17^{+0.12}_{-0.10}$

Table 4: Parameter estimates and 68% confidence intervals for various cosmological parameters. For f_ν and R , the 95% upper limits are quoted.

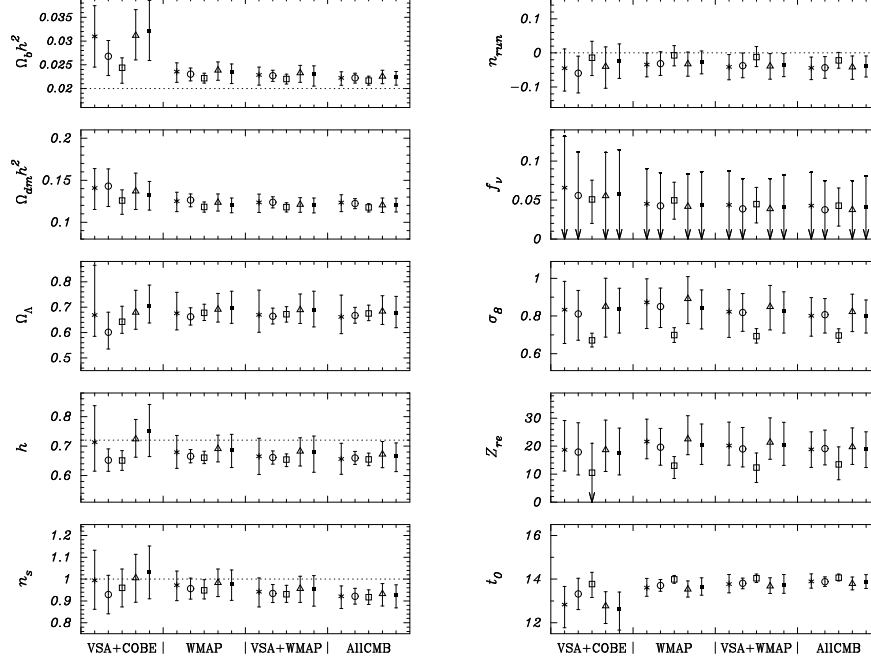


Figure 3: Estimates for cosmological parameters in the flat Λ CDM running spectral index model, extended to include f_ν . Four CMB data sets are considered and, for each data set, four determinations are plotted, corresponding to different combinations of external priors. From left to right the external priors are: 2dF; 2dF+ f_{gas} ; 2dF+ $f_{\text{gas}}+\text{XLF}$; 2dF+HST and 2dF+CS. The points indicate the median of the corresponding marginal distributions. The error bars denote 68% confidence limits. If a distribution peaks at zero then the 95% upper limit is shown. The horizontal dashed lines plotted in some of the panels indicate BBN values for $\Omega_b h^2$, the value of h given by the HST key project, the Harrison-Zeldovich value of the spectral index of fluctuations and a zero value for the running index.

8.4 General Λ CDM model

Thus far we have considered only a limited range of flat Λ CDM models. In principle, one should properly include all the relevant unknowns into the analysis in order to obtain conservative confidence limits. In this section, we consider a more general Λ CDM model. In addition to including f_ν and n_{run} , the standard six-parameter flat Λ CDM model is further extended by including Ω_k , w , $R = A_T/A_S$ and n_T . This gives 12 variable parameters in total, for which we adopt the top-hat priors listed in Table 8.2.

For this model, we consider the three CMB data sets WMAP, WMAP+VSA and ALLCMB. In addition, we now use both 2dF and SNeIa as our basic external priors, which are required in order to set constraints on our 12-dimensional cosmological parameter space. The corresponding confidence limits on the parameter values are given in Table 8.3.

For $\Omega_b h^2$ we see a clear trend towards a lower preferred value (closer to the BBN estimate) as one adds first VSA data and then all remaining CMB data sets. This effect is accompanied by a gradual upwards trend in the preferred $\Omega_{\text{dm}} h^2$ value. The other parameters exhibiting such trends are n_S and n_{run} . As more CMB data are included, the preferred value of n_S moves slightly below unity, although this value is by no means excluded. Perhaps more importantly, the upper limit on n_S is significantly reduced as more CMB data are added. An analogous effect is observed for n_{run} , for which the addition of VSA data significantly reduces the tail of the distribution for positive values of n_{run} .

We see that the inclusion of the f_{gas} and XLF external priors has the greatest effect on the confidence limits, and that this is most pronounced for the XLF prior and the parameters f_ν , σ_8 and z_{re} . It is reassuring, however, that the derived limits on f_ν for the general model are very similar to those obtained assuming the simpler flat model. We again find $f_\nu \approx 0.05$, with a zero-value excluded at about 92% confidence which is slightly lower than for the flat case. The effect of the XLF prior on σ_8 and z_{re} in the general model is also similar to that observed in the simpler flat case.

9 Conclusions

We have used recent data from the Very Small Array, together with other CMB datasets and external priors, to set constraints on cosmological parameters. We have considered both flat and non-flat Λ CDM models and the results are consistent.

Within the flat Λ CDM model, we find that the inclusion of VSA data suggests that the initial fluctuation spectrum that is not described by a single power-law. The negative running, which reduces the amount of power on small scales and hence the amount of structure at early times, leads to predictions for the epoch of reionization at odds with the best fit to the CMB data. We shall caution that this result may

be affected by the absolute calibration uncertainty of the VSA power spectrum and the residual point source correction due to sources below our subtraction limit of 20mJy. It is possible that an imperfect subtraction, either an over-estimate or an under-estimate, could lead to inaccuracies in the derived limits on the cosmological parameters, in particular on n_S and n_{run} .

For the general 12-parameter Λ CDM model, we find that our marginalized distributions for n_S and n_{run} are broadened, as one would expect. Nevertheless, even in this case, the addition of VSA data significantly reduces tails of the distributions for n_S greater than unity and for positive n_{run} , as compared with using WMAP as the only CMB data set. Indeed, these effects are reinforced by the use of the ALLCMB data set. The inclusion of additional CMB data beyond WMAP also leads to a noticeable reduction in the preferred value of ω_b and a corresponding increase in ω_{dm} .

To summarize, we find that there is evidence for $n_{\text{run}} < 0$ in a limited class of models, but within the general Λ CDM model with 12 parameters the evidence is much weaker. Standard models of inflation are generally incompatible with such large negative values of n_{run} , but the data appears to point in that direction, although not totally conclusively. The inclusion of an external prior from 2dF appears to weaken the result by fixing $\Omega_m \approx 0.3$ in conjunction with the CMB data. The measurement of $\Omega_m h$ using the galaxy power spectrum is responsible for this shift. It is an interesting question as to how reliable this measurement is since a slight shift in the results, a preference for $\Omega_m h \approx 0.17$ rather than $\Omega_m h \approx 0.21$ would bring their preferred value into line with that suggested by the CMB alone and would uphold the possibility of $n_{\text{run}} < 0$. Since none of the galaxy redshift surveys have conclusively observed the turnover in the power spectrum on which this determination of $\Omega_m h$ is based we assert that there is still room for some doubt. We set an upper limit on the mass of each of the three neutrino flavours of $m_\nu < 0.32\text{eV}$ (95 C.L.). We have shown that measurements of the CMB power spectrum beyond $\ell = 1000$ can have an impact on the estimation of cosmological parameters and that future measurements in this region by the VSA, the PLANCK satellite and others will enable us in the future to make more definitive statements.

Acknowledgements: We thank the staff of Jodrell Bank Observatory, Mullard Radio Astronomy Observatory and IAC for assistance in the day-to-day operation of the VSA. We thank PPARC and the IAC for funding and supporting the VSA project. Partial financial support was provided by Spanish Ministry of Science and Technology project AYA2001-1657.

References

- [1] Fixen, D. J., Cheng, E. S., Gales, J. M., Mather, J. C., Shafer, R. A., Wright, E. L. 1996, ApJ, 473, 576

- [2] Peebles, P.J.E. and Yu, J. T. 1970, ApJ, 162, 815
- [3] Sunyeav, R. A., Zeldovich, Y. B. 1970, ApJSS, 7, 3
- [4] Smoot G. F. et al. 1992, ApJ, 396, L1
- [5] de Bernardis, P. et al. 2000, Nature, 404, 955
- [6] Lee A. T. et al. 2001, ApJ, 561, L1
- [7] Netterfield C. B. et al. 2002, ApJ, 571, 604
- [8] Halverson N. W. et al. 2002, ApJ, 568, 38
- [9] Benoit A. et al. 2003, A&A, 399, L19
- [10] Scott P. F. et al. 2003, MNRAS, 341, 1076
- [11] Pearson T. J. et al. 2003, ApJ, 591, 556
- [12] Grainge K.J.B. et al. 2003, MNRAS, 341, L23
- [13] Kuo C. L. et al. 2004, ApJ, 600, 32
- [14] Bennett C. L. et al. 2003a, ApJSS, 148, 1
- [15] Hinshaw, G. et al. 2003a, ApJSS, 148, 135
- [16] Spergel D. N. et al. 2003, ApJSS, 148, 175
- [17] Dickinson C. et al. 2004, MNRAS, submitted
- [18] White, M., Carlstrom, J. E., Dragovan, M., and Holzapfel, W. L. 1999, ApJ, 514, 12
- [19] Rebolo R. 2002, Space Sci. Rev., 100, 15
- [20] White, M., Srednicki, M. 1995, ApJ, 443, 6
- [21] Webster, A. 1994, MNRAS, 268, 299
- [22] Church, S. E. 1995, MNRAS, 272, 551
- [23] Dicker, S. R., Melhuish, S. J., Davies, R. D., Gutiérrez, C. M., Rebolo, R., Harrison, D. L., Davis, R. J., Wilkinson, A., Hoyland, R. J., Watson, R.A. 1999, MNRAS, 309, 750
- [24] Harrison, D. L., Rubiño-Martín, J. A., Melhuish, S. J., Watson, R.A., Davies, R.D., Rebolo, R., Davis, R. J., Gutiérrez, C. M., Macías-Pérez 2000, MNRAS, 316, L24
- [25] Padin et al. 2001, ApJ, 549, L1
- [26] Watson R. A. et al. 2003, MNRAS, 341, 1057
- [27] Taylor A. C. et al. 2003, MNRAS, 341, 1066
- [28] Ebeling, H., Edge, A. C., Böhringer, H., Allen, S. W., Crawford, C. S., Fabian, A. C., Voges, W., Huchra, J. P. 1998, MNRAS, 301, 881
- [29] Abell G. O. 1958, ApJSS, 3, 211
- [30] Condon, J. J., Cotton, W. D., Greisen, E. W., Yin, Q. F., Perley, R. A., Taylor, G. B., Broderick, J. J. 1998, AJ, 115, 1693
- [31] Gregory, P. C., Scott, W. K., Douglas, K., Condon, J. J. 1996, ApJSS, 103, 427
- [32] Maisinger, K., Hobson, M. P., Saunders, R.D.E., Grainge, K.J.B. 2003, MNRAS, 345, 800
- [33] Mason, B. S., Leitch, E. M., Myers, S. T., Cartwright, J. K., Readhead, A.C.S. 1999, AJ, 118, 2908
- [34] Page L. et al. 2003, ApJSS, 148, 39

- [35] Waldram, E. M., Pooley, G. G., Grainge, K.J.B., Jones, M. E., Saunders, R.D.E., Scott, P. F., Taylor, A. C. 2003, MNRAS, 342, 915
- [36] Toffolatti, L., Argueso Gomez, F., de Zotti, G., Mazzei, P., Franceschini, A., Danese, L., Burigana, C. 1998, MNRAS, 297, 117
- [37] Giardino, G., Banday, A.J., Fosalba, P., Górski, K. M., Jonas, J. L., O'Mullane, W., Tauber, J. 2001, A&A, 371, 708
- [38] Haslam, C.G.T., Klein, U., Salter, C. J., Stoffel, H., Wilson, W. E., Cleary, M. N., Cooke, D. J., Thomasson, P. 1981, A&A, 100, 209
- [39] Haffner, L. M., Reynolds, R. J., Tufte, S. L., Madsen, G. J., Jaehnig, K. P., Percival, J. W. 2003, ApJSS, 149, 405
- [40] Schlegel, D. J., Finkbeiner, D. P., Davis, M. 1998, ApJ, 500, 525
- [41] de Oliveira-Costa, A., Tegmark, M., Davies, R. D., Gutiérrez, C. M., Lasenby, A. N., Rebolo, R., Watson, R. A., ApJ, submitted (astro-ph/0312039)
- [42] Draine, B. T., Lazarian, A. 1998, ApJ, 494, L19
- [43] Zeldovich, Y. B., Sunyaev, R. A. 1969,ApJSS, 4, 301
- [44] Battye, R. A., Weller, J. 2003, Phys. Rev. D, 68, 083506
- [45] Maisinger, K., Hobson, M. P., Lasenby, A. N. 1997, MNRAS, 290, 313
- [46] Hobson, M. P., Maisinger, K. 2002, MNRAS, 334, 569
- [47] Verde L. et al. 2003, ApJSS, 148, 195
- [48] Peiris, H. V. et al. 2003, ApJSS, 148, 213
- [49] Leach, S., Liddle, A. R. 2003, astro-ph/0306305
- [50] Bennett, C. L. et al. 1996, ApJ, ApJ, 464, L1
- [51] Kogut A. et al. 2003, ApJSS, 148, 161
- [52] Hanany S. et al. 2002, ApJ, 545, L5
- [53] Freedman W. L. et al. 2001, ApJ, 553, 47
- [54] Colless M. et al 2001, MNRAS, 328, 1039
- [55] Percival W. J. et al. 2001, MNRAS, 327, 1297
- [56] Percival W. J. et al. 2002, MNRAS, 337, 1068
- [57] Perlmutter S. et al. 1999, ApJ, 517, 565
- [58] Reiss A. et al. 1998, AJ, 116, 1009
- [59] Allen, S., Schmidt, R. W., Fabian, A. C. 2002, MNRAS, 334, L11
- [60] Allen, S., Schmidt, R. W., Fabian, A. C., Ebeling, H. 2003a, MNRAS, 342, 287
- [61] Hoekstra, H., Yee, H.K.C., Gladders, M. D. 2002, ApJ, 577, 595
- [62] Lewis, A. L., Bridle S. L. 2002, PRD, 66, 103511
- [63] Slosar, A. et al. 2003, MNRAS, 341, L29
- [64] Burles, S., Nollett, K. M., Turner, M. S. 2001,ApJ, 552, L1
- [65] Fukuda Y. et al. 1998, Phys. Rev. Lett., 81, 1562
- [66] Fukuda Y. et al. 2002, Phys. Lett. B, 539, 179
- [67] Allison W.W.M. et al. 1999, Phys. Lett. B, 449, 137
- [68] Ambrosio M. et al 2000, Phys. Lett. B, 478, 5
- [69] Allen, S. W., Schmidt, R. W., Bridle, S. L. 2003b, MNRAS, 346, 596
- [70] Cleary, K. 2003, Ph.D thesis, University of Manchester

WHITE DWARFS AND THE AGE OF THE UNIVERSE

JORDI ISERN

Institut d'Estudis Espacials de Catalunya, E-08034 Barcelona, SPAIN

*Institut de Ciències de l'Espai (Consejo Superior de Investigaciones Científicas),
E-08034 Barcelona, SPAIN*

ENRIQUE GARCIA-BERRO

Institut d'Estudis Espacials de Catalunya, E-08034 Barcelona, SPAIN

*Departament de Física Aplicada, Escola Politècnica Superior de Castelldefels,
Universitat Politècnica de Catalunya, E-08860 Castelldefels, SPAIN*

Abstract: White dwarfs are the final remnants of low and intermediate mass stars. Their evolution is essentially a cooling process that lasts for ~ 10 Gyr and allows to obtain information about the age of the Galaxy as well as about the past stellar formation rate in the solar neighborhood. One of the most important applications is to pose a severe constrain to the age of the Universe. For this reason it is important to identify all the relevant sources of energy as well as the mechanisms that control its flow to the space. In this paper we describe the state of the art of the white dwarf cooling theory and we discuss the uncertainties still remaining.

1 Introduction

The test of self-consistency that all the cosmological models have to fulfill is that the Universe cannot be younger than anyone of the objects it contains. For this reason a huge effort has been invested to identify and determine the age of the oldest objects in the Universe: globular clusters and long-lived stars. In this contribution we examine the role that white dwarfs can play in this affair.

White dwarfs represent the last evolutionary stage of stars with masses smaller than $10 \pm 2 M_{\odot}$, with the upper mass limit not yet well known. Most of them are composed of carbon and oxygen, but white dwarfs with masses smaller than $0.4 M_{\odot}$ are made of helium, while those more massive than $\sim 1.05 M_{\odot}$ are made of oxygen and neon. The exact composition of the carbon-oxygen cores critically depends on the evolution during the previous asymptotic giant branch phase, and more specifically on the competition between the $^{12}\text{C}(\alpha, \gamma)^{16}\text{O}$ reaction and the triple- α reaction, on the details of the stellar evolutionary codes and on the choice of several other nuclear

cross sections. In a typical case, a white dwarf of $0.58 M_{\odot}$, the total amount of oxygen represents the 62% of the total mass while its concentration in the central layers of the white dwarf can be as high as 85%.

In all cases, the core is surrounded by a thin layer of pure helium with a mass in the range of 10^{-2} to $10^{-4} M_{\odot}$. This layer is, in turn, surrounded by an even thinner layer of hydrogen with mass lying in the range of 10^{-4} to $10^{-15} M_{\odot}$. This layer is missing in 25% of the cases. From the phenomenological point of view, white dwarfs containing hydrogen are classified as DA while the remaining ones (the non-DA) are classified as DO, DB, DQ, DZ and DC, depending on their spectral features, and constitute a sequence of decreasing temperatures. The origin of these spectral differences and the relationship among them is not yet elucidated although it is related to the initial conditions imposed by the evolution of AGB stars, the diffusion induced by gravity, thermal diffusion, radiative levitation, convection at the H-He and He-core interfaces, proton burning, stellar winds and mass accretion from the interstellar medium.

The structure of white dwarfs is sustained by the pressure of degenerate electrons and these stars cannot obtain energy from thermonuclear reactions. Therefore, their evolution can be described just as a simple cooling process [1] in which the internal degenerate core acts as a reservoir of energy and the outer non-degenerate layers control the energy outflow. If it is assumed that the core is isothermal, which is justified by the high conductivity of degenerate electrons, and that the envelope is thin, then

$$L \approx -\frac{dU_{\text{th}}}{dt} = -\bar{c}_{\text{V}} M_{\text{WD}} \frac{dT_{\text{c}}}{dt} \quad (1)$$

where U_{th} is the thermal content, \bar{c}_{V} is the average specific heat, T_{c} is the temperature of the (isothermal) core and all the remaining symbols have their usual meaning. To solve this equation it is necessary to provide a relationship among the luminosity and the temperature of the core:

$$\frac{L}{M_{\text{WD}}} = f(T_{\text{c}}) \quad (2)$$

A simple calculation indicates that the lifetime of these stars is very long, ~ 10 Gyr, and thus they retain important information about the past history of the Galaxy. In particular, it is possible to obtain the stellar formation rate and the age of the different galactic components: disk, halo and globular clusters.

2 The evolution of the envelope

As it has been mentioned earlier, the envelope of white dwarf stars is a very thin layer ($M_{\text{e}} < 10^{-2} M_{\odot}$), partially degenerate, partially or totally ionized and sometimes

convective, that completely controls the emergent flux of energy. Its behavior is the result of:

1. A non-standard initial chemical composition resulting from hydrogen and helium shell burning in AGB stars,
2. A very efficient gravitational settling that induces the stratification of the envelope in almost chemically pure layers with the lightest element in the top [2], and
3. The existence of mechanisms tending to restore the homogeneity, like convective mixing [3, 4, 5, 6], radiative levitation [7, 8], thermal diffusion [2], accretion from the interstellar medium [9], winds and so on.

There is now a broad opinion that the distinction among the character DA and non-DA is inherited (i.e., it is linked to the origin of the white dwarf itself) although a fraction of them can change their external aspect during the evolution [10]. Standard evolution theory predicts that typical field white dwarfs have a core mass in the range of 0.5 to 1.0 M_{\odot} made of a mixture of carbon and oxygen surrounded by a helium mantle of $M_{\text{He}} \simeq 10^{-2} M_{\text{WD}}$, surrounded itself by a hydrogen envelope of $M_{\text{H}} \simeq 10^{-4} M_{\text{WD}}$ [3, 11, 12]. Adjusting the parameters in the AGB models it is possible to obtain in the 25% of the cases a white dwarf totally devoid of the hydrogen layer. Since the relative number of DA/non-DA stars changes as the evolution proceeds, a mechanism able to change this property must exist [10, 13].

The idea is that DA white dwarfs start as a central star of a planetary nebula. When its temperature is high enough ($T_{\text{eff}} > 40,000$ K) radiative levitation brings metals to the photosphere and heavy element lines appear in its spectrum. As the temperature goes down, these elements settle down and disappear. When DAs arrive to the instability strip they pulsate as ZZ Ceti stars. Pulsational data indicates that the masses of the hydrogen layer are in the range between 10^{-8} and $10^{-4} M_{\odot}$ thus indicating that DAs are born with a variety of layer masses. As the DA star cools down, the convective region deepens and, depending on the mass, reaches the helium layer. When this happens, helium is dredged up and the DA white dwarf turns into a non-DA. Consequently, the ratio between the number of DAs and non-DAs decreases. Stars with a thin H layer ($< 10^{-9} M_{\odot}$) mix at high temperatures while those having a thick layer ($\sim 10^{-4} M_{\odot}$) never do it.

The evolution of a non-DA star is more complex. They are born as He-rich central stars of planetary nebulae and, as they cool down, they become first PG 1159 stars and then DO stars. The trace amounts of hydrogen still present in the helium envelope gradually float up to the surface and when the effective temperature is of the order of 50,000 K the outer H layer becomes thick enough to hide the He layer and to convert the star into a DA star. When the temperature drops below 30,000 K,

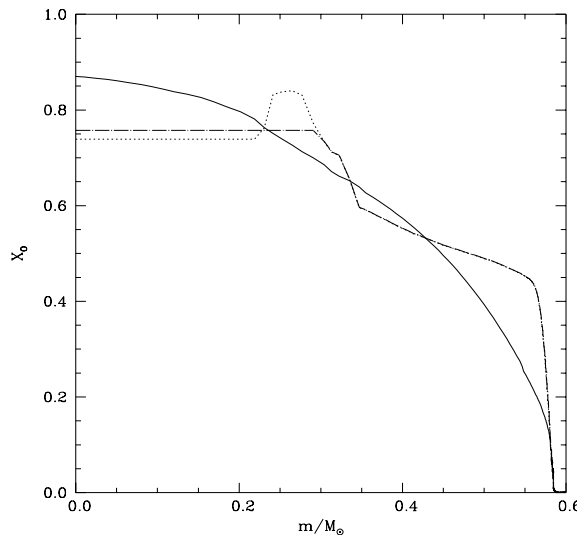


Figure 1: Oxygen profile of a $0.61 M_\odot$ white dwarf at the beginning of the thermally-pulsing AGB phase (dotted line), the same after rehomogenization by Rayleigh-Taylor instabilities during the liquid phase (dotted-dashed line) and after total freezing (solid line).

the helium convection zone increases and hydrogen is engulfed and mixed within the helium layer once more. The white dwarf is observed as a non-DA, more precisely as a DB. This lack of non-DA stars in the temperature range of 30,000 to 45,000 K is known as the DB gap. The DB stars gradually cool down and become DZ and DC stars (a fraction of them being DAs in origin). Due to the convective dredge up at the bottom of the helium envelope, some of the non-DAs show carbon in their spectra (DQ stars). Because of accretion from the interstellar medium some of them show hydrogen lines in their spectrum (they are known as DBA class).

3 Overview of white dwarf evolution

The evolution of white dwarfs from the planetary nebula phase to its disappearance depends on the properties of the envelope and the core and has been discussed in detail [11, 12, 14, 15, 16]. To summarize, the cooling process can be roughly divided in four stages: neutrino cooling, fluid cooling, crystallization and Debye cooling.

- *Neutrino cooling:* $\log(L/L_\odot) > -1.5$. This stage is very complicated because of the dependence on the initial conditions of the star as well as on the complex and not yet well understood behavior of the envelope. For instance, it

has been found that the luminosity due to hydrogen burning through the pp chains would never stop and could even become dominant at low luminosities, $-3.5 \leq \log(L/L_\odot) \leq -1.5$. It is worth noting that, if this were the case, the cooling rate would be similar to the normal one (i.e., the one that neglects this source) and it would be observationally impossible to distinguish between both possibilities. However, the importance of such a source strongly depends on the mass, M_H , of the hydrogen layer. If $M_H \leq 10^{-4} M_\odot$, the pp contribution quickly drops and never becomes dominant. Since astero-seismological observations seem to constrain the size of M_H well below this critical value, this source can be neglected. Fortunately, when neutrino emission becomes dominant, the different thermal structures converge to a unique one, making sure the uniformity of the models with $\log(L/L_\odot) \lesssim -1.5$. Furthermore, since the time necessary to reach this value is $\lesssim 8 \times 10^7$ years for any model, its influence in the total cooling time is negligible.

- *Fluid cooling:* $-1.5 \geq \log(L/L_\odot) \geq -3$ The main source of energy is the gravothermal one. Since the plasma is not very strongly coupled ($\Gamma < 179$), its properties are reasonably well known. Furthermore, the flux of energy through the envelope is controlled by a thick nondegenerate layer with an opacity dominated by hydrogen (if present) and helium, and weakly dependent on the metal content. The main source of uncertainty is related to the chemical structure of the interior, which depends on the adopted rate of the $^{12}\text{C}(\alpha, \gamma)^{16}\text{O}$ reaction and on the treatment given to semiconvection and overshooting. If this rate is high, the oxygen abundance is higher in the center than in the outer layers, resulting thus in a reduction of the specific heat at the central layers where the oxygen abundance can reach values as high as $X_O = 0.85$ [17].
- *crystallization:* $\log(L/L_\odot) < -3$. Crystallization introduces two new sources of energy: latent heat and sedimentation. In the case of Coulomb plasmas, the latent heat is small, of the order of $k_B T_s$ per nuclei, where k_B is the Boltzmann constant and T_s is the temperature of solidification. Its contribution to the total luminosity is between ~ 5 and 10% [18].

During the crystallization process, the equilibrium chemical compositions of the solid and liquid plasmas are not equal. Therefore, if the resulting solid is denser than the liquid mixture, it sink towards the central region. If they are lighter, they rise upwards and melt when the solidification temperature, which depends on the density, becomes equal to that of the isothermal core. The net effect is a migration of the heavier elements towards the central regions with the subsequent release of gravitational energy [19]. Of course, the efficiency of the process depends on the detailed chemical composition and on the initial chemical profile and it is maximum for a mixture made of half oxygen and half

carbon uniformly distributed through all the star.

- *Debye cooling:* When almost all the star has solidified, the specific heat follows the Debye's law. However, the outer layers still have very large temperatures as compared with the Debye's one, and since their total heat capacity is still large enough, they prevent the sudden disappearance of the white dwarf in the case, at least, of thick envelopes.

Figure 1 displays the oxygen profiles for the CO core of a $\sim 0.6 M_{\odot}$ white dwarf progenitor obtained just at the end of the first thermal pulse (dotted line). The inner part of the core, with a constant abundance of ^{16}O , is determined by the maximum extension of the central He-burning convective region while the peak in the oxygen abundance is produced when the He-burning shell crosses the semiconvective region partially enriched in ^{12}C and ^{16}O , and carbon is converted into oxygen through the $^{12}\text{C}(\alpha, \gamma)^{16}\text{O}$ reaction. Beyond this region, the oxygen profile is built when the thick He-burning shell is moving towards the surface. Simultaneously, gravitational contraction increases its temperature and density, and since the ratio between the $^{12}\text{C}(\alpha, \gamma)^{16}\text{O}$ and 3α reaction rates is lower for larger temperatures the oxygen mass fraction steadily decreases in the external part of the CO core.

The ^{12}C and ^{16}O profiles at the end of the first thermal pulse have an off-centered peak in the oxygen profile, which is related to semiconvection. Since [17] chose the rate of [20] for the $^{12}\text{C}(\alpha, \gamma)^{16}\text{O}$ reaction, they were forced to use the Schwarzschild criterion for convection and, therefore, they did not find the chemical profiles to be Rayleigh-Taylor unstable during the early thermally-pulsing AGB phase. After the ejection of the envelope, when the nuclear reactions are negligible at the edge of the degenerate core, the Ledoux criterion can be used and, therefore, the chemical profiles are Rayleigh-Taylor unstable and, consequently, are rehomogenized by convection. Notice that, in any case, this rehomogenization minimizes the effect of the separation occurring during the cooling process. Figure 1 also shows the resulting oxygen profile after rehomogenization (dotted-dashed line), and the oxygen profile after complete crystallization (solid line).

4 The physics of the cooling

The local energy budget of the white dwarf can be written as:

$$\frac{dL_r}{dm} = -\epsilon_{\nu} - P \frac{dV}{dt} - \frac{dE}{dt} \quad (3)$$

where all the symbols have their usual meaning. If the white dwarf is made of two chemical species with atomic numbers Z_0 and Z_1 , mass numbers A_0 and A_1 , and

abundances by mass X_0 and X_1 , respectively ($X_0 + X_1 = 1$), where the suffix 0 refers to the heavier component, this equation can be written as:

$$\begin{aligned} -\left(\frac{dL_r}{dm} + \epsilon_\nu\right) &= C_v \frac{dT}{dt} + T \left(\frac{\partial P}{\partial T}\right)_{V,X_0} \frac{dV}{dt} \\ &\quad - l_s \frac{dM_s}{dt} \delta(m - M_s) + \\ &\quad \left(\frac{\partial E}{\partial X_0}\right)_{T,V} \frac{X_0}{dt} \end{aligned} \quad (4)$$

where l_s is the latent heat of crystallization and \dot{M}_s is the rate at which the solid core grows; the delta function indicates that the latent heat is released at the solidification front. Notice that chemical differentiation contributes to the luminosity not only through compressional work, which is negligible, but also through the change in the chemical abundances, which leads to the last term of this equation. Notice, as well, that the largest contribution to L_r due to the change in E exactly cancels out the $P dV$ work for any evolutionary change (with or without a compositional change). This is, of course, a well known result [1, 18, 21, 22] that can be related to the release of gravitational energy [23].

Integrating over the whole star, we obtain:

$$\begin{aligned} L + L_\nu &= - \int_0^{M_{WD}} C_v \frac{dT}{dt} dm \\ &\quad - \int_0^{M_{WD}} T \left(\frac{\partial P}{\partial T}\right)_{V,X_0} \frac{dV}{dt} dm \\ &\quad + l_s \frac{dM_s}{dt} \\ &\quad - \int_0^{M_{WD}} \left(\frac{\partial E}{\partial X_0}\right)_{T,V} \frac{dX_0}{dt} dm \end{aligned} \quad (5)$$

The first term of the equation is the well known contribution of the heat capacity of the star to the total luminosity [1]. The second term represents the contribution to the luminosity due to the change of volume. It is in general small since only the thermal part of the electronic pressure, the ideal part of the ions and the Coulomb terms other than the Madelung term contribute [18, 21]. However, when the white dwarf enters into the Debye regime, this term provides about the 80% of the total luminosity preventing the sudden disappearance of the star [22]. The third term represents the contribution of the latent heat to the total luminosity at freezing. The fourth term represents the energy released by the chemical readjustement of the white dwarf, i.e., the release of the energy stored in the form of chemical potentials. This term is usually negligible in normal stars, since it is much smaller than the energy

Mixture	ΔE (erg)	Δt (Gyr)
C/O	1.95×10^{46}	1.81
A/Ne	1.52×10^{47}	9.09
A/Fe	2.00×10^{46}	1.09
C/O/Ne	0.20×10^{46}	0.60

Table 1: Energy released by the chemical differentiation induced by crystallization and the corresponding delays.

released by nuclear reactions, but it must be taken into account when all other energy sources are small.

The last term can be further expanded and written as [23]:

$$\int_0^{M_{\text{WD}}} \left(\frac{\partial E}{\partial X_0} \right)_{T,V} \frac{dX_0}{dt} dm = (X_0^{\text{sol}} - X_0^{\text{liq}}) \left[\left(\frac{\partial E}{\partial X_0} \right)_{M_s} - \left\langle \frac{\partial E}{\partial X_0} \right\rangle \right] \frac{dM_s}{dt} \quad (6)$$

where

$$\left\langle \frac{\partial E}{\partial X_0} \right\rangle = \frac{1}{\Delta M} \int_{\Delta M} \left(\frac{\partial E}{\partial X_0} \right)_{T,V} dm \quad (7)$$

and it is possible to define the total energy released per gram of crystallized matter as:

$$\epsilon_g = -(X_0^{\text{sol}} - X_0^{\text{liq}}) \left[\left(\frac{\partial E}{\partial X_0} \right)_{M_s} - \left\langle \frac{\partial E}{\partial X_0} \right\rangle \right] \quad (8)$$

The square bracket is negative since $(\partial E / \partial X_0)$ is negative and essentially depends on the density, which monotonically decreases outwards.

The contribution of any source or sink of energy to the cooling rate can be easily computed. For instance, the delay introduced by solidification can be easily estimated to a good approximation if it is assumed that the luminosity of the white dwarf is just a function of the temperature of the nearly isothermal core [23]. In this case:

$$\Delta t = \int_0^{M_{\text{WD}}} \frac{\epsilon_g(T_c)}{L(T_c)} dm \quad (9)$$

where ϵ_g is the energy released per unit of crystallized mass and T_c is the temperature of the core when the crystallization front is located at m . Of course, the

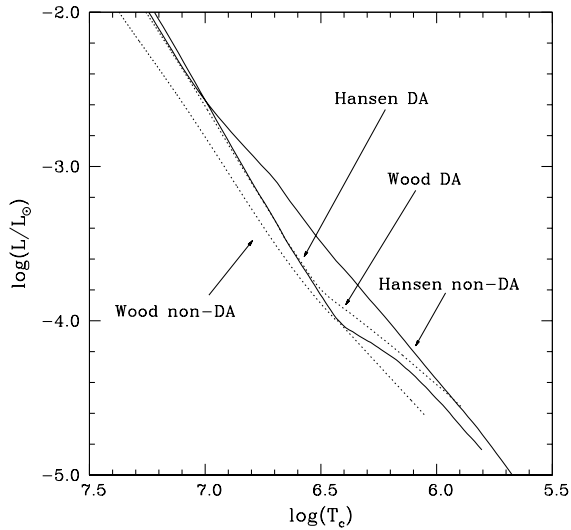


Figure 2: The relationships between the core temperature and the luminosity for various model atmospheres, see text for details.

total delay essentially depends on the transparency of the envelope. Any change in one sense or another can amplify or damp the influence of solidification and for the moment there are not reliable envelope models at low luminosities.

Table 4 displays the energy released in a, otherwise typical, $0.6 M_{\odot}$ white dwarf and the delays introduced by the different cases of solidification discussed here assuming that the envelope is the same as in [23] and [15] and that the white dwarf is made of half carbon and half oxygen. The symbol A represents the effective binary mixture. Its use is probably justified in the case of impurities of very high number such as iron. However, in the case of Ne this assumption is most probably doubtful.

As previously stated, the total delay depends on the transparency of the envelope. In order to illustrate the effects of the transparency of the envelope in the cooling times, in Figure 2 we show several different core temperature–luminosity relationships. The first model atmosphere was obtained from the DA model sequence of [24], which has a mass fraction of the helium layer of $q_{\text{He}} = 10^{-4}$ and a hydrogen layer of $q_{\text{H}} = 10^{-2}$; the second model atmosphere is the non-DA model sequence [25] which has a helium layer of $q_{\text{He}} = 10^{-4}$. However it should be noted that between these two model sequences there was a substantial change in the opacities, and therefore the comparison is meaningless (i.e., the non-DA model is more opaque than the DA one). The remaining two model atmospheres are those of [26] for both DA and non-DA white dwarfs. These atmospheres have been computed with state of the art physical inputs for both the equation of state and the opacities for the range of densities and

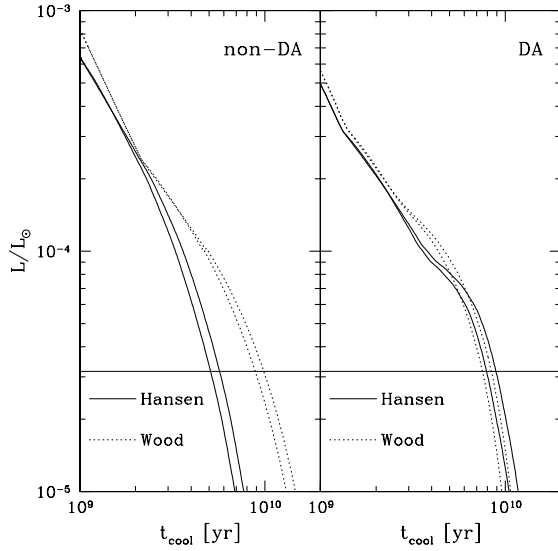


Figure 3: Cooling curves (time is in yr) for the white dwarf models described in the text, the thinner horizontal line corresponds to $\log(L/L_{\odot}) = -4.5$, which is the approximate position of the observed cut-off of the white dwarf luminosity function.

temperatures relevant for white dwarf envelopes (although it should be mentioned that the contributions to the opacity of H^{3+} and H^{2+} ions were neglected in this calculation) and have the same hydrogen and helium layer mass fractions as those of [24] and [25], respectively. In all the cases, the mass of the white dwarf is $0.606 M_{\odot}$ and the initial chemical profile of the C/O mixture is that of [17].

From Figure 2 one can clearly see that the DA model atmospheres of [24] and [26] are in very good agreement down to temperatures of the order of $\log(T_c) \simeq 6.5$, whereas at lower temperatures the model atmospheres of [26] predict significantly lower luminosities (that is, they are less transparent). In contrast, the non-DA model atmosphere of [26] is by far more transparent at any temperature than the corresponding model of [25]. This is clearly due to the fact that this model was based on the old Los Alamos opacities and include a finite contribution from metals whereas the non-DA atmospheres of [26] are made of pure helium.

With these two sets of model atmospheres [27] computed cooling sequences for the following two cases: 1) crystallization and no phase separation and 2) crystallization and phase separation. The results are shown in Figure 3. The left panel of this figure shows the cooling sequences for the non-DA model envelopes of Hansen — solid lines — and Wood & Winget — dotted lines. The sequences with phase separation correspond, obviously, to the cooling curves with larger cooling times for the same luminosity. The right panel of the figure shows the same set of calculations for the

Input	Δt (Gyr)	Comments
DA/non-DA	$\lesssim 3.0$	Very uncertain
Core composition	$\lesssim 0.5$	Depending on the $^{12}\text{C}(\alpha, \gamma)^{16}\text{O}$
Opacity	$\lesssim 0.4$	
Metals in the envelope	≈ 0.2	
Additive contributions of the crystallization process		
C/O	0.8–1.2	Depending on the $^{12}\text{C}(\alpha, \gamma)^{16}\text{O}$
Fe	$\lesssim 1.3$	
Ne	$\lesssim 9.0$	Binary mixture
	$\lesssim 0.5$	Ternary mixture
Observational	1–2	

Table 2: Uncertainties in the estimates of the cooling time of white dwarfs.

hydrogen-dominated white dwarf envelopes described previously. Clearly the cooling times are very different depending on the assumed physical characteristics of the adopted atmosphere.

Table 4 displays the uncertainties in the time necessary to fade until $\log(L/L_\odot) = -4.5$. In the lower section of this table the additive contributions to the uncertainty due to the physics of crystallization are shown, whereas the upper section describes the uncertainties due to the rest of the input physics. As it can be seen, the major contribution is provided by the minor chemical species.

On the other hand, it is worth noticing at this point that white dwarfs provide the unique opportunity to check their cooling process in nearly real time. In particular, it is of interest to note that among white dwarfs there is a specific class of stars, known as ZZ-Ceti objects, which have a hydrogen-rich envelope (thus being classified as DA white dwarfs) and show periodic variations in their light curves. G117-B15A belongs to this particular set of stars. The observed periods of pulsation are 215.2, 271 and 304.4 s together with harmonics and linear combinations of the quoted periods, being the dominant pulsation mode the 215.2 s mode. The luminosity variations have been successfully explained as due to g -mode pulsations. G117-B15A has been recently claimed to be the most stable optical clock ever found, being the rate of change of the 215.2 s period very small: $\dot{P} = (2.3 \pm 1.4) \times 10^{-15} \text{ s s}^{-1}$, with a stability comparable to that of the most stable millisecond pulsars [28]. The rate of change of the period is closely related to its cooling timescale, which can be accurately computed, thus offering a unique opportunity to test any additional (or hypothetical) sink of energy.

$$\frac{d \ln P}{dt} \propto -\frac{d \ln T}{dt} \propto \frac{1}{\tau_{\text{cool}}} \quad (10)$$

We have looked for a model that matches the three observed modes as good

as possible [29]. The model that provides the best fit to the observations is $M_\star = 0.55 M_\odot, l = 1, k = 2, 3, 4$ and $\log M_H/M_\star = -4.0$. The rate of change of the period for this model is $\dot{P} = 3.9 \times 10^{-15} \text{ s s}^{-1}$. Therefore, the agreement between observations and theory is better than a factor of two. After examining all the possible uncertainties a few words are necessary to justify the discrepancy between this value and the measured rate of change of the period of the 215.2 s mode, $\dot{P} = (2.3 \pm 1.4) \times 10^{-15} \text{ s s}^{-1}$, and its computed value for the fiducial model. First, the theoretical uncertainties performed in this work can account for a spread of about $\pm 1 \times 10^{-15} \text{ s s}^{-1}$. Second, the parallax and proper motion [28, 30] contribute as much as $\dot{P} = (9.2 \pm 0.5) \times 10^{-16} \text{ s s}^{-1}$. We thus conclude that taking into account all this uncertainties our preferred model could be safely considered as satisfactory and that our value for \dot{P} is fully consistent with the observed rate of change of the period.

5 The age and the properties of the Galactic disk and halo

The white dwarf luminosity function is defined as the number of white dwarfs with bolometric magnitude M_{bol} per cubic parsec and unit bolometric magnitude. The first luminosity functions were obtained by [31]. Since then it has been largely improved [32, 33, 34, 35, 36]. The two main properties of this empirical luminosity function are its monotonic increase when the luminosity decreases, which indicates the cooling nature of the evolution of white dwarfs, and the existence of a short fall at $\log(L/L_\odot) \approx -4.5$ which is interpreted as a consequence of the finite age of the Galaxy. From the comparison between this empirical function and the theoretical one, it is possible to obtain the age of the disk, T , and the star formation rate, $\Psi(t)$, as a function of time [37, 38, 39, 40, 41].

Regarding the luminosity function of halo white dwarfs very few things can be said due to the lack of observational data. However there have been considerable efforts to improve the actual situation [42, 43]. Hopefully, future missions like GAIA will remedy this situation [44].

The luminosity function can be computed as

$$n(l) \propto \int_{M_i}^{M_s} \Phi(M) \Psi(T - t_{\text{cool}}(l, M) - t_{\text{MS}}(M)) \tau_{\text{cool}}(l, M) dM \quad (11)$$

where l is the logarithm of the luminosity in solar units, M is the mass of the parent star (for convenience all white dwarfs are labelled with the mass of the main sequence progenitor), t_{cool} is the cooling time down to luminosity l , $\tau_{\text{cool}} = dt/dM_{\text{bol}}$ is the characteristic cooling time, M_s and M_i are the maximum and the minimum masses of the main sequence stars able to produce a white dwarf of luminosity l , t_{MS} is the main sequence lifetime of the progenitor of the white dwarf, and T is the age

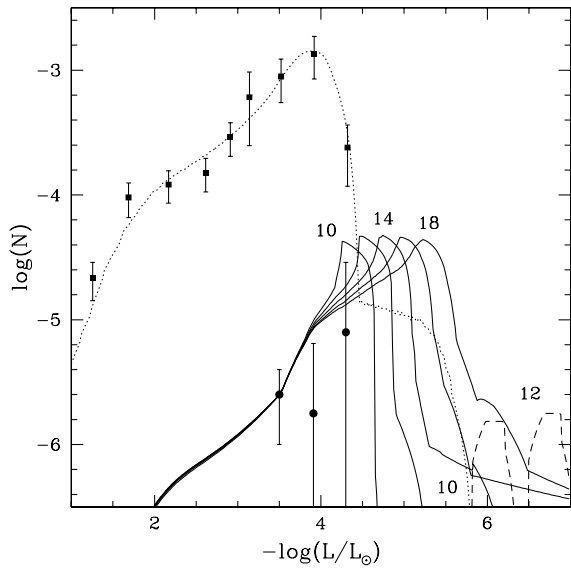


Figure 4: Luminosity functions of disk and halo white dwarfs as a function of the luminosity.

of the population under study. The remaining quantities, the initial mass function, $\Phi(M)$, and the star formation rate, $\Psi(t)$, are not known a priori and depend on the astronomical properties of the stellar population under study.

In order to compare with the observations properly, it is convenient to bin this function in intervals of magnitude ΔM_{bol} , usually one or half magnitudes, in the following way:

$$\langle n(l) \rangle_{\Delta l} = \frac{1}{\Delta l} \int_{l-0.5\Delta l}^{l+0.5\Delta l} n(l) dl \quad (12)$$

where Δl is the size of the luminosity bin that corresponds to ΔM_{bol} . It is important to notice here that this binning procedure smooths and ultimately erases the spikes introduced by the sedimentation of Ne and Fe in the observational luminosity function. Therefore, in order to observationally detect the influence of these impurities it would be necessary to have high resolution luminosity functions.

Figure 4 displays the luminosity functions of halo and disk white dwarfs computed with the standard initial mass function. The adopted cooling sequences were those of those from [17], which do not include the effects of Ne and Fe. The theoretical luminosity functions were normalized to the points $\log(L/L_{\odot}) \simeq -3.5$ and $\log(L/L_{\odot}) \simeq -2.9$ for the halo and the disk respectively due to their smaller error bars [45]. The luminosity function of the disk was obtained assuming an age of the

disk of 9.2 Gyr and a constant star formation rate per unit volume for the disk, and those of the halo assuming a burst that lasted 0.1 Gyr and started at $t_{\text{halo}} = 10, 12, 14, 16$ and 18 Gyr respectively. Due to their higher cooling rate, O–Ne white dwarfs produce a long tail in the disk luminosity function and a bump (only shown in the cases $t_{\text{halo}} = 10$ and 12 Gyr) in the halo luminosity function. The detection of such peaks should allow the determination of the age of the galactic halo.

During the derivation of the age of the disk it has been assumed that the star formation rate per unit volume has remained constant all the time along the life of our Galaxy. However, some models of galactic evolution predict that the process of formation of stars started in the central regions of the Galaxy and propagated outwards. If this was the case, a gradual instead of a prompt increase of the star formation rate would be expected. As it can be seen from the definition of the luminosity function, it is impossible to separate the age of the Galaxy from the star formation rate because of the extremely long lifetimes of low mass main sequence stars. That is, very old low mass main sequence stars are able to produce young (in the sense of cooling times) and bright white dwarfs. This implies that the past star formation activity is still influencing the present white dwarf birthrate. This property offers the unique opportunity to obtain the true age of the solar neighborhood instead of just providing a lower limit [41].

The star formation rate can be obtained by solving the inverse problem posed by the definition of the luminosity function. However, since the kernel of the transformation is not symmetric and has a complicated behavior [41], it is not possible to obtain a direct solution and its unicity cannot be guaranteed. Therefore, the only procedure consists in the adoption of a trial function as a star formation rate. This trial function depends on a set of \mathbf{p} parameters, and we search for the values of these parameters that best fit the observed luminosity function. That is, we minimize the following function:

$$f(\mathbf{p}) = \sum_{i=1}^n \left[\frac{\phi_i(\mathbf{p}) - \Phi_i(l_i)}{\delta\Phi_i} \right]^2 \quad (13)$$

where $\phi_i(\mathbf{p})$ and Φ_i are the computed and the observed values of the luminosity function, respectively, and $\delta\Phi_i$ are the corresponding error bars of each bin.

As trial functions we have chosen the following three cases:

1. A constant star formation rate, Ψ ;
2. An almost constant star formation rate plus a relatively extended tail:

$$\Psi(t) \propto \frac{1}{1 + e^{(t-\tau)/\delta}};$$

and,

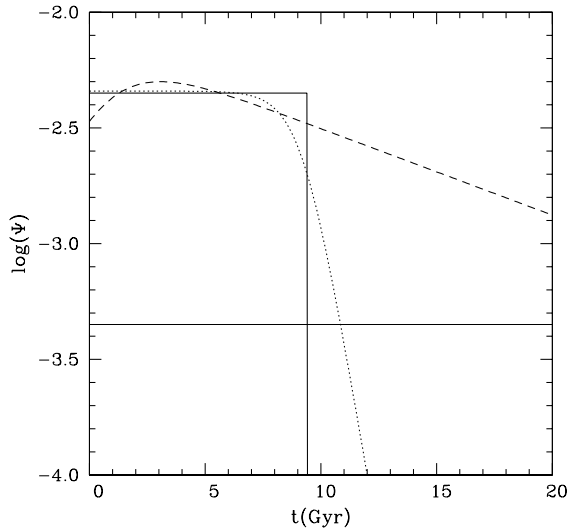


Figure 5: Star formation rates that provide a good fit to the observed luminosity function. The horizontal line correspond to 1/10 of the present star formation rate. The units of Ψ are (M_\odot pc $^{-3}$ Gyr $^{-1}$).

3. A star formation rate per unit surface that decreases with a timescale τ_s , divided by an scale height above the galactic plane that decreases with a timescale τ_h :

$$\Psi(t) \propto \frac{e^{-t/\tau_s}}{1 + A e^{-t/\tau_h}}.$$

As it is obvious the fits are better when more parameters are considered [41].

Figure 5 displays the star formation rates obtained by solving the inverse problem. It is clear that this function has remained nearly constant, within a factor 2, during the last 9–12 Gyr and that this behavior is compatible with a previous epoch, that could have lasted 2–8 Gyr, of lower activity before reaching the present values. The age of the solar neighborhood obtained in cases 1, 2 and 3 are 9.5, 11 and 20 Gyr respectively.

It is important to notice that since the bright side of the luminosity function is insensitive to the shape of the star formation rate [45], there is a degeneracy in the set of solutions to equation 1. This degeneracy can be removed by improving the dim branch, by obtaining the luminosity of massive white dwarfs and combining these data with statistical properties of red dwarfs.

6 Conclusions

White dwarf are well studied objects and the physical processes that control their evolution are relatively well understood. In fact most phases of white dwarf evolution can be successfully characterized as a cooling process. That is, white dwarfs slowly radiate at the expense of their residual grovothermal energy. This release of energy lasts for long time scales (of the order of the age of the galactic disk: 10^{10} yr). While their detailed energy budget is still today the subject of some debate, their mechanical structures, which are largely supported by the pressure of the gas of degenerate electrons, are very well modeled except for the outer layers. These layers control the output of energy and a correct modeling is necessary to understand the evolution of white dwarfs.

The sedimentation of chemical species induced by crystallization is a major source of energy of coolest white dwarf stars. The delay introduced by the C/O partial separation is of the order of 1 Gyr (this quantity depends on the model of atmosphere adopted). Minor species present in the white dwarf can also introduce huge delays that can range from 0.5 to 9 Gyr. This uncertainty will be solved when good ternary phase diagrams are available.

White dwarfs can provide important information about the age of the galactic disk by comparing their luminosity function at low luminosities, and specially the position of its cut-off, with the theoretical predictions. For this purpose it is necessary to have good theoretical models and good observational data. From the observational point of view, the main sources of uncertainty are the distance to the lowest luminosity white dwarfs, the bolometric corrections, and the chemical composition of the outer layers (i.e., DA if hydrogen is present non-DA if hydrogen is absent). Nowadays, the contribution of the observational uncertainties to the total error budget of the galactic age can be estimated to be as large as 2 Gyr. Of this amount, 1 Gyr comes directly from the binning and sampling procedure and the statistical noise of the low luminosity bins [46].

From the observational point of view, the obtention of good luminosity functions of the disk or globular clusters with resolutions in magnitude better than 0.5 magnitudes could easily allow to test the different phase diagrams. Furthermore, an accurate luminosity function of disk white dwarfs can not only provide a tight constrain to the galactic age and to the shape of the phase diagram of binary mixtures but also has the bonus of providing important information about the temporal variation of the star formation rate.

The scarcity of bright halo white dwarfs and the lack of the good kinematical data necessary to distinguish halo white dwarfs from those of the disk have prevented up to now the construction of a good luminosity function for the halo [43] but probably future missions like GAIA will completely change the situation since high-quality parallaxes and proper motions will result in accurate tangential velocities, thus allowing

a good discrimination of these two populations.

Theoretical models indicate that if the halo is not too old, about 12 Gyr, there would be a reasonable chance to detect the corresponding cut off ($M_V \sim 16$) with surveys as deep as $m_V \sim 20$, provided that the DA specimen were dominant. On the contrary, if non-DA white dwarfs turn out to be dominant, the cut-off would be placed at absolute magnitudes as large as 20 and there would be no chance to detect it and, thus to constrain in this way the age of the halo. In any case, indirect information about the halo (age, duration of the burst,...) will come from the comparison of the absolute numbers of red halo dwarfs and white dwarfs in a complete volume limited sample. Furthermore, a robust determination of the bright part of the halo luminosity function could provide important information on the allowed IMFs for the halo and decisively contribute to the solution of the problems posed by the gravitational lensing observations in our halo. Therefore, a simultaneous and self-consistent determination of photometric properties, parallaxes and proper motions of halo white dwarfs could provide us with an unique opportunity to set up a solid platform for the study of the halo properties and to set up constraints to its dark matter content.

Acknowledgements: This work has been partially supported by the MCyT grants AYA04094-C03-01 and 02, by the European Union FEDER funds, and by the CIRIT.

References

- [1] Mestel, L. 1952, MNRAS, 112, 583
- [2] Schatzman, E. 1958, *White Dwarfs*, (Amsterdam: North-Holland)
- [3] D'Antona, F., Mazzitelli, I. 1978, A&A, 66, 453
- [4] Fontaine, G., Villeneuve, B., Wesemael, F., Wegner, G. 1984, ApJ, 227, L61
- [5] Pelletier, C., Fontaine, G., Wesemael, F., Michaud, G., Wegner, G. 1986, ApJ, 307, 242
- [6] MacDonald, J., Hernanz, M., José, J. 1998, MNRAS, 296, 523
- [7] Fontaine, G., Michaud, G. 1979, ApJ, 231, 826
- [8] Vauclair, G., Vauclair, S., Greenstein, J. 1979, A&A, 80, 79
- [9] Alcock, C., Illarionov, A. 1980, ApJ, 235, 534
- [10] Shipman, H. 1997, in *White Dwarfs*, Ed.: J. Isern, M. Hernanz, E. García-Berro (Dordrecht: Kluwer), p. 165
- [11] Iben, I., Tutukov, A. V. 1984, ApJ, 282, 615
- [12] Koester, D., Schönberner, D. 1986, A&A, 154, 125
- [13] Fontaine, G., Wesemael, F. 1997, in *White Dwarfs*, Ed.: J. Isern, M. Hernanz, E. García-Berro (Dordrecht: Kluwer), p. 173
- [14] D'Antona, F., Mazzitelli, I. 1989, ApJ, 347, 934
- [15] Ségréain, L., Chabrier, G., Hernanz, M., García-Berro, E., Isern, J., Mochkovitch, R. 1994, ApJ, 434, 641

- [16] Isern, J., García–Berro, E., Hernanz, M., Mochkovitch, R. 1998, *J. Phys.: Condens. Matter*, 10, 11263
- [17] Salaris, M., Domínguez, I., García–Berro, E., Hernanz, M., Isern, J., Mochkovitch, R. 1997, *ApJ*, 486, 413
- [18] Shaviv, G., Kovetz, A. 1976, *A&A*, 51, 383
- [19] Mochkovitch, R. 1983, *A&A*, 122, 212
- [20] Caughlan, G.R., Fowler, W.A., Harris, M.J., Zimmerman, B.A. 1985, *Atomic Data and Nuclear Data Tables*, 32, 197
- [21] Lamb, D.Q., Van Horn, H.M. 1975, *ApJ*, 200, 306
- [22] D'Antona, F., Mazzitelli, I. 1990, *ARA&A*, 28, 139
- [23] Isern, J., Mochkovitch, R., García–Berro, E., Hernanz, M. 1997, *ApJ*, 485, 308
- [24] Wood, M.A., in *White Dwarfs*, eds. Koester, D., Werner, K. 1995, (Berlin: Springer), p. 41
- [25] Wood, M.A., Winget, D.E. 1989, in IAU Colloq. 114, *White Dwarfs*, ed. Wegner, G. (Berlin: Springer), p. 282
- [26] Hansen, B.M.S. 1999, *ApJ*, 520, 680
- [27] Isern, J., García–Berro, E., Hernanz, M., Chabrier, G. 2000, *ApJ*, 528, 397
- [28] Kepler, S.O., Mukadam, A., Winget, D.E., Nather, R.E., Metcalfe, T.S., Reed, M.D., Kawaler, S.D., Bradley, P.A. 2000, *ApJ*, 534, L185
- [29] Córscico, A.H., Benvenuto, O.G., Altahus, L.G., Isern, J., García–Berro, E. 2001, *New Astronomy*, 6, 197
- [30] Pajdosz, G. 1995, *A&A*, 295, L17
- [31] Weidemann, V. 1968, *ARA&A*, 6, 351
- [32] Fleming, T.A., Liebert, J., Green, R.F. 1986, *ApJ*, 308, 176
- [33] Liebert, J., Dahn, C.C., Monet, D.G. 1988, *ApJ*, 332, 891
- [34] Oswalt, T.D., Smith, J.A., Wood, M.A., Hintzen, P. 1996, *Nature*, 382, 692
- [35] Leggett, S.K., Ruiz, M.T., Bergeron, P. 1998, *ApJ*, 497, 294
- [36] Knox, R.A., Hawkins, M.R.S., Hambly, N.C. 1999, *MNRAS*, 306, 736
- [37] García–Berro, E., Hernanz, M., Isern, J., Mochkovitch, R. 1988, *A&A*, 193, 141
- [38] Yuan, J.W. 1989, *A&A*, 224, 108
- [39] Hernanz, M., García–Berro, E., Isern, J., Mochkovitch, R., Ségrétrain, L., Chabrier, G. 1994, *ApJ*, 434, 652
- [40] Díaz–Pinto, A., García–Berro, E., Hernanz, M., Isern, J., Mochkovitch, R. 1994, *A&A*, 282, 86
- [41] Isern, J., García–Berro, E., Hernanz, M., Mochkovitch, R., Burkert, A. 1995, in “*White Dwarfs*”, ed. Koester, D., Werner, K., Lecture Notes in Physics, 443 (Berlin: Springer), p. 19
- [42] Liebert, J., Dahn, C.C., Monet, D.G. 1989, in “*White Dwarfs*”, Eds.: Wegner, G., *IAU Coll. 114*, (Berlin: Springer), p. 15
- [43] Torres, S., García–Berro, E., Isern, J. 1998, *ApJ*, 508, L71
- [44] Figueras, F., García–Berro, E., Torra, J., Jordi, C., Luri, X., Torres, S., Chen, B. 1999, *Balt. Astron.*, 8, 291

- [45] Isern, J., García-Berro, E., Hernanz, M., Mochkovitch, R., Torres, S. 1998, ApJ, 503, 239
- [46] García-Berro, E., Torres, S., Isern, J., Burkert, A. 1999, MNRAS, 303, 173

KINEMATIC MEASUREMENTS OF GAS AND STARS IN SPIRAL GALAXIES

JOHN E. BECKMAN

Instituto de Astrofísica de Canarias, E-38200 La Laguna, SPAIN

Consejo Superior de Investigaciones Científicas, SPAIN

ALMUDENA ZURITA

Isaac Newton Group of Telescopes, E-38700 S.C. de La Palma, SPAIN

JUAN C. VEGA BELTRÁN

Departamento de Física, Universidad de La Laguna, E-38200 La Laguna, SPAIN

Instituto de Astrofísica de Canarias, E-38200 La Laguna, SPAIN

Abstract: In this article we first give a brief, historically based, survey of kinematic observations, essentially of rotation curves of spiral galaxies, produced as techniques have advanced and new wavelength ranges have opened up. We then describe the basic inferences from kinematic measurements relevant to galactic structure: the rotational velocity and the velocity dispersion in gas and stars, and how these are made. This is followed by a selection of observations of individual galaxies, picked to illustrate how structural components: bulges, discs, lenses and bars, can be detected and analyzed kinematically as a complement to, or even a substitute for surface photometry. A further section shows how two dimensional kinematic observations of galaxies are even more powerful than one dimensional long-slit optical observations. This is illustrated by Fabry-Pérot mapping of NGC 1530 in $\text{H}\alpha$, from which we can clearly detect streaming motions in the arms, high velocity flows on either sides of the bar, and inward spiralling gas flow towards the nucleus, and from which we can also relate velocity gradient behaviour with the enhancement or the inhibition of the star formation rate. Finally we explain how continued technical improvement will ensure continued progress in this mature but rewarding field.

1 Basic galactic kinematics: observational method

The fact that galaxies rotate on their axes was discovered in 1914 by [1] from the curved shapes of long slit spectra of M81 and M104. The first rotation curve of a galaxy was obtained in 1918 by [2] for the central part of the Andromeda nebula, M31, with photographic spectroscopy which needed 80 hours of exposure time! The classical piece of work on the rotation curve of M31 by [3] using emission spectra from

44 HII regions in the central zone of the galaxy and 4 towards the outside, required a total of 292 hours of photographic exposure. Small wonder that real progress in using kinematic measurements to investigate the internal dynamics of galaxies had to await the introduction of modern techniques on large telescopes. Even as late as 1970 Rubin and Ford's M31 rotation curve ([4]) containing 67 independent data points, was based on 112 hours of observations. The first major step came with the use of image tubes; a long slit spectrum of M31 of quality sufficient to obtain a good major axis rotation curve was possible on the Lick 3.5 m telescope in \sim 20 hours during the 1970's and early 80's. Since then there have been three major advances in optical rotation curve observing: the use of CCD's, the use of larger telescopes, and the use of Fabry-Pérot interferometry to obtain radial velocity maps in emission lines over the full face of a galaxy in times of order 3 hours on a 4m telescope.

Complementary rotational kinematic information can be obtained using neutral gas, in either atomic (HI) or molecular (H_2) form. The first rotation curve for an external galaxy using HI was obtained by [5], again for M31, and even in this pioneering measurement they showed that the curve in HI could be measured out to at least twice as far from the galactic centre as the stellar population. The use of HI gives far greater cover of a typical galaxy disc than that of optical emission lines, but suffers from poor angular resolution. One can reach arcsecond resolution with the VLA, but the exposure times reach tens of hours for a field of a few arcminutes, and all other telescopes give poorer resolution. The key molecule for cold gas observations is CO, and with modern millimetre wave interferometers one can go to a couple of arcsec resolution. The first rotation curve in CO was published for the Milky Way by [6]. Here too however exposure times are still rather long, and the number of galaxies observed in this way is limited. We should point out that in terms of the material sampled, HII, HI and CO (which represents H_2) cover the main phases of the interstellar medium (ISM) and in terms of physical information are complementary. In terms of kinematic information if all are available they can normally be used in parallel, because kinematically the three types of hydrogen behave essentially equally, but the coverage of the disc is also complementary. To simplify a little, H_2 (CO) samples well the centres of most disc galaxies, and their spiral arms, HI samples the whole disc out to large radii, but often with a "hole" in the centre, while HII (via $H\alpha$) samples star forming regions, with high precision but with incomplete bulge, bar and disc cover. The other way to map a galaxy kinematically is, of course via its stellar population. Stellar lines give intrinsically less precise velocities because they are broader and the stellar population often has a high velocity dispersion. We will see below that the kinematic behaviour of gas and stars can be different, and this gives us interesting information about the structural evolution of the galaxy.

2 Velocity fields and their broad interpretation

To first order it is found, from a distillation of much observational material, that disc galaxies are essentially in concentric circular rotation in a plane about a central axis. The velocity of this rotation varies with radius from the galactic centre, and is determined by the radial distribution of mass within the galaxy. The plot of circular velocity v_r versus galactocentric radius r (normally called the “rotation curve”) is observed to be divisible into two regimes: a rapidly rising regime from the centre

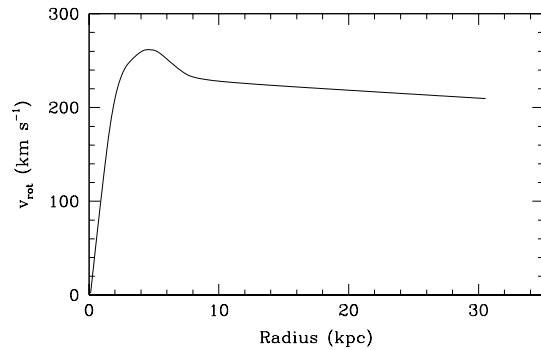


Figure 1: Basic rotation curve of a typical spiral galaxy, showing how the inner “solid body” curve changes to the outer curve at virtually constant velocity, passing through an intermediate zone with a flat maximum. This curve should follow the overall mass distribution within the galaxy.

out to a certain radius, r_c , followed by a virtually flat regime (almost constant value for v_r with r) from r_c out to very large radii. For a “standard” Milky Way mass galaxy r_c is of order a few kpc at which v_r attains a fairly flat maximum value v_{r_c} of between 200 and 250 km s $^{-1}$. At larger radii the value of v_r is almost constant at a value a little lower than v_{r_c} , out to radii of many tens of kpc; a sketch of this is given in Figure 1. The quasi-linear (“rigid body”) behaviour of the inner zone, and the quasi-constant behaviour of the outer zone of the rotation curve are the most standard observational characteristics of rotation curves, but although simple in form, they still defy comprehensive theoretical explanatory models. Of course the flat outer zone, whose great extent was measured in H I out to ten times beyond the limits marked by the stellar population, gave rise to the “missing mass” puzzle, which was a key step along the path to modern cosmologies.

When analyzing the observed two dimensional velocity field of a galaxy as projected onto the sky, taking into account that our observations always give only the

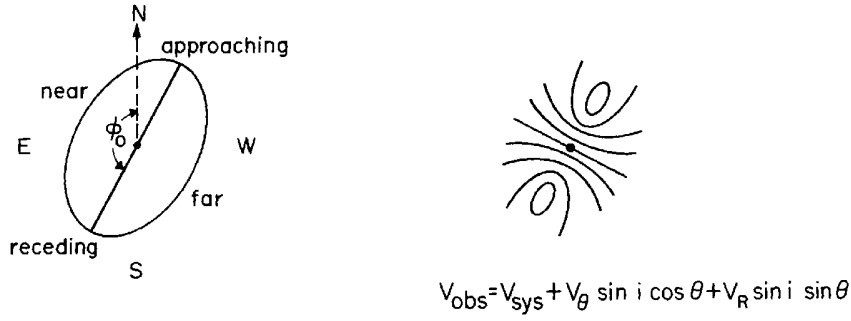


Figure 2: Schematic map of the “isovels” lines of constant observed radial velocity, which would be observed for a galaxy whose rotation curve measured along its major axis took the ideal form shown in Figure 1. This shows the form of the isovels which are subtracted from an observed two-dimensional velocity map of a galaxy, leaving residuals which give the non-circular velocity field.

radial component of velocity in the direction of the observer, we define the key parameters as: v_{sys} , the systemic velocity of the whole galaxy (i.e. its redshift); v_θ , the tangential velocity component in the plane of the galaxy, and v_r the radial component (with the initial assumption that there is no out of plane component); i is the angle of inclination between the galaxy and sky planes, and ϕ_0 the position angle of the galaxy major axis measured from north through east. With these definitions we can express the observed velocity v_{obs} at any point on the plane of the galaxy as seen projected onto the sky by:

$$v_{obs} = v_{sys} + v_\theta \sin i \cos \theta + v_R \sin i \sin \theta \quad (1)$$

where R and θ are the polar coordinates of a point $P'(R,\theta)$ in the plane of the galaxy, whose projection onto the plane of the sky is $P(r,\phi)$. These coordinates are related by:

$$\tan \theta = \tan(\phi - \phi_0) / \cos i \quad (2)$$

$$R = r \cos(\phi - \phi_0) / \cos \theta \quad (3)$$

In practice, as explained above, to simplify the analysis in order to get useful results from purely radially measured velocities, we first assume that radial velocities within the galaxy are small, setting v_R to zero. In this ideal purely rotating case, the resulting distribution of velocities radial to the observer will have a form given in Figure 2, where the lines drawn are termed “radial isovels”. The axis of symmetry of this

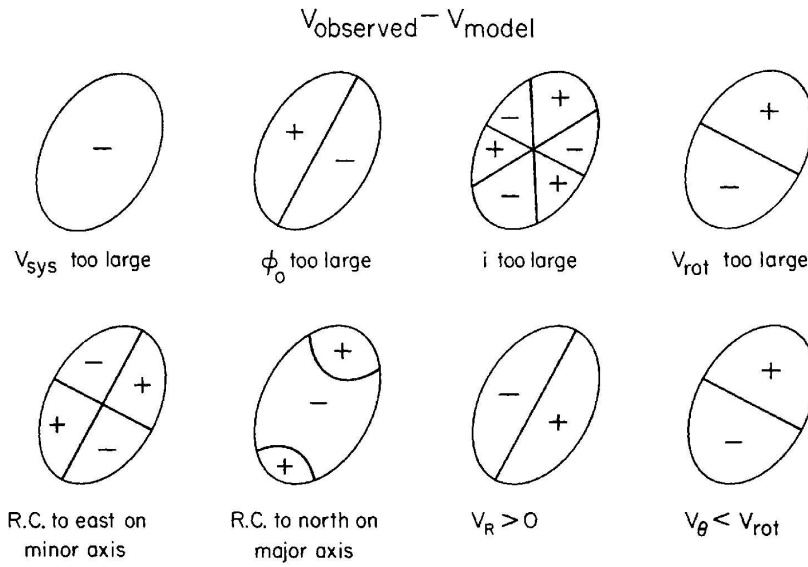


Figure 3: Schematic of systematic effects which may remain when a model two-dimensional rotation field is subtracted from an observed field in a spiral galaxy, when only one of the relevant parameters is badly selected or measured. From left to right and upper to lower panels: (a) Too large a systemic velocity chosen, (b) Position angle chosen for the analysis is too large, (c) The angle of inclination chosen is too large, (d) The rotation curve is scaled at too large a velocity, (e) The centre of rotation is to the east on the minor axis, (f) The centre of rotation is to the north on the major axis, (g) There is a positive expansion velocity, (h) There is a negative tangential velocity. Note that (a)-(e) represent measurement errors, while (f) and (g) imply true non-rotational velocity fields (in practice (d) and (g) are not easy to distinguish).

figure is the locus of maximum observed radial velocity, which should coincide with the major axis of the ellipse which defines the projected galaxy disc. The two implied methods of finding this axis, either from disc photometry or from velocity observations, should give indistinguishable results for a “well behaved” galaxy; measuring this axis yields the inclination angle i and position angle ϕ_0 for the later velocity analysis. Figure 2 shows the effect of projecting the rotation curve in Figure 1 into two dimensions and shows what we would expect to measure in a galaxy without radial or vertical motions. Any differences between this map and an observed map can then be

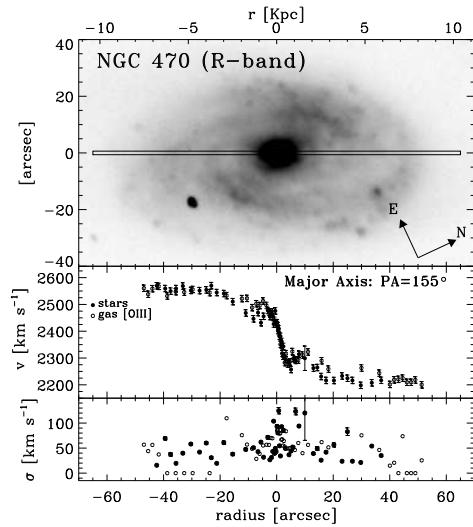


Figure 4: Major axis kinematic data for NGC 470, an Sbc galaxy, showing good coincidence between stellar and gas velocities, and low velocity dispersion even at the centre, as predicted for an object with little or no bulge concentration.

carefully analyzed to detect such motions. However one must be sure that the map itself gives correct values of a projected rotation curve. Some of the systematic errors possible which can be detected and corrected in this process are shown in Figure 3, where the assumption is made that a rotationally projected model rotation curve has been subtracted in two dimensions from the observational map. The diagram shows where positive and negative differences are found for different zones in the subtracted map for different types of bad adjustment between model and observations. We can see that some types of errors are best accounted for by systematic errors in the measurements of the systemic velocity, the major axis position angle, or the inclination angle, and others by an error in the position of the centre of rotation. However there are always possibilities of true non-circular velocity components, and as we will see later if the mass distribution within the galaxy suggests that such components should be present, it may be possible to measure them from the velocity field.

It is useful to point out here that when a spectral line measurement is made with the purpose of making a velocity map and extracting a rotation curve, if the spectral resolution is adequate one can derive the dispersion in the velocity of the stars or gas along the line of sight of the observation. In the basic case this dispersion is just measured as the full width at half maximum, or the Gaussian sigma, of the measured

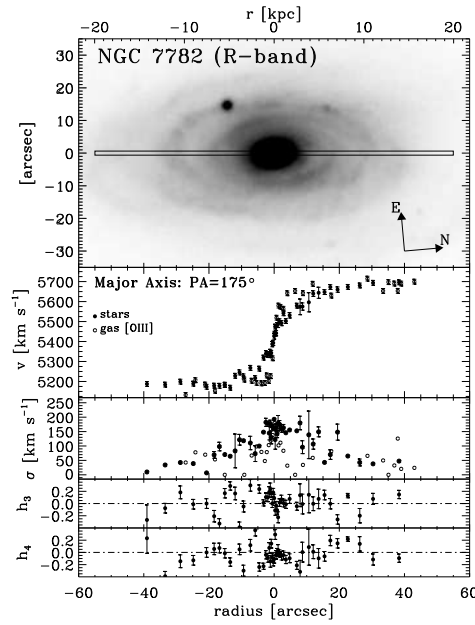


Figure 5: Major axis kinematics of NGC 7782 (Sb) showing how in the bulge the stars are supported against infall partly by pressure and partly by rotation, so their rotation velocities fall below those of the gas; also the stellar velocity dispersion is notably higher in the centre than that of NGC 470 in Figure 4.

line profile, either in absorption or in emission. To first order, the stars formed once the gas in a galaxy has settled into a disc will have a relatively low collective velocity dispersion, while the stars formed by gas in essentially radial collapse to form a bulge will have a relatively high dispersion. Typical values for the former are $\sim 50 \text{ km s}^{-1}$ and for the latter are $\sim 200 \text{ km s}^{-1}$. This difference may be used to help distinguish bulge from disc symmetry in a stellar component where this is not obvious from photometry alone, or even pick out a disc where this has previously been termed a bulge from photometric arguments ([7]). Since a stellar population or even a gas component, is supported against gravitational collapse by a combination of its axial rotation (circular motion) and its pressure (radial motion) we would expect to see zones with enhanced velocity dispersion having reduced rotational velocity, and vice versa, so the combination of velocity dispersion with rotation observations give complementary information on dynamic properties. It is also important to note that both emission lines from gas and absorption lines from stars can show multiple peaks

in their line of sight velocity distributions, and these can be interpreted as multiple population components, e.g. prograde and retrograde stellar motion, or strongly non-circular gas motion due to the presence of a bar. We will see some of these cases in the following sections.

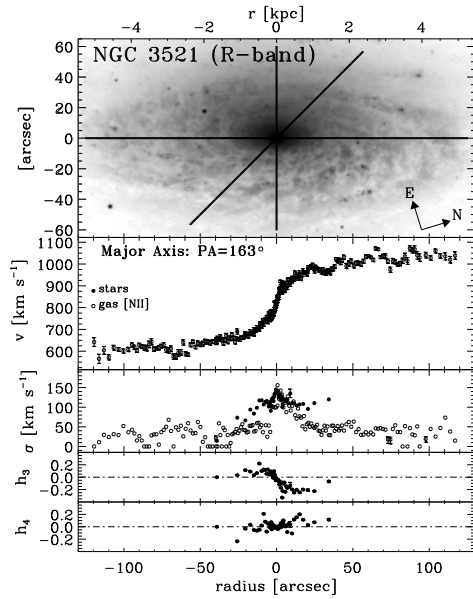


Figure 6: Major axis kinematics of NGC 3521 (Sb); here stars and gas rotate in unison, and the velocity dispersion in the centre is not high, in spite of the bulge. Note that the departures from zero of the symmetry parameter h_3 is a clue to a counter rotating component (see Figure 7).

3 Varied phenomenology in galactic rotation curves and velocity dispersions

There is considerable interest for dynamical and structural diagnostics in comparing the rotation curve measurements for stars and gas within the same galaxy. We will use here the rather rich sample presented completely in [9] and followed up in a number of relevant papers ([10], [11]; [8]). In late type galaxies, (Sc and later) the rotation curves measured using stellar absorption lines and gaseous emission lines are almost

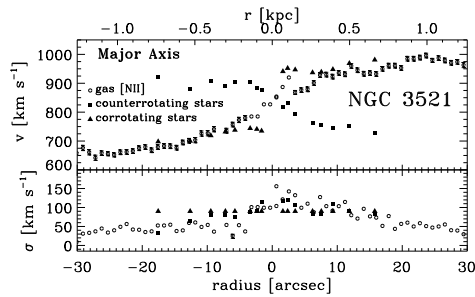


Figure 7: Result of gaussian decomposition of the spectra from which the kinematics of NGC 3521 (presented in Figure 6) were derived. This reveals a fraction of stars in counter rotation with the gas and the remaining stars in the bulge region, due either to a previous merger, or to the rotational properties of an end-on bar (see [8]).

always in excellent agreement, and the velocity dispersions of both components are relatively low. We will see that this is predicted for a system with a small or virtually absent central bulge. These results hold quite generally, except where the velocity and dispersion are measured close to a galactic bar, when deviations can occur. A good example of these properties is the kinematic information on NGC 470, in fact classified as Sbc, obtained with a long slit spectrum along its major axis, as shown in Figure 4 (from [12]). We can see good agreements between the rotation curves, and dispersion values in general below 100 km s^{-1} , which is low compared with values for galaxies with major bulges (see below). As well as the rising inner curve, and the near constant outer curve, we can see a sharp dip (symmetrical on either side of the centre) in velocity, followed by an oscillatory range, just outside 10 arcsec from the centre of the galaxy. This behaviour is what one would predict if the slit cuts zones of non-circular motion associated with the sides of a bar, and the presence of the bar is indeed seen well in the R-band image in Figure 4.

As we move to earlier type galaxies the gas and stars show diverging kinematic behaviour. This is essentially because a classical stellar bulge in any galaxy contains stars which are on “pressure supported” orbits, i.e. their orbits have strong radial velocity components, consistent with bulge formation by radial gravitational collapse of an initial gas cloud, or by near radial infall of captured material. Once a star has condensed out of a collapsing cloud, frictional dynamical processes are greatly reduced, so any effects tending to circularize orbits have extremely long timescales. Gas, on the other hand, always tends to relax into a plane perpendicular to the spin axis of the galaxy, and except in the presence of bars or other strongly non-axisymmetric components, into circular orbits. An excellent example is given by the

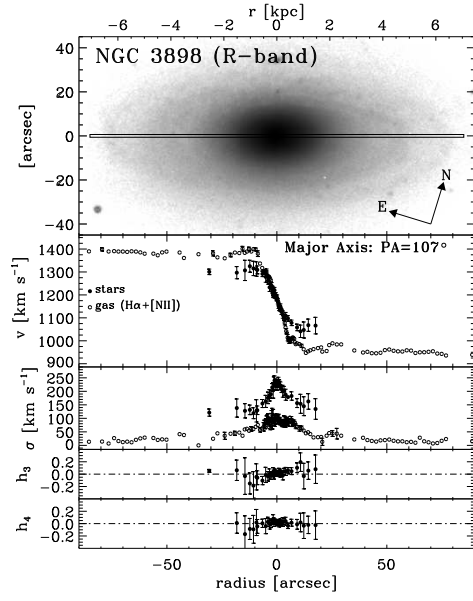


Figure 8: Major axis kinematic data for NGC 3898 (Sa), characteristic of galaxies with large bulges. The pressure supported stellar component shows much lower velocities, and much higher velocity dispersions in the bulge than does the gas.

Sb galaxy NGC 7782, in Figure 5 (from [12]) where the results of long slit spectroscopy along the major axis are shown. It is clear that in the inner zone where we can see an obvious bulge in the image, the stellar rotation curve falls well below the velocity of material in rotational equilibrium, which is well represented by the O III emission line rotation curve on the same diagram. While the gas is entirely supported by rotation, the stars are partly supported by “pressure” i.e. they have strong radial components in their orbits. This is well confirmed by the high value of the observed stellar velocity dispersion in the inner part of the galaxy, i.e. over 200 km s^{-1} . In the outer part of the rotation curve, corresponding to the exponential disc, the stellar curve rises and matches the gas curve very well, which is just what one would predict. A particularly interesting case is that of NGC 3521 shown in Figure 6 (from [12]). Here we have a case where the stars and gas apparently rotate in perfect unison, but the velocity curves have been obtained from long slit spectra, using only the velocities of the line peaks. However in Figure 6 we can see that the stellar spectral lines are far from symmetric, as shown by the behaviour of the line asymmetry parameter h_3 (for a description of the definitions of h_3 and h_4 , not used elsewhere in this paper,

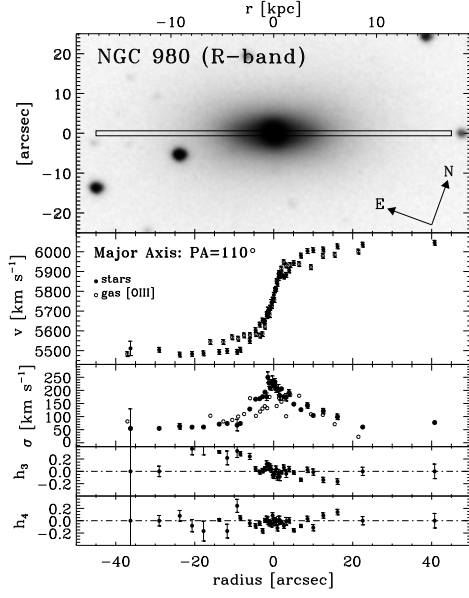


Figure 9: Major axis kinematic data for NGC 980, taken as a typical S0 galaxy. However the detailed analysis of the velocity dispersion and line symmetry parameters as functions of galactocentric radius, strongly suggests a rather small bulge embedded in a central disc plus a larger lens component, in interesting agreement with the conclusion of [7] that a significant fraction of S0's in fact have small bulges embedded in uniform discs, rather than large bulges as their classification would imply.

but appearing in the figures of this section, the reader is referred to [9]). A closer inspection of the lines reveals that they are double peaked, and when two gaussians are fitted, and new rotation curves plotted, we find an additional stellar rotation curve in the opposite sense to the first one, as seen in Figure 7. This counter rotating component could either be due to the acquisition of stars in a merger, or to the predicted phenomenon of a set of retrograde orbits within a bar ([13]). For further discussion of this case see [8], where it is suggested that an oscillatory pattern in the “flat” outer part of the rotation curve just beyond the steep inner rise, detected in a long slit spectrum from an angle intermediate between major and minor axes of the galaxy, indicates the presence of a bar. This bar must be virtually end on to us, and impossible to detect photometrically. This is an example of how the use of kinematics can enable us to detect, and often resolve structure in galaxies which is not detectable photometrically (see also [9]).

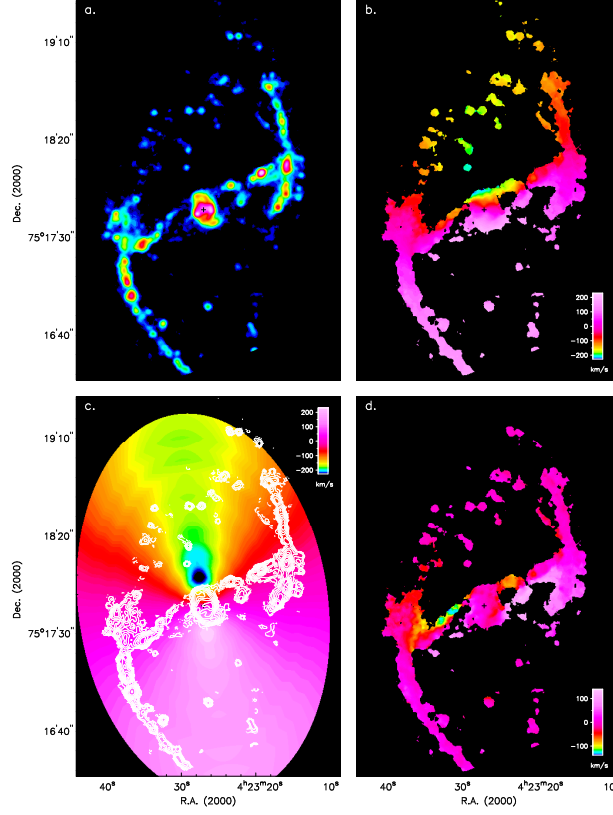


Figure 10: **a)** Intensity map (zeroth order moment) of the H α emission in NGC 1530. **b)** Velocity map (first moment) of the H α emission in NGC 1530. **c)** Model velocity map of NGC 1530, obtained from the H α rotation curve of the galaxy shown in Figure 11, with H α isointensity contours overlaid. We can clearly see “wiggles” at the radii of the spiral arms, due to the density wave streaming motions not subtracted off from the rotation curve. **d)** Map of the residual velocities of NGC 1530, obtained by subtracting the model velocity field (Figure 10c, after taking out the ripples due to the streaming motions in the spiral arms from the velocity map (Figure 10b).

The rotation curves and velocity dispersion curves for the gas and stars in the Sa

galaxy NGC 3898 are fairly characteristic of those for galaxies with major bulge components, but there is also evidence for an inner “thick, hot” disc as well as the normal outer disc. We can see this evidence in Figure 8 (from [12]), in which the curves have been derived from a long slit spectrum along the major axis of the galaxy. The stellar rotation curve falls well below that of the gas in the inner zone, as seen above for NGC 7782, and the velocity dispersion is very high in the centre, falling quite rapidly from 250 km s^{-1} to a plateau at $\sim 150 \text{ km s}^{-1}$; both types of behaviour are characteristic of the stars in a pressure supported bulge. The line shape parameters h_3 and h_4 show clear departures from zero, indicating the presence of more than one gaussian component in the stellar absorption lines. Close analysis of the individual lines ([10]) reveals that the lines come to us from a rapidly rotating disc superposed on a virtually non-rotating bulge. The separate hot disc is revealed by the plateau in the velocity dispersion of the stars between 12 arcsec and 25 arcsec from the centre of the galaxy, with a value of 110 km s^{-1} as shown in Figure 8. Beyond this, only the gas velocities can be well measured, and these show a very flat rotation curve with a very slowly declining velocity dispersion in the range $\sim 50 \text{ km s}^{-1}$, characteristic of normal galaxy discs. As an example of an S0 galaxy we have chosen NGC 980 because its kinematic differences between stars and gas are not very complex, for example it shows no evidence for counter-rotation, though many similar galaxies do show such evidence. The rotation curves and velocity dispersion curves for this galaxy are shown in Figure 9 (from [12]). The velocity dispersions of both gas and stars are high, $\sim 250 \text{ km s}^{-1}$ in the very centre, showing the presence of a dynamically hot bulge, but fall quite rapidly and are below 150 km s^{-1} at 5 arcsec radius. As for rotational velocity, the gas curve rises more rapidly than the stellar curve between 3 and 10 arcsec from the centre, which is normal for galaxies with bulge components. The stellar velocity shows a plateau, but at 10 arcsec the velocity of the gas dips below that of the stars, and remains lower out to some 20 arcsec, which is certainly unusual. If we look at the line asymmetry parameter h_3 it departs strongly from zero between 5 and 20 arcsec from the centre. [12] explains these features as due to an almost edge on disc component embedded in a more extended lens component, with a very compact luminous bulge with a 2 arcsec extent. This conclusion is in interesting agreement with that of [7] who showed, combining photometric and kinematic arguments, that a fair fraction of S0 galaxies have small bulges embedded in discs, rather than large bulges, as previously understood. The unusual behaviour of the gas rotation curve is explained as being due to a misalignment between gaseous and stellar components, and the whole system is modelled dynamically to fit the observed velocity and other line parameters. As the purpose of this article is to give an overview of the kinds of information which kinematic measurements provide, we will not go more deeply into these inferences here, but refer the reader to [10] and [12], to [8] and to [11], as well as to the most complete source, [9]. We must point out the general conclusion that even single slit rotation curves, obtained with high S:N ratio, high spectral and high spatial

resolution can offer us very powerful kinematic clues to the structure and dynamical history of galaxies, as illustrated here. Naturally two dimensional spectroscopy is in principle even more powerful, and we will describe one particularly interesting data set of this type here below.

4 The velocity field of the ionized gas in NGC 1530

As an excellent illustration of the use of a full two dimensional velocity field we take the case of the strongly barred galaxy NGC 1530 which we have mapped in velocity with a resolution of $\sim 15 \text{ km s}^{-1}$ and an angular resolution of $\sim 1 \text{ arcsec}$ across the full face of the galaxy using a scanning Fabry-Pérot, in H α emission. A detailed analysis of the kinematics and its implications for star formation (SF) can be found in [14]. Here we will stress some of the technicalities of the method and the types of information derivable which cannot be obtained using other methods. In Figure 10 we give a general display of how the observations give us information about the surface brightness and velocity distribution of the ionized gas in the galaxy. The original “data cube” gave a set of individual maps of the galaxy, each in a set narrow wavelength channel, of width $\sim 15 \text{ km s}^{-1}$ in this case. The analysis goes via a set of moment maps: the “zeroth” moment is the integrated surface brightness over all the channels, i.e. the full surface brightness of the galaxy in H α (Figure 10a), the first moment map (Figure 10b) is a two dimensional map of the local radial velocity, as dealt with theoretically in section 1, and the second moment map (not shown in Figure 10, but see [14]) is of the velocity dispersion in the ionized gas.

Here we concentrate on the first moment map which is essentially a map of the velocities of the peaks of the H α emission lines coming from all the pixels in the galaxy. The first step in its analysis gives us the rotation curve, and for NGC 1530 our first order measured rotation curve is shown in Figure 11. The fact that it is symmetric on either side of the centre of the galaxy suggests that we are not falling into any of the gross errors illustrated in Figure 3. However there are some subtle traps which we have not avoided, and which must be corrected in order to give a better plot of the true rotational velocity with radius. Within 5 arcsec of the centre there is a bump where the curve rises more steeply and then falls back to a linear regime, and between 40 and 100 arcsec there is a series of smaller bumps which differ from one side to the other, but with amplitudes well above the error bars. These outer bumps coincide in radius with the spiral arms and are due to non-circular motions associated with these streaming motions. Their amplitudes can be estimated by assuming that the mean matter distribution is radially smooth so that the true rotation curve is smooth. The differences between an interpolated smoothed curve and the observed curve in this range can be converted into amplitude estimates for the streaming motions, and are typically of between 10 and 40 km s^{-1} . This process is illustrated in Figure 12. In

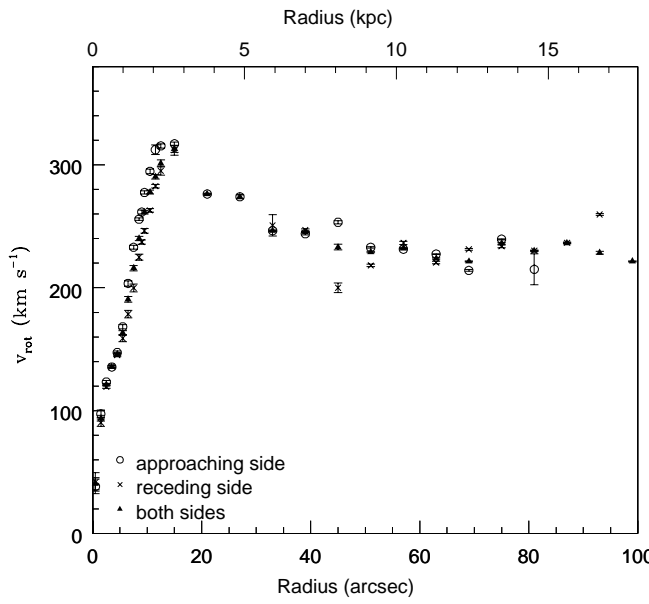


Figure 11: H α rotation curve of the disc of NGC 1530, for the receding and the approaching sides of the galaxy separately. The agreement between the two sides shows the symmetry of the velocity field and the reliability of the rotation centre.

Figure 10c we show the rotation curve projected into the plane of the sky to give a model which can then be subtracted from the original map, yielding a “residual” map of truly non-circular velocities. The presence of uncorrected streaming motions in this model is notable, and for detailed work on these motions we produced a corrected smoothed model.

The inner bump might be due to the presence of a small massive bulge or central bar but as we showed from HST imaging in the NIR in [14], no such massive features are in fact present. We therefore interpret this bulge as due to gas spiralling in towards the nucleus along interlocking tracks, a phenomenon predicted by [15], and observed clearly for the first time in this work, down to within 300 pc from the nucleus, a limit imposed by the resolution as NGC 1350 is not very nearby (~ 30 Mpc).

In Figure 10d we show the non-circular velocity field of NGC 1530. It is clear that we are detecting fast non-circular components, produced by the presence of the strong bar. Their presence is in fact detectable in the original velocity field, Figure 10b, and the skewed isovels in this figure are a classical illustration of the effects of a bar on

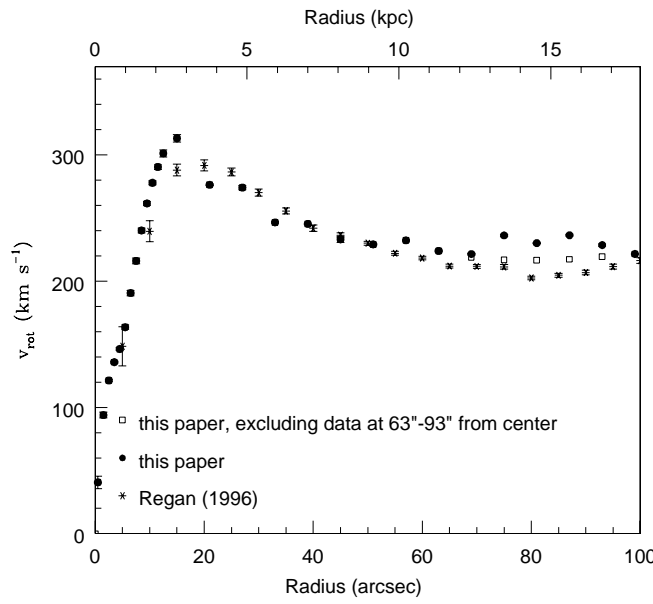


Figure 12: H α rotation curve of the disc of NGC 1530. This rotation curve has been obtained by subtracting the effect of the streaming motions in the spiral arms of the galaxy from the mean rotation curve shown in Figure 11.

the velocity field of a galaxy. This skew can be seen directly by comparing the field in Figure 10b with the idealized field in Figure 2, but in Figure 10d we have isolated the non-circular field, which can then be quantified. The amplitudes of these non-circular flows are well illustrated in Figure 13, with cross-sections perpendicular to the bar across the residual velocity map. The maximum amplitudes are found at some 20 arcsec from the nucleus, where the flows, in directions essentially parallel to the bar, stream past the bar in opposite directions at either side of it, with vector amplitudes of 100 km s $^{-1}$. These form a general field of gas flowing around the bar in quasi elliptical orbits, and exchanging angular momentum with the stellar mass of the bar where they form shocks as they approach its central axis, notably towards the ends of the bar in zones of high H α surface brightness.

A more graphic illustration of the power of this high resolution two-dimensional velocity mapping is given in Figure 14 where we have derived a map of the velocity gradients of the non-circular velocity components perpendicular to the bar direction. What is most striking is that the loci of maximum gradient along the bar trace

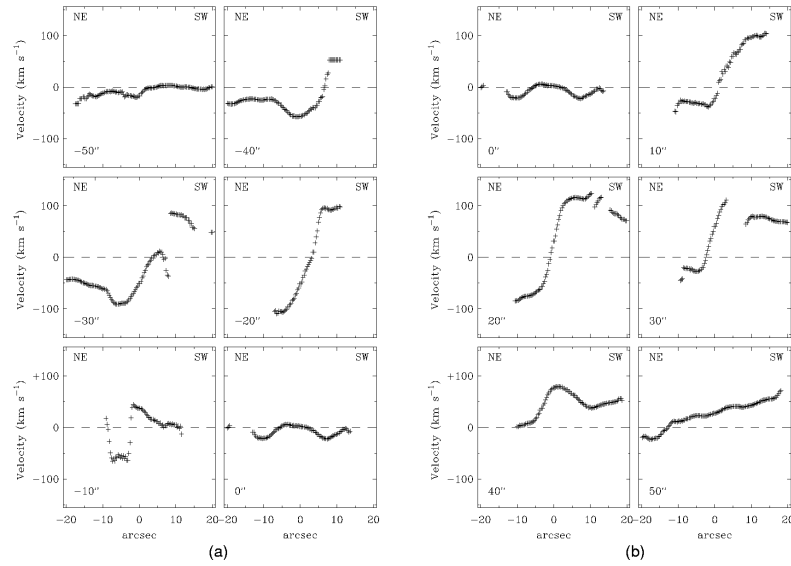


Figure 13: Profiles of the residual velocity perpendicular to the bar of the galaxy: to the SE (a) and to the NW (b). The distances of the profile tracks to the galaxy kinematic centre are indicated in the bottom-left hand corner of each plot.

perfectly the paths of the dust lanes (the only difference being that the velocity gradient map lacks complete continuity as the velocity measurements require local H α to be present in fair strength). This is because these loci, of maximum shear, are where the flow direction reverses, so the dust will tend to gather around these lines of low net velocity around the bar. Although this effect was predictable, this is the first detection and it tends to confirm what has become the classical theory of gas dynamics around bars ([16]). Further developments here will allow us to measure directly the net inflow rate of gas to the centre of galaxies like NGC 1530, giving valuable data to compare with models of how circumnuclear activity is fuelled in barred galaxies.

One very interesting general result of this kind of studies is the relation between velocities, velocity gradients and SF in the ISM. Figure 15(left) gives a plot of the H α surface brightness and the amplitude of the non-circular velocity field as functions of position on the bar of NGC 1530. We can see that there is a clear tendency for an anticorrelation between the two variables, i.e. high values of surface brightness correspond in general to low values of local non-circular velocity and vice versa. A

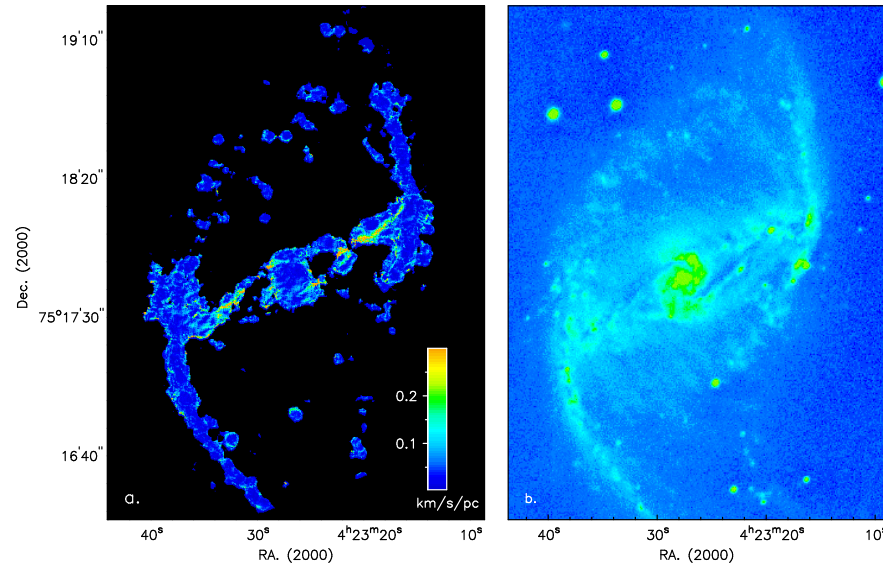


Figure 14: **a)** Velocity gradient map perpendicular to the bar. Zones of maximum shear are clearly seen (cf. the dust lanes in Figure 14b). **b)** Image of NGC 1530 in the optical V -band obtained with the KPNO 4-meter Mayall telescope.

quick inference from this would be that high local velocities act to inhibit SF. However we can go on to learn more by comparing the velocity gradient with the H α surface brightness, as shown in Figure 15(right). There is an even clearer anti-correlation between surface brightness and velocity gradient, and we can summarize by noting ([14]) that in the galaxy as a whole there are a few areas of high surface brightness which are in zones of high local non-circular velocity, but where the velocity gradient is low, whereas there are no high surface brightness areas where the velocity gradient is high. Thus the physical variable which best anti-correlates with local SF rate is non-circular velocity gradient, but in a direction perpendicular to the line of flow. We can explain this by understanding that high shear will tend to disrupt large gas clouds thus inhibiting SF. This qualitative conclusion deserves quantitative follow-up. It is also interesting that SF tends to occur at a small offset from zones of large velocity gradient perpendicular to the line of flow. This suggests that shocks which compress the gas are enhancing the local SF rate in these zones. There is a rather rich field to be explored here, given access to the relevant observing techniques.

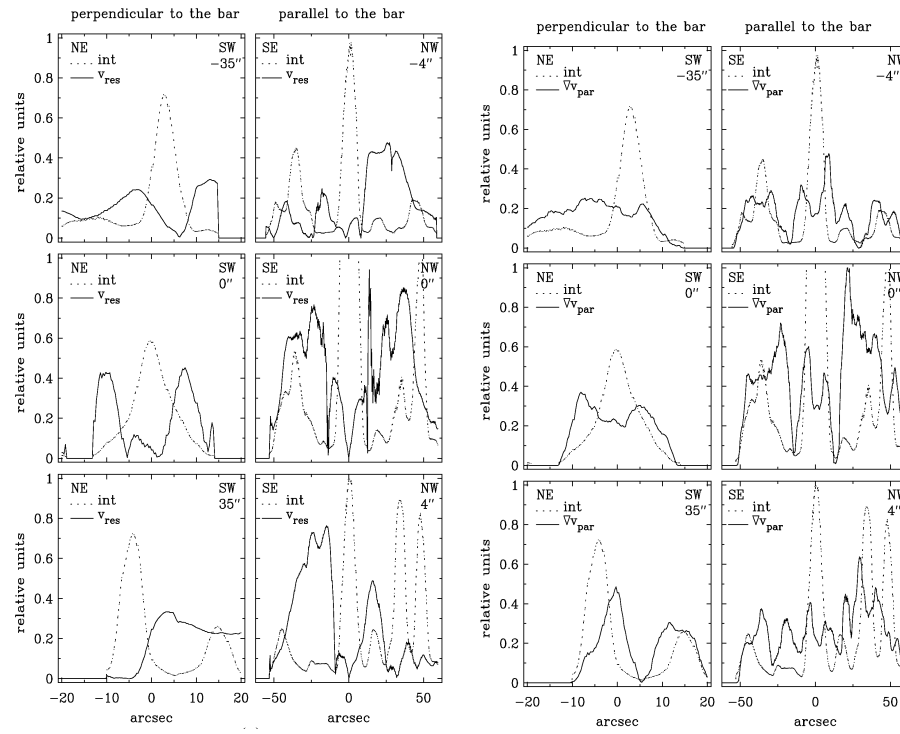


Figure 15: (left) Profiles of the normalized surface brightness in H α emission and residual velocity parallel and perpendicular to the bar. The distance of each profile track from the kinematic centre is indicated in the top right corner of each plot. (right) Profiles of the normalized H α surface brightness and residual velocity gradient parallel to the bar. The tracks of the profiles are the same as those in Figure 15(left).

5 Discussion: future kinematic observations

This article is designed to illustrate some of the inferences which can be made using kinematic mapping of galaxies, with emphasis on the rotation curve and departures from simple form, and the relationship of velocity to velocity dispersion where appropriate. While the use of HI has in the past given the most extensive coverage to this type of measurements, in the future we must use techniques which offer the best resolution and signal to noise as well as picking out the different structural components of galaxies. These include two dimensional optical and NIR spectroscopy

using fibre-fed systems, which have the advantage of simultaneous stellar and gas observations, but whose complete fields are small for the kinds of observations shown in section 3, and Fabry–Perot based systems, which can yield large fields at adequate spatial and spectral resolution, permitting rapid observing of complete galaxies, but which give us information in only one spectral emission line at a time, and coming from the relatively patchy emission of ionized regions. Both types of systems can be improved technically for the specific needs of kinematic mapping of galaxies. In the mid-term the use of ALMA in mapping the gas component via its molecular emission will certainly be an important boost for this line of investigation, which though now a mature method, will contribute much to our understanding of galaxies in the coming years.

References

- [1] Wolf, W. 1914, Astronomische Nachrichten, 199, 319
- [2] Pease, F.G. 1918, Proc. Nat. Acad. Sci., 4, 21
- [3] Babcock, H.W. 1939, Lick Obs. Bull., 498, 41
- [4] Rubin, V.C., Ford, W.K.Jr. 1970, Astr. & Sp. Sc., 159, 379
- [5] van de Hulst, H.C., Raimond, E., van Woerden, H. 1957, Bull. Astron. Neth., 14, 1
- [6] Blitz, L. 1975, ApJL, 231, 115
- [7] Erwin, P.E., Vega Beltrán, J.C., Graham, A., Beckman, J.E. 2003, ApJ, 597, 929
- [8] Zeilinger, W.W., Vega Beltrán, J.C., Rozas, M., Beckman, J.E., Pizzella, A., Corsini, E.M., Bertola, F. 2001, Astr. & Sp. Sc., 276, 643
- [9] Vega Beltrán, J.C. 1999, PhD. Thesis, Universidad de La Laguna, Spain.
- [10] Vega Beltrán, J.C., Pignatelli, E., Zeilinger, W.W., Pizzella, A., Corsini, E.M., Bertola, F., Beckman, J.E. 2001a, Astr. & Sp. Sc., 276, 509
- [11] Pignatelli, E., Corsini, E.M., Vega Beltrán, J.C., Scarlata, C., Pizzella, A., Funes, J.G., Zeilinger, W. W., Beckman, J.E., Bertola, F. 2001, MNRAS, 323, 188
- [12] Vega Beltrán, J.C., Pizzella, A., Corsini, E.M., Funes, J.G., Zeilinger, W.W., Beckman, J.E., Bertola, F. 2001b, A&A, 374, 394
- [13] Wozniak, H., Pfenniger, D. 1997, A&A, 317, 14
- [14] Zurita, A., Relaño, M., Beckman, J.E., Knapen, J.H. 2004, A&A, 413, 73
- [15] Englmaier, P., Shlosman, I. 2000, ApJ, 528, 677
- [16] Huntley, J.M., Sanders, R.H., Roberts, W.W.Jr. 1978, ApJ, 221, 521

OBSERVATIONS AND MODELS OF THE GENERAL CIRCULATION OF JUPITER AND SATURN

AGUSTÍN SÁNCHEZ-LAVEGA, RICARDO HUESO, SANTIAGO
PÉREZ-HOYOS

*Departamento de Física Aplicada I, Escuela Superior de Ingenieros, Universidad del
País Vasco, E-48013 Bilbao, SPAIN*

ENRIQUE GARCÍA-MELENDO

Esteve Duran Observatory Foundation, Seva, E-08553 Barcelona, SPAIN

JOSE FÉLIX ROJAS

*Departamento de Física Aplicada I, Escuela Universitaria de Ingeniería Técnica
Industrial, Universidad del País Vasco, E-48012 Bilbao, SPAIN*

Abstract: We review our current understanding of the general circulation at cloud top levels in the atmospheres of the giant planets Jupiter and Saturn.

1 Introduction

The giant planets of our Solar System are divided according to their size and properties in two groups: “gas giants” (Jupiter and Saturn, equatorial radius 71,300 km and 60,330 km respectively) and “icy giants” (Uranus and Neptune, radius $\sim 25,000$ km). Their aspect in images taken at wavelengths ranging from the ultraviolet to the near infrared, is dominated by the diffuse reflection of the sunlight (scattering and absorption) on gases and particles (clouds and hazes located typically at pressure levels $\sim 0.3 - 2$ bar) (Figure 1). Tracking cloud elements along a given temporal interval allows to measure atmospheric motions at these levels. Wind velocities are measured relative to the rotation of the magnetic field, which is assumed to be that of the planet itself (the magnetic field is rooted to the deep interior). Ground-based and spacecraft observations have revealed that the gas giant circulation is dominated by a system of zonal jets, i.e. directed along the parallels, and alternating their direction with latitude. There are 8 and 4 eastward jets per hemisphere in Jupiter and Saturn respectively. A conspicuous characteristic is the existence of a broad in latitude eastward equatorial jet with peak velocities of $\sim 150\text{ ms}^{-1}$ in Jupiter and $\sim 475\text{ ms}^{-1}$ in Saturn (the velocities are taken positive for motions in the eastward direction). On the contrary, the “icy giants” show an eastward hemispheric jet and

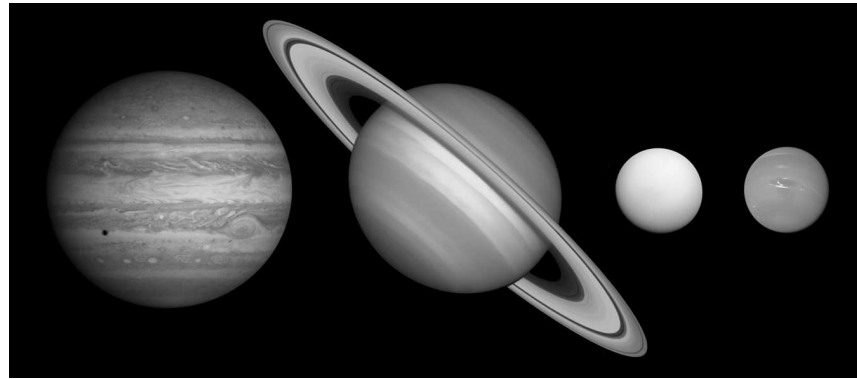


Figure 1: Visual aspect to scale of Jupiter, Saturn, Uranus and Neptune (from left to right) as imaged by the HST (Jupiter) and Voyager space crafts (rest). Credit: NASA-JPL.

a broad westward equatorial jet that amounts to $\sim 400 \text{ ms}^{-1}$ on Neptune (see Figure 2). At present, there is no accepted theory to explain the nature of these motions [1], and the models presented so far are on a rudimentary stage [2]. This represents a major challenge to a wide community formed by planetary scientists, astrophysicists and meteorologists. Here we will summarize the “state of the art” of this problem, from both observations and theory, but focusing on the gas giant planets for which we have much more data. The interest in these planets has largely grown in the last years in view of their similarities with the recently discovered giant extrasolar planets.

2 Gas giant planets: basic properties

In Table 1 we give the basic properties of the planets that are relevant for the general circulation models including the best studied extrasolar planet, HD 209458b that pertains to the so called family of “hot Jupiters” [3]. The most remarkable physical aspects of the giant planets are [1, 2, 3]:

- Their size is ~ 10 times that of the Earth.
- They have high angular rotation velocity (periods ~ 10 hr), except for the close-in extrasolar “hot Jupiters”, assumed to be spin-orbit locked (periods $\sim 3 - 4$ days).
- The atmospheres of the giants are deep, since they occupy an important fraction of the planetary radius, and frictionless when compared to the Earth due to the lack of a solid surface.
- They have a significant internal energy source coming mainly from the slow cool-

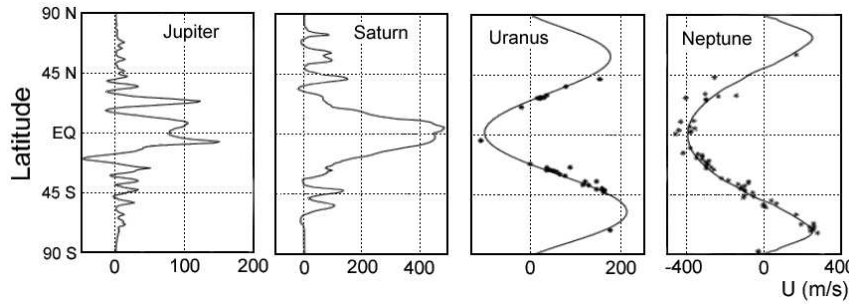


Figure 2: Comparison of the latitudinal zonal wind velocity profiles at cloud level in the giant and icy planets. Adapted from [4].

ing of the planet, i. e. they are releasing the heat accumulated during its formation. This energy is radiated as a black body with peak emission in the infrared (Figure 3). The internal energy source is a factor ~ 1.7 of the absorbed sunlight radiation for Jupiter and Saturn but it is insignificant at cloud levels in the “hot Jupiters” when compared to the strong stellar flux. Whereas the sunlight absorption depends strongly on the sub-solar latitude (due to the planetary axis tilt), the emitted energy is independent of latitude. The total thermal energy available in Jupiter and Saturn is a factor $\sim 1/25$ and $1/100$ respectively of that received on the Earth. Paradoxically the winds are ten times stronger.

- These planets are fully cloud covered. The clouds and aerosol optical depths are high enough to block the visible incident solar radiation in the upper few atmospheric bars. The clouds also partially block the emergent infrared radiation from the interior

Planet	R_P (km)	X	T (hr)	F_{int} (Wm $^{-2}$)	F_{star} (Wm $^{-2}$)
Jupiter	71400	0.8	9.925	5.44	13.6
Saturn	60330	0.5	10.66	2.01	4.6
HD 209458b	96400	~ 0.5	67.67	3	1.2×10^6

Table 1: Main properties of the giant planets. *Notes:* $X = (R_p - D)/R_p$, where D is the thickness of the H₂ molecular layer, T = rotation period, F_{int} = internal energy flux, F_{star} = external (stellar energy flux). For these planets, the range of values for the adimensional numbers in the atmosphere (they depend on altitude) are: $Pr = 10^{-4} - 1$; $Ra = 10^{12} - 10^{24}$; $E = 10^{-10} - 10^{-15}$; $Re = 10^9 - 10^{11}$.

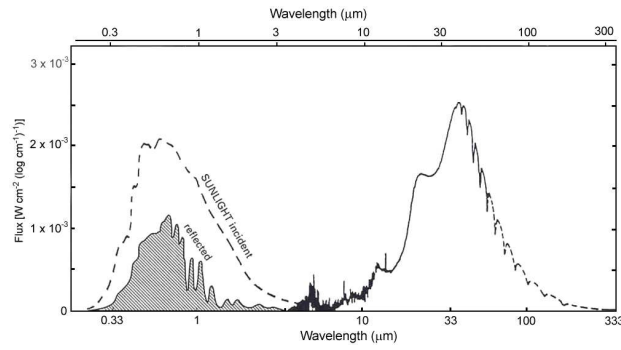


Figure 3: Jupiter’s spectrum from the ultraviolet to submm wavelengths. The left part shows the received and absorbed solar radiation (shaded area) and the right part the emitted infrared radiation, escaping from the interior. Adapted from [5].

(see Figure 4).

- Thermodynamic effects related to latent heat release from cloud condensation and, to a minor extent, ortho-para conversion of molecular hydrogen could have an important influence on global dynamics in the upper atmosphere.

- The poorly known internal structure and composition of these planets could have a significant role on the observed motions (Figure 5). Among them, the magnetic and friction effects in the metallic-molecular transition region, and the existence of opacity sources could be important.

In view of the preceding points, the basic unresolved questions are: How is the powerful system of zonal jets generated? How does the intense eastward and broad equatorial jet form? How deep do the winds extend into the interior? These questions come down to know how a thermodynamic machine is able to produce the highly energetic jets and their latitudinal distribution employing such low energy sources.

3 Wind velocity measurements

As already mentioned, observations of the motions of individual cloud features in a given temporal interval are used to measure the winds, either by cloud tracking or by correlation of the zonal albedo patterns. The pressure level at which these winds are measured is about 0.5 ± 0.2 bar where cloud optical depths ~ 1 to 3 are reached on both planets. High spatial resolution images obtained by means of cameras onboard various spacecrafts have provided the best wind data. In Jupiter these images were obtained by the Voyager 1 and 2 in 1979 [6, 7], by the Hubble Space Telescope from

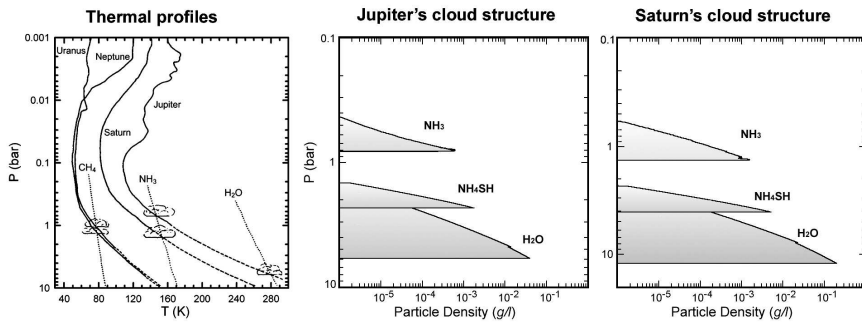


Figure 4: Left: Vertical temperature profiles in the visible part of the four planets. The main composition and altitude of the main clouds are indicated. From [10]. Center and Right: Altitude location and densities of the main clouds in Jupiter and Saturn as calculated from thermochemical models.

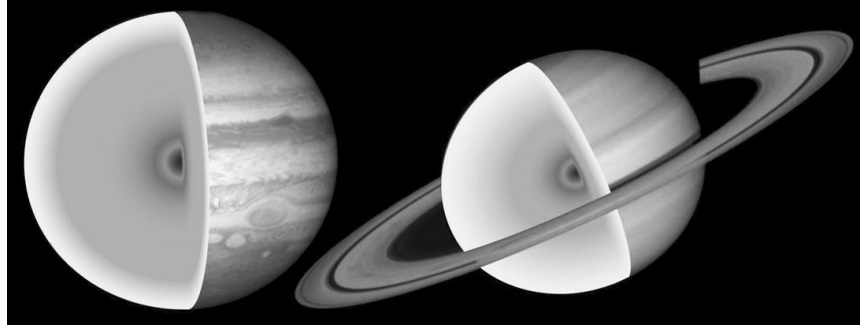


Figure 5: Static models of the internal structure of Jupiter and Saturn. The following regions are expected (from the upper clouds to interior): (a) An hydrogen molecular layer (the atmosphere), (b) A plasma (fluid) metallic hydrogen layer, (c) A central region formed by a coating of “ices” surrounding a central rocky core. The extension of each layer is to scale. Adapted from [11]

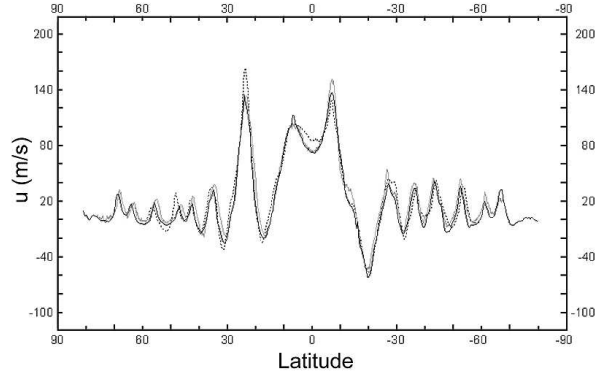


Figure 6: A comparison of different Jupiter's wind profiles as a function of time: Dotted line (Voyagers, 1979) [7]; Continuous gray line, (HST, from 1996 to 2000) [8]; Continuous dark, (Cassini 2000) [9]).

1995 to 2000 [8], by the Cassini Orbiter during its flyby in route to Saturn in 2000 [9], and by the Galileo Orbiter for some particular regions from 1996 to 2002 [12]. The maximum resolution attained in Jupiter is ~ 50 km/pixel. For Saturn the data came from the Voyager 1 and 2 flybys in 1980 and 1981 [13, 14] and from HST from 1994 to 2003 [15, 16, 17, 18], with a maximum resolution ~ 150 km/pixel. The Cassini Orbiter will also provide similarly accurate data during its mission starting in mid-2004.

Measurements of wind velocity vectors are usually affected by different types of errors (e. g. limb fitting of the planet, position determination of the targets and target identification), amounting to values 5 to 10 ms^{-1} for Jupiter and $10\text{-}15\text{ ms}^{-1}$ for Saturn. The maximum number of wind vectors measured was $N \sim 14,000$ for Jupiter and $N \sim 2,300$ for Saturn. Mean zonal velocities $\langle u \rangle$ (averaged in longitude) must be retrieved taking into account the local motions related to the particular features present in the flow (vortices, waves, turbulence) [8]. In Figure 6 we compare the mean zonal Jupiter profile as measured in three periods. Although changes in the jets intensity have been detected (for example at 23°N latitude, see below), the long-term ground-based observational records starting at the end of the 19th century, indicate that the Jovian winds show high stability in latitudinal location and intensity [19, 20]. Zonal motions are dominant in Jupiter and Saturn. The mean meridional velocity, $\langle v \rangle$, measured in Voyager images is typically smaller or of the same order as the errors ($\sim 5\text{-}10\text{ ms}^{-1}$), so few conclusions can be drawn on meridional motions. Some authors have claimed that a correlation exists between the averaged value of the cross

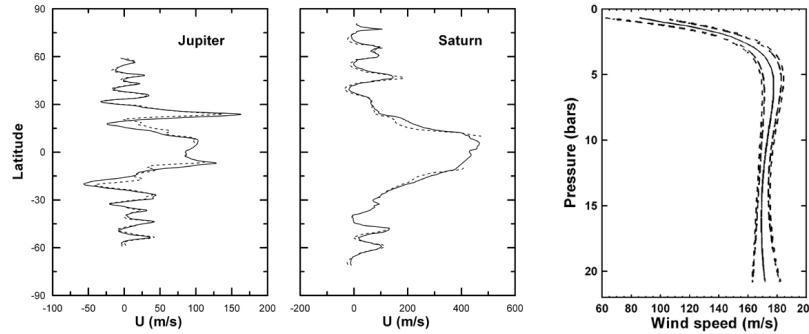


Figure 7: Left and Center: Jupiter and Saturn zonal wind profiles as determined at cloud levels around 700 mbar (continuous lines) and 50 mbar (dashed lines). The 50 mbar data were derived using eq. (2) and the temperature data from [22] and [23]. Right: Vertical wind velocity profile retrieved by the Galileo probe during its descent in 1995 in a point located at latitude 7°N [24].

products of the zonal and meridional velocity residuals $\rho \langle u'v' \rangle$ and the meridional zonal shear $d\langle u \rangle/dy$ [6, 21]. Here u' and v' are the velocity residuals obtained at a given latitude band, by subtracting the zonal mean velocity (averaged with respect to longitude) from the wind vector components. If this correlation exists, then the “eddies” will be transferring momentum to the jets, as in the case of the Earth’s atmosphere. However, this correlation has been questioned by other authors [25]. New careful analyses of the available data (and future data for Saturn) are necessary. A calculation of the eddy heat flux $\rho C_p \langle v'T' \rangle$ is also required.

Above the clouds, the measurements of the meridional temperature profile allow us to retrieve the vertical wind shear from the thermal-wind equation [26]. This relation is obtained from the momentum equation assuming hydrostatic equilibrium and geostrophic balance between the pressure gradient and the Coriolis force:

$$\frac{\partial u}{\partial z} = -\frac{g}{f R_p T} \left(\frac{\partial T}{\partial \varphi} \right)_p . \quad (1)$$

Here z is the vertical coordinate, g the acceleration of gravity, $f = 2\Omega \sin \varphi$ the Coriolis parameter, R_p the planetary radius, T the temperature and φ the latitude. The meridional wind profile at a pressure level P above the clouds can be vertically integrated to obtain

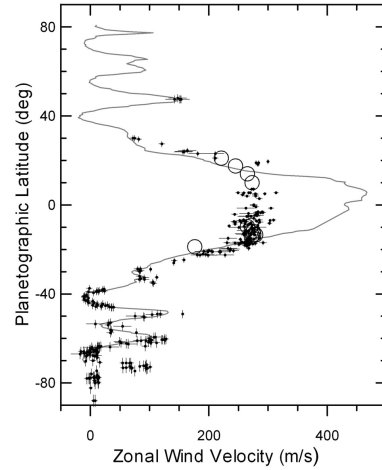


Figure 8: Saturn’s wind profile in time: Continuous line from Voyagers images in 1980-81 [14], circles and dots from 1994 to 2002 using ground-based and HST images [15]

$$u_g(P) \approx u_{clouds} - \frac{g}{f} \frac{\Delta T}{TL} H \ln \left(\frac{P_{clouds}}{P} \right), \quad (2)$$

where ΔT is the difference in temperature between two latitudes separated a distance L , $H = (R_g/m)(T/g)$, is the vertical scale height (being R_g the universal gas constant and m the atmospheric molecular weight), and L is a characteristic horizontal length (e.g. the jet width). As it can be seen in Figure 7 (left), the wind jet system decreases in intensity with altitude.

Below the upper ammonia cloud, the only direct measurement of the winds was done by the Galileo probe in December 1995 which determined that the winds increased with depth from 1 to 4 bars and remained constant at least down to the level of 24 bars [24] (Figure 7, right). However, this result cannot be extrapolated to other latitudes in view of the particular meteorology of the “hot spot” area where the probe entered [27, 28].

For Saturn the number of wind vectors measured is smaller (see above) but this situation will be soon improved by the Cassini Orbiter. Figure 8 shows the zonal wind profile measured during the Voyagers flybies in 1980-81 [14] and with the HST between 1996-2003 [15]. The most conspicuous result is the apparent drop in the equatorial jet intensity during the HST period amounting to $\sim 200 \text{ ms}^{-1}$ (or 40% of the peak value). The jets outside the equator did not change and show high symmetry

with respect to the equator. The few available ground-based historical data on cloud features motions suggests that, on the long-term, the winds are stable [29]. However, the outbreak of very rare but large-scale storms, the “Great White Spots” [29] can disturb the zonal winds by injecting or extracting momentum. This is one of the possible explanations for the observed wind drop measured between 1994 to 2003 since this period follows the two GWS outbursts of 1990 and 1994 [16, 17, 30]. This aspect will be discussed later.

4 General Circulation Models

General circulation models presented to date have some common basic assumptions: (1) Spherical geometry on a planet 10 times bigger than the Earth, (2) Low viscosity and energy dissipation; (3) Rapid rotation and validity of the quasigeostrophic approximation as suggested by the low values of the Rossby number:

$$R_0 = \frac{u}{fL} < 1. \quad (3)$$

The models differ on the dominant energy source driving the motions and, consequently, on their extent in depth. We focus on two main cases: “Deep” models, that have the internal heat source as the basic energy mechanism and where motions extend along the whole hydrogen molecular layer (down to pressures of ~ 1 Mbar), and “Shallow layer” models, that extend a few bars below the main upper cloud and have the solar radiation as the main energy source. In addition, we will present other proposals that assume the interplay of different energy mechanisms to produce the observed motions.

4.1 Deep circulation models

This family of models was firstly introduced for the giant planets by Busse [31]. For an inviscid and incompressible fluid confined on an spherical layer heated from below and in rapid rotation, the fluid dynamic equations show that the convective motions transporting the heat from the base to the top are subject to the constraint of the “Taylor-Proudman” theorem [32]:

$$(2\vec{\Omega} \cdot \nabla) \vec{u} = 0. \quad (4)$$

This equation states that the flow is confined to rotating columns around the rotation axis (with no vertical motions along the columns). That generates a secondary circulation in form of counter-rotating cylinders concentric with the rotation axis (Figure 9). The cylinders develop in the molecular hydrogen layer and are assumed not to penetrate the metallic hydrogen region. When the cylinders reach the

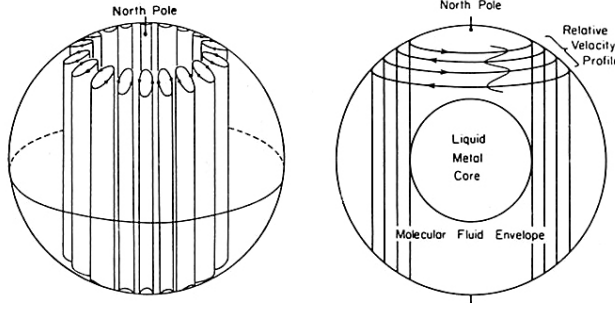


Figure 9: Scheme of the deep circulation models (columnar convection and coaxial cylindrical circulation) for the giant planets. From [13].

upper atmosphere, they give rise to the observed pattern of alternating jets. According to this hypothesis, the flow is deeply driven by the internal heat source. It extends along the whole atmosphere from one hemisphere to the other, generating a jet pattern hemispherically symmetric. The inertia of the cylinders would be so high (due to the mass they involve in the motions) that they must be very stable in time. However, if the metallic layer acts as an impenetrable barrier for the cylinders, the jet pattern should be limited in latitude by the cylinder that is tangent in the equator to the metallic region. In other words the pattern will be constrained by the width of the molecular layer (see Figure 9).

The complete set of equations that describe these motions are the continuity equation for an incompressible fluid, the Navier-Stokes equation on a rotating sphere and the thermodynamic equation:

$$\nabla \cdot \vec{u} = 0, \quad (5)$$

$$\frac{\partial u}{\partial t} + (\vec{u} \cdot \nabla) \vec{u} + 2\vec{\Omega} \times \vec{u} = -\frac{\nabla P}{\bar{\rho}} - \left(1 + \frac{\rho'}{\bar{\rho}}\right) \nabla \Phi + \nu \nabla^2 \vec{u}, \quad (6)$$

$$\frac{\partial T}{\partial t} + (\vec{u} \cdot \nabla) T = k \nabla^2 T - \left(\frac{dT}{dr}\right) \hat{k} \vec{u}, \quad (7)$$

$$\Phi = g \left(r - \frac{\Omega^2}{2g} r^2 \sin^2 \varphi \right), \quad (8)$$

being ν the kinematic viscosity, k the thermal diffusivity r the distance to the axis and \hat{k} the unitary vector on the radial direction. The Boussinesq approximation is used in the continuity equation. It assumes that the fluid density is constant except

in the buoyancy term, with the temperature and density fluctuations related to their mean value by:

$$T = T + T', \quad (9)$$

$$\rho'/\bar{\rho} = -T'/\bar{T}. \quad (10)$$

The fact that the non-linear terms are small relative to Coriolis forces in the giant planets means that the Taylor-Proudman theorem remains valid. Stress-free ($u = 0$, $T = 0$) or stress-rigid ($\partial u / \partial x = 0$) are used as boundary conditions in the spherical layer. This set of equations is best studied using the classical adimensional numbers:

$$\begin{aligned} \text{Prandtl: } & Pr = \frac{\nu}{k} \\ \text{Ekman: } & E = \frac{\nu}{2\Omega D^2} \left(\text{or Taylor: } Ta = \frac{4}{E^2} \right) \\ \text{Rayleigh: } & Ra = \frac{g\alpha(dT/dr)D^4}{\nu k} \end{aligned}$$

where α is the thermal expansivity and the critical Rayleigh number (Ra_{crit}) for the onset of convection depends on the Ekman number as

$$Ra_{crit} \sim E^{-4/3}.$$

The characteristic temporal scales for the diffusion processes are

$$t \approx \frac{L^2}{\nu}, \frac{L^2}{k}.$$

The equations describing the motions can then be rewritten adimensionally as

$$\nabla \cdot \vec{u} = 0, \quad (11)$$

$$E \frac{\partial u}{\partial t} + \hat{k} \times \vec{u} + \nabla P - RaET\hat{r} - E\nabla^2 \vec{u} = -E\vec{u} \cdot \nabla \vec{u}, \quad (12)$$

$$\left(Pr \frac{\partial}{\partial t} - \nabla^2 \right) T - \frac{1}{r} \frac{dT}{dr} \hat{r} \cdot \vec{u} = Pr \vec{u} \cdot \nabla T. \quad (13)$$

Linear analytical solutions to this system of equations [33, 34] and, the most complete numerical solutions [35, 36, 37], show the development of the columnar modes and deep cylinder circulation as suggested by the Taylor-Proudman theorem. The main limitation of these numerical calculations relies, firstly, on the restriction for the fluid to be incompressible and, secondly, on the numerical calculations imposed

by CPU time. This restricts calculations to values of $E > 10^{-6}$ and $Ra < 10^6$ whereas for Jupiter $E \sim 10^{-10} - 10^{-15}$ and $Ra \sim 10^{10} - 10^{15}$. In addition, it is assumed that $Pr \sim 0.01 - 10$, but indeed this parameter is not well known for Jupiter. Figure 10 shows some numerical results. The major success of these models is that they reproduce the eastward equatorial jet, showing that for high Rayleigh numbers, the kinetic energy is mainly zonal (up to 98 %) with the zonal flow driven by Reynolds stresses. The numerical models provide the Rossby number for the zonal flow and, to first order, the zonal jets have intensities $u \sim R_0 \Omega D$.

For Jupiter, using $\Omega = 1.75 \times 10^{-4} s^{-1}$, $D \sim 10 \times 10^7 m$ (the depth of the hydrogen molecular layer) and $Ro \sim 0.04$ (as obtained by the numerical calculations) we get $u \sim 70 \text{ ms}^{-1}$ in agreement with typical Jovian flow velocities. The numerical experiments also show that quasi-columnar motions develop outside the tangent cylinder limitation imposed by the hydrogen metallic layer (Figure 11). They were also predicted by the linear approach [34], but the induced zonal motions at high latitudes have low intensities since they do not reproduce the alternating jet pattern. The numerical simulations also indicate that, when a stress-rigid boundary condition is imposed at the bottom of the atmosphere, a “multi-jet” pattern develops. In this case, however, the intensity of the wind decreases at the equator [36].

Contrary to what it could be expected, these models show that, if the convecting atmosphere has an internal statically stable layer, as suggested from calculations of the molecular hydrogen opacity in Jupiter’s interior [39], the development of columnar convection can penetrate the stable layer in a phenomenon called “teleconvection” [38]. The columnar motions can propagate to the upper atmosphere and manifest themselves as a deep cylinder circulation.

A variant of the deep models that assumes the giant planet interiors to be incompressible fluids under geostrophic balance, and that pre-imposes an initial state of rotating columns (parallel to the rotation axis and traversing from one hemisphere to the other), has been recently presented [40]. The change of the column length with the distance to the rotation axis has a similar effect to the “shallow” layer β -effect (see below) in generating a turbulent pattern that evolves toward steady zonal winds. The difference with the “shallow” turbulence is that the deep “equivalent β -effect” has the opposite sign to the shallow one, and then the equatorial winds flow eastward, i. e. in the right direction. However, this model does not consider the metallic hydrogen internal region and the multi-jet pattern is not obvious in the calculations, contrarily to what the authors claim [40].

4.2 Shallow layer models

According to these models the motions are confined to the upper part of the atmospheric layer (the “troposphere”). This layer is differentially heated in latitude by the solar radiation. The meridional gradient of temperature drives the motions in a

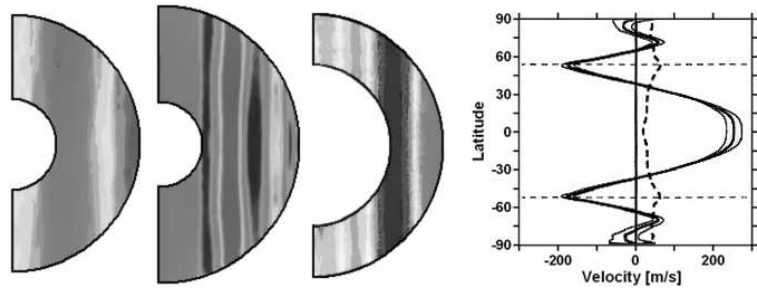


Figure 10: Numerical calculations of the columnar convection model. The figures show North-South cuts of different calculations. From left to right the following values for the adimensional numbers were used: $Pr = 1, E = 10^{-5}, Ra = 4.5 \times 10^8$ [37]; $Pr = 1, E = 10^{-5}, Ra = 10^6$ [38]; $Pr = 1, E = 3 \times 10^{-5}, Ra = 10^8$ [35]; cloud top zonal wind profile derived from the third case.

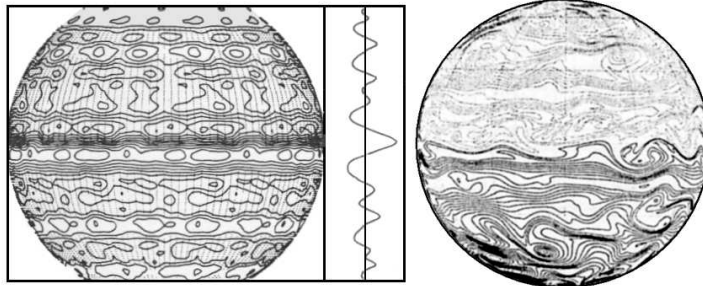


Figure 11: Shallow layer model numerical calculations. The flow field is represented by the streamlines (left) and potential vorticity (right) on the planet sphere according to calculations by two different teams [41, 42]. For the first case, an equatorially enhanced wind profile is also drawn.

frictionless (or under a weak linear drag friction) and hydrostatic quasigeostrophic balance. Williams [41, 43] was the first to formulate and solve the equations of motion for the Jovian case. In general, these models assume that an active “weather” shallow layer sits above a deep inactive “abyss”. Following [42] the motions in the upper layer of this system can be rewritten as

$$\frac{\partial \vec{u}}{\partial t} + (\vec{u} \cdot \nabla) \vec{u} = -g \nabla h - f \hat{k} \times \vec{u} + F_a, \quad (14)$$

$$\frac{\partial h}{\partial t} + (\vec{u} \cdot \nabla) h = -K h \nabla \cdot \vec{u} + F_d. \quad (15)$$

Here h is the active layer depth, F_a the adiabatic heating powering the motions and F_d a friction force [44].

Two important parameters that emerge in these models are the Rossby deformation radius, L_D , and the Rhines scale, L_β . The first represents the typical range of influence of a vortex patch on a rapidly rotating planet [20, 32]. The second represents the critical width of the zonal jets required for stability [1, 42]. They are given respectively by

$$L_D = (NH/f), \quad (16)$$

$$L_\beta = \sqrt{u/\beta}, \quad (17)$$

where $N(z)$ is the Brunt-Väisälä frequency, a measure of the vertical static stability of the atmosphere [26, 32]

$$N^2 = \frac{g}{T(z)} \left(\frac{dT}{dz} + \frac{g}{C_p} \right). \quad (18)$$

Given a random initial velocity, the system (14-15) is solved for h and \vec{u} , in order to retrieve the potential vorticity field $q(x, y)$,

$$q = \frac{\zeta + f}{h}, \quad (19)$$

$$\zeta = \hat{k} \nabla \times \vec{u}. \quad (20)$$

Here ζ is the relative vorticity and f , the Coriolis parameter, represents the planetary vorticity. Starting from a two-dimensional turbulent velocity field (the so-called “quasigeostrophic turbulence” [32]), the system evolves by means of a process known as “inverse cascade of energy” (merging the smaller scales of motion to larger structures), towards a zonally dominant jet pattern. Figure 11 shows the flow field maps for Jupiter according to this model as calculated by two different authors [41, 42].

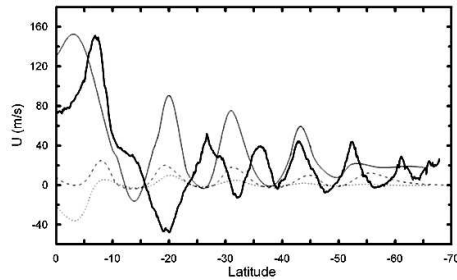


Figure 12: Zonal wind profiles at different altitudes of Jupiter according to a baroclinic intermediate “shallow” model, following [45]. Vertical levels represented are: $z = 0$ (continuous line), $z = -200\text{km}$ (dotted) and $z = -300\text{ km}$ (dashed). The Voyager wind profile is also shown for comparison (thick dark line).

The main problem in these models is that the equatorial jet flows in the westward direction (opposite to that observed). To get an eastward equatorial jet, as the one seen on Figure 11 (left panel), an enhancement by an *ad hoc* forcing is needed. Recent simulations of the two-dimensional turbulence on the surface of a sphere resulting from a small-scale forcing and a large-scale drag, have shown that the flow becomes anisotropic with energy concentrated in the zonal direction [4]. The spectrum of energy density distribution has the form

$$E(n) \approx L_\beta n^{-5}, \quad (21)$$

being n the zonal wavenumber. The calculated spectrum agrees reasonably well with the observed zonal jet pattern of Jupiter and Saturn.

Advanced models that include a full baroclinic treatment of the thin hydrostatic “weather” layer for different vertical thermal structures and with a weak linear drag in the deep layer are able to reproduce the system of alternating jets and generate the equatorial superrotation in the right sense. In order to obtain these results the model requires appropriate functions for the temperature distribution in the vertical-meridional plane [45] (Figure 12). For Jupiter, the calculations indicate that the jet system extends about 200 km in depth down to ~ 50 bar. One important problem of this model is that it predicts jet system to migrate in latitude as a response to the seasonal insolation cycle, but this has not been observed (see section 2). Another problem is that an unobserved equator to pole temperature difference of $10 - 20^\circ\text{ C}$ must be imposed to power the jets.

It has also been proposed that in the giant planets, the “shallow” meteorologically active layer could be dynamically similar to the Earth’s ocean “thermocline”, an upper

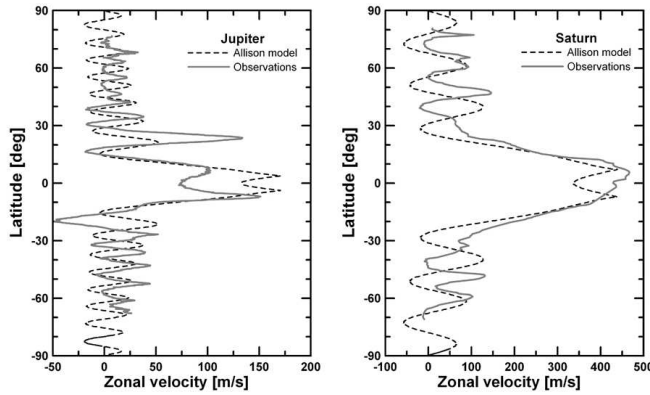


Figure 13: Zonal wind profiles (dashed lines) at cloud tops ($P \sim 0.5$ bar) in Jupiter and Saturn calculated according to the intermediate “shallow” thermocline hypothesis, as derived from [46]. They are compared to the observed profiles (continuous line).

oceanic layer of ~ 2 km depth where there is a high temperature gradient [46]. For a carefully chosen potential temperature distribution layer, an alternating zonal jet system could form down to depths ~ 50 bar in Jupiter and ~ 100 bar in Saturn. To first order, the winds should have velocities of $\sim \beta L_D^2 \cot \phi$, which amounts to $u_J \sim 130 \text{ ms}^{-1}$ for Jupiter and $u_S \sim 360 \text{ ms}^{-1}$ for Saturn (for typical values of $L_D \sim 1400$ and 3000 km respectively). The jet spacing will be then $\sim 2\pi L_D / (\sin \phi)^{1/2}$, in close agreement to that observed (Figure 13). The results are attractive but it is still to be known how this particular temperature structure is produced at those deep levels.

5 Other mechanisms that could act on the cloud level winds

Some teams have proposed that the shallow quasigeostrophic layer is bounded at its bottom by a deep but dynamically active layer that could be in solid body rotation or have a jet-like structure similar to that observed in the upper layer [47, 48]. These are “one and a half layer” models. The deep abyssal circulation corresponds to the special case $L_D = L_\beta$. Using $L_D \sim 1800$ km, as obtained from the measurements of the waves generated by the impact of the SL9 comet with Jupiter, this model predicts Jupiter’s westward jets to have small variations with depth, but the eastward jets to

increase by 50-100% with depth [48]. Then the question is how these deep jets form.

An important aspect, not usually covered by these models, is the role that the magnetic field plays on the observed circulation. The magnetic field is generated by a dynamo mechanism in the inner metallic region and it may influence the deep rotating cylinders discussed in section 4.1 [49]. The toroidal magnetic field generated will produce a Lorentz force per unit mass

$$\vec{F}_L = \frac{1}{\mu_0} (\nabla \times \vec{B}) \times \vec{B} \approx \frac{R_m B^2}{4\pi\rho l}, \quad (22)$$

$$R_m = \frac{lv}{\eta(T)} \approx \frac{Hw}{\eta(T)} > 1. \quad (23)$$

Here B is the magnetic field intensity, $l \sim H$ and w are a characteristic vertical length and velocity, R_m is the magnetic Reynolds number, and $\eta(T)$ is the magnetic diffusivity. Large and broad equatorial flows could form as a result of the magnetic force [49] if it had a real effect over the upper atmosphere.

Additional external forcing on the flow can be caused by the gravitational tides raised by the massive and innermost satellites of Jupiter and Saturn [50]. For example Io produces a 116 times more intense tide than that of the Moon on the Earth, and Titan's tides on Saturn are 5 times larger than the Moon's ones on the Earth. The tides accelerate the zonal flow specially if the interior is slightly stable to convection. The calculations show that tides can accelerate the Jovian atmosphere by ~ 1 cm s⁻¹/day [50]. Although this idea is suggestive, it can neither explain Saturn's equatorial flow being 5 times more intense than Jupiter's nor how the steady situation is reached.

Dynamical models that include a statically stable layer near the water clouds (above ~ 6 bar in Jupiter and ~ 10 bar in Saturn) have been generally successful in explaining the existence of the anticyclonic vortices. This layer extends below the penetration level of the solar radiation, and it has been argued that the increasing stability forms as a result of the latent heat release at the water clouds [51, 52] or by other thermodynamic effects (e.g. hydrogen ortho-para conversion) [53]. These thermodynamic effects could take part on the generation and maintenance of the zonal jets [54]. Moist convection can develop powerful storms transforming latent heat into intense upward motions [55] that are transformed into eddies through Coriolis forces and turbulent effects [56]. The eddies introduce momentum to the flow via a turbulent eddy flux $\langle \rho u'v' \rangle$ that accelerates the jets [57]. However, the Galileo probe data indicate that the Jovian winds are not confined to the altitudes above the water cloud base at ~ 6 bars, and apparently the flow is deeply rooted. Other clouds can form at much deeper levels near $T = 2000$ K [58]. They could have important effects over the deep dynamics stabilizing intermediate atmospheric layers and acting

as opacity sources for energy transfer. They certainly should be considered in future dynamical models.

6 Models of motions above the clouds

Different hypotheses have been suggested for the observed decrease of the wind pattern above cloud level (see section 3). One possible mechanism is that the upper flow decreases with altitude due to the friction imposed on the mean zonal flow at cloud top level. This process can be simulated by a parameterization of a dynamical balance between Coriolis forces and a Rayleigh friction drag, and by a thermodynamic balance using a Newtonian radiative damping [22, 23]. As a consequence, mass upwelling and downwelling above the clouds must occur. This motion is part of a mean meridional overturning that balances the Coriolis acceleration and the vertical advection of temperature with the dissipative effects, i.e. $fv \sim u/\tau_f$, $wHN^2/R_g \sim -\Delta T/\tau_{rad}$, where τ_f is a characteristic damping time, w the vertical velocity and τ_{rad} the radiative damping time. Another possibility is that the development of shear instabilities in the stable layer above the clouds produce large-scale eddies that give the required decay of jets within the upper troposphere and provide a physical mechanism for the underlying drag coefficient parameterization [59, 60, 61].

The dynamics in the upper troposphere and lower stratosphere is complicated by the presence of large-scale waves and by the belt-zone temperature differences produced by the differential sunlight absorption of the aerosols. The aerosols are specially abundant over the polar regions [62]. Models of the residual mean meridional circulation that take into account the solar deposition heating rates of the aerosols, result in an hemispheric-wide circulation cell (Hadley-like) that vertically extends from 1 mbar to 100 mbar [63, 64]. A two-year tracking of the aerosol debris left by the SL9 comet impact with Jupiter in 1994 supports the existence of a large meridional hemispheric circulation, but unfortunately this circulation has a sign contrary to the predictions of such models [65].

7 Laboratory Experiments

Several fluid dynamics experiments have been performed on ground and space-based laboratories aiming to simulate the general circulation on the giant planets. Many others have been done to simulate vortex formation, but these are not described here. Thermal convection experiments on a rapidly rotating sphere heated from below under microgravity conditions were performed by astronauts onboard the Spacelab [66, 67], confirming the formation of the columnar convection modes. Their experiments used $Pr = 8$, $E = 2.6 \times 10^{-3}$ and $Ra_{crit} = 2000$. Columnar motions taking place at

the onset of convection have been also observed on ground laboratories where the centrifugal force is used to compensate the gravity [34].

A deep convection laboratory analog consisting of a rotating bowl of warm water uniformly cooled at the free surface was demonstrated to generate convection cells that give rise to azimuthal jets when they encounter the free surface [68]. Symmetric bands and zonal jets in a rotating convecting fluid sphere have also been found for the following values of the characteristic numbers: $Pr = 6$, $E = 10^{-5} - 10^{-6}$ and $Ra_{crit} \sim 800$. However a low velocity equatorial jet flowing westward forms contrarily to what is observed in Jupiter and Saturn [69].

These results demonstrate that some features of the theoretical models can be captured on laboratory experiences, but new careful experiments resembling as much as possible the conditions on the giant planets interior (with respect to the values for Pr , E and Ra_{crit}) must be performed. Experiments under microgravity conditions would be specially useful (perhaps this could be an experience to develop in the International Space Station).

8 Final comments

One important point that can shed light on the general circulation is the study of the long-term temporal variability of the jet structure. A first simple argument is that if the insolation forcing dominates, as expected in most “shallow” water models, then a planet like Saturn that suffers intense seasonal insolation changes, enhanced in the equator by the ring shadowing, should follow the sunlight cycle. Its zonal jet system should change in jet location and intensity as a response to seasons. Our recent observation of a drop in Saturn’s equatorial wind velocity could point in this direction [15]. However, the observed stability of the non-equatorial jets together with the scarce available historical observations of Saturn’s winds suggest global long-term stability.

A second point is that we need details of the non-zonal component of the flow, including the momentum and heat transfer by eddies. In other words, we need to clarify what is the role the vortices and local motions (e. g. convective storms) play on the zonal circulation. The equatorial wind drop of Saturn could be simply the result of the large convective storm that erupted few years before the drop was detected. The change observed in the strongest jet of Jupiter [70] could have also been the result of a large disturbance that occurred there [71]. The hemispherical asymmetry observed between the tropical jets of Jupiter (compare the jets at latitudes 23°S and 23°N in Figure 6) could be due to the presence of the Great Red Spot that modifies the jets by deflecting them meridionally. If this were the case, the presence of the vortices could play an important role in shaping and pumping the jets. However, Saturn lacks in number and size the kind of large vortices present in Jupiter (at least

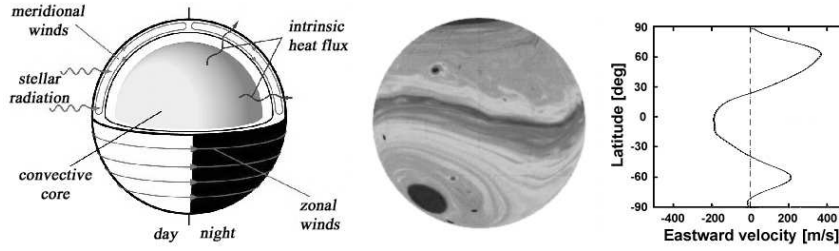


Figure 14: Proposed circulations on the extrasolar planet HD 209458b (a “hot Jupiter” class) according to the “shallow” layer hypothesis. Scheme at left is from [76]. The central sphere shows lines of potential vorticity and the plot at the right shows the derived zonal wind profile [44].

as observed at cloud level).

The stability of the jets against disturbances needs further theoretical analysis. Some westward jets are unstable according to the barotropic stability criterion [26]. The flow is stable provided that $\beta - \partial^2 \langle u \rangle / \partial y^2 > 0$ at all latitudes [6]. However, other kind of stability criteria should be applied for the zonal flow if, as expected, the fluid is baroclinic [72] or deep [73]. To solve these questions we need continuous high-resolution observations of the circulation. The upcoming research by the Cassini Orbiter on Saturn, will add much data to this aspect.

New perspectives in the studies of the giant planet dynamics have been opened with the discovery of giant extrasolar planets (see reviews in [3, 11, 74, 75]). Although still at an infancy theoretical level, the variety of properties of these planets relative to those of Jupiter and Saturn with respect to their internal structure, energy sources, rotation rates, and upper clouds (see Table 1), allows the exploration of a new larger ensemble of dynamical regimes [77].

The first quantitative efforts on the development of dynamical models have been directed to the planet HD 209458b that pertains to the “hot Jupiter” family of extrasolar planets. The reason is that its properties are the best determined among all them by observations of transits in front of its central star. In particular, its radius and mass and its rotation rate, assumed to be synchronous to the orbit, have been accurately determined. Figure 14 shows the predicted flow from two simulations based on a “shallow water” model for this planet [76, 44]. These calculations show the value of comparative fluid dynamic experiments and their future application to the exploration of these new worlds.

Acknowledgements: This work has been supported by Spanish MCYT research project PNAYA2000-0932, and the Universidad del País Vasco Grupos grant 13697/2001. RH

thanks a post-doctoral fellowship from Gobierno Vasco. SPH acknowledges a PhD fellowship from Spanish MECD.

References

- [1] Ingersoll, A.P. 1990, *Science*, 248, 308
- [2] Ingersoll, A.P., Dowling, T.E., Gierasch, P.J., Orton, G.S., Read, P.L., Sánchez-Lavega, A., Showman, A.P., Simon-Miller, A.A., Vasavada, A.R. To appear in: *Jupiter: The Planet, Satellites, and Magnetosphere* (F. Bagenal, W. McKinnon and T. E. Dowling, Ed.) Cambridge University Press, (in the press)
- [3] Burrows, A., Hubbard, W.B., Lunine, J.I., Liebert, J. 2001, *Rev. Modern Phys.* 73, 719
- [4] Sukoriansky, S., Galperin, B., Dikovskaya, N. 2002, *Phys. Rev. Lett.*, 89, 124501
- [5] Hanel, R., Conrath, B., Herath, L., Kunde, V., Pirraglia, J. 1981, *J. Geophys. Res.*, 86, 8705
- [6] Ingersoll, A.P., Beebe, R.F., Mitchell, J.L., Garneau, G.W., Yagi, G.M., Muller, J.P. 1981, *J. Geophys. Res.*, 86, 8733
- [7] Limaye, S.S. 1986, *Icarus*, 65, 335
- [8] García-Melendo, E., Sánchez-Lavega, A. 2001, *Icarus*, 152, 316
- [9] Porco, C.C., and co-authors 2003, *Science*, 299, 1541
- [10] Gierasch, P.J., Conrath, B.J. 1993, *J. Geophys. Res.*, 98, 5459
- [11] Guillot, T. 1999, *Science*, 286, 72
- [12] A. R. Vasavada, A.R., Ingersoll, A.P., Banfield, D., Bell, M., Gierasch, P.J., Belton, M.J.S., Orton, G.S., Klaasen, K.P., De Jong, E., Breneman, H.H., Jones, T.J., Kaufman, J.M., Magee, K.P., Senske, D.A. 1998, *Icarus*, 135, 265
- [13] Ingersoll, A.P., Beebe, R.F., Conrath, B.J., Hunt, G.E. 1984, Structure and dynamics of Saturn's atmosphere, in *Saturn*, T. Gehrels and M. S. Matthews (eds.), University of Arizona Press, Tucson, 195
- [14] Sánchez-Lavega, A., Rojas, J.F., Sada, P.V. 2000, *Icarus*, 147, 405
- [15] Sánchez-Lavega, A., Pérez-Hoyos, S., Rojas, J.F., Hueso, R., French, R.G. 2003, *Nature*, 423, 623
- [16] Sánchez-Lavega, A., Colas, F., Lecacheux, J., Laques, P., Miyazaki, I., Parker, D. 1991, *Nature*, 353, 397
- [17] Barnet, C.D., Beebe, R.F., Conrath, B.J. 1992, *Icarus*, 98, 94
- [18] Sánchez-Lavega, A., Lecacheux, J., Colas, F., Laques, P. 1993, *J. Geophys. Res.*, 98, 18857
- [19] Peek, B.M. 1958, *The Planet Jupiter*, Faber & Faber, London
- [20] Rogers, J.H. 1995, *The Giant Planet Jupiter*, Cambridge University Press, Cambridge
- [21] Beebe, R.F., Ingersoll, A.P., Hunt, G.E., Mitchell J.L., Muller, J.P. 1980, *Geophys. Res. Lett.*, 7, 1

- [22] Gierasch, P.J., Conrath, B.J., Magalhaes, J.A. 1986, *Icarus*, 67, 456
- [23] Conrath, B.J., Gierasch, P.J., Leroy, S.S. 1990, *Icarus*, 83, 255
- [24] Atkinson, D.H., Pollack, J.B., Seiff, A. 1998, *J. Geophys. Res.*, 103, 22911
- [25] Sromovsky, L.A., Revercomb, H.E., Suomi, V.E., Limaye, S.S., Krauss, R.J. 1982, *J. Atmos. Sci.*, 39, 1433
- [26] Holton, J.R. 1992, *An Introduction to Dynamical Meteorology*, Academic Press, San Diego
- [27] Showman, A.P., Ingersoll, A.P. 1998, *Icarus*, 132, 205
- [28] Showman, A.P., Dowling, T.E. 2000, *Science*, 289, 1737
- [29] Sánchez-Lavega, A. 1982, *Icarus*, 49, 1
- [30] Sánchez-Lavega, A., Lecacheux, J., Gómez, J.M., Colas, F., Laques, P., Noll, K., Gilmore, D., Miyazaki, I., Parker, D. 1996, *Science*, 271, 631
- [31] Busse, F.H. 1976, *Icarus*, 30, 255
- [32] Pedlosky, J. 1987, *Geophysical Fluid Dynamics*, Second Edition, Springer-Verlag, New York
- [33] Busse, F.H. 1983, *Pageoph*, 121, 375
- [34] Busse, F.H. 1994, *Chaos*, 4, 123
- [35] Christensen, U.R. 2001, *Geophys. Res. Lett.*, 28, 2553
- [36] Arnou, J.M., Olson, P.L. 2001, *Geophys. Res. Lett.*, 28, 2557
- [37] Christensen, U.R. 2002, *J. Fluid Mech.*, 470, 115
- [38] Zhang, K., Schubert, G. 2000, *Science*, 290, 1944
- [39] Guillot, T., Chabrier, G., Morel, P., Gautier, D. 1994, *Icarus*, 112, 354
- [40] Yano, J.I., Talagrand, O., Drossart, P. 2003, *Nature*, 421, 36
- [41] Williams, G.P. 1978, *J. Atmos. Sci.*, 35, 1399
- [42] Cho, J.Y.K., Polvani, L.M. 1996, *Science*, 273, 335
- [43] Williams, G.P. 1985, *Advances in Geophysics*, 28, 381
- [44] Cho, J.Y.K., Menou, K., Hansen, B.S., Seager, S. 2003, *ApJL*, 587, L117
- [45] Williams, G.P. 2003, *J. Atmos. Sci.*, 60, 1270
- [46] Allison, M. 2000, *Planet Space Sci.*, 48, 753
- [47] Ingersoll, A.P., Cuzzi, J.N. 1969, *J. Atmos. Sci.*, 26, 981
- [48] Dowling, T.E. 1995, *Icarus*, 117, 439
- [49] Kirk, R.L., Stevenson, D.J. 1987, *ApJ*, 316, 836
- [50] Ioannou, P.J., Lindzen, R.S. 1994, *ApJ*, 424, 1005
- [51] Barcilon, A., Gierasch, P.J. 1970, *J. Atmos. Sci.*, 27, 550
- [52] Gierasch, P.J. 1976, *Icarus*, 29, 445
- [53] Smith, M.D., Gierasch, P.J. 1995, *Icarus*, 116, 159
- [54] Allison, M., Stone, P.H. 1984, *Icarus*, 54, 296
- [55] Hueso, R., Sánchez-Lavega, A. 2001, *Icarus* 151, 316
- [56] Hueso, R., Sánchez-Lavega, A., Guillot, T. 2002, *J. Geophys. Res. Planets*, 107
- [57] Ingersoll, A.P., Gierasch, P.J., Banfield, D., Vasavada, A.R. 2000, *Nature*, 403, 630
- [58] Fegley, B., Lodders, K. 1994, *Icarus*, 110, 117
- [59] Pirraglia, J.A. 1989, *Icarus*, 79, 196

- [60] Orsolini, Y., Leovy, C.B. 1993, *Icarus*, 106, 392
- [61] Orsolini, Y., Leovy, C.B. 1993, *Icarus*, 106, 406
- [62] Moses, J.I., Fouchet, T., Yelle, R.V., Friedson, A.J., Orton, G.S., Bezard, B., Drossart, P., Gladstone, G.R., Kostiuk, T., Livengood, T.A. To appear in *Jupiter: The Planet, Satellites, and Magnetosphere* (F. Bagenal, W. McKinnon and T. E. Dowling, Ed.) Cambridge University Press, in press.
- [63] West, R.A., Friedson, A.J., Appleby, J.F. 1992, *Icarus*, 100, 245
- [64] Moreno, F., Sedano, J. 1997, *Icarus*, 130, 36
- [65] Sánchez Lavega, A., Gómez, J.M., Rojas, J.F., Acarreta, J.R., Lecacheux, J., Colas, F., Hueso, R., Arregu, J. 1998, *Icarus*, 131, 341
- [66] Hart, J.E., Toomre, J., Deane, A.D., Hurlburt, N.E., Glatzmaier, G.A., Fichtl, G.H., Leslie, F., Fowlis, W.W., Gilman, P.A. 1986, *Science*, 234, 61
- [67] Hart, J.E., Glatzmaier, G.A., Toomre, J. 1986, *J. Fluid Mech.*, 173, 519
- [68] Condé, S.A., Rhines, P.B. 1994, *J. Fluid Mech.*, 280, 349
- [69] Manneville, J.B., Olson, P. 1996, *Icarus*, 122, 242
- [70] García-Melendo, E., Sánchez-Lavega, A., Gómez, J.M., Lecacheux, J., Colas, F., Miyazaki, I., Parker, D. 2000, *Icarus*, 146, 514
- [71] Sánchez-Lavega, A., Miyazaki, I., Parker, D., Laques, P., Lecacheux, J. 1991, *Icarus*, 94, 92
- [72] Dowling, T.E. 1995, *Ann. Rev. Fluid Mech.*, 27, 293
- [73] Ingersoll, A.P., Pollard, D. 1982, *Icarus*, 52, 62
- [74] Perryman, M.A.C. 2000, *Rep. Prog. Phys.*, 63, 1209
- [75] Hubbard, W.B., Burrows, A., Lunine, J.I. 2002, *ARA&A*, 40, 103
- [76] Showman, A.P., Guillot, T. 2002, *A&A*, 385, 166
- [77] Sánchez Lavega, A. 2001, *A&A*, 377, 354

ASTRONOMICAL TELESCOPES AT THE TURN OF THE CENTURY

JOSÉ M. RODRÍGUEZ ESPINOSA

Instituto de Astrofísica de Canarias, E-38200 La Laguna, SPAIN

Abstract: The final years of the XXth Century and the initial years of the XXIst Century are witnessing a revolution in the construction of large telescopes. This has been possible thanks to the availability of both thin mirror technologies and large computing power. Astronomy is thus benefiting from this. Indeed the turn of the century has been rich with new discoveries, from the detections of extrasolar planets to the discovery of the farthest galaxies ever seen or the detection of acceleration in the expansion of the Universe.

Spain is leaving her imprint on the telescope making revolution and is promoting the construction of a 10.4 metre telescope in the “El Roque de Los Muchachos” observatory, on the Island of La Palma, Spain. The Gran Telescopio Canarias (GTC) is currently at an advanced stage of construction, with science operation expected to start early in 2006.

1 Introduction

Modern technology telescopes started to be made at the turn of the XIX century when precision mechanics and precision optics started to be common use. In the past, telescopes suffered from poor optics, as optical glasses were very difficult to manufacture, and aluminization techniques were far from perfect. Nonetheless Astronomy had continued its advance during the XIX century. This was the century of the stellar catalogues, the initial steps in stellar spectroscopy, with the generalized use of photographic plates.

The beginning of the XXth century brought us the HR diagram and the first attempts to study the stellar evolution. In the 20's, the Curtis-Shapley controversy on the size of the Milky Way was resolved and astronomers realised that the Universe was a few orders of magnitude larger than previously thought. At that time the recently built Mt. Wilson 2.5m telescope was used to observe galaxies and with it Hubble discovered the general expansion of the Universe. Extragalactic Astronomy was starting prompting the construction of a 5 metre telescope a top Palomar Mountain to put on a firmer basis the expansion claim by observing the farthest galaxies. The Palomar

5m telescope was finished in 1945, in the midst of the European War. The Hale 5m telescope, as the Palomar telescope was later known, has been one of the pillar of the development of astronomy during the XXth Century. Much of the theory of Stellar Nucleosynthesis was based on observation done with the Hale telescope. The discovery of the Quasars was also done with this telescope. The Hale telescope also set the standards for telescope making technology, later followed by many other telescopes built around the world.

2 Progress in Telescope Making

A key aspect that I would like to stress at this point is that the construction of new and better telescopes has been fundamental in the advancement of astronomy. New and better telescopes and instruments have always resulted in clear advances in most if not all branches of Astronomy.

It is interesting to note that as the XXth Century advanced new telescopes were getting built, however with no increase in the size of their primary mirrors. Several telescope built from the 50's to the 80's include the Shane 3m telescope at Lick, the Crimean 6 m telescope, the Kitt Peak 4m telescope, the ESO 3.6 m in La Silla, the German 3.6 m telescope in Calar Alto (Spain), the Anglo-Australian and the William Herschel 4m telescopes in Australia and at La Palma respectively, amongst others.

Except for the Crimean 6m telescope, it is interesting to note that most other telescope built during the XXth Century were of the so called 4m class. Astronomy was advancing though at quite a fast pace, with the discovery of AGNs and quasars, the most luminous objects known to date, or the many advances in the study of the chemical abundances in many different kinds of galaxies and environments. However as I say, all this progress was being made with 4m class telescopes.

The important aspect to notice is that the photon collecting power of these telescopes was being increased enormously. Not by making the telescopes bigger but by making the focal plane instruments more efficient and sensitive. This was so because in the early XXth century the most common detector used was the photographic plate. Around that time, advances in electronic devices resulted in a large improvement of the performance of detectors. First phototubes, and photomultipliers, later semiconductor devices such as the Charge Coupled Devices, resulted in almost two orders of magnitude increase in detecting power, or quantum efficiency as it is generally known. Indeed the quantum efficiency of detectors was augmented from a few percent for photographic plates to almost 99% for modern CCD arrays. This was combined with the availability of panoramic arrays, allowing multi-object capabilities, or wide area surveys. The clear advantage for astronomy was that even if the size of telescopes did not increased, astronomers were having a bonus in the improvement of detector devices.

In parallel, telescopes were being made better. Telescope mechanics was greatly improved with the use of Horizontal Mounts. These provided better mechanical stability for pointing and tracking, offering at the same time large Nasmyth platforms for the location of both heavy and sturdy high resolution spectrographs that allowed the study of lines profiles with unprecedented resolution. Horizontal mounts were known from several centuries back. Their astronomical use was however not widespread due to the complexity of the motion involved in tracking objects in the sky, necessary to correct for the motion of the Earth. Not until the advent of powerful enough computers was it possible to perform real time computations of the positions of the telescope axes required to follow a given object on the sky.

Summarizing, from the mid 40's to the mid 80's, Astronomy advanced at a great pace while the size of the telescopes remained rather constant at a canonical size of about 4 meter for the primary mirror. During this time the great development was in detector technology that evolved from photographic plates with quantum efficiencies of a few percent, to electronic devices bringing the quantum efficiency to almost 100%. Detectors also were enlarged in size from single unit detectors to arrays reaching several millions detectors per device. Science instruments benefited also from the availability of new detectors. New and much better instruments were therefore built for the 4m class telescopes. These allowed the fast advancement of astronomy that was made during the XXth century.

Telescope making also progressed. Mechanical precision was substantially improved. Optical fabrication and finishing, as well as metrology were also greatly improved in the interim. Finally, electronics, software and control did really come of age, thus setting up the stage for the revolution that was about to come in the last years of the XXth century.

3 Thin Mirrors

In the mid 80's it was clear that further advances in Astronomy required further increases in light gathering power. QSO research demonstrated that these were the nuclei of very faint galaxies that were very difficult to detect. QSO's were also the objects with the highest redshift known. QSO's were nonetheless pathological objects. If the high-z Universe was made of QSOs only it would have been difficult to reconcile the present day Universe with the high-z Universe. Therefore, it was clear that larger and more powerful telescopes were needed to, amongst other things, detect faint "normal" galaxies at high-z.

The road to higher quantum efficiency detector had already been explored. Further improvements in detector would come from either larger panoramic formats, better cosmetic or less electronic noise. However, even if these improvements were indeed welcome, the gain in actual photon collecting power would not be of order of

magnitude, as would be required for the kind of Astronomy that people were trying to do.

Astronomy thus demanded larger telescopes. Telescope making technology had been largely improved in the past 50 years or so. Perhaps, the only stumbling block was the fact that increasing the size of primary mirrors had to be done not at the expense of heavier mirrors, as this would have resulted in much heavier mechanical structures that would have been poised to wild flexure problems.

The solution to this impasse came from the great creativity and insight of people like Jerry Nelson in California who proposed the use of thin mirrors. Thin mirrors had the great advantage of being much lighter and the disadvantage of being fairly deformable, requiring some active mechanisms for maintaining the optical figure as required, both when the mirror is static and against deformation by gravity as the mirror is changed in position.

Fortunately, the technology was ready to take up the challenge of actively controlling the shape of thin mirrors. Realising this was Nelson's greatest achievement. The road was therefore open to new increases in telescope sizes.

The late 80's were full of enthusiasm for the design of larger telescopes both in the US and in Europe. Thin mirror technology was indeed the default, although a large spree of technological developments were necessary before these ideas could be put into practice. These included polishing large thin mirrors, or in the case of segmented mirror, polishing off-axis powered mirrors. The segmented approach was developed by Jerry Nelson during the conceptual design of the Keck telescope. In Europe the preferred approach was to produce large monolithic thin meniscus mirrors. The support strategy was common to both. The mirror production strategy was very different though.

By the early 90's both in the US engineers were advancing in the construction of the Keck telescope, a 10 metre segmented primary telescope, and in Europe the canonical project was the VLT, an array of 4 eight meter telescopes to be located in Chile. Soon there was also the GEMINI partnership (UK, US, Argentina, Brazil and Chile), two eight metre meniscus type telescopes to be placed both in Hawaii and Chile, as well as the SUBARU telescope, a Japanese 8 metre meniscus telescope that was also to be located in Hawaii. Quite an impressive number of eight to ten metre telescopes at once!

The first of these telescopes to enter in operation was the Keck telescope. It was also the first large telescope to install a segmented primary mirror, and therefore to have solved all the difficulties related with the alignment and phasing of the 36 segments making up the full primary mirror. The success of this first large telescope was such that it prompted the Keck Foundation to fund a second one with the goal of making optical and infrared interferometry. Yet a step forwards towards increasing the spatial resolution of the observations.

Soon thereafter the European VLT, the Japanese SUBARU and the international

GEMINI projects commissioned its first telescopes. In a few years, the total collecting area had increased several times the total collecting area ever built in the past. Results from these telescopes appeared immediately after their commissioning. High redshift galaxies, extrasolar planets, brown dwarfs, high-z supernovae, etc. Results that have put Astronomy in the first pages of mass media. Results, like the accelerated expansion of the Universe, obtained through the observation of high redshift supernovae, that have been considered by the US scientific journal “Science” one of the major physics discoveries of the decade.

4 The Spanish 10 metre telescope

In this scenario of excitement for new discoveries, Spain, through the pro-active promotion of the Instituto de Astrofísica de Canarias, started what will be the first European large segmented telescope. By the time of the Spanish decision to embark on the construction of a large telescope both approaches, the segmented and monolithic meniscus ones, had been demonstrated although only the Keck had recently started operation.

Prior to this, Spain, or rather the IAC had worked in a monolithic meniscus type eight metre telescope project together with the UK. This project, which was carried out till the production of a conceptual design document, was however abandoned when the UK joined forces with the US to constitute the GEMINI consortium. The IAC nonetheless insisted in pursuing the idea of having a large telescope in its observatory and continued its development work for controlling thin mirrors. Equally importantly though was the formation at the IAC of a group of scientists and engineers whose aim was the promotion and initial design of a Spanish large telescope.

This group produced a first design of a eight metre meniscus type mirror and called on a group of international experts to review the concept and make recommendations to pursue the idea of building a large telescope in Spain. It is interesting to note that the review panel consisted of the top leaders of the large telescopes projects then in the making. The panel was chaired by Paul Murdin, who had been in charge of the commissioning and first years of operation of the Williams Herschel telescope in La Palma. Jerry Nelson, from the Keck telescope, was also in the committee, and he represented the only large telescope that had started operation by then. Other members in the panel included Matt Mountain from GEMINI, Massimo Tarenghi, from VLT, Masanori Iye from SUBARU, John Hill, from LBT, and Arne Ardeberg from the NOT telescope. Soon after this meeting the idea of changing the project to a segmented telescope instead was taking shape.

The final decision to promote a segmented 10 metre telescope was taken after the visit of a group of scientists and engineers to the US to visit the Keck facilities, as well as some of the contractors that had participated in the production of the Keck

mirror segments.

Reason for the change of concept were diverse. Certainly the success of the Keck telescope was taken into account. However other considerations were also important. For instance, the difficulty in bringing a monolithic meniscus through the narrow and winding road to the observatory weighed heavily on the decision. The thought that a 10 metre segmented primary mirror telescope could be done for about the same price tag as an eight metre monolithic thin meniscus one was also important. Finally, although not considered at that time, it was soon realised that any future larger telescope would have to be segmented, thus Spain would be in a very good position for contributing actively to future large telescopes.

5 THE GTC

The Gran Telescopio Canarias (GTC) will be an advanced telescope when it enters operation at the Observatorio del Roque de los Muchachos (ORM) in the island of La Palma. It will carry a segmented primary mirror, consisting of 36 hexagonal segments. The secondary mirror will be a light weighted hexagonal mirror made of beryllium. The GTC will carry a third mirror, the tertiary mirror to fold the light beam to any of the Nasmyth or the folded Cassegrain foci. The optical design of the GTC is a Ritchey-Chretien with an effective focal ratio of $f/17$. This results in a focal plane scale of 1.21 arcsecond per millimetre.

6 The GTC: Status and perspectives

The Gran Telescopio Canarias (GTC) is currently being assembled at the ORM in La Palma. First light is expected for mid 2005 with the first science observations expected by mid 2006. As of this writing the enclosure, building and dome, are finished, with minor problems pending. These are related to the shutter motion and the ventilation windows. Solutions for fixing the problems exist already to be implemented by the summer 2004.

By the time the telescope is turned to the operation team, the two Nasmyth platforms will have been commissioned together with two science instruments (CANARICAM and OSIRIS/ELMER).

For the time being, the main milestones are the completion of the telescope mount inside the dome, the reception of the first batch of segments, the acceptance of both the Acquisition and Guiding boxes and the Commissioning Camera. Further tasks for the immediate future are the start of the Astronomy operation group and the integration of the first science instruments. These first two instruments will provide the GTC with capabilities for low resolution multi-object spectroscopy, imaging in

both lines and continuum in the optical and mid infrared, as well as polarimetry and, for the first time ever, coronagraphy in the mid infrared.

6.1 Enclosure

Work inside the enclosure is progressing. Offices are being furnished and labs are being supplied with their necessary equipment. The air conditioning system is working normally.

The GTC enclosure has been provided with 32 ample independently operated ventilation windows, allowing for 432 squared metre of clear opening spaces, to help maintain a laminar flow of air during the night. This is important to keep the inside temperature equal to the outside temperature, thus reducing temperature gradients that may degrade the quality of the images produced by the telescope.

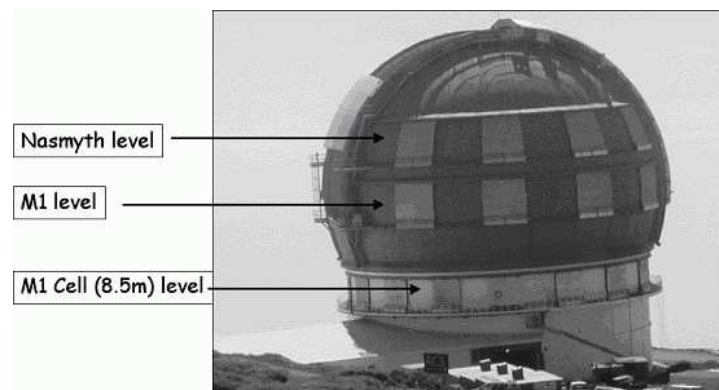


Figure 1: GTC enclosure showing the ventilation windows in three rows.

The azimuth pier is ready to take up the azimuth ring. As of this writing the azimuth ring is being mounted and adjusted. Figure 2 shows the interior of the dome with the azimuth pier in the centre. Figure 3 shows the azimuth ring already set over the pier.

6.2 Telescope Mount

Once all homogeneity, roughness, eccentricity, etc. tests are finished for the azimuth ring, the rest of the telescope will continue being mounted. Most major pieces of the telescope structure are at the site waiting to be installed. Those not needed in the



Figure 2: Interior of the dome showing the azimuth pier.

immediate future are still undergoing tests in their respective factories. That is the case for instance of the instrument rotator bearings (Figure 4).

Next steps in the mounting process will consist of the installation of the hydrostatic bearings and the rotating floor, allowing to test the azimuth rotation. Once this is achieved the azimuth encoder tape will be installed, and in parallel the yoke of the telescope will be erected, to continue with the elevation ring and mirror cell, the elevation trunnions and Nasmyth platforms, the tertiary tower, upper tube, spider ring and secondary support structure. This will take the rest of 2004 and some time in 2005.

By then, and once the necessary performance tests are satisfactorily passed, the telescope will be ready to take up the optics.

6.3 Telescope Optics

All 36 (+6 spare) segment blanks are fabricated. Made of Zerodur by SCHOTT, their measured properties comply with the specifications in all respects, in particular in term of low thermal coefficient of expansion and homogeneity of this coefficient.

The segment blanks are now at SAGEM, near Paris, where they are being polished. The polishing process is a lengthy and complicated one due to the extreme accuracy required to meet the strict image quality requirements of the GTC.

The secondary mirror is also being polished after a complicated blank production process in which several blanks were broken. The secondary mirror is made out of Beryllium as it needs to be very light while being fairly rigid. The GTC secondary mirror (Figure 5) is an important part of the telescope as it defines the entrance aper-



Figure 3: The azimuth ring on top of the pier.



Figure 4: Instrument rotators bearings being tested.

ture of the telescope. This is to maintain low thermal emissivity for better infrared performance of the telescope. The secondary mirror has five degrees of freedom, to maintain the correct alignment between the primary and secondary mirrors when the telescope changes elevation, to perform fast guiding and to correct for wind buffeting on the telescope structure, and finally to perform chopping for infrared observations.

Other important optical systems include the Tertiary mirror that is being polished in Moscow and it is expected to be finished by mid 2004, the Commissioning Camera, that is being made in Mexico and is about to be completed, and the Acquisition and Guiding (A&G) boxes. Both the Commissioning Camera and the A&G boxes are complicated subsystems, employing several cameras (Figure 6) as well as several wavefront sensing devices. The Commissioning Camera is meant to help during the initial alignment and phasing of the primary mirror segments. The A&G boxes will be in charge not only of acquiring the object to be observed and keeping it within



Figure 5: Secondary mirror.

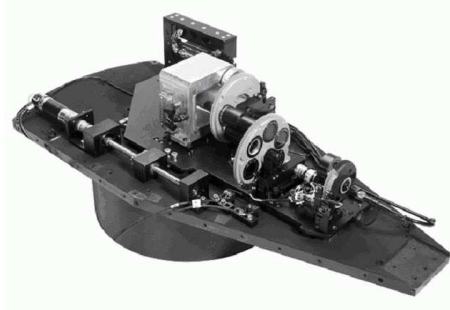


Figure 6: One of the arms of the Acquisition and Guiding boxes. The picture shows the optics inside this arm.

the aperture of the instrument, which is the classical use of the A&G boxes, but also will perform wavefront sensing to regularly monitor the status of the telescope optics. This is an advantage with regards to the Keck telescopes. These can not perform wavefront sensing on real time except when their Alignment Camera is installed, which is not always the case.

6.4 Software and Control

The GTC will be controlled by an overall software system that sees the GTC as a single unit. Every subsystem will be included in this software, from the dome and the different equipment in the dome to the telescope, optics, instruments, and including the data acquisition and processing pipelines from the moment a proposal is submitted

by an astronomer to the moment the data are sent to the astronomer and archived in the GTC archive. The control system is therefore key to the successful operation of the GTC.

Of great interest for astronomers is every thing that is related with the science instruments and the scientific data. The software for generating the observing proposals is quite advanced, with test versions already available. This software will use a scheme of two phases. Phase II will be used by those astronomers granted time by the different allocation committees, to introduce enough details of their observations to produce the observing blocks that will be used by the observatory staff to perform the observations.

The control system includes data reduction pipelines, consisting of a basic reduction pipeline and a more advanced data reduction. The basic reduction is meant to correct those effects that are originated in the detector arrays, i.e. bias, dark current, flats, cosmetic, etc. Then, depending on the observing mode, there may be a more advanced pipeline that might perform wavelength calibration and a spectral extraction. This software may be of valuable use for the astronomer, at least to make an assessment of the data present in the archive. The software is also of good use for the observatory crew to ascertain the quality of the observation being done during the night, and indeed for monitoring the performance of the instruments.

7 The Science Instruments

The GTC will be equipped with a suite of facility instruments presently under construction. The first generation instruments will be OSIRIS and CANARICAM. A third instrument under construction, ELMER, is a backup instrument meant to be used if the main instruments are not on time when they are required at the telescope.

A instrument belonging to the second generation of facility instruemns, EMIR, has been started, so that there is not a big gap between the arrival of the first instruments, and that of the second generation. To complete the picture, some visiting instruments that have been proposed will be mentioned. These are CIRCE and UES.

In what follows there is a brief description of these instruments.

7.1 OSIRIS

OSIRIS is instrument whose primary design goal is to perform wide field ($8' \times 8'$) optical imaging with tuneable filters, therefore being specially suited for performing surveys and detailed studies of emission line objects. OSIRIS will also be capable of performing low resolution spectroscopy ($R= 500$ to 2500), both multi-object and long slit, as well as fast photometry and spectrophotometry.

OSIRIS will be equipped with two modern 2Kx4K CCD arrays, with frame transfer

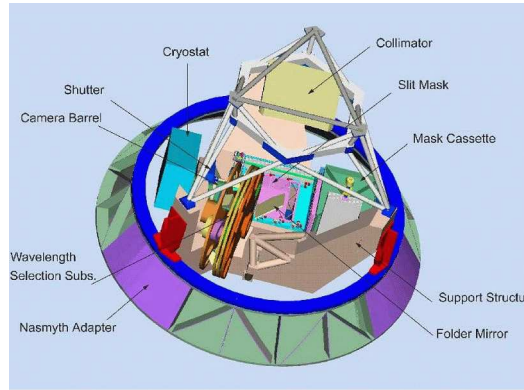


Figure 7: A drawing of OSIRIS showing its main parts.

capabilities, allowing observations of the line and continuum, followed by on chip subtraction before reading out the array, therefore substantially reducing the noise.

OSIRIS is a project led by Jordi Cepa, from the IAC, with strong collaborations from the Institute of Astronomy at the UNAM (Mexico) and the University of Cantabria (Spain). OSIRIS will be an excellent instrument to study the evolution of galaxies both in clusters and in the field, as well as detailed observations of nearby galaxies. Figure 7 shows a drawing with the main parts of OSIRIS marked. OSIRIS is in a fairly advanced state of construction. Integration is expected to start in the second half of 2004, with completion expected by June 2005, well in time of being installed at the telescope for tests and commissioning.

OSIRIS should be able to reach 26 magnitude objects in the r (SDSS) band with a signal to noise ratio of 5 in 1000 seconds. In spectroscopy, OSIRIS should be able to observe objects of magnitude between 20.5 and 22 depending upon the wavelength and the dispersion employed.

7.2 CANARICAM

CANARICAM is a thermal infrared instrument being built at the University of Florida, Gainsville. Charlie Telesco is the Principal Investigator. Charlie Telesco is very well known for the constructions of several first class thermal IR instruments both for space and the ground. CANARICAM will be capable of performing imaging, spectroscopy, polarimetry and coronagraphy in the mid IR bands from 8 to 25 micron. CANARICAM will be specially suited for observing brown dwarfs and exo-solar planets, as well as dust enshrouded objects like protostars, regions of star

formation, and high redshift star forming galaxies.

CANARICAM is fairly advanced with most optical components already fabricated. The cryostat (Figure 8) is undergoing tests, and will be ready to start integrating all components soon. CANARICAM is expected to be delivered in June 2005.

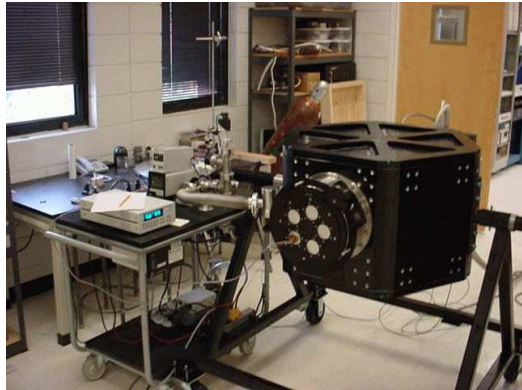


Figure 8: The CANARICAM dewar undergoing tests in the laboratory.

CANARICAM will be able to observe point sources as faint as $30 \mu\text{Jy}$ ($\text{S/N}=1$ in 1 hour) in the $10 \mu\text{m}$ band or perform line spectroscopy of objects with $0.7 \times 10^{-18} \text{ W m}^{-2}$ with the high resolution grating ($R \sim 1300$).

7.3 ELMER

ELMER is an instrument for performing imaging and low to intermediate resolution spectroscopy in the optical range. With a field of view of over 3×3 arcminutes squared ELMER is optimised for maximum throughput. The design of ELMER (Figure 9) has been made in such a way as to minimise risks maintaining a tight budget.

ELMER is advancing quite satisfactorily under the leadership of Marisa García Vargas, from the GTC Project Office. ELMER will perform imaging with conventional narrow and broad band filters, and low resolution ($R=500$) spectroscopy with prisms, medium resolution ($R=1500$) spectroscopy with grisms, and relatively high ($R=5000$) resolution with Volume Holographic Prisms.

ELMER is also capable of performing fast photometry as well as fast spectrophotometry. This is achieved, as in OSIRIS, by using the charge transfer capability of the array detectors combined with adequate masks and a clocking strategy for fast shifting of the charge up in the array.

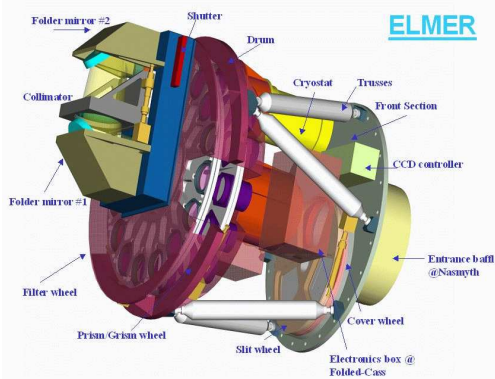


Figure 9: Drawing of ELMER showing the main parts and the compact design.

It is expected that ELMER will attain very high sensitivities. Current estimations provide figures like 26.8 magnitude in the r band (S/N: 5 in 1 hour with 1 arcsecond seeing). For spectroscopy the expected sensitivity is 20-22 magnitude (depending on wavelength) for a S/N= 20 under 0.6 arcsecond seeing in 1 hour.

ELMER is designed to be eventually installed at one of the GTC Folded Cassegrain foci, providing therefore an excellent standby instrument for imaging and spectroscopy even when the primary instrument may be any other of the GTC facility instruments.

7.4 EMIR

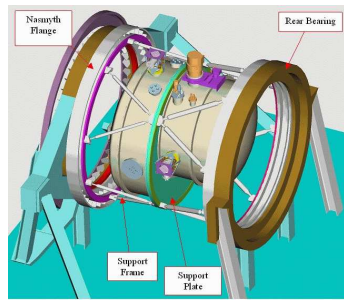


Figure 10: Drawing of EMIR showing the main parts and the compact design. The outer shield is a cryostat

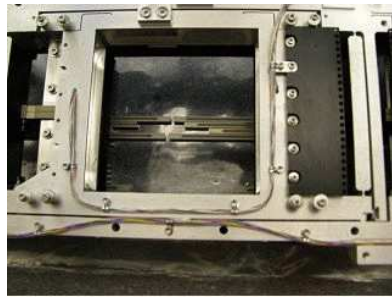


Figure 11: Prototype of the EMIR slit mask unit. Note the sliding blades that make up the slit of the desired size.

EMIR is a wide field multi-object cryogenically cooled near IR spectrograph (Figure 10). EMIR is being designed and fabricated at the IAC under the leadership of Francisco Garzón, with strong collaborations from the Universidad Complutense de Madrid and the Observatoire de Midi-Pyrénées. The design of EMIR is driven by COSMOS, a scientific project which aim is to make a census of the star forming galaxian population out to redshift 2.5, in order to set quantitative limits to the star formation density when the Universe was much younger than it is now.

EMIR will perform imaging and spectroscopy from 1 to $2.5 \mu\text{m}$. Key features in EMIR are the very wide field of vision, 6×6 arcminutes squared, and the relatively high resolution required to perform an adequate subtraction of the OH telluric lines. EMIR will perform multi-object spectroscopy with masks that will be cryogenically cooled. One of the challenges of EMIR is to produce a mask changing mechanism that does not involve warming up and cooling down the instrument every time that the masks need to be changed. The current baseline for EMIR is to implement a robot (Figure 11) that will be in charge of producing the masks whenever needed. This robot will use a set of cryogenically cooled sliding blades that can be software controlled. EMIR is expected to be completed by the end of 2006.

7.5 Visiting Instruments

The GTC is adopting a policy for visiting instruments in order to fill some niches not covered by the initial facility instruments. There are several instruments that have been proposed as visiting instruments. Perhaps the two more interesting ones are CIRCE and UES.

CIRCE is a near IR camera that will fit into one of the Folded Cassegrain foci. CIRCE will be provided by the University of Florida and will add near IR capabilities

to the GTC before the arrival of EMIR.

UES is a high resolution echelle spectrographs that has been in use at the Williams Herschel telescope for more than ten years. UES has been recently decommissioned. Ramón García López from the IAC is leading the conversion of UES to the GTC, through a fibre plus micro lenses link. UES will be upgraded with new coatings, new detectors and new software. UES will provide high resolution ($R = 50000$) to the GTC.

8 Adaptive Optics

The quest for image quality can be taken beyond the optics of a given telescope. Once a telescope is built with precise requirements on the quality of the optics, reality tells that the atmosphere is then the limiting factor dictating the image quality obtained on the array detectors. This is commonly known by the term “seeing limited” images. Space telescopes on the contrary are limited by the quality of their optics, or in other words, they produce diffraction limited images.

Ground based telescopes are actively working on methods to circumvent the atmosphere in their quest for image quality. One method that is actively being developed is “Adaptive Optics”. Adaptive Optics is a technique that tries to correct for turbulence in the atmosphere therefore producing nearly diffraction images. There are two main elements to an adaptive optics system, namely the characterization of the turbulence pattern in the atmosphere and the reconstruction of the corrected light beam. The first one requires the availability of a bright enough reference source. The second one is done with a deformable mirror that produces positive or negative phase shifts in the footprint of the beam in order to flatten it out.

The first part is achieved with a wavefront sensor that analyses that light from the reference source on almost real time, thereby determining the aberrations that the light beam carries after its passage through the atmosphere. The measurements need to be done relatively fast as the atmosphere is constantly changing. This requires a relatively bright source close to the object of interest. This is not always possible and in order to increase the fraction of sky over which the correction can be made artificial laser reference stars are produced. This is a technique that has been tested satisfactorily, however the availability of sufficiently powerful lasers is still a problem.

Once the signal has been processed by the wavefront sensor and the aberrations have been determined the loop is closed with the deformable mirror, and this is programmed in such a way as to correct the beam. Deformable mirror technology is advancing quite rapidly.

The GTC has an Adaptive Optics programme, still in the design phase, that will allow for adaptive correction of the beam, delivering corrected images in the J, H and K bands. The baseline is to have an Adaptive Optics system by early 2007, to be used with natural reference stars. This initial system will be upgradeable to its use with a

laser reference star system, and subsequently further upgraded with the utilization of a second deformable mirror. This produces better correction and a larger and more homogeneously corrected field.

9 The Future

The Kecks in the States and the GTC in Spain will be the only segmented telescopes with strict image quality requirements produced so far. Future large telescopes however will also be segmented. Thus the technology demonstrated by the Kecks and much improved by the GTC will be instrumental for the development of future larger telescopes.

The construction of larger telescopes is also very much dependent on the availability of adaptive optics. This is mostly because the size of the focal plane instruments grows with the size of the telescope except in the case of telescopes that are diffraction limited. Large telescopes will also be very much dependent on the active correction of its optics. This will be complicated due to the large number of segments required to fill a large aperture. Indeed large telescopes are truly challenging projects.

There are at present several very large telescope projects. Most of these projects are still at a very preliminary stage of development. Some do not even have funds to go beyond a more or less detailed design stage. However the name of the game is telescopes of sizes ranging from 30 to 100 metre that should be ready in the next decade.

The most advanced project is perhaps the California Extremely Large Telescope or CELT, which is led by Jerry Nelson from the University of California. CELT is a partnership of the University of California and Caltech. Also in the US there is the Giant Segmented Mirror Telescope (GSMT) concept, a 30m telescope project promoted by the AURA New Initiatives Office. In Europe there are two projects with a very differing approach. The EURO50 is a 50 metre aspheric primary telescope, very much along the design lines of the US projects CELT and GSMT. EURO50 is being promoted by the Lund telescope group with participation of groups from other European countries like Spain, Ireland and the UK. The second European project is the OverWhelmingly Large (OWL) telescope. The baseline is a 100 metre spherical primary telescope.

All these projects are expensive, with price tags ranging from 700 to 1000 M. Whether one or more of these very large telescopes is made is still to be seen. The odds favour the CELT, which with private funds is progressing quite fast in its design stage. Europe is lagging behind for lack of funding. Two outcomes are possible. Either the European Union come up with a fair fraction of the funds required, or there is a world wide effort to converge to a single project.

10 Summary

The GTC is a 10m telescope currently being built in La Palma, Spain. The GTC is a collaboration between Spain (90%), Mexico (5%) and the University of Florida (5%). The expected day for completion of the project is May 2006, after several difficulties have resulted in some delay. A set of facility instruments will be ready by then. I do expect that the GTC will be an outstanding telescope at the disposal of the Spanish, Mexican and Floridian astronomical communities.

Acknowledgements: I am grateful to Profs. Minia Manteiga and Ana Ulla for the organisation of the Astronomy session in the Centennial Meeting of the Real Sociedad Española de Física. I am also grateful for their patience in waiting for this manuscript. Ana Pérez was, as always, of great help with the Latex manuscript.

FULLERENES AND BUCKYONIONS IN THE INTERSTELLAR MEDIUM

SUSANA IGLESIAS GROTH

Instituto de Astrofísica de Canarias, E-38200 La Laguna, SPAIN

Departamento de Física Fundamental II, Universidad de La Laguna, E-38204 La Laguna, SPAIN

Abstract: We have studied the contribution of single fullerenes and buckyonions to the interstellar extinction. The photoabsorption spectra of these molecules is predicted and compared with some of the most relevant features of interstellar extinction, the UV bump, far UV rise and the diffuse interstellar bands. We conclude that fullerenes and buckyonions may explain these features and make a preliminary estimate of the carbon fraction locked in these molecules.

1 Introduction

The most prominent feature in the interstellar medium extinction curve is the UV bump at 2175 Å. The carrier of this band has been frequently associated to some form of carbonaceous material (graphitic spheres, polycyclic aromatic hydrocarbons (PAHs), hydrogenated amorphous carbon, etc.) but there is no definitive conclusion on the ultimate responsible for the band. The increase in the extinction at higher energies and the existence of many much weaker diffuse interstellar bands (DIBs) in the optical [1] of unknown origin are also some of the intriguing observational properties of the interstellar material. Recently, it has been claimed the detection of fullerenes with 60-240 carbon atoms in the Allende and Murchison meteorites [2]. This is the first direct indication that fullerenes were present in the presolar nebula and strongly support previous suggestions [3] that fullerenes may exist in the interstellar medium.

In this work, we study the possible contribution of single fullerenes and buckyonions (multishell fullerenes) to the interstellar extinction. We predict their photoabsorption spectra and we compare the main features of these spectra with some of the observational properties of interstellar extinction, in particular with the characteristics of the UV bump and with the distribution of diffuse interstellar bands (DIBs) in the optical and near infrared.

2 General properties of fullerenes

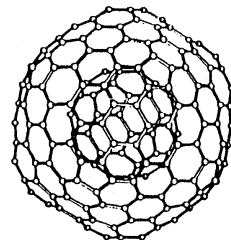


Figure 1: Buckyonion $C_{60} @ C_{240}$

The archetype of the icosahedric fullerenes is the C_{60} a closed cage formed by 60 carbon atoms distributed on the surface of a sphere of radius $\sim 3.55 \text{ \AA}$ following the symmetry of a truncated icosahedron. In 1970, Osawa suggested that a molecule with this geometry would be chemically stable. In this molecule, each carbon atom with four valence electrons is bounded to the three nearest carbon atoms. Two of the bounds are single and link a hexagon with a pentagon, the third is double and links two hexagons. The molecule is formed then, by 30 double and 60 single bounds. The distances between atoms in single and double bounds are 1.45 and 1.37 \AA , respectively. In the study of the electronic properties of the C_{60} we will consider only the four valence electrons $2s, 2p_x, 2p_y, 2p_z$ of each carbon atom. Each of the 60 atomic orbitals $2p_z$ is aligned in the radial direction, leading to the π molecular states. The three atomic orbitals $2s, 2p_x$ y $2p_y$ are distributed in the tangential plane to the molecular surface at the carbon atom position producing σ molecular states in the direction of the molecular bounds. The lineal combination of these three orbitals at each atomic site produces three hybrid orbitals sp^2 , one is in the direction of the double bound and the other two are aligned with the single bounds. The 60 π orbitals are relevant for the conductivity properties of the molecule , as in the case of graphite, and the 180 σ orbitals are mainly responsible for the elastic properties.

The most prominent features of the empirical photoabsorption spectrum of C_{60} are two bands located at about 6 and 23 eV. These bands have been interpreted as colectiv excitations similar to the π and σ plasmon. In the fullerene C_{60} these type Mie plasmons are due to the strong delocalization of the valence electrons. The σ -type is much more intense than the π -type plasmon. It has been proposed [4] that the π transition could be related to the UV bump in the interstellar extinction.

2.1 Fullerenes with multiple spheric layers: Buckyonions

Ugarte discovered in 1991 that fullerenes can adopt multilayered configurations where one is encapsulated inside each other (see Figure 1), like onion layers [5]. In his experimental study, Ugarte used electron bombarding techniques on carbon dust using current densities of between 100 and 200 Å/cm². He observed the transformation of polymeric particles of carbon in others with multiple spheric layers. Diverse laboratory experiments have proven that these groups of carbon, commonly known as buckyonions can be formed by tens of layers. Electronic microscopy has determined that the separation between layers is of the order of 3.4-3.5 Å, that is approximately the separation between sheets of graphite. The buckyonions have also been synthesized exposing carbon dust to thermal treatments. Several theoretical results seem to indicate that the multilayered spheric fullerenes are the most stable form of carbon groups. Very little is known about the electronic structure of these molecules.

3 Fullerenes and astrophysical environments

The C₆₀ molecule is obtained at high temperatures and is difficult to destroy by ultraviolet radiation or by collisions with other particles. While the other molecules have serious difficulties to survive in the interstellar medium, the robustness of C₆₀ and of the other fullerenes allows their long survival. The bonds between carbon atoms make them at least as robust against dissociation in the interstellar medium as PAHs can be.

3.1 Meteorites

As soon as fullerenes were proposed as a form of carbon, searches in meteorites were planned. The other allotropic forms of carbon, diamonds and graphite, had been found in numerous condrites. Although at the beginning fullerenes were not detected on the Allende meteorite, more refined studies succeeded in detecting the C₆₀ and C₇₀ in very low densities. It is estimated that the C₆₀ content of this meteorite is of 0.1 ppm. The isotopic ratios of noble gases found encapsulated in these meteoritic fullerenes are very different to the terrestrial values, supporting the theory that these molecules were not generated during the impact of the meteorite with Earth but instead were present in the original matter from which the meteorites formed. PAHs that have been proposed as precursor molecules for formation of fullerenes in the gas phase, have also been detected in meteorites. Possibly the hydrogenated form of the C₆₀, that is the C₆₀ fullerane, can be found in meteorites and although little is known about which could be the properties of these hydrogenated forms in the physical circumstances and conditions of the pre-solar cloud, the presence of hydrogen in most of astrophysical contexts makes likely the conversion of fullerenes in fullerenes.

The studies of the meteorite contents of the diverse forms of carbon and its isotopic composition raise interesting questions about how these molecules could have originated. Diamonds could have been produced in the primitive pre-solar cloud at low temperatures and low pressure processes, and also in processes associated with the shock waves that may be produced in the interstellar medium as a consequence of explosions of stars or violent expulsions of mass.

3.2 Carbon stars and planetary nebulae

It is thought that fullerenes and graphite could originate abundantly in stellar atmospheres rich in carbon like those of some giant stars and some progenitors of planetary nebulae, objects that are characterized for important mass loss rates and therefore able to greatly enrich the interstellar medium. Carbon rich giant stars are highly evolved stars that have a greater concentration of carbon than oxygen in their atmospheres. This superficial enrichment is the consequence of nuclear reactions that take place in their interiors and of the efficient convection that transports the nucleosynthesis products to the most external layers. Carbon stars have effective temperatures in the range 2000-3000 K and are some 10,000 times brighter than the sun. They often present important mass loss rates higher, in some cases, than $10^{-5} M_{\odot}/\text{yr}$. The brightest stars can remain in this phase for more than 10^5 yr. Thus, they are an important enriching agent of carbon for the interstellar medium. In the extended envelopes surrounding these stars, a very active chemistry takes place, in particular, solid dust grains can be nucleated. These particles could grow to sizes of $1\mu\text{m}$ although the most typical are likely of size $0.005\mu\text{m}$ or smaller. The evidence of solid grains in the mass expulsed by carbon stars comes from the continuum infrared emission much greater than expected from a photosphere. This excess of radiation is thought to be due to the emission of the circumstellar dust grains. Many carbon rich stars also present an important emission at $11.3\mu\text{m}$ associated with solid carbon and some of them present nebulosity of reflection as a consequence of the scattering of the circumstellar grains. There are indications that in the material ejected by these stars, carbon must exist, apart from CO molecules and solid grains, in some other form or species until now unknown, fullerenes are a possibility. Unfortunately, there is very little information about the presence of molecules of intermediate size (between 10 and 10^6 atoms) in circumstellar regions. Thanks to infrared spectroscopy, it is known that there exists some bands in carbon rich planetary nebulae, for example those of 3.3, 6.2, 7.7, 8.6 and $11.3\mu\text{m}$ which have not been detected in carbon stars but are observable in transition objects evolving among the giant red phase and the planetary nebula as for example, the Egg Nebula, AFGL 2688 and the Red Rectangle. These infrared bands are normally associated with the vibration modes of materials based on carbon, possibly PAHs. But until now it has not been possible to make a conclusive identification of the carrier.

3.3 Interstellar medium

Since the discovery of the fullerenes it has been suggested that these or particles of similar nature, could be related to one of the most intriguing problems of astrophysics: the diffuse interstellar bands discovered more than 8 decades ago, but not yet explained, and with the ultraviolet band centered in 2175 Å, which is the most intense band in the interstellar medium discovered more than 30 years ago. The origin of the UV bump is attributed to carbon particles of small size whose characteristics are not yet conclusively established. Since the 30s, it is known that there exists interstellar regions with absorption bands whose width vary between 0.5 and 50 Å. For example, between 4400 and 8900 Å, tens of these bands have been detected whose origin has not yet been clarified. They do not seem to correspond to any known spectrum of atomic or molecular origin [6]. Evidence of a relation between carbon particles and DIBs can be found in the analysis of the Red Rectangle spectrum. This object is a losing mass carbon star probably evolving to a planetary nebula phase. Diverse spectroscopic studies have revealed the good agreement between the emission lines found at 5799, 5855, 6380, and 6615 Å and some of the most intense diffuse bands of the interstellar medium. It is likely that the carrier of some of these interstellar bands is also present in the material ejected by this object.

Although the high level of symmetry of C_{60} indicates that this particular fullerene is unlikely as a carrier of the complex spectrum of the diffused interstellar bands, diverse studies have investigated possible mechanisms for which this molecule can acquire a complex spectrum of absorption in the optical. [6] already presented a model to describe the lines of resonance of several atoms (O, N, Si, Mg, Al, Na and S) trapped in the molecule of C_{60} and argued that these systems, quite stable according to laboratory tests, could be responsible for some of the DIBs. [7], suggested that the spectrum of ionized C_{60} is much more complex than the neutral molecule and could produce absorption bands in the optical and in the infrared. Foing and Ehenfreund [8] found two diffuse bands at 9577 and 9632 Å coinciding within 0.1 % with the laboratory measurements of the bands of C_{60}^+ observed in a Neon mould. This was considered as evidence of the existence of the C_{60}^+ in the interstellar medium. There are also several proposals associating DIBs with the hydrides of the C_{60} ($C_{60}H_n$). There are also alternative suggestions that the carrier of these bands could be related to PAHs and hydrogenated amorphous carbon (HACs) compounds.

4 Theoretical spectra

Under some simplifications associated with the symmetry of fullerenes, it has been possible to perform [9] calculations of type Hartree-Fock in which the interelectronic correlation has been included up to second order Møller-Plesset [10, 11, 12], and calculations based on the density functional [13]. However, given the difficulties faced

by *ab initio* computations when all the electrons of these large molecules are taking into account, other semiempirical methods of the Hückel type or *tight-binding* [14] models have been developed to determine the electronic structure of C₆₀ [12, 15] and associated properties like polarizabilities [16, 17], hyperpolarizabilities [18], plasmon excitations [19], etc. These semiempirical models reproduce the order of monoelectronic levels close to the Fermi level. Other more sophisticated semiempirical models, like the PPP (Pariser-Parr-Pople) [20] obtain better quantitative results when compared with photoemission experiments [21].

We have used semiempirical Hückel-type and Pariser-Pople molecular models and the random phase approximation for valence electrons to predict the electronic photoabsorption spectra of the icosahedral fullerenes C₆₀, C₂₄₀, C₅₄₀, C₉₆₀, C₁₅₀₀ which belong to the $60n^2$ Goldberg family of polyhedral and for C₁₈₀ and C₇₂₀ which belong to the family $20(n+1)^2$ [22]. The model parameters were first derived by fitting the available experimental photoabsorption spectrum of C₆₀, and then suitably modified to describe larger fullerenes [23, 24]. We excluded an approach based on *ab initio* calculations for obvious practical reasons.

This study has also been extended to multishell spheric fullerenes. The microscopic electronic structure of the system is provided by an effective one-electron model and the screening effects are treated within the random phase approximation (RPA). The particular spherical geometry of these multishell fullerenes makes possible the use of electrostatic arguments to derive a simple expression for the RPA which gives the polarizability of the buckyonion and the dipole moment induced on each shell in terms of either the screened or unscreened polarizabilities of the isolated shells. A systematic analysis as a function of the buckyonion size has been performed [25].

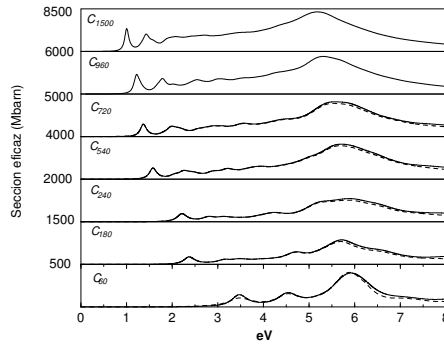


Figure 2: Photoabsorption spectra of the icosahedral fullerenes C₆₀, C₂₄₀, C₅₄₀, C₉₆₀, C₁₅₀₀ [23, 24]

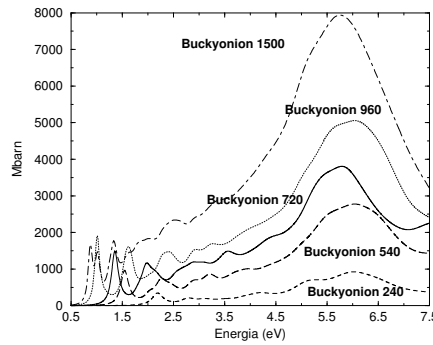


Figure 3: Photoabsorption spectra of the icosahedral buckyonions of the Goldberg family with 2, 3, 4 and 5 layers and the buckyonion $C_{180}@\mathcal{C}_{720}$ [24]

5 Interstellar extinction and the UV bump

When radiation propagates a given distance z through a medium with extinction coefficient $\tau_{ext}(\lambda)$, it is progressively attenuated according to the law

$$I(z) = I_0 \exp(-\tau_{ext}z) \quad (1)$$

where I_0 is the intensity at the origin ($z=0$). The extinction at a certain wavelength is frequently measured in magnitudes and denoted as $A(\lambda_i)$. The colour index of an interstellar cloud is defined as

$$E_{i-j} = A(\lambda_i) - A(\lambda_j) \quad (2)$$

The reddening factor is defined as the absorption in the V-band relative to the colour index B-V

$$R_V = \frac{A(\lambda_V)}{E_{B-V}} \quad (3)$$

This value in the diffuse interstellar medium is $R_V \sim 3.1$ [26].

The normalized absorption at a certain wavelength λ also known as reddening function or extinction law can be written as

$$k(\lambda) = \frac{E_{\lambda-V}}{E_{B-V}} = \frac{A(\lambda) - A(V)}{E_{B-V}} \simeq \frac{1.086}{E_{B-V}} [\tau_{ext}(\lambda) - \tau_{ext}(V)] \quad (4)$$

It is rather usual to express the extinction law as a function of the reddening factor

Following the parameterization proposed by Fitzpatrick and Massa [26] it is possible to reproduce the extinction curves in different lines of sight in the range 3 to 8

μm^{-1} with the function:

$$k(\lambda) = \frac{E_{\lambda-V}}{E_{B-V}} = a_1 + a_2x + a_3D(x, x_0, \gamma) + a_4F(x) \quad (5)$$

where x is energy or λ^{-1} . The linear component is associated to extinction by silicates and the Drude function with center in x_0 and width γ is defined as

$$D(x, x_0, \gamma) = \frac{x^2}{(x^2 - x_0^2)^2 + \gamma^2 x^2} \quad (6)$$

Finally, the function $F(x)$ takes into account the UV rise at energies higher than 7eV. This extinction is described

$$F(x) = 0.5392(x - x_0)^2 + 0.0564(x - x_0)^3 \quad (7)$$

The shape, wavelength and intensity of the 2175 Å band has been measured in a large number (more than 50) lines of sight [26]. It shows a profile similar to a Lorentzian or to a Drude curve [27]. The central wavelength of the bump is very stable, with changes of less than 1% from one direction to another. This small variation is, however, beyond the uncertainty of the measurements, typically smaller than 5 Å. The width of the band, γ , changes significantly (more than 30%) with line of sight. The average value is ~ 1.23 eV ($0.99 \mu^{-1}$) and the observed range is $0.96 \leq \gamma \leq 1.5 \text{ eV} \mu^{-1}$ [26]. The changes in width and peak position are apparently not correlated [26]. At energies higher than 7 eV the extinction curve is similar for the various lines of sight and its intensity is not correlated with the lineal component associated to silicates, but it is weakly correlated with the height and width of the UV bump [28].

5.1 Theoretical spectra and the 2175 Å band

We find that, in general, the photoabsorption cross section of individual and multishell fullerenes reproduce the behaviour of the interstellar extinction curve in the near UV. Our spectra show a prominent absorption band around 5.7 eV which fits well the position and width of the 2175 Å bump. Our photoabsorption cross sections also predict an increased extinction towards higher energies (down to 1000 Å) with a shape very similar to that measured in interstellar extinction curves. The fullerenes that better reproduce the UV bump have radii in the range 7 -13 Å. Buckyonions with a complete number of shells can also reproduce the observations.

In Figures 2 and 3 the cross sections for individual and multishell fullerenes with a complete number of layers are represented. Both types of molecules suitably reproduce the peak energy and width of the interstellar band. The similarity between the theoretical cross sections and the observed extinction in the low energy range is also remarkable, we also predict here a large number of weaker bands that could be related to the DIBs.

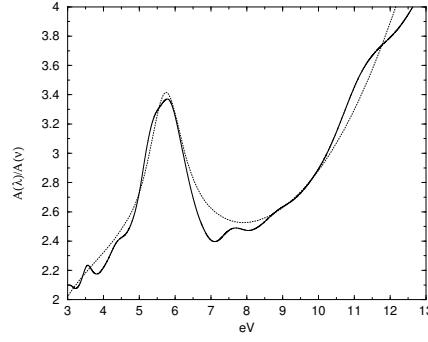


Figure 4: Photoabsorption cross section for the buckyonion $C_{180}@\text{C}_{720}$ (continuous line) compared with the interstellar extinction curve for the reddening factor $R_V \sim 3.1$ (dashed line) [24]

5.2 Carbon fraction in fullerenes and buckyonions

The comparison of the computed cross sections of fullerenes and buckyonions with observations of the UV bump for $R_V=3.1$ allow an estimate of the number of these molecules in the diffuse interstellar medium. Let us describe the extinction curve as $a_1 + a_2x + a_3\Upsilon(x)$ where $\Upsilon(x)$ is the theoretical cross section computed for each fullerene or buckyonion. Here we assume that indeed the extinction at the energy of the bump is the result of the fullerene plus silicate contributions. We obtain via a least squared fit the relative contribution of the two components (see Figure 4). The coefficients of this lineal component do not depend significantly on the particular fullerene under consideration taking typical values of $a_1 \simeq 1.6$ and $a_2 \simeq 0.07$ with a relative error of 20 %.

It is known experimentally that the hydrogen column density is related with the excess colour index [29] through

$$\frac{N(H)}{E_{B-V}} = 5.9 \times 10^{21} \text{ cm}^{-2} \quad (8)$$

Assuming $A(V) \simeq 3.1E_{B-V}$ for the diffuse interstellar medium, we obtain

$$A(V) \simeq 5.3 \times 10^{-22} \text{ mag cm}^2 N(\text{H}) \quad (9)$$

and the relative number density of any particular fullerene can be then estimated from the a_3 coefficient

$$\frac{N(\text{full})}{N(H)} \simeq 5 \times 10^{-22} a_3 \Upsilon(x_0) \quad (10)$$

The typical values for a_3 are of order 0.3×10^{15} (when cross sections are expressed in barns). This coefficient changes according to the type of fullerene considered but less than 50 %, corresponding to the lowest values of the largest buckyonions. We find then that fullerenes and buckyonions may have densities in the range 0.2-0.08 particles per million (ppm) hydrogen atoms. Remarkably similar to the values found in meteorites. In the unlikely case that all types of fullerenes considered in this study had the same density in interstellar space, it would require that of order 100-200 atoms of carbon per 10^6 hydrogen atoms be locked in these molecules. This is a large fraction of the total carbon expected in the interstellar medium which we can assume equal to the solar atmosphere abundance of 355 ± 50 [30]. It is also known from observations with the *Goddard High Resolution Spectrograph* of the Hubble telescope that in interstellar space there are 140 ± 20 carbon atoms per million hydrogen atoms in gaseous form [31], therefore the maximum number of carbon atoms available for fullerenes can not be larger than 200 per million hydrogen atoms.

Indeed, the actual carbon fraction in fullerenes depend of the proper mixture of these molecules in the interstellar medium. It is likely that the number density of fullerenes and buckyonions will decrease with increasing radius (R). A distribution of the type $N(\text{full}) \sim R^{-m}$ has been frequently considered in the literature on interstellar grain populations [32]. We have studied how a mixture of fullerenes and buckyonions following such size distribution may reproduce the observed UV bump and find that the best fits to the shape, peak energy and width of the bump are obtained for m values in the range 2.5-4.5. Such values for the power-law index lead to a lower number of carbon atoms locked in fullerenes consistent with the interstellar carbon budget. The precise determination of the actual carbon fraction requires further study and will be the subject of a forthcoming paper.

6 Diffuse interstellar bands

We predict that fullerenes and buckyonions, contrarily to other suggested carriers for the UV bump, display weak bands in the optical part of the spectrum. These bands populate with relatively high density this spectral range. Similar to what is seen in the diffuse interstellar bands, we find for each fullerene and buckyonion a progressive decrease of the number of transitions towards the red and infrared. Some of these bands have wavelengths consistent with known diffuse interstellar bands, reinforcing the arguments for the ubiquitous presence of these molecules in the interstellar medium.

More than 200 DIBs have been identified in the optical, most of them are found in the range 5350- 8000 Å. The stability of wavelengths and profiles suggest that the carrier of the bands is more associated with gaseous molecules than with solid grains. The widths range between 0.8 and 30 Å, thus much larger than the widths of many of

the interstellar atomic lines. The bands are not significantly polarized [33]. The most intense bands are listed in Table 1. Two DIBs at 9577 y 9632 Å have been associated to C_{60}^+ [8] and a correlation has been claimed between the DIB at 4430 Å (2.8 eV) and the UV bump [34, 35].

Wavelength(Å)	W(mÅ)	Wavelength(Å)	W(mÅ)
4180	0.70	6284	1.95
4429	3.40	6533	1.89
4760	0.70	6940	0.40
4882	0.89	7429	0.56
5535	0.53	8620	0.42
5779	0.95	9577	0.50
5780	0.80	9632	0.78
6177	2.40	13170	0.40

Table 1: The most intense diffuse bands in the interstellar medium, where W is the equivalent width [1].

In Figure 5 we plot theoretical absorption bands in the optical and near infrared obtained for individual fullerenes and buckyonions. Opposite to other molecules that have been proposed as an explanation for the UV bump, fullerenes display a rich optical spectrum populated with relatively weak bands, of strength consistent with those of DIBs. Almost all the fullerenes and buckyonions considered here, present a strong band at energies close to the DIB at 4430 Å. We mark in Figure 5 the bands of fullerenes and buckyonions which have a potential DIB counterpart in the list of Herbig 1995, with a wavelength difference of less than 1%.

7 Formation of fullerenes and buckyonions

The mechanism of fullerene formation is only partially known [36]. They may be produced at relatively high temperatures by “annealing” of large plane monocyclic carbon molecules. Buckyonions may be produced from carbon soot and from nanodiamonds [37]. It is known that nanodiamonds of size (30-60 Å) can be transformed in particles very similar to buckyonions when heated to temperatures of 1200-1800 K [38] which are typical of carbon rich giant stars. The process may work as follows [37]: the (111) surfaces of nanodiamonds are the first to graphitize when treated at high temperature, a first graphitic layer is generated on the surface and later new concentric layers are added toward the interior in an analogous way to the process of buckyonion formation through energetic electron irradiation. Since diamond is more dense than graphite, the final particle has a larger size. Since the transformation takes

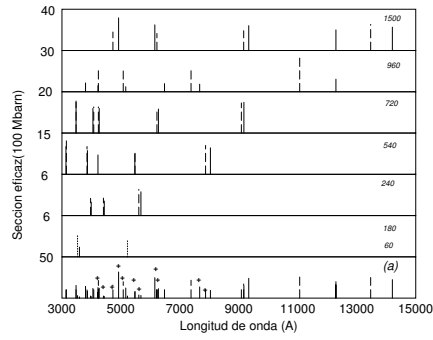


Figure 5: Comparation of the positions of weak bands in the theoretical spectrum of some fullerenes (dashed line) and buckyonions (continuous line) with known diffuse bands in the interstellar medium (crosses).

place from the surface to the interior, the final particle is of spheroidal form and very compact with the inner layer of less than 10 Å of diameter. Nanodiamonds have been detected in meteorites [39], where they are much more abundant than graphite, and possibly in the circumstellar envelope of post-AGB stars.

References

- [1] Herbig, G.H. 1995, *ARA&A*, 33, 19
- [2] Becker, L., Poreda, R.J., Bunch, T.E. 2000, *Lunar and Planetary Science* 31, 1803
- [3] Kroto, H.W. 1988, *Science*, 243, 1139
- [4] Braga, M., Larsson, S., Rosén, A., Volosov, A. 1991, *A&A*, 245, 232
- [5] Ugarte, D. 1992, *Nature*, 359, 707
- [6] Ballester, J.L., Antoniewicz, P.R., Smoluchowski, R. 1990, *ApJ*, 356, 507
- [7] Léger, A., d'Hendecourt, L., Verstrate, L., Schmidt, W. 1988, *A&A*, 203, 145
- [8] Foing, B.H., Ehrenfreund, P. 1994, *Nature*, 369, 296
- [9] Alasia, F., Broglia, R.A., Roman, H.E., Serra, L.L., Colo, G., Pacheco, J.M. 1994, *J. Phys. B*, 27, L643
- [10] Møller, C., Plessset, M.S. 1934, *Phys. Rev.*, 46, 618
- [11] Pople, J.A., Binkley, J.S., Seeger, R. 1976, *Int. J. Quant. Chem. Symp.*, 10, 1
- [12] Cioslowski, J. 1995, *Electronic Structure Calculations on Fullerenes and their Derivatives* (Oxford University Press, New York)
- [13] Rubio, A., Alonso, J.A., López, J.M., Stott, M.J. 1993, *Physica B*, 183, 247
- [14] Haddon, R.C. 1992, *Accounts of Chemical Research*, 25, 127

- [15] Lin, Y.L., Nori, F. 1996, Phys. Rev. B, 53, 1641
- [16] Bonin, K.D., Kresin, V.V. 1997, Electric Dipole Polarizabilities of Atom, Molecules and Clusters, World Scientific, Singapore
- [17] Ruiz, A., Hernández-Rojas, J., Bretón, J., Gómez Llorente, J.M. 1998, J. Chem. Phys., 109, 3573
- [18] Fanti, M., Orlandi, G., Zerbetto, F. 1995, J. Am. Chem. Soc., 117, 6101
- [19] Bertsch, G.F., Bulgac, A., Tománek, D., Wang, Y. 1991, Phys. Rev. Lett., 67, 2690
- [20] Pariser, R., Parr, R.G. 1953, J. Chem. Phys., 21, 466; Pariser, R., Parr, R.G. 1953, J. Chem. Phys., 21, 767; Pople, J.A. 1953, Trans. Faraday Soc, 49, 1375
- [21] Tomanek, D., Guo, T., Jiu, C., Haufer, R.E., Chibante, L.P.F., Fure, J., Wang, L., Alford, J.M., Smalley, R.E. 1991, J. Phys. Chem., 95, 7564
- [22] Yoshida, M., in <http://shachi.cochem2.tutkie.tut.ac.jp/Fuller/fsl/goldberg.html>.
- [23] Iglesias-Groth, S., Ruiz, A., Bretón, J., Gómez Llorente, J.M. 2002, Journal of Chemical Physics, 116, 1648
- [24] Iglesias-Groth, S. 2003, Tesis Doctoral, Universidad de La Laguna, Spain
- [25] Iglesias-Groth, S., Ruiz, A., Bretón, J., Gómez Llorente, J.M. 2003, Journal of Chemical Physics, 118, 7103
- [26] Fitzpatrick, E.L., Massa, D. 1986, ApJ, 307, 286; Fitzpatrick, E.L. 1999, PASP, 111, 63
- [27] Savage, B.D. 1975, ApJ, 199, 92
- [28] Jenniskens, P., Greenberg, J.M. 1993, A&A, 274, 439
- [29] Bohlin, R.C., Savage, B.D., Drake, J.F. 1978, ApJ, 224, 132
- [30] Grevesse, N., Noels, A. 1993, in Origin and Evolution of the Elements, ed. N. Prantzos, E. Vangioni-Flam and M. Cassé (Cambridge Univ. Press), p. 15
- [31] Cardelli, J.A., Meyer, D.M., Jura, M., Savage, D. 1996, ApJ, 467, 334
- [32] Mathis, J.S., Rumpl, W., Nordsieck, K.H. 1977, ApJ, 217, 425
- [33] Fahlman, G.G., Walker, G.A.H. 1975, ApJ, 200, 22
- [34] Nandy, K., Thompson, G.I. 1975, MNRAS, 173, 237
- [35] Webster, A. 1993, MNRAS, 265, 421
- [36] Curl, R.F., 1993 1993, Nature, 363, 14
- [37] Ugarte, D. 1995, ApJ, 443, L85
- [38] Kuznetsov, V.L., Chuvalin, A.L., Butenko, Y.V., Mal'kov, I.Y., Titov, V.M. 1994, Chem. Phys. Letters, 202, 343
- [39] Blake, D.F. et al. 1988, Nature, 332, 611

COOL STARS: CHROMOSPHERIC ACTIVITY, ROTATION, KINEMATIC AND AGE

DAVID MONTES, INÉS CRESPO-CHACÓN, M. CRUZ GÁLVEZ, M. JOSÉ FERNÁNDEZ-FIGUEROA, JAVIER LÓPEZ-SANTIAGO, ELISA DE CASTRO, MANUEL CORNIDE, MAGDALENA HERNÁN-OBISPO

Departamento de Astrofísica, Facultad de Ciencias Físicas, Universidad Complutense de Madrid, E-28040 Madrid, SPAIN

Abstract: We summarize here our ongoing project of multiwavelength high and medium resolution optical observations aimed at studying the chromosphere of different kinds of late-type stars including pre-main sequence stars (weak-lined T Tauri stars), chromospherically active binaries, flare stars, and young single stars members of stellar kinematic groups. We quantify the phenomenology of chromospheric activity using the information provided by several optical spectroscopic features (from the Ca II H & K to the Ca II IRT lines) that are formed at different heights in the chromosphere. In addition, we obtain a better determination of the stellar parameters, spectral type, and possible binarity. With all these information we study the flux-flux and rotation-activity relationships in order to get insights into the mechanisms which drive the solar-like stellar activity.

1 Introduction

Cool stars (stars with spectral type later than F2) have an outer differentially rotating convection zone. As in the Sun, a positive temperature gradient have been found in the outer atmosphere of these stars. Above the photosphere the temperature increases through the chromosphere (where it reaches $\approx 10^4$ K) and transition region and into the corona, where it is $\approx 10^6$ K. This heating is thought to be due to the dissipation of energy carried by magnetohydrodynamic waves, and/or from reconnection of stressed magnetic field lines, but the precise physics involved is not yet understood. It is believed that convection coupled with high stellar rotation results in a dynamo mechanism which converts the mechanical energy of rotation and convection into magnetic energy. On the one hand the rotation rate in late-type stars moderates the dynamo mechanism which generates and amplifies the magnetic field in the convection zone, but there is a further relationship between rotation and age. Rotation rate declines with age because stars lose angular momentum through the

coupling of magnetic field and stellar mass loss, and thus there is an indirect trend of decreasing magnetic activity with increasing age.

The stars that are rapidly rotating by virtue of their youth or presence in a close-binary system, are orders of magnitude more active than the Sun. The observations of these extremely active stars have revealed some very non-solar-like characteristics as confined cool material at large distances, infalling matter, and high latitude magnetic flux emergence.

Our group have been working during the last years in the analysis of high and medium resolution spectroscopic observations that allow us to quantify the phenomenology of the chromospheric activity of different kinds of cool stars. We include in our studies stars with different levels of activity and rotation rate, from very young stars (pre-main sequence stars of weak-lined T Tauri type) to evolved stars in chromospherically active binaries (RS CVn type). Late-type stars members of young stellar kinematic groups (age from 20 to 600 Myr) are being also analysed. In addition, we are studying the behaviour of very frequent flares and microflares that take place in dMe dwarfs of UV Cet type (flare stars).

In the next sections we describe the methods used in our analysis, the results from our previous studies as well as the most recent results we have obtained for all these cool stars.

2 Observations

High and medium optical spectroscopic observations of different kinds of cool stars, covering the most of the spectral lines widely used as chromospheric activity indicators, have been obtained during several observing runs using different telescopes and instrumental configurations: the 2.5 m Isaac Newton Telescope (INT) with the Intermediate Dispersion Spectrograph (IDS) and the ESA-MUSICOS Echelle spectrograph, the 4.2 m William Herschel Telescope (WHT) with the Utrecht Echelle Spectrograph (UES), the 2.56 m Nordic Optical Telescope (NOT) using the Soviet Finish High Resolution Echelle Spectrograph (SOFIN) and the 3.5 m Telescopio Nazionale Galileo (TNG) using the Spectrografo di Alta Resoluzione (SARG) at the Observatorio del Roque de Los Muchachos (La Palma, Spain); the 2.2 m telescope at the German-Spanish Observatory (CAHA) in Calar Alto (Almería, Spain), using a Coudé spectrograph and the Fibre Optics Cassegrain Echelle Spectrograph (FOCES); the 2.1 m telescope using the Sandiford Cassegrain Echelle Spectrograph and the 9.2 m Hobby-Eberly Telescope (HET) with the High Resolution Spectrograph (HRS) at the McDonald Observatory (Texas, USA). The spectral resolution achieved range from 0.05 to 0.5 Å.

3 Spectroscopic analysis

3.1 Chromospheric activity indicators

The simultaneous analysis of the different optical chromospheric activity indicators using the spectral subtraction technique (see below), allow us to study in detail the chromosphere, discriminating between the different structures: plages, prominences, flares and microflares. The most relevant optical spectroscopic features that can be used as chromospheric activity indicators are:

The Ca II H & K lines: the emission reversals above these two strong absorption resonance lines (see Figure 1) are the most widely used optical indicators of chromospheric activity, since their source functions are collisionally controlled and represent an extremely important cooling mechanism.

The Ca II infrared triplet (IRT) lines: these lines share the upper levels of the Ca II H & K transitions and are formed in the lower chromosphere. The ratio of excess emission equivalent width, E_{8542}/E_{8498} , is an indicator of the type of chromospheric structure (plages, prominences) that produces the observed emission.

The H α and other Balmer lines: these lines are formed at the middle chromosphere, but are only in emission above the continuum in very active stars, and in less active stars only a filled-in absorption line (see Figure 2) is observed. The $E_{H\alpha}/E_{H\beta}$ ratio can be used as a diagnostic for discriminating between the presence of plages and prominences in the stellar surface.

The Na I D₁, D₂ and Mg I b triplet: The Na I doublet lines are collisionally dominated and are good indicators of changes in the upper photosphere and lower chromosphere. The Mg I b triplet lines originate in the same region. Both Na I and Mg I lines are detected during flares as emission reversal or as filling-in.

The He I D₃ line: it originates in the upper chromosphere and the observation of this line in emission supports the detection of flare like events. This line could be also filling-in due to frequent low-level flaring activity.

The spectral subtraction technique

We determine the chromospheric contribution in these features subtracting the underlying photospheric contribution by using the spectral subtraction technique (see [21, 22, 23, 26, 27, 34]). This technique consists of the subtraction of a synthesized stellar spectrum constructed from artificially rotationally broadened, radial-velocity shifted, and weighted spectra of inactive stars chosen to match the spectral types and luminosity classes of the components of the active system under consideration (see Figs. 1, 2, 7). The synthesized spectrum is constructed using the program STARMOD developed at Penn State [1]. The inactive stars that we have used as reference stars in the spectral subtraction have been observed during the same observing run as the active stars, or taken from our libraries of late-type stars (see [32]).

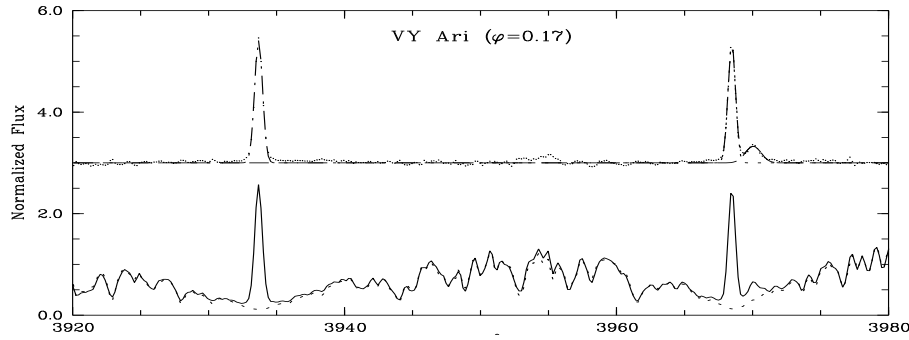


Figure 1: Ca II H & K observed and subtracted spectra of the chromospherically active binary VY Ari.

3.2 Radial and rotational velocities

Heliocentric radial velocities have been determined by using the cross-correlation technique. The spectra of the program stars were cross-correlated order by order, using the routine `FXCOR` in IRAF, against spectra of radial velocity standards of similar spectral types. We have used these heliocentric radial velocities together with precise measurements of proper motions and parallaxes taken from Hipparcos and Tycho-2 Catalogues, to calculate Galactic space-velocity components (U, V, W) (see [35]). In the case of binary systems [12]) we have used these radial velocities to determine the radial velocity curve and obtain a minimum χ^2 fit orbit solution (see Figure 3).

We have determined the rotational velocities ($v \sin i$) of our star sample by using the cross-correlation technique. The spectrum of the program star is cross-correlated against the spectrum of a template star (a slowly rotating star of similar spectral type) and the width of the cross-correlation function is determined (see [36, 12]). The calibration of this width, to yield an estimate of $v \sin i$, is determined by cross-correlating artificially broadened spectra of the template star for a range of $v \sin i$ with the original template star spectrum.

3.3 Age from the Li I 6708 Å line

In order to obtain an estimate of the age of our stars we have used the resonance doublet of Li I at $\lambda 6707.8$ Å which is an important diagnostic of age in late-type stars, since it is destroyed easily by thermonuclear reactions in the stellar interior. The measured equivalent width of this line, $EW(\text{Li I})$, (corrected from the blended Fe I $\lambda 6707.41$) is compared with the one of stars in well-known young open clusters

of different ages (see [36]).

4 Results

4.1 WTTS, weak-lined T Tauri stars

The weak-lined T Tauri stars (WTTS) are low mass pre-main sequence stars (PMS) with H α equivalent widths $\leq 10 \text{ \AA}$ in which no signs of accretion are observed. The emission spectrum of these stars is not affected by the complications of star-disk interaction which often masks the underlying absorption lines as well as extincts the stellar light in classical T Tauri stars (CTTS). The WTTS are thus ideal targets to study the behaviour of surface activity in the PMS stage of the stellar evolution. A large number of WTTS have been recently discovered by the ROSAT All-Sky Survey. Many of them have been found far away from the star formation clouds and whether these stars are really WTTS, or post TTS, or even young main sequence stars is a matter of ongoing debate.

We have started a high and medium resolution optical observational program dedicated to study the chromospheric activity of late-type pre-main sequence stars. We include in our study both bona-fide WTTS in Taurus with known rotational period, and WTTS recently discovered by the ROSAT All-Sky Survey, which have been very little studied until now. Simultaneous H α and Ca II H & K INT/IDS spectroscopic observations of a sample of 20 bona-fide WTTS in Taurus-Auriga molecular clouds, with well determined photometric rotational periods, have been analysed [43, 38]. The results of high resolution echelle spectroscopic observations of six ROSAT discovered WTTS, located in and around the Taurus-Auriga molecular clouds, can be found in [31].

4.2 Chromospherically active binaries

The chromospherically active binaries (CABS) are detached binary systems with cool components characterized by strong chromospheric, transition region, and coronal activity. The RS CVn systems have at least one cool evolved component whereas both components of the BY Dra binaries are main sequence stars [9].

In previous work [10, 21, 22] we have studied the Ca II H & K and H α lines in a large sample of CABS. The activity-rotation and flux-flux relations for these systems have been analysed [21, 23, 24].

Multiwavelength optical observations of well known CABS

We analyzed, using the spectral subtraction technique, IDS/INT simultaneous H α , Na I D₁, D₂, and He I D₃ spectroscopic observations of 18 CABS [25, 26]. High

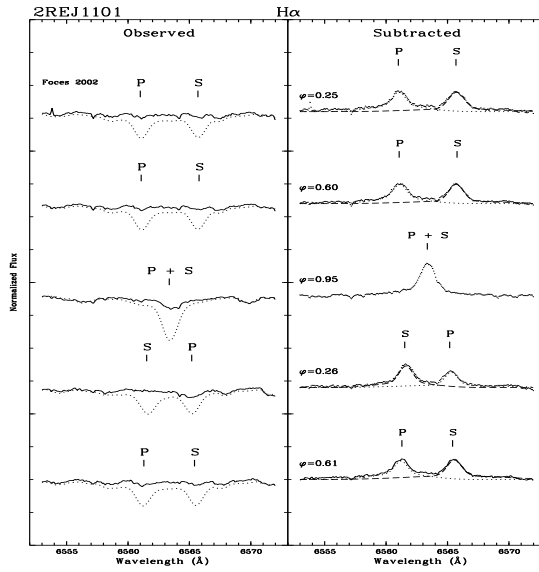


Figure 2: Spectra of 2RE J1101+223 (HD 95559) in the $H\alpha$ line region. The observed spectrum (solid-line) and the synthesized spectrum (dashed-line) are plotted in the left panel and the subtracted spectrum (dotted line) in the right panel. The positions of the $H\alpha$ line for the primary (P) and secondary (S) components are marked

resolution echelle spectra including all the optical chromospheric activity indicators from the Ca II H & K to Ca II IRT lines are analysed in the binary EZ Peg [27] and in other 16 CABS [34]. The subtracted $H\alpha$ profile of the more active stars of the sample ($H\alpha$ in emission above the continuum) has very broad wings, and is well matched using a two-components Gaussian fit (narrow and broad). The broad component is primarily responsible for the observed variations of the profile, and its contribution to the total equivalent width (EW) increases with the degree of activity. So we have interpreted this broad component emission as arising from microflaring activity that take place in the chromosphere of these very active stars (see also [28]). Prominence-like extended material has been detected in a near-eclipse $H\alpha$ observation of the system AR Lac. The excess emission found in the Na I D₁ and D₂ lines by application of the spectral subtraction technique, and the behaviour of the $H\alpha$ line in the corresponding simultaneous observations indicate that the filling-in of the core of these lines is a chromospheric activity indicator. In giant stars of the sample the He I D₃ line has been detected in absorption in the subtracted spectra.

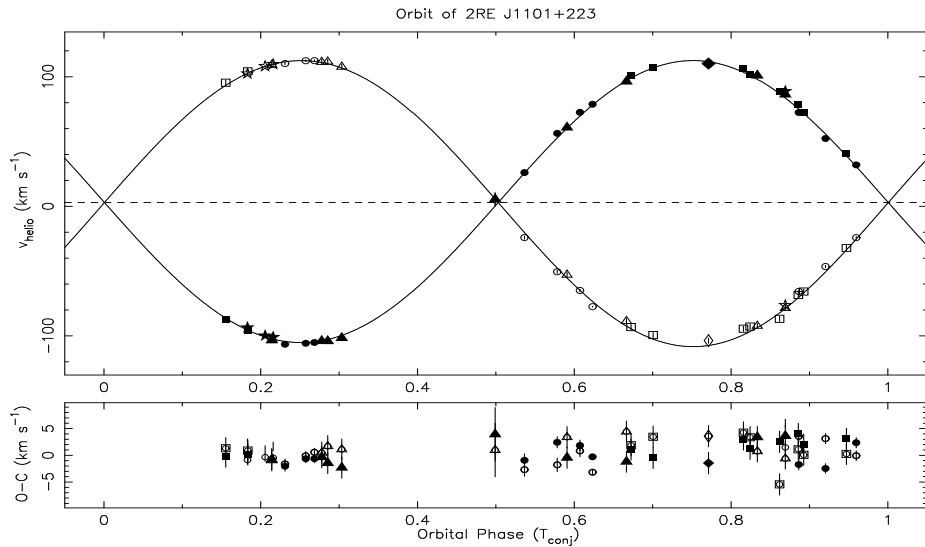


Figure 3: Radial velocity data and fit vs the orbital phase of 2RE J1101+223 (HD 95559). Solid symbols represent the primary and open symbols represent the secondary. Squares for [17], triangles for [9], rhombus for [44], and circles and stars are our data [13]

Multiwavelength optical observations of X-ray/EUV selected CABS

As an extension of our study of well known CABS we have started to observe also CABS recently discovered by their X-ray and EUV emission detected by the ROSAT satellite. We have analysed the H α and Ca II IRT lines of the binary system 2RE J0743+224. We have found that this star, previously classified as single-lined spectroscopic binary, is a double-lined spectroscopic binary (SB2) with a K1 III primary and an orbital period of 10 days. During the observations an unusual long-duration flare took place [30]. A Li I λ 6708 Å line enhancement was detected during the flare, which we suggest is produced by spallation reactions during the flare [29, 30]. Our observations during four observing runs from 1999 to 2001 of BK Psc (2RE J0039+103) [12] confirm the single-lined spectroscopic binary (SB1) nature of this system and allow us to obtain, for the first time, the orbital solution of the system as in the case of a SB2 system. The minimum masses ($M \sin^3 i$) resulting from the orbital solution are compatible with the observed K5V primary and an unseen M3V secondary. Both components of the binary system show high levels of chromospheric activity. H α emission above the continuum from both components is a persistent

feature of this system. Finally the SB2 binaries 2RE J0725-002 (V789 Mon) and 2RE J1101+223 (HD 95559) [13] are analysed in detail (see the H α emission of HD 95559 in Figure 2) and an improved orbital solution has been obtained (see Figure 3).

4.3 Flare stars

Flares are events in which a large amount of energy is released in a short interval of time, taking place changes at almost all frequencies in the electromagnetic spectrum.

The first flare ever detected was discovered in the Sun on 1 September 1859 when Carrington [4] observed a large sunspot group looking at the solar photosphere. Since then, flares have been observed in many types of cool stars [42], sometimes radiating at levels several orders of magnitude more energetic than solar flares [14]. In UV Cet type stars (late Ke or Me dwarfs) optical flares are a common phenomenon. On the other hand, flares produced by more luminous stars are usually only detected through UV or X-ray observations. Flares from UV Cet type stars present the greatest analogy to solar flares, in contrast to other stellar sources (e.g. Algol type and RS CVn binary systems and pre-main sequence objects) [40, 2] whose flares have probably got more differences than similarities with respect to the solar case. Even though flares of UV Cet type stars present many analogies with solar flares, there are also significant differences, such as the amount of energy released [41]. The question is: are these differences only due to the different physical conditions of the atmosphere of these stars and the solar one, or are the environments so different that even the basic flare mechanisms may be different?

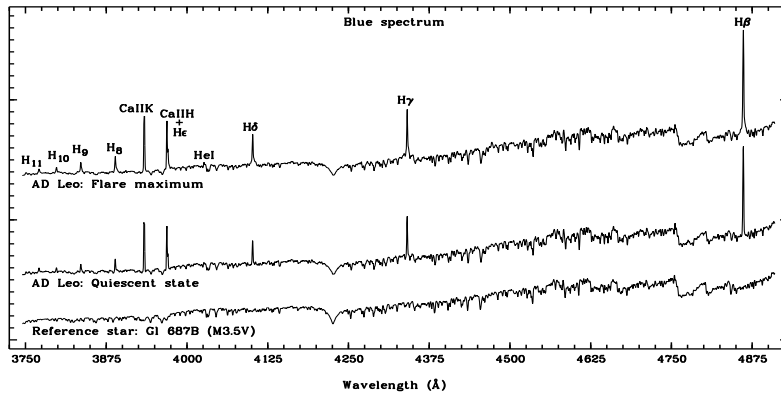


Figure 4: Flare and quiescent spectra of AD Leo, compared with the spectrum of the reference star Gl 687B (M3.5V).

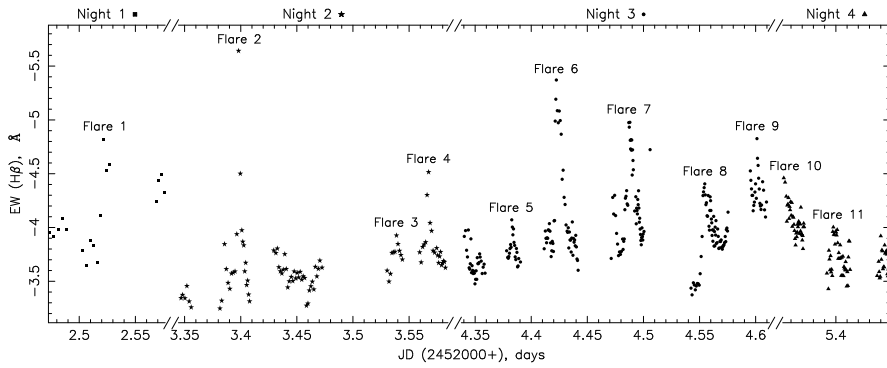


Figure 5: EW($H\beta$) of AD Leo versus time (JD) (MUSICOS 2001 observing run).

As in the Sun, stellar flares are believed to result from the release of free magnetic energy stored in the corona due to reconnection of magnetic field lines [11, 16]. Generally, there are two different kinds of flares [39]: *confined flares*, in which loops in an active region suddenly brighten and slowly decay, and *eruptive flares*, in which the whole configuration of magnetic loops is disrupted and must be newly rebuilt. In eruptive flares the originally closed magnetic field suddenly opens, flowing plasma upward to the corona [18]. Then, magnetic pressure begins to prevail, leading to sequential reconnections of the open field lines which create new loops. The reconnection process produces intense heating which is conducted downwards to the chromosphere and it also accelerates particles that flow along the loop. Then, the gas at the chromospheric loop footpoints is strongly heated and evaporated, making it visible in X-rays and high-temperature lines [3]. Afterwards, the loop cools, making it visible at higher wavelengths. Meanwhile, other new loops are formed above it. The problem concerning the energy release and the overall spectral distribution in stellar flares has recently been discussed in view of new theoretical models and multi-line observations, but the exact physical mechanisms involved in flares remain poorly understood.

High spectroscopic resolution observations of different flare stars

In our previous work high resolution spectroscopic observations of several flare events have been analysed in different kinds of active stars. In the RS CVn systems UX Ari and II Peg flares have been detected in the H α , Na I D₁ & D₂ and He I D₃ lines [25, 26]. A long-duration (>8 days) optical flare has been found in the recently discovered, X-ray/EUV selected, chromospherically active binary 2RE J0743+224 [29]. During this flare we have also detected a Li I $\lambda 6708 \text{ \AA}$ line enhancement probably produced by

spallation reactions during the flare. We have analysed high resolution optical echelle spectra and IUE observations during a strong flare on 22 December 1993 in the very active, young, fast rotator, single K2 dwarf LQ Hya [33]. We have estimated the total energy of this flare, and discussed the broad components, asymmetries, and Doppler shifts seen in some of the emission lines. During the MUSICOS (MULTi-SIte COntinuous Spectroscopy) 1998 campaign we have observed almost continuously the RS CVn system HR 1099 for more than 3 weeks in which two flares were monitored [15].

High temporal resolution observations of Me dwarfs

The purpose of our present work is to study dMe flare stars with high temporal resolution to analyse the evolution of the observed emission lines, that are formed from the upper photosphere to the upper chromosphere, during the different phases of the detected flares. Results will be used to test different flare models. We have already studied in detail the dM3.5e flare stars AD Leo and V1054 Oph [37, 5, 6]. Both stars were monitored with high temporal resolution during the MUSICOS 2001 observing run (2–5 April 2001) using the Isaac Newton Telescope (INT) of the El Roque de Los Muchachos Observatory (La Palma, Spain). We have not detected strong flares (see e.g. Figure 4, where the spectrum of AD Leo in the maximum of the strongest flare has been plotted in comparison to its quiescent spectrum and the one of the reference star Gl 687B) but we have found interesting short and weak variations with properties very similar to flares (microflares) that are produced with high temporal frequency (see e.g. Figure 5, where the detected flares of AD Leo have been identified). These flares last from 14 ± 1 to 31 ± 3 min in the case of AD Leo and from 21 ± 2 to 96 ± 6 min in V1054 Oph. The EW rise of the Balmer lines is larger

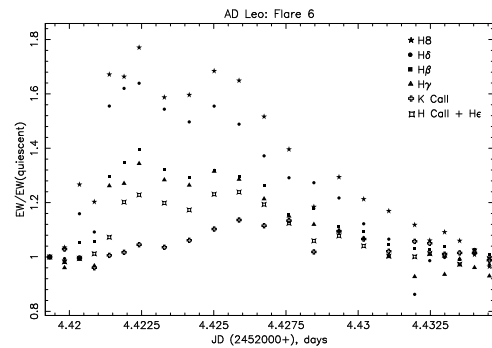


Figure 6: EW ratio (relative to the quiescent state) of different lines during the best monitored flare of AD Leo in our observations.

at shorter wavelengths (e.g. Figure 6), but their temporal evolution is quite similar. It also seems that the Ca II H & K lines are less affected by flares, suffering a lower increase than the Hydrogen lines and reaching the maximum at a different time. The Balmer lines show a red-asymmetry that becomes larger in the flare maxima (despite the broadening of the blue wing during flares).

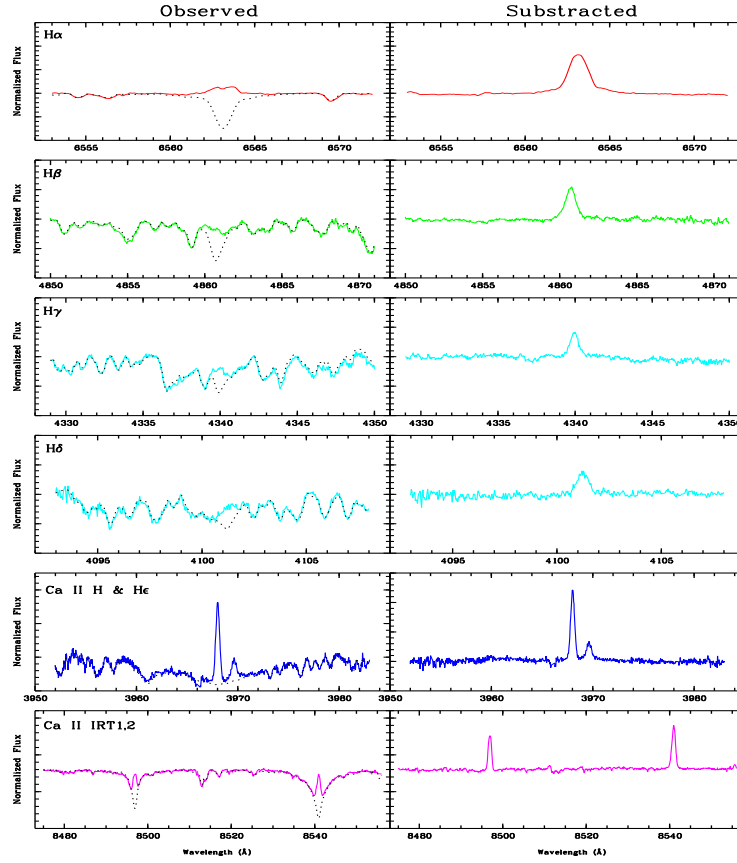


Figure 7: Representative spectra of PW And in the quiescent state in several chromospheric activity indicators.

4.4 Cool stars in young moving groups

Moving groups (MG) are kinematic coherent groups of stars [7] that could share a common origin. In our previous work [35] we have compiled a sample of late-type stars possible members of the youngest and best documented MG: Local Association or Pleiades moving group (20 to 150 Myr); IC 2391 supercluster (35-55 Myr); Castor moving group (200 Myr); Ursa Mayor group or Sirius supercluster (300 Myr); and Hyades supercluster (600 Myr). These stars have been selected from previously established members of MG based on photometric and kinematic properties, as well as from new candidates based on other criteria as their level of chromospheric activity, rotation rate and lithium abundance.

In order to better establish the membership of these candidate stars in the different young MG we have started a program of high resolution echelle spectroscopic observations [36, 20]. The spectroscopic analysis of these stars allow us to obtain a better determination of their radial velocity, lithium ($\lambda 6707.8 \text{ \AA}$ line) EW , rotational velocity and level of chromospheric activity. The high resolution spectroscopic observations (150 stars until now) were taken during 12 observing runs from 1999 to 2002. Our results confirm the membership of several previously established members, but in other cases the kinematic and spectroscopic criteria indicate the membership in a different MG or that the star should be considered only as a young disk star with no clear membership in any MG. Some new spectroscopic binaries have been identified. The rotational modulation of the photospheric and chromospheric activity of the young, single K2-dwarf PW And (member of the Local Association) has been analysed in detail [19].

Acknowledgements: We would like to thank our collaborators J. Sanz-Forcada, L.W. Ramsey, B.H. Foing, D. García-Alvarez. This work was supported by the Universidad Complutense de Madrid and the Spanish Ministerio de Ciencia y Tecnología (MCYT), Programa Nacional de Astronomía y Astrofísica under grant AYA2001-1448. I. Crespo-Chacón would like to thank the Spanish Ministerio de Educación, Cultura y Deporte for the PhD. grant AP2001-0475.

References

- [1] Barden, S. C. 1985, ApJ, 295, 162
- [2] Byrne P. B. 1989, Solar Physics, 121, 61
- [3] Cargill P. J., Priest, E. R. 1983, ApJ, 266, 383
- [4] Carrington, R. C. 1859, MNRAS, 20, 13
- [5] Crespo-Chacón, I., Montes, D., López-Santiago, J. et al. 2003, in: *Highlights of Spanish Astrophysics III*, Kluwer Academic Publishers, 468
- [6] Crespo-Chacón, I., Montes, D., Fernández-Figueroa, M.J., et al. 2004, Astr. & Sp. Sc., 291, Vols 1-4

- [7] Eggen, O. J. 1994, *Galactic and Solar System Optical Astrometry*, Cambridge University Press, 191
- [8] Fekel, F. C., Boop, B. W., Africano, J. L., et al. 1986, AJ, 92, 1150
- [9] Fekel, F. C., Gregory, W. H. 2000, ApJ, 120, 3265
- [10] Fernández-Figueroa, M.J., Montes, D., De Castro, E., Cornide, M. 1994, ApJSS, 90, 433
- [11] Foing, B. H. 1989, Solar Physics, 121, 117
- [12] Gálvez, M.C., Montes, D., Fernández-Figueroa, M.J., et al. 2002, A&A, 389, 524
- [13] Gálvez, M.C., Montes, D., Fernández-Figueroa, M.J., et al. 2004, A&A, in press
- [14] García-Alvarez, D., Jevremović, D., Doyle, J. G., Butler, C. J. 2002, A&A, 383, 548
- [15] García-Alvarez, D., Foing, B., Montes, D., et al. 2003, A&A, 397, 285
- [16] Haisch, B., Strong, K.T., Rodonò, M. 1991, ARA&A, 29, 275
- [17] Jeffries, R. D., Bertram, D., Spurgeon, B. R. 1995, MNRAS, 276, 397
- [18] Kopp, R. A., Pnewman, G. W. 1976, Solar Physics, 50, 85
- [19] López-Santiago, J., Montes, D., Fernández-Figueroa, M. J., Ramsey, L.W. 2003, A&A, 411, 489
- [20] López-Santiago, J., Montes, D., et al. 2004, A&A(in press)
- [21] Montes, D., Fernández-Figueroa, M.J., De Castro, E., Cornide, M. 1995, A&A, 294, 165
- [22] Montes D., Fernández-Figueroa M.J., De Castro E., Cornide, M. 1995, A&A, 109, 135
- [23] Montes, D., De Castro, E., Fernández-Figueroa, M.J., Cornide M. 1995, A&ASS, 114, 287,
- [24] Montes, D., Fernández-Figueroa, M.J., Cornide, M., De Castro, E. 1996, A&A, 312, 221
- [25] Montes, D., Sanz-Forcada, J., Fernández-Figueroa, M.J., Lorente, R. 1996, A&A, 310, L29
- [26] Montes, D., Fernández-Figueroa, M. J., de Castro, E., Sanz-Forcada J. 1997, A&A, 125, 263
- [27] Montes, D., Sanz-Forcada J., Fernández-Figueroa M.J., et al. 1998, A&A, 330, 155
- [28] Montes, D., Fernández-Figueroa, M.J., De Castro, E., et al. 1998, ASP Conf. Ser. 154, CD-1516
- [29] Montes, D., Ramsey, L. W., A&A, 340, L5
- [30] Montes, D., Ramsey, L. W. 1999, ASP Conf. Ser. , 158, p. 226
- [31] Montes, D., Ramsey, L. W. 1999, ASP Conf. Ser., 158, p. 302
- [32] Montes, D. 1999, A&ASS, 263, 275 (<http://www.ucm.es/info/Astrof/spectra.html>)
- [33] Montes, D., Saar, S. H., Collier-Cameron, A., Unruh, Y. C. 1999, MNRAS, 305, 45
- [34] Montes, D., Fernández-Figueroa, M.J., De Castro, E., et al. 2000, A&ASS, 146, 103

- [35] Montes, D., López-Santiago, J., Gálvez, M. C., et al., MNRAS, 328, 45
- [36] Montes, D., López-Santiago, J., Fernández-Figueroa, M. J., et al. 2001, A&A, 379, 976
- [37] Montes, D., Crespo-Chacón, I., Fernández-Figueroa, M.J., et al. 2004, in: *Proceedings of the IAU Symp.219* (A. Dupree & A. Benz eds.), in press
- [38] Montes, D., Miranda, L.F. 2004, A&A, (in preparation)
- [39] Pallavicini, R., Serio, S., Vaiana, G. S. 1977, ApJ, 216, 108
- [40] Pallavicini, R., Tagliaferri, G. 1989, in: *Solar and Stellar Flares* (B. M. Haisch & M. Rodonò eds.), 17
- [41] Pallavicini, R. 1990, IAU Symp.142, 77
- [42] Pettersen, B. R. 1989, Solar Physics, 121, 299
- [43] Poncet, A., Montes, D., et al. 1998, ASP Conf. Ser., 154, CD-1772
- [44] Strassmeier, K., Washuettl, A., Granzer, T., et al. 2000, A&ASS, 142, 275

ASTEROSEISMOLOGY OF HOT SUBDWARF STARS

RAQUEL OREIRO REY

Instituto de Astrofísica de Canarias, E-38200 La Laguna, SPAIN

Departamento de Astrofísica, Universidad de La Laguna, E-38200 La Laguna, SPAIN

CRISTINA RODRÍGUEZ LÓPEZ, ANA ULLA

Departamento de Física Aplicada, Universidad de Vigo, E-36200 Vigo, SPAIN

FERNANDO PÉREZ HERNÁNDEZ

Instituto de Astrofísica de Canarias, E-38200 La Laguna, SPAIN

Departamento de Astrofísica, Universidad de La Laguna, E-38200 La Laguna, SPAIN

RAFAEL GARRIDO

Instituto de Astrofísica de Andalucía-CSIC, E-18008 Granada, SPAIN

MINIA MANTEIGA

Departamento de Ciencias de la Navegación y de la Tierra, Universidad da Coruña, E-15011 A Coruña, SPAIN

JAMES MACDONALD

Department of Physics and Astronomy, University of Delaware, Newark, DE 19716, USA

Abstract: We present a summary of the current state of the art in the study of hot subdwarf stars by using asteroseismological techniques. We first briefly describe the main physical aspects of these objects, to then analyze the different groups of hot subdwarfs from a seismological point of view.

1 Introduction

Since 1947, when Humason & Zwicky discovered *hot subdwarfs* on a survey of faint blue stars [1], and from 1960, when Greenstein established them as a spectroscopically differentiated class of stars [2], they had been scarcely studied by the scientific community. A situation that reversed after the discovery of pulsations in some *hot subdwarfs* stars in 1997 [3].

This class of objects consists mainly of subluminous stars with a canonical mass of $0.5M_{\odot}$; they have blue colors and effective temperature (T_{eff}) and logarithm of surface

gravity ($\log g$) in the ranges 20 000 – 100 000 K and 4.0 – 6.5 dex, respectively. *Hot subdwarfs* reveal themselves as abundant objects in faint and blue stellar surveys [4]. Due to their high temperatures they have been considered as ionizing sources of interstellar gas at high galactic latitudes [5], and they are thought to be responsible for the UV-upturn found in elliptical galaxies and galaxy bulges [6], [7], [8].

Their evolutionary status corresponds to a lower main sequence star that has evolved through the Red Giant Branch, but that has not yet arrived at the cooling sequence of White Dwarfs (WDs). The specific details of their evolution, as well as other aspects –such as the population they belong to (they are found both in the disk and the galactic halo [9], their anomalies in metal abundances [10], their binary fraction, and the nature of the detected oscillations– are still a matter of investigation.

A definite spectroscopic classification has not yet been established either, despite various existing proposals [11], [12]. However, we can segregate *hot subdwarfs* into three main spectroscopic sequences, sdBs, sdOs and sdOBs, according to composition and effective temperatures:

- sdBs have hydrogen dominated atmospheres, with T_{eff} between 20 000 and 40 000 K, and $\log g$ between 5.2 and 6.5 dex.
- sdOs have helium rich atmospheres, with T_{eff} between about 40 000 K and 100 000K and $\log g$ between 4.0 and 6.5 dex.
- sdOBs share characteristics of the above types, both hydrogen and helium are present in their atmospheres and they have T_{eff} around 40 000K.

2 Subdwarf B-Type Stars

The physical parameters specified in the previous section place subdwarf B-type stars (the sdBs) in the area of the Hertzsprung Russell Diagram (HRD) known as the Extended Horizontal Branch ([15], EHB) a region that corresponds to the bluest part of the Horizontal Branch. This location is reproduced by theoretical models of He-core burning stars having $q \sim 0.95$, where $q = M_{\text{core}}/M_{\text{total}}$ [13], [14]. They also have a radiative He-layer plus a small ($M_{\text{H}} \simeq 0.02M_{\odot}$) and inert hydrogen envelope, that makes the model behave almost like a helium Main Sequence star [15], [16].

Although their evolutionary path is not yet completely understood, they are thought to be descendants of Red Giant Branch (RGB) stars that have undergone such substantial mass loss that they have lost most of their H envelope and bypass the Asymptotic Giant Branch evolving directly into the White Dwarf cooling sequence. However, the exact mechanism that produces such mass loss at or near the tip of the RGB is unclear. Because at least 44% of the sdBs show signs of binarity, a binary origin involving common envelope phases has also been proposed [17]. Some binary scenarios of sdB formation have been studied [18] from a theoretical point of view.

Subdwarf-B stars are all chemically peculiar, with spectra dominated by the Balmer lines; they show an underabundance of He that can be very noticeable in some particular cases [19]. Other elements, such as C and Si, appear depleted in their spectra while N is approximately solar. The chemical abundances could result from the balance between gravity and radiative levitation, but this does not seem to be the case: the radiative and gravitative mechanisms alone can not explain the observations [10]. Other mechanisms such as mass loss, rotation or magnetic fields, have been proposed in the attempt of reproducing observed sdB spectra [20], [21].

2.1 Pulsations in sdBs

The discovery of pulsations in some of the sdBs allows us to improve our knowledge of these stars interior structure by making use of asteroseismological techniques.

The first pulsating sdB, EC14026-2647, was found in 1997 [3]. Several observational campaigns were then organized to search for similar objects. The intense searches performed by the South African Astronomical Observatory ([22] and references therein), University of Montreal [23], Nordic Optical Telescope [24] and recently, by Green and collaborators [25], established two subclasses of pulsating sdBs. They display the following differences:

- The objects in the “EC14026” subclass have fast pulsations, with periods that tend to cluster in the range (80-250) s. There exist, however, some particular cases (Feige 48, HS 2201+2610, HS 0702+6043 and PG 1605+072) with longer periods (up to 600 s) that are explained by a frequency dependence on the physical parameters of the star [26]. The detected frequencies are explained as p modes, both radial and non radial, of low degree and low radial order excited by the κ mechanism associated with an opacity bump due to the enhancement of the iron abundance in the sdB envelopes, probably caused by diffusion processes [27]. The T_{eff} and $\log g$ of EC14026 stars, between 28 400 – 35 700 K and 5.25 – 6.11 dex, respectively, place them in an area of the HRD where they coexist with constant sdBs. To date, it remains unknown what causes some stars to pulse while others, with the same physical parameters, do not. The explanation could involve weak winds that, at different ages, would lead to differences in the amount of iron in the pulsation driving region [28].
- The subclass known as “Betsy” stars, discovered in 2002 [25], show periods of oscillation on the order of one hour, that are attributed to g modes of high radial order excited by the same mechanism acting in the EC14026 stars. We find Betsy stars in the HRD area enclosed by the values of $T_{\text{eff}} \in [25\,000, 30\,000]$ K and $\log g \in [5.4, 5.7]$, respectively. In this case, it seems that all the stars lying

in this region oscillate and there is no co-existence of pulsating and constant objects.

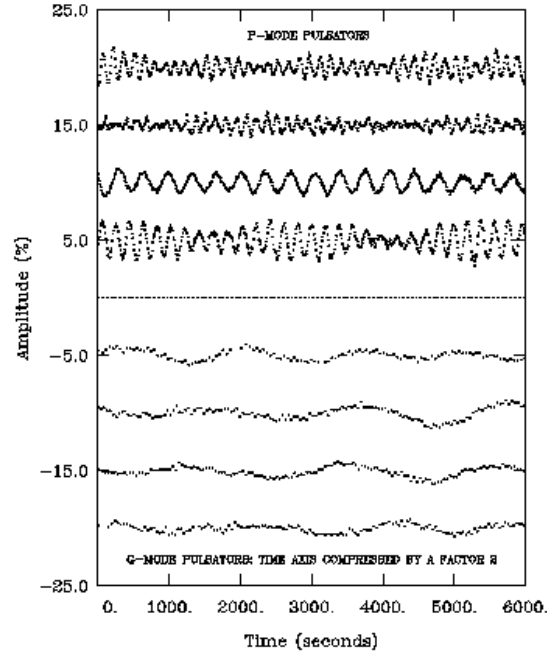


Figure 1: Some typical light curves of EC14026 (top) and Betsy stars (bottom) [29].

In Figure 1 some typical light curves of the two subclasses of pulsating sdBs are shown.

The observational discovery of the first pulsating sdB almost coincided with the theoretical prediction of the viable existence of pulsations in this class of stars. Motivated by the presence of a HeII-HeIII convection zone in the sdB envelopes that could excite pulsation modes, Charpinet *et al.* made the first theoretical study of the possible oscillating nature of sdBs [30]. Contrary to their expectations, they found a negligible contribution to driving from the HeII-HeIII region but an important contribution due to ionization of heavy elements. The same authors obtained excited pulsation modes in sdB models with enhanced Fe abundances [27]. They established that sdB models with an inhomogeneous iron distribution could present excited modes if enough of this element were present in the driving region, and proposed that the

iron opacity κ mechanism is responsible for pulsations in EC14026 stars. The studies above mentioned formed the basis for an asteroseismological study of sdBs.

Fontaine *et al.* provided a theoretical explanation for the occurrence of oscillations in the Betsy stars [29]. The same κ mechanism that excites p modes in EC14026 stars is proposed as responsible for the light curve variations on Betsy stars, but leading to excited g modes of high radial order in this case.

The discovery of an oscillatory behaviour for some sdBs has led to investing great effort in trying to remove some of their uncertainties but, above all, it has opened the possibility of using seismological techniques to probe their interiors and, hence, to gain more information about this still puzzling stellar evolutionary phase. However, this task is not lacking of problems: the low number of detected pulsation frequencies in some cases, the complexity of the amplitude spectra in others, and the low amplitudes of pulsation, of the order of a few milli-magnitudes, that prevent us from accurate mode identifications, are delaying the application of seismology techniques to studying sdBs in detail. In the near future, with the aid of space missions, like COROT [31], these problems may be overcome, but to date, the only existing complete asteroseismological analysis of a sdB can be found in [32] and [33].

On this scene, our group is working both observationally and theoretically. The use of the IAC80 telescope (Teide Observatory) has led to the discovery of the latest EC14026 star known to date: Balloon090100001 [34], which is the brightest ($B = 11.8$) and has one of the greatest pulsation amplitudes (~ 60 mmag) among its class. On the other hand, we are able to compute full stellar evolution structural models of sdB stars by using the code of one of us (JM, [35]), and their corresponding theoretical frequencies of pulsation by using the adiabatic code of Christensen-Dalsgaard [36]. These computational results are used to carry out the seismological analysis of the observational data.

3 Subdwarf O-Type Stars

Hot subdwarfs O-type (hereafter sdOs) are helium rich objects with a mean canonical mass of $M = 0.5M_{\odot}$. They most likely have C/O cores with a helium burning shell. Their exact evolutionary state is still uncertain, in part due to a paucity of stellar evolution calculations for these objects. Nevertheless, two possible scenarios explaining the origin of sdOs have been proposed based on their location in the HR diagram [37]:

- The post-AGB (Asymptotic Giant Branch) or “luminous” sdOs are found in a region of the HRD crossed by tracks leaving the AGB.
- The post-EHB (Extended Horizontal Branch) or “compact” sdOs sit on the HRD near the EHB region. The majority of sdOs are found in this location.

Both of these scenarios pose a number of yet unanswered questions:

The “luminous” sdOs would be the descendants of AGB objects and would evolve like central stars of planetary nebulae. However, only four sdOs are known that show signs of a surrounding nebula [38], [39]. Some explanations to why this is have been proposed by [40] and [42].

The “compact” sdOs would be the sdBs (EHB) descendants. The main question is how a hydrogen rich star (a sdB) may have evolved into a helium rich one (a sdO). There are only a few calculated tracks for the post-HB state (see [13], [43], [44], [45] and [46]). Recently, Lanz *et al.* have used “deep helium flash-mixed models” to account for helium enriched sdBs [47]. Their models yield effective temperatures on the Zero Age Horizontal Branch higher than the canonical value which may explain the helium enrichment and give subsequent evolution to the sdOs.

A binary origin of sdOs has been addressed in [41] and [48]. It is proposed that single sdOs may be the merger of a pair of low-mass helium WDs which lose angular momentum by gravitational wave radiation. There are a few studies which estimate the binary fraction of sdOs ([17], [49], [50], [51] and [52]) at between 30 and \sim 64%.

The highly inhomogeneous sdOs spectra (with the common characteristic of a usually strong HeII λ 4686Å spectral line) echo the peculiarities of their atmospheres. There are to date few exhaustive spectral analyses of sdOs (see *e.g.*: [53], [54], [55]). From them, we know that the helium abundance (from 50% to a 100%) shown in their spectra is usually accompanied by nitrogen enhancement and carbon depletion, pointing to the action of the CNO cycle, while sometimes carbon is enhanced which shows the action of the 3α process. Enhancement and depletion, in various degrees, of other metals like oxygen, silicon, magnesium, neon and iron in different stages of ionization are also found [56], rendering the spectral classification into subclasses of these objects still a matter of debate [12].

3.1 Search for pulsations in sdOs

Tracing back the history of pulsations in sdOs, as early as 1957 (only ten years after the discovery of *hot subdwarfs*) J. L. Greenstein in his paper “Evidence for instability among sub-luminous stars” [57] recommended observations to detect possible short-period pulsations among sdOs and WDs.

Bartolini *et al.* were the next to consider variability among sdOs [58]. They carried out a photometric study searching for variability in 6 hydrogen-poor stars, 3 of them being sdOs. They claimed to have found microvariability in all of them, although they were only able to estimate periodicities qualitatively.

The same authors stated the pulsational behavior of a binary system composed of the sdO star HD 128220 and a subgiant type-G companion [59]. However, it was not clear if the observed small amplitude variations were due to the sdO star or to its companion, or to fluctuations in atmospheric transparency [60]. Some non-pulsating

episodes in the system, attributed to destructive interference of nearby frequencies, were also reported.

Motivated by the exciting discovery of pulsations in sdBs, and taking into consideration the related studies above [59], we have begun a photometric study of a sample of about 60 sdOs. Our objective is to search for possible pulsations among them, with the final aim of shedding some light on their evolutionary state.

11 sdOs and one sdOB have been observed in three observational campaigns: one at the Sierra Nevada Observatory (OSN) in December 1999, where 4 channel simultaneous Strömgren photoelectric photometry was performed with a 90 cm telescope, and two in April and August-September 2003 at the IAC80 telescope (Teide Observatory; OT) where fast photoelectric photometry was made with the 3 channel Tromsø-Texas photometer in white light. On the latter occasion, B Johnson CCD photometry was also acquired with the Tromsø-Texas CCD photometer.

From our spectral analysis, the star HIP 52181 stands out with a frequency of 1,04 mHz and with an amplitude over $2,5\sigma$ times the mean noise, which makes it a good candidate for pulsations. The amplitude spectrum is plotted in Figure 2. The horizontal dotted line is $2,5\sigma$ times the mean value of the amplitude, and the solid line is 3 times this value which yields roughly a 99% confidence level.

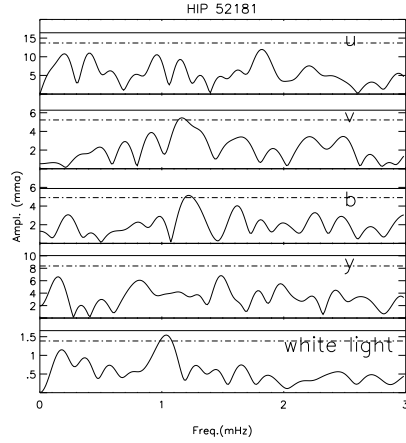


Figure 2: Amplitud spectra for HIP 52181.

For this candidate star a preliminary asteroseismological study was implemented. Two sdO models with atmospheric parameters roughly reproducing those of HIP 52181, were computed with the stellar evolution code of JM [35] by evolving $Z=0.02$, $1.0M_{\odot}$ stars from the main sequence with enhanced mass loss. These were then used as input to the stellar evolution code to produce 19 more evolved structural models. The

evolution was stopped at $\log g \sim 7$, when the star is entering the WD phase. The two evolutionary tracks are plotted in the HRD (Figure 3).

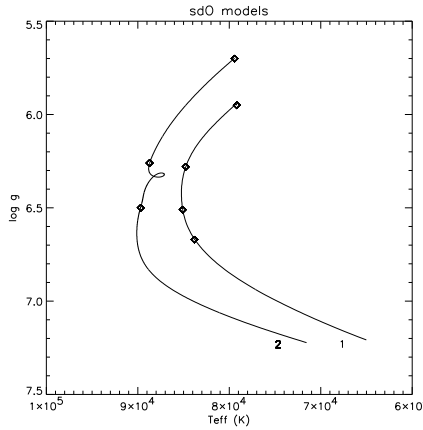


Figure 3: Traks in the HRD computed after evolving two sdOs structural models to the WDs phase.

We chose the 7 models marked with diamonds on Figure 3 and used them as input for the adiabatic pulsation code of Christensen-Dalsgaard [36]. Only for one of the models were two theoretical frequencies obtained that consistent with our observational data. Both frequencies are identified with high order g modes. Further observational and theoretical work is required to asses the eventual meaning of these preliminary results. In particular, one of our immediate goals is to construct more accurate structural models of sdOs and to use them with a non-adiabatic pulsation code [61] that includes the interaction between pulsation and the atmosphere to determine the unstable oscillation modes.

About 20 more sdOs of the ongoing study were observed from 1-14 December 2003 at OSN with a 1.5 m telescope with a B Johnson filter. The data obtained are under analysis. If the pulsating/non-pulsating rate is similar to that found for the sdBs, at least 1 or 2 new sdO pulsators are expected on the completion of the photometric study.

Acknowledgements: Part of this work was supported by MCyT under project AYA2000-1691. R. Oreiro acknowledges CajaCanarias and C. Rodríguez López Xunta de Galicia for its financial support. We thank the Centro de Supercomputación de Galicia for the use made of their computational facilities.

References

- [1] Humason, M.L., Zwicky, F. 1947, ApJ, 105, 85
- [2] Greenstein, J.L. 1960 in *Stellar atmospheres*, University of Chicago Press
- [3] Kilkenny, D., Koen, C., O'Donoghue, D., Stobie, R. S. 1997, MNRAS, 285, 640
- [4] Green, R. F., Schmidt, M., Liebert, J. 1986, ApJSS, 61, 305
- [5] de Boer, K.S. 1985, A&A, 142, 321
- [6] Bica, E., Bonatto, C., Pastoriza, M. G., Alloin, D. 1996, A&A, 313, 405
- [7] Brown, T. M., Ferguson, H. C., Davidsen, A. F., Dorman, B. 1997, ApJ, 482, 685
- [8] Yi, S. 1997, Bull. of the American Astron. Soc., 29, 1407, 19112402
- [9] Colin, J., et al. 1994, A&A, 287, 38
- [10] Michaud, G., Bergeron, P., Wesemael, F., Fontaine, G. 1985, ApJ, 299, 741
- [11] Moehler, S., Riehler, T., de Boer, K.S., Dettmar, R.J., Heber, U. 1990, A&A Sup. Ser., 86, 53
- [12] Jeffery, C.S., Drilling, J.S., Harrison, P.M., Heber, U., Moehler, S. 1997, A&A Sup. Ser., 125, 501
- [13] Dorman, B., Rood, R.T., O'Connell, R.W. 1993, ApJ, 419, 596
- [14] Oreiro, R., Ulla, A., Pérez Hernández, F., MacDonald, J., García, R., Zapatero, M.R. 2004, in preparation
- [15] Heber, U. 1986, A&A, 155, 33
- [16] Saffer, R., Bergeron, P., Koester, D., Liebert, J. 1994, ApJ, 432, 351
- [17] Ulla, A., Thejll, P. 1998, A&A Sup. Ser., 132, 1
- [18] Han, Z., Podsiadlowski, Ph., Maxted, P.F.L., Marsh, T.R., Ivanova, N. 2002, MNRAS, 336, 449
- [19] Heber, U., Reid, I.N., Werner, K. 2000, A&A, 363, 198
- [20] Unglaub, K., Bues, I. 1998, A&A, 338, 75
- [21] Elkin, V.G. 1996, A&A, 312, L5
- [22] Koen, C., O'Donoghue, D., Kilkenny, D., Stobie, R. S., Saffer, R. A. 1999, MNRAS, 306, 213
- [23] Billères, M., Fontaine, G., Brassard, P., Liebert, J. 2002, ApJ, 578, 515
- [24] Oestensen, R., Solheim, J.-E., Heber, U., Silvotti, R., Dreizler, S., Edelmann, H. 2001, A&A, 368, 175
- [25] Green, E. et al. 2003, ApJ, 583, L31
- [26] Charpinet, S., Fontaine, G., Brassard, P., Dorman, B. 2002, ApJSS, 139, 487
- [27] Charpinet, S., Fontaine, G., Brassard, P., Chayer, P., Rogers, F. J., Iglesias, C. A., Dorman, B. 1997, ApJ, 483, L123
- [28] Chayer, P. 2003, ApJSS, in press
- [29] Fontaine, G., Brassard, P., Charpinet, S., Green, E. M., Chayer, P., Billères, M., Randall, S. K. 2003, ApJ, 597, 518
- [30] Charpinet, S., Fontaine, G., Brassard, P., Dorman, B. 1996, ApJ, 471, 103
- [31] Baglin, A., Vauclair, G. & The COROT team 2000, JApA, 21, 319

- [32] Brassard, P., Fontaine, G., Billères, M., Charpinet, S., Liebert, J., Saffer, R. A. 2001, ApJ, 563, 1013
- [33] Charpinet, S., Fontaine, G., Brassard, P. 2001, ASP, 113, 775
- [34] Oreiro, R., Ulla, A., Pérez Hernández, F., Oestensen, R., Rodríguez López, C., MacDonald, J. 2004, ApJ, accepted
- [35] Jimenez, R., MacDonald, J. 1996, MNRAS, 283, 721
- [36] Christensen-Dalsgaard, J., Berthomieu, G. 1991, *Solar interiors and atmospheres*, ed., A: N: Cox, W. C. Livingston & M. Mathews (Univ. Arizona Press), 401
- [37] Husfeld, D. 1987, *Proc. of the 2nd Conference on Faint Blue Stars*, Schenectady, NY, L. Davis Press, p.237
- [38] Pritchett, C. 1984, A&A, 139, 230
- [39] Kwitter, K. B., Congdon, C. W., Pasachoff, J. M., Massey, P. 1989, AJ, 97, 1423
- [40] Schönberner, D. 1983, ApJ, 272, 708
- [41] Iben, I. Jr., Tutukov, A.V. 1986, ApJ, 311, 753
- [42] Brocato, E., Matteuci, F., Mazzitelli, I., Tornambé, A. 1990, ApJ, 349, 458
- [43] Sweigart, A. V., Mengel, J. G., Demarque, P. 1974, A&A, 30, 13
- [44] Gingold, R. A. 1976, ApJ, 204, 116
- [45] Caloi, V., 1989, A&A, 221, 27
- [46] MacDonald, J., Arrieta, S. 1994 *Hot Stars in the Galactic Halo*, Cambridge University Press, p. 238
- [47] Lanz, T., Brown, T. M., Sweigart, A. V., Hubeny, I., Landsman, W. B. 2004, ApJ, 602, 342
- [48] Webbink, R. F. 1984, ApJ, 277, 355
- [49] Thejll, P., Ulla, A., MacDonald, J. 1995, A&A, 303, 773
- [50] Williams, T., McGraw, J.T., Grashuis, R. 2001, PASP, 113, 490
- [51] Williams, T., McGraw, J.T. 2001, PASP, 113, 94
- [52] Stark, M. A., Wade R. A. 2003, ApJ, 126, 1455
- [53] Dreizler, S., Heber, U., Werner, K., Moehler, S., de Boer, K. S. 1990, A&A, 235, 234
- [54] Thejll, P., Bauer, F., Saffer, R. et al 1994, ApJ, 433, 819
- [55] Bauer, F., Husfeld, D. 1995, A&A, 300, 481
- [56] Heber, U. 1998, *Proc. of the conference UV Astrophysics. Beyond the IUE Final Archive'*, ESA, SP-413
- [57] Greenstein, J.L. 1957, *Proc. of the 4th IAU Sym.*, Cambridge University Press, p. 179
- [58] Bartolini, C., Bonifazi, A., D'Antona, F. et al. 1982, ApJSS, 83, 287
- [59] Bartolini, C., Bernabei, S., Bruni, I. et al. 2001, Mem.S.A.It, 72, 4
- [60] Piccioni, A., Bartolini, C., Bernabei, S. et al. 2002, *Proc. of the 1st Eddington Workshop*, ESA SP-485, p. 305
- [61] Moya, A., Garrido, R., Dupret, M. A. 2004, A&A, 414, 1081

HELIUM CATACLYSMIC VARIABLES

RICARDO MORENO, ANA ULLA

Departamento de Física Aplicada, Universidade de Vigo, E-36200 Vigo, SPAIN

Abstract: The so-called AM CVn systems, or Interacting Binary DB White Dwarf stars, have grown from four members in 1992 to twelve in 2003; five out of the eight new discoveries were found during the 21st century. Also, the observational properties of these systems show nowadays a widespread and unexpected range of characteristics, which seems to confirm the existence of “subclasses” within the group. Four objects at least show X-ray emission. For two objects at least, H seems to have been detected in their optical spectra. A brief review of the recent findings for this peculiar group among the Cataclysmic Variables is here presented.

1 Introduction

A Cataclysmic Variable (CV) is, by its usual definition, a close interacting binary system where a solar-type secondary star overflows its Roche Lobe and donates matter, mostly hydrogen from its atmosphere, in a stable manner onto a White Dwarf (WD) primary accretor, within orbital time spans in the range of hours. Excellent reviews on the topic can be found in, e.g., [1], [2], [3], [4].

Helium Cataclysmic Variables (He CVs), also referred to as AM CVn systems ([5], [6]) or Interacting Binary DB White Dwarf stars (IBDBWDs: [7], [8], [9]), constitute a subclass of the CVs where the secondary star is a Helium-rich WD (i.e., of DB type), donating matter onto the primary object, which is also a DB WD. Two main characteristics distinguish them from the bulk of the H-rich CVs: their composition (with spectra entirely depleted from H and dominated by He lines) and their ultra-short orbital periods (on the order of minutes). See for example [10], [5], [9], [11], for a revision of their properties.

Until 1992 only four AM CVn objects were known (AM CVn, V803 Cen, CR Boo and GP Com), despite the prototype, AM CVn itself, had been discovered as a variable object by [12] and classified as an IBDBWD system by [13]. A review of their characteristics published to that date can be found in [9]. Tables listing the twelve AM CVn systems known to date, together with a summary of some of their properties, can be found in, e.g., [14].

In the next sections, some of the main recent findings for the objects will be summarized, together with a discussion of their implications in the context of the Cataclysmic Variables.

2 The objects

There are at present twelve AM CVn systems identified and catalogued as such, namely AM CVn, HP Lib, GP Com, CE 315, V803 Cen, CR Boo, CP Eri, KL Dra, 2003aw, V407 Vul, ES Cet and RX J0806.3+1527 (RX J0806, hereafter), which, according to [14] could be grouped into three classes: the “high state” objects AM CVn and HP Lib, with orbital periods shorter than 1200 seconds, a high mass transfer accretion rate and a thick disk, showing absorption He lines in their optical spectra; the “low state” objects GP Com and CE 315, with orbital periods larger than 2500 seconds, a low mass transfer accretion rate and a thin disk, showing emission lines; and those objects in an “unstable (or cyclic) state”, with periods ranging from about 1200 to 2500 seconds and showing both He emission (when in low state) and absorption (when in high state) lines. These would be V803 Cen, CR Boo, CP Eri, KL Dra and 2003aw.

It is worth noting that already in 1992 V803 Cen and CR Boo were considered “intermediate” objects between AM CVn (assumed in a permanent high state) and GP Com (in a permanent low state), according to the variations of their observed magnitudes: $V \sim 14$ for AM CVn, $V \sim 16$ for GP Com, and V between ~ 13 and 18 for V803 Cen and CR Boo ([9]). So, we see that nowadays more systems have been found to fit within the three classes.

On the other hand, V407 Vul and RX J0806 are found to display X-ray emission ([15], [16]) while [17] suspected ES Cet to be a soft X-ray source. The three systems have been proposed to host magnetic primaries ([18], [17]). They display periods ranging from 321.5 to 620.26 seconds; periods that would place them inside the “high state” regime of the AM CVn systems as previously defined. However, while V407 Vul does not display emission lines and only a dubious Mg I absorption line was detected in its optical spectrum ([19]), ES Cet and RX J0806 only display emission lines of He ([17], [20]), a characteristic of the “low state” objects. Besides, [21], [22] claim the detection of Balmer lines in the optical spectra of ES Cet and RX J0806, respectively, disregarding therefore their classification as AM CVn systems. All these peculiarities render the three objects as most peculiar and worth studying ones.

In what follows, a brief summary of characteristics and findings –which does not mean to be complete, will be included for each of the twelve AM CVn systems.

2.1 “High state” objects:

AM CVn: Until 1999 two main photometric periods, ~ 1051 and ~ 1028 seconds, coexisted for the prototype of the IBDBWD stars group, when [23] confirmed that the orbital period was 1028.73 seconds, a value also later on confirmed by [24]. [25] and [26] supported the interpretation of 1051 seconds as the “superhump” period for the

system. These two findings were crucial for a significant advance in the understanding of the binary nature of AM CVn, which, for several authors had not even been proven beyond doubt before (see, e.g., [9]).

To date, after several disk models have been proposed for the system (e.g., [5], [27], [28], [29], [25], [24]), an accretion rate of 10^{14} kg/s, a precession period of 13.38 hours and an inclination of about $\sim 15^\circ$ – 45° , are suggested. Also, the masses for the primary and secondary components would be, respectively, 0.84 and $0.07 M_\odot$, yielding a mass ratio (q) of 0.087 ([25]). Instead, [30] reports values of $0.5 M_\odot$ and 0.22 for the primary mass and q , respectively.

HP Lib : EC15330-1403, also known as HP Lib ([31]), was discovered as an AM CVn system by [32]. The object did not display magnitude variations within several days, staying around a magnitude of $V=13.6$. A value of 1102.7 seconds was assigned to its orbital period ([31]). Only HeI absorption lines were found in its optical spectrum, with no traces of H. The system is thought to remain in a permanent high state, as AM CVn itself, and a period of 1119 seconds ([32]) has been identified as the superhump period of the object ([31]).

2.2 “Low state” objects:

GP Com: When only five AM CVn systems were known, around 1993, GP Com was suggested to be the most different object among them, based on its observational characteristics ([33], [34], [35]). A most intriguing feature was a variable “central spike” displayed by its triple-peaked emission lines of He, of unknown origin. Nowadays, it seems well established that GP Com is an AM CVn system, with an orbital period of 2794 seconds, a mass ratio on the order of 0.02 and a primary mass around $1 M_\odot$ ([36]). [37] reported that observed flares in its light curve are generated at the inner disk, which is thin, in a permanent (quiescent) low state and with a low mass transfer rate ([27], [25]). As a major discovery for GP Com, the origin of its “central spike” is found to be very close to the accreting primary WD, and it is due to Stark effect ([37]). X-ray emission has been reported for the system ([38], [39], [40], [35], [41]).

CE 315: It was discovered spectroscopically by [42], who reported the presence of HeI and HeII lines and no traces of H, and classified it as an AM CVn system. The optical spectrum of the target was found to resemble very closely that of GP Com, with triple-peaked emission lines –as stated, its most peculiar and unique feature among the AM CVn’s, with the central spike variable. The orbital period reported by the authors, of 3906 seconds, is the largest one found to date for an AM CVn system. They also suggested values of 0.77 and $0.017 M_\odot$ for the masses of the primary and secondary component, respectively, and a mass ratio q of 0.022 . [43] detected the

existence of CNO material in CE 315, according to their spectroscopical analyses, a characteristic also shared by GP Com ([44]).

2.3 “Cyclic state” objects:

V803 Cen: Like several other AM CVn systems, V803 Cen has a thermally unstable disk ([27], [45]), where a variable mass transfer rate makes the system oscillate among a high ($V \sim 13$), a low ($V \sim 17$) and a “cyclical” ($V \sim 13.5 - 14.5$ for more than 50% of the time) states ([46]). Its optical spectrum shows HeI lines ([47], [48]), both in emission (when at low state) and in absorption (when at high state).

[46] have suggested that the system undergoes normal outbursts, like the Dwarf Novae ([45]), a possibility already pointed out by [49]. A period of 1618 seconds displayed by the object was suggested by the authors to be attributable to its superhumps; a possibility confirmed by [45] who reported values of 1614.5 and 1618.1 seconds for its superhump period and “late” superhumps, respectively. [45] also reported a value of 1594 seconds for the orbital period of V803 Cen, although no conclusively results exist for that issue so far.

[50] reported a low X-ray count rate detection for the system, compatible with a 10 keV bremsstrahlung source.

CR Boo: PG1346+082, also known as CR Boo, shares many observational properties with V803 Cen. In this case, several precession periods for its small disk ([27], [51]) have been suggested: 1.18 days by [52]; 36 hours by [51]; and 32 hours by [25]. Superhumps have been observed when in high state with a superhump period of 1487.29 seconds, while its orbital period seems to be established around 1471 seconds ([51]). [52] also compared the object with a Dwarf Nova and provided the following values for its q and secondary mass: 0.057 and $0.057 M_{\odot}$, respectively. [25] gave a value of 43.8° for the disk inclination angle and values of 0.05 and $0.05 M_{\odot}$ for q and the secondary mass, respectively. Meanwhile, [27] assigned to the secondary mass a value of $0.14 M_{\odot}$.

CP Eri: [53] classified CP Eri as an IBDBWD star, of similar characteristics to those of V803 Cen and CR Boo. They found a period of 1724 seconds, no H in its optical spectrum, and a transition between emission and absorption of its He lines from low (at a V magnitude of ~ 19.7) to high (V magnitude of ~ 16.5 ; see [53] for details), respectively, of its thermally unstable disk ([25], [27]). A clear orbital nature for that dominant period has not been established yet, as far as we can tell. [54] reported double-peaked lines of He I in emission, similar to those found for GP Com and CE 315, together with emission lines of Si II. The authors also reported a primary mass of at least $0.27 M_{\odot}$ and an inclination angle for the disk in the range $33^\circ - 80^\circ$.

KL Dra: KL Dra ([55]) was discovered as an apparent supernova (SN 1998d,I) by [56]. [57] reported He I spectral absorption lines, on a blue continuum, for its optical spectrum, which was found to resemble that of CR Boo at maximum, by the same authors. Magnitude variations between V=16.8 and V=20, together with transitions between a high and a low states, were reported by [58]. The same authors confirmed KL Dra as a new member of the AM CVn family, with similar characteristics to those of CR Boo, V803 Cen and CP Eri. A light curve, also closely resembling that of CR Boo, was obtained by [58], who reported as well the existence of superhumps for the system when in high state, with a period of 1530 seconds. Besides, they provided a value of 1500 seconds for its suspected orbital period, and values of 0.075 and 0.76 M_⊕ for q and the primary mass, respectively.

2003aw: This system was discovered by [59] as a suspected supernova, and studied spectroscopically by [60] who found it to display a blue continuum with emission lines of He, with resemblances to KL Dra. The same authors reported the presence of Ca II, H and K in absorption. [61] studied its light curve and found its behaviour very similar to that of CR Boo and V803 Cen. Its visual magnitude was found to vary between V=16.5 and V=20.3 and to display cyclic brightness changes. The authors suggested an IBDBWD model for the system, which displays faint eclipses ([62]) and superhumps when at high state. A superhump period of 2041.5 seconds has been determined by [61], who also suggested an orbital period in the range 1200–2500 seconds.

2.4 “Magnetic” objects:

RX J1914.4+2456: This object, also known as V407 Vul, was reported by [63] as a soft X-ray ROSAT object ([64]), with an optical magnitude V=19.7. A preliminary classification as Intermediate Polar was assigned to the object by [15].

A value of 569.38 seconds was measured for its orbital period by [65] who, based on the accumulated evidence, concluded that V407 Vul is the first He double-degenerate Polar; this is, the first AM CVn system where the presence of a magnetic field of a few MG was proposed to exist. Related to this, [66] also reported variations in the X-rays light curve of the object, similar to those found for other Polars. However, they did not detect neither emission lines nor polarization, as expected for a true Polar, which therefore casted some doubts on its classification as such.

While [14] indicated that the 569 seconds value did not conclusively correspond to the object’s orbital period, [22] stated that the absence of emission lines reported by [19], both in the optical and in the IR, could be due to a high mass accretion rate together with a low (0°) inclination for the orbital plane. This inclination result contradicts the one previously reported by [65], of 90°.

To date, the classification of V407 Vul according to its magnetic nature seems far from being well established. Besides a Polar ([65]) and an Intermediate Polar ([15] or [68]), [69] and [19] suggested it to be an “Electrical Powered” system, while [70] proposed a double-degenerate Algol as an alternative possibility.

ES Cet: KUV 01584-0939, also known as ES Cet o Cet3 ([71]), was discovered by [72] as an UV object of the Kiso survey [72]. [21] reported the detection of strong HeII lines in emission. [14] signed the presence of double emission lines, as measured by [73]. [17] reported emission lines of CIV, together with values of 0.094 for the mass ratio, $0.7 M_{\odot}$ for the primary mass, a visual magnitude of $V=16.9$ and a period of 620.26 seconds. These authors also suggested that the system must be a high luminosity soft X-rays source, and perhaps a Polar; they found it similar to V407 Vul, and suggested it as a potential source of strong gravitational radiation. A mass transfer rate value of $10^{-8} M_{\odot}/\text{yr}$ was also proposed for the system by [17] who speculated with the possible existence of permanent superhumps, although a superhump period has not been detected yet.

RX J0806.3+1527: [74] discovered this object as a ROSAT source and they suggested to catalogue it as an Intermediate Polar (see also [75], who reported a V magnitude of 21.1 for the system). [18] compared this system, for their similarities, to V407 Vul and they suggested to catalogue it as a “Electric Star” –i.e., in disagreement with the IBDBWD model proposed by [67]. [75] reported a period of 321.5 seconds and [67] confirmed its orbital nature. [75] also reported soft X-rays for the object, based on which a neutron star hypothesis ([67]) for its nature was discarded. [20] reported the detection of emission lines of He, as found for other AM CVn systems, and suggested a classification for RX J0806 as an IBDBWD system (see also [67]). However, [22] discarded such a model, based on the detection of H lines in the optical spectrum of the object. [20] detected C and N for the system, while [18] found C and Ne. [20] provided values between 0.2 and 0.5, and $0.12 M_{\odot}$, respectively, for the primary and secondary masses.

3 Summary and discussion

To date, twelve AM CVn, or Interacting Binary DB White Dwarf (IBDBWD), systems are known. The AM CVn systems share, as a main distinguishing characteristic among the Cataclysmic Variables, a remarkable absence of H in their optical spectra. Also, their ultrashort orbital periods (in the range 321-3906 seconds) render them unique and support the model most widely accepted, of a two He (i.e., DB-type) WD binary system, for their natures. Here, a secondary DB WD would transfer He from its atmosphere onto the primary WD, also of DB type (see, e.g., [14]). The presence

of H detected in the spectra of three of the new objects (i.e., ES Cet, RX J0806 and 2003aw) seems to cast however some doubts on their classification as AM CVn systems.

Far from sharing homogeneous appearances and behaviours, at least three subgroups seem to coexist in the class, according to their observed photometric properties: AM CVn itself, the prototype, and HP Lib display absorption lines of He and are thought to remain in a so-called permanent “high state” of mass transfer; GP Com and CE 315, in a permanent “low state”, display emission lines of He, double and triple-peaked; and V803 Cen, CR Boo, CP Eri, KL Dra and 2003aw form the so-called “cyclic state” objects with transitions between low –typically V~20– and high –typically V~13– states, over time spans ranging from days to months.

Besides, three more systems, V407 Vul, ES Cet and RX J0806, have been proposed to contain magnetic accreators, in what would constitute the first examples of double-degenerate Polars known (see, e.g., [65]). However, this classification is not exempt from controversy as alternative possibilities (such a double-degenerate Algol model, for example) have also been suggested ([70]).

The existence of superhumps in many of the systems, together with several accretion disk models –containing or not tidal and/or ellipticity effects– considered (see, e.g., [25], [27]), open broad possibilities of study for the properties of the, most likely, unstable mass transfer processes at place in the systems.

Although the number of AM CVn systems known has grown from 4 objects in 1992 [9] to 12 in 2003 ([14]), [24] have estimated that the total number of objects in our Galaxy would be of approximately 10^7 , so that realistic possibilities exist of enlarging considerably the amount of new AM CVn detections ([14]). Since the exact role played by the AM CVn systems as end points of cataclysmic binary evolution has not been definitively established yet, an exhaustive study of the observational properties of those eventual detections in the context of the already known AM CVn binaries, would be of crucial interest to the further understanding of this class.

Acknowledgements: RM greatly acknowledges financial support from the Real Sociedad Espanola de Física.

References

- [1] Smak, J. 2001, Lecture Notes in Physics, vol. 563, p. 110. F.C. Lázaro and M.J. Arévalo (eds.). Springer, Berlin
- [2] Warner, B. 1995, Cataclysmic Variable stars, Cambridge Univ. Press
- [3] Hack, M., La Dous, C., Marsh, T.R. 1995, Cataclysmic Variables and related objects, NASA SP-507
- [4] Hellier, C. 2001, Cataclysmic Variable stars, Springer.
- [5] Solheim, J.-E. 1995, Baltic Astron., 4, 363

- [6] Iben, I.J., Tutukov, A.V. 1991, ApJ, 370, 615
- [7] Provencal, C. 1995, The IBWD systems, Lectures Notes in Physics, 443, Springer.
- [8] Solheim, J.E. 1992, Interating Binary White Dwarf Stars, Proceeding of the 151st Symposium of the International Astronomical Union, Kluwer Acad. Pub., p.461
- [9] Ulla, A. 1994, Space Sci. Rev., 67, 241
- [10] Warner, B. 1995, Astr. & Sp. Sc., 225, 249
- [11] Solheim, J.-E. 2003, White Dwarfs, proceedings of the conference held at the Astronomical Observatory of Capodimonte, Napoli, Italy. Edited by D. de Martino, R. Silvotti, J.-E. Solheim, and R. Kalytis. Kluwer Academic Publishers. NATO Science Series II – Mathematics, Physics and Chemistry, Vol. 105, p. 299.
- [12] Smak, J. 1967, Acta Astronomica, 17, 255
- [13] Faulkner, J., Flannery, B.P., Warner, B. 1972, ApJ, 175, L79
- [14] Woudt, P.A., Warner, B. 2003 MNRAS, 345, 1266
- [15] Motch, C., Haberls, F., Guiulot, P., Pakull, M. et al. 1996, A&A, 307, 459
- [16] Israel, G.L., Covino, S., Stella, L. et al. 2003, ApJ, 598, 492
- [17] Warner, B., Woudt, P.A. 2002, PASP, 114, 129
- [18] Cropper, M., Ramsay, G., Wu, K. 2003, submitted (astro-ph/032240)
- [19] Ramsay, G., Wu, K., Cropper, M. et al. 2002, MNRAS, 333, 575
- [20] Israel, G.L., Hummel, W., Covino, S. et al. 2002, A&A, 386, L13
- [21] Wegner, G., McMahan, R.K., Boley, F.I. 1987, AJ, 94, 1271
- [22] Norton, A.J., Haswell, C.A. and Wynn, G.A. 2004, A&A, 419, 1025
- [23] Skillman, D.R., Patterson, J., Kemp, J., Harvey, D.A. et al. 1999, PASP, 111, 1281
- [24] Nelemans, G., Steeghs, D., Groot, P.J. 2001, MNRAS, 326, 621
- [25] El-Khoury, W., Wickramasinghe, D. 2000, A&A, 358, 154
- [26] Patterson, J., Harper, J., Shambrook, A. 1993, ApJ, 419, 803
- [27] Tsugawa, M., Osaki, Y. 1997, PASJ, 49, 75
- [28] Solheim, J.-E. et al. 1998, A&A, 332, 939
- [29] Semionovas, D. 1998, Baltic Astron., 7, 269
- [30] Pearson, K.J. 2003, MNRAS, 346, L21
- [31] Patterson, J., Fried, R.E., Rea, R., Kemp, J. et al. 2002, PASP, 114, 65
- [32] O'Donoghue, D., Kilkenney, D., Chen, A., Stobie, R.S. et al. 1994, MNRAS, 271, 910
- [33] Marsh, T.R. 1993, comm.cep7.dur.ac.uk/News/News21/marsh.ps
- [34] Marsh, T.R., Wood, J.H., Horne, K., Lambert, D. 1995, MNRAS, 274, 452
- [35] Ulla, A., Mantel, K.H., Batwig, H., La Dous, C. et al. 1996, Astr. Soc. of the Pacific Conf. Series, 96, p.313
- [36] Marsh, T.R. 1999, MNRAS, 304, 443
- [37] Morales-Rueda, L., Marsh, T.R., North, R.C. 2003, A&A, 405, 249
- [38] Strohmayer, T.E. 2004, ApJ, 608, L53
- [39] Ueda, Y., Ishisaki, Y., Takahashi, T., Makishima, K., Ohashi, T. 2001, ApJSS, 133, 1

- [40] Verbunt, F., Bunk, W.H., Ritter, H., Pfeffermann, E. 1997, A&A, 327, 602
- [41] Ulla, A. 1995, A&A, 301, 469
- [42] Ruiz, M.T., Rojo, P.M., Garay, G., Maza, J. 2001, ApJ, 552, 679
- [43] Gänsicke, B.T., Szkody, P., De Martino, D., Beuermann, K. et al. 2003, ApJ, 594, 443
- [44] Marsh, T.R., Horne, K., Rosen, S. 1991, ApJ, 366, 535
- [45] Kato, T., Stubbings, R., Monard, B., Butterworth, N.D., Bolt, G., Richards, T. 2004, PASJ, 56, 89
- [46] Patterson, J., Walker, S., Kemp, J., O'Donoghue, D. et al. 2000, PASP, 112, 625
- [47] O'Donoghue, D., Menzies, J.W., Hill, P.W. 1987, The Second Conf. on faint Blues Stars, 693-695, L. Davis Press.
- [48] O'Donoghue, D., Menzies, J.W., Hill, P.W. 1987, MNRAS, 227, 347
- [49] Ulla, A. 1993, PhD Thesis, La Laguna University (Spain)
- [50] Szkody, P., Nishikida, K., Liller, W. 2000, PASP, 112, 1607
- [51] Patterson, J., Kemp, J., Shambrook, A., Thomas, E. et al. 1997 PASP, 109, 1100
- [52] Provencal, J.L., Winget, D.E., Nather, R.E., Robinson, E.L. et al. 1997 ApJ, 480, 383
- [53] Abbot, T.M.C., Robinson, E.L., Hill, G.J., Haswell, C.A. 1992, ApJ, 399, 680
- [54] Groot, P.J., Nelemans, G., Steeghs, D., Marsh, T.R. 2001, ApJ, 558, L123
- [55] Samus, N.N. 2000, IAU Circ., 7382, 3
- [56] Schwartz, M. 1998, IAU Circ., 6982, 1
- [57] Jha, S., Garnavich, P., Challis, P., Kirshner, R., Berlind, P. 1998, IAU Circ., 6983, 1
- [58] Wood, M.A., Casey, M.J., Garnavich, P.M., Haag, B. 2002, MNRAS, 334, 87
- [59] Wood-Vasey, W.M., Aldering, G., Nugent, P., Li, K. 2003, IAU Circ, 8077, 1
- [60] Chornock, R., Filippenko, A.V. 2003, IAU Circ., 8084, 3
- [61] Woudt, P.A., Warner, B. 2003, submitted (astro-ph/0310494)
- [62] Woudt, P.A., Warner, B. 2003, IAU Circ, 8085, 3
- [63] Motch, C., Haber, F. 1995, ASP Conference Series, 85, p.109
- [64] Voges, W. 1992, Proc. of the "European International Space Year" Conf., ESA ISY-3, 9
- [65] Cropper, M., Harrop-Allin, M.K., Mason, K.O., Mittaz, J.P.D. et al. 1998, MNRAS, 293, L57
- [66] Ramsay, G., Cropper, M., Wu, K., Mason, K.O., Hakala, P. 2000, MNRAS, 311, 75
- [67] Ramsay, G., Hakala, P., Cropper, M. 2002, MNRAS, 332, L7
- [68] Norton, A.J., Somerscales, R.W., Wynn, C.A. 2003, submitted (astro-ph/0301351)
- [69] Wu, K., Cropper, M., Ramsay, G., Sekiguchi, K. 2002, MNRAS, 331, 221
- [70] Marsh, T.R., Steeghs, D. 2002, MNRAS, 331, L7
- [71] Downes, R., Webbink, R.F., Shara, M.M. 1997, PASP, 109, 345
- [72] Kondo, M., Noguchi, T., Maehara, H. 1984, Tokio Astron. Observ. Annals. Sec. Series, 20, 130

- [73] Steeghs, D., Marsh, T., Nelemans, G., Groot, P. 2003, 25th meeting of the IAU, Joint Discussion 5, 31, Sydney
- [74] Israel, G.L., Hummel, w., Covino, S., Campana S. et al. 1999, A&A, 349, L1
- [75] Burwitz, V., Reinsch, K. 2001, AIP Conf. Proc., 599, 522
- [76] Roelofs, G.H.A., Groot, P.J., Steeghs, D., Nelemans, G. 2004, to appear in proceedings of the IAU Coll. 194 "Compact Binaries in the Galaxy and Beyond", La Paz (Mexico), November 17-21, 2003 (astro-ph/0402042)

NOTE ADDED IN PROOF: A new AM CVn candidate, SDSS J1240-01, has been reported by [76].

AUTOMATIC CLASSIFICATION OF STELLAR SPECTRA

ICIAR CARRICAJO, MINIA MANTEIGA OUTEIRO

Departamento de Ciencias de la Navegación y de la Tierra, Universidad da Coruña, E-15011 A Coruña, SPAIN

ALEJANDRA RODRIGUEZ, CARLOS DAFONTE, BERNARDINO ARCA

Departamento de Tecnología de la Información y de las Comunicaciones, Universidad da Coruña, E-15071 A Coruña, SPAIN

Abstract: We propose and discuss the application of Artificial Intelligence techniques to the classification of stellar spectra. Two types of systems are considered, knowledge-based systems (Expert Systems) and different classes of neural networks. After analysing and comparing the performance of both systems in the classification of stellar spectra, we reach the conclusion that neural networks are more adequate to determine the spectral types and luminosity of stars, whereas knowledge-based systems are more performative in determining global temperatures.

In order to determine the best approach to the classification of each spectrum type, we describe and analyse the performance and results of various neural networks models. Backpropagation networks, self-organising maps and RBF networks in particular were designed and tested, through the implementation of different topologies, to obtain the global classification, spectral type and luminosity of stars. The best networks reached a success rate of approximately 97% for a sample of 100 testing spectra.

The morphological analysis algorithms that were developed in the knowledge-based systems are used to extract and measure spectral features, and to obtain the input patterns of the neural networks. Some networks were trained with this parameterisation, others with flux values of specific spectral zones; it was the first strategy that resulted in a better performance.

Our approach is focused on the integration of several techniques in a unique hybrid system. In particular, signal processing, expert systems, fuzzy logic and artificial neural networks are integrated by means of a relational database, which allows us to structure the collected astronomical data and to contrast the results of the different classification methods.

In addition, we designed several models of artificial neural networks that were trained with synthetic spectra, and included them as an alternative classification method.

The proposed system is capable of deciding the most appropriate classification method for each spectrum, which widely opens the research in the field of automatic classification.

1 Introduction

The MK Spectral classification system (MK system) was proposed by W.W. Morgan and P.C. Keenan with the publication of the first photographic spectral classification atlas, *An Atlas of Stellar Spectra*, [1]. Ever since that publication, the MK system has been revised and refined by Morgan, Keeman and others.

The MK classification system is defined by a set of standard stars and is based on the visual appearance of the spectra.

The classification process is often directly performed by experts, who analyse and classify the spectra by hand. Not only are these manual techniques very time-consuming and involve a great amount of human resources, they also constitute a subjective process, since a given spectrum may be classified differently by different people. These problems could be resolved through the use of computational techniques.

Among the different techniques of Artificial Intelligence, knowledge-based systems and neural networks seem the most appropriate answers to approach the problem of stellar classification. Knowledge-based systems can reproduce the spectral classification reasoning of the experts in the field. Neural networks have already proved their success in classification problems [2]: they are generally capable of learning the intrinsic relations that reside in the patterns with which they were trained.

Some well-known previous works have also applied this Artificial Intelligence technique to the problem of stellar classification ([3], [4]), obtaining different grades of resolution in the classification. Rather than trying to test models that have already demonstrated their suitability, we implement different models of neural networks that allow us to perform a sensibility analysis of this technique in the classification of spectra. We simultaneously try to determine the best learning algorithm and the best network structure for this specific problem.

Having tested both techniques (expert systems and neural networks) we are ready to analyse their respective adaptation to the problem, and to compare their results. Our main objective is the formalisation of a hybrid system that integrates all the developed artificial techniques and is able to choose the most appropriate classification method for each spectrum type. Because it combines several techniques, this type of system is more versatile than a system that uses only one technique, and it presents a greater capability of adaptation to the stellar classification problem.

The different methods, algorithms and techniques that were used for the development of the proposed system are described in the next sections.

2 Morphological Analysis

The spectra are stored in a relational database that was implemented with PostgreSQL running under Linux [5]. As a first step in the pre-processing module, the unclassified spectra are retrieved from the astronomical database and adjusted to flux 100 at wavelength 5450 Å for their comparison with a reference spectral catalogue. We opted for the Silva spectral catalogue [6] because of its completeness and coverage. The 50 spectra of this catalogue are sampled in the range of 3500 to 8900 Å with 5 Å resolution, and scaled to flux 100 at 5450 Å.

Our analysis considers 10 bands, 9 lines and the relevant relationships between them as classification parameters. Given the fact that a spectrum is a signal that relates wavelengths to energy fluxes, we included signal processing techniques to search and measure the spectral features [7]. The implemented algorithms are mainly based on continuum estimation and energy calculation.

To calculate the intensity of each line accurately, we estimate the local spectral continuum. The signal is smoothed with a low pass filter that excludes the peaks in an interval around the sample where the line was detected. This filter is implemented by a five-point moving average method that selects the five more stable fluxes. That is

$$C_j = \left(\frac{\sum_{j-n}^{j+n} E_i * X_i}{N} \right) , \quad (1)$$

where C_j is the estimation of the continuum for the sample j , E_i is the flux in the sample i , N is the number of values used in the moving average method to calculate the local spectral continuum, and X is a binary vector that indicates the representative fluxes of the spectral continuum in the zone. $X_i = 1$ if E_i is a flux value representative of the local spectral continuum, and $X_i = 0$ if E_i is a peak. The intensity is positive for the absorption lines and is negative for the emission lines.

As for the molecular bands, we only have to measure their energy to decide whether they are significant. In this case, the upper threshold line for each band is calculated by means of linear interpolation between the fluxes in the limits of the interval defined for each band. Then, the area between this line and the axis of abscissas is calculated with a discrete integral, and the area that surrounds each band is calculated by integrating the flux signal between the extremes of the band. Finally, the flux of the band is obtained by subtracting both calculated energies. That is

$$B_{lr} = \int_l^r L(\lambda_i) - \int_l^r E(\lambda_i) , \quad (2)$$

where B_{lr} is the value of the band between the samples l and r , L is the projection line, E is the flux function, λ the wavelength, l the left limit of the band and r the

right limit. The obtained value becomes more negative as the band becomes deeper and wider, so positive or negative fluxes close to zero are not considered bands.

The morphological analysis module was developed in C++ [8]. The graphical options include the representation of the absorption/emission lines and the molecular bands that were detected during the analysis. This facility is essential when debugging the system with the help of the human experts.

3 Automatic Classification

3.1 Expert System

In this computational approach, the classification module simulates the manual process of stellar classification. Since the human reasoning in this field includes uncertainty and imprecision, we designed an expert system that combines traditional production rules with credibility factors [9] and fuzzy logic [10]. The manual classification criteria are the result of the experience of experts in classifying spectra and are combined in a forward reasoning. Our study considers approximately 200 classification criteria.

As a previous step to the design of the expert system, we carried out a sensibility analysis of the classification parameters in order to define the different fuzzy sets, variables and membership functions. We analysed the parameters of the spectra from the reference catalogue by means of the previously described algorithms, and determined the different spectral types that each parameter discriminates. As a final result of this analysis, we defined as many fuzzy variables as levels of classification (global, type and subtype) for each luminosity class, as well as the fuzzy sets and membership functions determined by the values of the spectral features in the spectra from the guiding catalogue.

The developed expert system stores the information that is necessary to initiate the reasoning process in the *base of facts*. This descriptive knowledge of the spectra is represented by means of frames [11], that is, objects and properties structured by levels. We opted for this model because it is the simplest and most adequate to transfer the analysis data to the classification module, and because it allows the equivalence between analysis data and knowledge. The knowledge of the base of facts includes general information, e.g. the name of the stars, and the results of the morphological analysis, i.e., the value of the classification parameters.

The real parameters of spectral classification and the limit values of each type and subtype were included in the expert system in the shape of fuzzy rules. The *base of rules* is the part of the system where the human classification criteria are reproduced. We adopted production rules of the IF-THEN type to implement this module because they easily reproduce the reasoning followed by the experts in the

field. The conditions of these rules refer to the values of the parameters that are stored in the current base of facts (working memory). The conclusions allude to the three levels of spectral classification. In this way, this module actively communicates with the base of facts.

We have used the Shortliffe and Buchanan methodology [9] to carry out an evolution that includes fuzzy sets and membership functions, contextualised for each spectral type and allowing superposition between them. In addition, we obtain the spectral classification of stars with a probability value that indicates the confidence grade. Sometimes this module can conclude an alternative classification of the spectra, in the case of obtaining a first classification with a significantly small truth value.

Since it could be interesting for the user to follow the reasoning process, the system includes an explanation module in the rules base which reveals how the system reached a final conclusion.

The classification module was developed in OPS/R2 [12].

3.2 Artificial neural networks

The application of neural networks to the problem of stellar classification requires a complete and consistent set of spectra that constitute the basis on which those networks are designed and tested. Our research team selected 285 spectra from public catalogues [6] [13], and a number of spectra from various telescopes; this selection covers all the known types and luminosities and guarantees a continuous transition of the spectral features between each spectral type and its adjacent types. In order to obtain the best possible generalisation of the networks, the training set was built with approximately 50% of the spectra of each spectral type and luminosity, leaving the remaining 50% for the validation and testing of the networks. The input patterns include the measurement of 25 spectral features that can be divided into three categories:

- Absorption and emission lines: including hydrogen, helium and metallic lines (Ca, K).
- Molecular bands: hydrogen and carbon absorption bands.
- Rates between lines: CH-K rates, He-H rates.

These spectral features are extracted and measured by means of the signal processing algorithms described in Sect. 2. Once the spectral analyser obtains the input values, they are normalised and presented to the neural network. We have standardised the inputs of the networks by applying a specific sigmoidal function to each parameter:

$$1/\left(1 + e^{-(a*x+b)}\right) \text{ with } a > 0 . \quad (3)$$

The input patterns of the proposed models consist of the complete set or a subset of the 25 normalised spectral parameters, although for some networks we have considered full spectral zones in the training process.

The neural networks that were used in the experimentation are based on both supervised and non-supervised learning models, in particular backpropagation, Kohonen and Radial Basis Functions (RBF) networks. The networks were trained with these three models and by applying different topologies, including global and hierachic approaches; we have also implemented several enhanced learning algorithms. The topologies, the learning functions and the results obtained by these networks are described below.

Backpropagation Networks

Backpropagation is a supervised learning algorithm that belongs to the general feed-forward model. This model is based on two learning stages: forward propagation and backward propagation.

Training a feed-forward neural network with supervised learning consists of presenting a set of input patterns that are propagated forward by the net until the activation reaches the output layer. This phase is called the forward propagation phase. When the activation reaches the output layer, the output is compared with the teaching input (provided in the input patterns). The error, or difference between the output and the teaching input of a target output unit, is then used together with the output of the source unit to compute the necessary changes of the link between both units. Since the errors are propagated backwards, this phase is called backward propagation [14].

We have made use of three different backpropagation learning algorithms:

- Standard backpropagation: this very common learning algorithm updates the weights after each training pattern.
- Enhanced backpropagation: this algorithm uses a momentum term that introduces the old weight change as a parameter for the computation of the new weight change.
- Batch Backpropagation: in standard backpropagation, an update step is performed after each single pattern, whereas in batch backpropagation all the weight changes are summed over a full presentation of all the training patterns (one epoch). Only then, an update with the accumulated weight changes is performed.

We have tested the three backpropagation learning algorithms for the spectral types, spectral subtypes and luminosity classes. As for the topology, the different implemented networks are shown in Table 1. These topologies were tested for the three backpropagation learning algorithms.

Network	Input patterns	Hidden layer
Type/subtype	25 spectral parameters	10
Type/subtype	25 spectral parameters	5x5
Type/subtype	25 spectral parameters	10x10
Type/subtype	16 spectral parameters	10
Type/subtype	16 spectral parameters	10x5x3
Type/subtype	400 flux values	100x50x10x3
Luminosity	25 spectral parameters	10x10
Luminosity	16 spectral parameters	10x5x2

Table 1: Results of various Topologies for Backpropagation Networks.

The aforementioned networks were implemented with the Stuttgart neural network Simulator (SNNS v.4.1).

Kohonen Networks

Kohonen's Self-Organising Map (SOM) algorithm is based on non-supervised learning. SOMs constitute a unique class of neural networks, because they construct topology-preserving mappings of the training data there where the location of a unit carries semantic information [15].

Self-Organising maps consist of two unit layers: a one-dimensional input layer and a two-dimensional competitive layer, organised as a 2D grid of units. Each unit in the competitive layer holds a weight vector that, after training, resembles a different input pattern.

The learning algorithm for the SOM networks meets two important goals: the clustering of the input data, and the spatial ordering of the map, so that similar input patterns tend to produce a response in units that are close to each other in the grid. In the learning process, the input pattern vectors are presented to all the competitive units in parallel, and the best matching unit is chosen as a winner.

We have tested Kohonen networks for the spectral types/subtypes and luminosity classes, using bidimensional maps from 2x2 to 24x24 units.

RBF Networks

Networks based on Radial Basis Functions (RBF) combine non-supervised learning for hidden units and supervised learning in the output layer. The hidden neurons

apply a radial function (generally Gaussian) to the distance that separates the input vector and the weight vector that each one stores, called centroid [14].

We tested the RBF algorithm for the spectral types, spectral subtypes and luminosity classes. As for the topology, the different networks that were implemented are shown in Table 2.

Network	Input patterns	Hidden layer
Type/subtype	25 spectral parameters	16
Type/subtype	25 spectral parameters	8
Type/subtype	25 spectral parameters	4
Type/subtype	16 spectral parameters	8
Type/subtype	16 spectral parameters	4
Type/subtype	400 flux values	124
Luminosity	25 spectral parameters	8
Luminosity	16 spectral parameters	8

Table 2: Results of various Topologies for RBF Networks.

3.3 Synthetic Spectra

We used version 2.56 of the SPECTRUM software, written by Richard O. Gray, to generate a set of synthetic spectra. Spectrum is a stellar spectral synthesis program that computes the emerging flux from a stellar atmosphere under the assumption of Local Thermodynamic Equilibrium (LTE). It considers most of the atomic and molecular transitions in the optical spectral region 3500 Å to 6800 Å, suitable for computing synthetic spectra with temperatures between approximately 4500K and 20000K. The details on the physics included in SPECTRUM can be found in [16].

We also selected the atmospheric models set that was calculated by Robert Kurucz [17]. Each model is characterised by four parameters: effective temperature, T_{eff} , metallicity $[M/H]$, microturbulence velocity V_{micro} and surface gravity, $\log g$. These parameters must be specified to generate each of the synthetic spectra. We generated a total of 170 solar metallicity spectra with effective temperatures ranging from 4000K to 15000K, and the surface gravity, $\log g$, with values of 0.5, 1.0, 1.5, 2.0, 2.5, 3.0. This set of synthetic spectra covers the spectral range K-B with luminosity classes I, II and III (giants and super giants). The synthetic spectra were generated with a sufficiently small wavelength step, 0.02 Å, and a microturbulence velocity of 2.0 Km s⁻¹ over the 3500-6800 Å range.

The neural networks that were used for the experimentation are based on supervised learning models. We tested various topologies and enhanced learning algorithms on backpropagation networks, as can be seen in Table 3.

The input patterns of the nets are the 659 flux values (from 3510 Å to 6800 Å); the output is a continuous function of the effective temperature. The networks were trained with the whole set of 170 synthetic spectra and tested with the spectra from the Silva catalogue [6].

Network	Input patterns	Hidden layers
Type/subtype	659 flux values	10x5x3
Type/subtype	659 flux values	5x5
Type/subtype	659 flux values	100x50x10x3

Table 3: Results of various Topologies for Synthetic Spectra.

4 Hybrid System

After analysing the performance of the proposed techniques, we integrate them into a unique system, implemented in C++, that guarantees a reliable, consistent and adapted classification of stars.

The final analysis and classification system can be divided into three main logical modules, as shown in Figure 1.

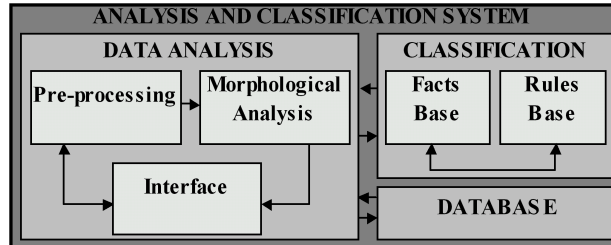


Figure 1: General System Scheme.

The relational database was developed to securely store and organise astronomical data. The data analysis module makes an exhaustive morphological analysis (calculation of maxima, minima, energy, etc.) of the spectra, treating them as a temporal series in order to obtain numerical parameters. The classification module is based on the development of expert systems and artificial neural networks that obtain the temperature and luminosity of stars through the parameterisation that resulted from the morphological analysis.

5 Results

According to the classification made by the human experts involved in this project, the automatic hybrid system is able to classify stars with an error rate below 20%.

Table 4 shows a comparison between the developed automatic classification systems and two human experts. We have analysed the performance of each technique for each classification level: global temperature of the star (early, intermediate, late), spectral type (BAFGKM), and luminosity level (I,III,V). In the neural network approach, ambiguous classifications were considered errors (outputs in [0.45, 0.55]). As for the expert systems, classifications with a low probability (less than 75%) were excluded.

Technique	Global Temp.	Spectral Type	Luminosity
Human Expert A	99%	92%	81%
Human Expert B	95%	85%	70%
Expert Systems	96.5%	88%	65%
Expert Systems with fuzzy logic	98.6%	90.3%	78.2%
Backpropagation Networks	97%	95.4%	81%
Kohonen Networks	80%	65%	60%
RBF Networks	95%	93%	79%

Table 4: Performance of the tested Classification Techniques

In the synthetic approach, the networks were tested with spectra from the Silva catalogue [6]. The preliminary results show that the net is able to correctly classify 80% of the input spectra (with a maximum deviation of 300 K in the worst cases).

6 Conclusions

This paper has presented an approach to the automation of the spectral analysis and classification process, by means of a hybrid system that provides users with a comfortable tool for spectra processing.

By integrating signal processing, knowledge-based techniques, fuzzy logic and artificial neural networks, we obtained a very satisfactory emulation of the current classification process.

Finally, all the artificial techniques were integrated into a hybrid system that determines the most appropriate classification method for each spectrum. This implies that our hybrid approach becomes a more versatile and more flexible automatic technique for the classification of stellar spectra.

The final system classifies more than 80% of the tested stars, confirming the conclusion that neural networks are more performative in determining the spectral types

and luminosity of stars, whereas knowledge-based systems obtain a higher performance in determining the global temperature.

As an additional research, we have generated synthetic spectra and used them to train backpropagation networks that determine the temperature of stars on the basis of full spectral regions. The obtained results encourage us to continue in this direction: it offers the advantage that physical properties, such as effective temperatures, gravity or metal contents, could eventually be extracted from the classified spectra.

At present, we are refining the expert systems towards new aspects of the spectral analysis; we are working on the design of new neural networks, based on synthetic spectra, that refine the current classification system; and we are completing the development of our stellar database, STARMIND (<http://starmind.tic.udc.es>), to make it accessible through the Internet. Our aim is to enable users worldwide to store and classify their spectra, and directly contribute to improve the adaptability and accuracy of our automatic analysis and classification system.

Acknowledgements: The authors acknowledge support from grants AYA2000-1691 and AYA2003-09499, financed by the Spanish Ministerio de Ciencia y Tecnología.

References

- [1] Morgan, W. W., Keenan, P.C., Kellman, E. 1943, An Atlas of Stellar Spectra with an outline of Spectral Classification. University of Chicago Press, Chicago
- [2] Haykin, S. 1994, Neural Networks: A Comprehensive Foundation, Macmillan College Publishing, New York
- [3] Weaber, W.B., Torres-Dodgen, A.V. 1995, ApJ, 446, 300
- [4] Singh, H.P., Gulati, R.K., Gupta, R. 1998, MNRAS, 295, 312
- [5] Momjian, B. 2000, PostgreSQL: Introduction and Concepts, Addison-Wesley Pub Co.
- [6] Silva, D.R., Cornell, M.E. 1998, PASP, 110, 863
- [7] Kalouptsidis, N. 1997, Signal Processing Systems: Theory and Design, Wiley & Sons
- [8] Hollingworth, J., Butterfield, D., Swart, B., Allsop, J. 2000, C++ Builder 5.0. Developer's Guide, SAMS
- [9] Buchanan, B., Shortliffe, E. 1984, Ruled-Based Expert Systems, Adisson-Wesley
- [10] Zadeh, L. 1965, Fuzzy Sets. Information and Control, 8, 338
- [11] Sowa, J. F. 1999, Knowledge Representation: Logical and Computational, Brooks Cole Publishing Co
- [12] Forgy, C. L. 1986, The OPS'83 User's Manual System Version 2.2., Production Systems Technologies Inc.
- [13] Pickles, A.J. 1992, ApJ, 81, 865
- [14] Hilera, J.R., Martínez, V. 1995, Redes Neuronales Artificiales: Fundamentos, modelos y aplicaciones; RA-MA Eds, Madrid

- [15] Kohonen, T. 1987, Self-Organization and Associative Memory, Springer-Verlag, New York
- [16] Spectrum: A Stellar Spectra Synthesis Program. [Online]. Available: <http://www1.appstate.edu/dept/physics/spectrum> (2003)
- [17] Kurucz, R. L. 1979, ApJ, 40, 1

GEOMAGNETIC STORMS: THEIR SOURCES AND A MODEL TO FORECAST THE DST INDEX

YOLANDA CERRATO, ELENA SAIZ, CONSUELO CID, MIGUEL ANGEL HIDALGO
Departamento de Física, Universidad de Alcalá, E-28871 Alcalá de Henares, SPAIN

Abstract: One of the applications of space weather is to forecast storm events. With this aim, a great effort has to be made in the development of models that let us to predict the Dst index, as indicator of geomagnetic storms. We propose a new model that determines the Dst index from the current induced over the ring current that flows around the Earth, assuming that solar wind electric field is the responsible of these variations. We also study which are the triggers of intense geomagnetic storms both at interplanetary space and at the Sun, and their dependence with solar cycle.

1 Introduction

The study of magnetic storms is one of the main topics of space weather. During a geomagnetic storm, the Sun and the magnetosphere are *connected*, giving rise severe changes both in interplanetary space and terrestrial environment. Some examples are the acceleration of charged particles, enhancement of electric currents, auroras and magnetic field variations on the Earth surface. These changes can produce important damages in electric power supplier, radio communications and spacecrafts.

It is assumed that Sun-Earth interaction depends on solar wind. In fact, intense geomagnetic storms seem to be related to intense interplanetary magnetic field (IMF) with a southern component for a long time [1, 2]. Several papers about geomagnetic storms [3, 4, 5, 6, 7] have pointed out the reconnection between a southern IMF and the magnetospheric magnetic field as the physical mechanism responsible of Sun-Earth connection. Although several aspects on this mechanism are still open questions, it is accepted that reconnection in the day-side of magnetosphere produces a transference of magnetic flux to the magnetotail [8]. Then energetic particles of solar wind can go into the magnetosphere, along magnetic field lines, yielding an injection of plasma in the night-side of the magnetosphere.

The radiation belts are regions of terrestrial environment where charged particles become trapped on closed geomagnetic field lines. These particles show drifts due to

magnetic field gradient and curvature as well as to gyration orbit effects. As drifts depend on the sign of charge, ions travel to west and electrons to east, giving rise a ring current (RC) which extends from 4 to 8 terrestrial radii. Variations on this current produce variations into the magnetic field on the Earth surface.

All processes explained above involve energy transference from the solar wind to magnetosphere-ionosphere system, which modify plasma and magnetic field of magnetosphere. This perturbation can develop into a geomagnetic storm. Efficiency of process seems to depend on the southern component of magnetic field (a negative B_z value) and on the solar wind speed (v_x), that is, on the dawn-dusk component of solar wind electric field [9].

When the electric field is intense enough as to enhance the current of the RC above a value, a geomagnetic storm is produced. The Dst index is considered to be an indicator of the current of the RC [10, 11]. This hourly index is calculated as the horizontal variation of geomagnetic field measured at four different observatories distributed in longitude and near Earth equator. Then, if Dst index reaches -50 nT the event is considered as a geomagnetic storm and if it passes -100 nT the storm is considered as intense. Major geomagnetic storms can reach more than -300 nT.

Although the current of the RC is one of the major current systems of the magnetosphere [12, 13, 14], other low latitude currents also contribute to Dst index: magnetotail currents, substorms induced currents, and induced currents in the solid Earth [15, 16, 17]. All these currents can affect the magnetic field on the Earth surface and then, they have to be considered in those periods of intense geomagnetic activity to calculate the Dst index.

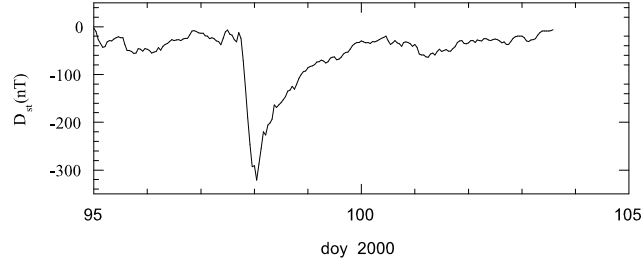


Figure 1: Hourly Dst values for a storm event.

In a geomagnetic storm can usually be distinguished two phases (Figure 1). The first one, the main phase, when energy passes from solar wind to magnetosphere enhancing the current of the RC and producing a strong decrease of Dst index. After, a recovery phase, when the magnetic field on the Earth surface goes back to the value

of quiet time because of a decay of the current of the RC. This decay is due basically to loss processes as exchange of charge [9, 18], Coulomb interaction [19], and particle-wave interaction [20]. Each process is sensitive to ions energy, composition, pitch angle, distribution, etc. Then, decay time is a mean value in the RC as a whole that includes all these contributions.

In last decade great efforts have been made to develop models to predict the Dst index from solar wind data. The aim of these models is double: to know the physical mechanisms of RC dynamics and to study the influence of solar wind in the terrestrial environment. These models can be summarized into three groups: those based in a first order differential equation, those with linear filters [21] and those developed from neural networks [22]. In the first group outstands the work of [23], where the time evolution of Dst is modeled as a difference between an injection function, $Q(t)$, and a recovery term of the RC with a characteristic time τ . The injection function is associated to the energy coming by reconnection. Although the expression for $Q(t)$ has been discussed in many papers (see as an example [24]), it is accepted that magnetospheric injection is directly related to dawn-dusk component of solar wind electric field [25, 9, 26]. On the other hand, the recovery term is associated to the decay due to any loss process in the RC and it is proportional to the own Dst index.

Several corrections to the model proposed by [23] for Dst have been introduced trying to consider the contributions the dynamic pressure effect and the contribution of other currents (tail and magnetopause currents) that can also affect the magnetic field on the Earth surface [7, 17]. But a substantial modification was that of McPherron and O'Brien [26]. They assumed that the parameters involved in the model of Burton et al. have not a constant value, but depended on the dawn-dusk component of solar wind electric field. About the value of the decay time, it has varied from 7.7 hours (assumed by [23]) to a value which decreases in an exponential way as geomagnetic activity increases, varying nearly from the order of 15 hour for low geomagnetic activity to 5 hours for high level of activity.

Predictions on growing and decay of geomagnetic storms from solar wind conditions follow on improving. Nowadays, it is possible to reproduce roughly the hourly variation of the index Dst from solar wind data by several techniques (linear and non-linear). The problem arises when a storm is made of several substorms nearly in time. Then, the main phase of Dst index is not properly reproduced by any technique. Moreover, the relative importance of storms and substorms in building of RC is still an open problem.

2 Modeling the Dst index

We have developed a model to calculate the Dst index based only on the response of the RC to movement of IMF. The starting point of our model is considering the RC

as if it would be an electrical circuit and solar wind as a power supplier. Although the dynamics of the RC is very complex, we will only consider global effects. Then, this approach does not let us to analyze those phenomena which are taking place inside the RC, but it let analyze in a simple way the effect of this current in the magnetic field measured on the Earth surface.

The energy by unit of charge that feeds this circuit at every time t depends on the dawn-dusk solar wind electric field and can be determined by the expression $v_x B_z l$, being l the longitude of the circuit. By separating the contribution of quiet solar wind and that of disturbed solar wind, we can represent the power of that circuit as two batteries serial connected: a *quiet* battery and an *extra* one. In this scenario, the first one would be related to the current of the RC in quiet time (I_{quiet}) and then to H component measured at the equator on quiet days (H_{quiet}).

When a disturbance occurs in the solar wind, the *extra* battery connects, supplying more electromotive force and enhancing the current of the RC. This current induced will produce a variation in the magnetic field measured on the Earth surface which is identified as the value of Dst index, and can be easily calculated, considering the magnetic field in the center of a ring:

$$Dst = H_{disturbed} - H_{quiet} = \mu_0 \frac{I_{quiet} + I_{extra}}{2R_{RC}} - \mu_0 \frac{I_{quiet}}{2R_{RC}} \quad (1)$$

In order to obtain I_{extra} , we have to take into account that at storm events, sudden variations in the current induced are produced. Then autoinduction cannot be neglected. Assuming a resistance R and an autoinduction coefficient L for the circuit, and having into account the initial conditions, I_{extra} can be determined from:

$$\xi_{extra} = RI_{extra} + L \frac{dI_{extra}}{dt} \quad (2)$$

Up to now, our model has been undiscriminating with the sign of the dawn-dusk electric field, that is, with the orientation of B_z . However, as has been said before, reconnection between the magnetospheric magnetic field and a southern IMF favors the entrance of energy into the magnetosphere. This fact is outstanding in fast changes of B_z . Experimental data show that when changes in electromotive force are due to an increase in southern component of IMF, the response of the magnetosphere is very fast. On the other hand, if changes are due to an increase in northern component, the response is slower and we can neglect autoinduction term.

Two different cases are considered that let us to simplify the general model in order to calculate R and L : a purely resistive case and a case with a sudden increase in *extra* battery electromotive force (or in dawn-dusk electric field), followed by a disconnection of that battery.

In the first case the current induced presents a smooth variation, or which is the same, there are not sharp changes in solar wind dawn-dusk electric field. Then the

second term can be neglected in eq 2 and

$$Dst = -\frac{\mu_0 \pi}{R} v_x B_z \quad (3)$$

By fitting equation 3 to experimental data (Figure 2), our results indicate that $R = 0.12\Omega$.

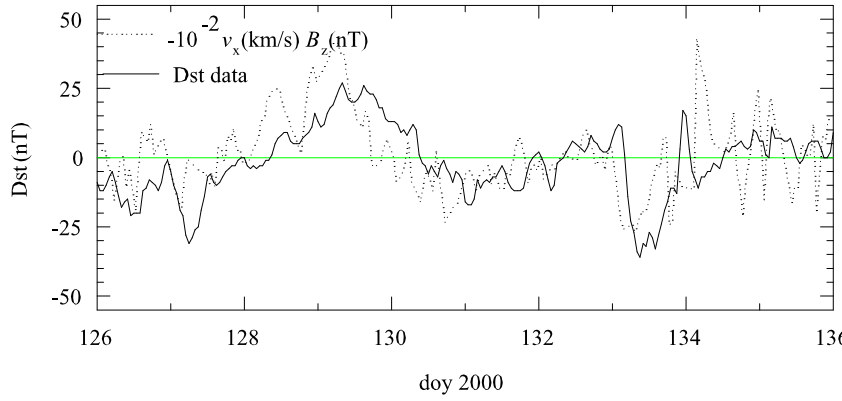


Figure 2: Figure shows one of the intervals in experimental data analyzed in order to determine the resistance of the RC.

In the second case, in order to obtain the value of L , it is necessary to analyze cases where we can consider that the *extra* battery has been disconnected after providing a sudden enhancement of the current of the RC. That is, we have to observe in the solar wind dawn-dusk electric field data a sharp discontinuity (at $t = t_0$) followed by a nearly zero value (Figure 3). In this case equation 2 is reduced to $I_{extra} = -\frac{L}{R} \frac{dI_{extra}}{dt}$, for the interval where $\xi_{extra} = 0$, which solution is $I_{extra} = I_0 e^{(t_0-t)\frac{R}{L}}$. Then we obtain that

$$Dst = C_0 e^{(t_0-t)\frac{R}{L}}, C_0 = \frac{\mu_0 I_0}{2R_{RC}} \quad (4)$$

Although C_0 and t_0 depend on the interval analyzed, the value of $\frac{R}{L}$ that we have obtained in all cases is always 1.1day^{-1} (see bottom panel of Figure 3 as an example). This indicates that $L = 9425\text{H}$, having into account the value of the resistance obtained before.

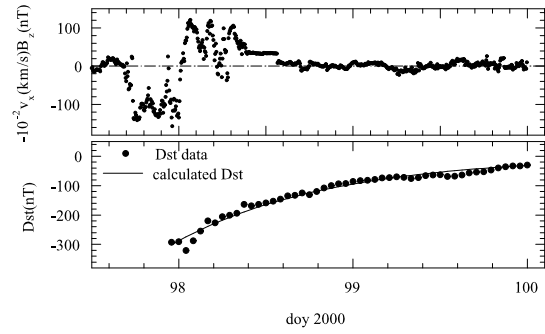


Figure 3: An interval in experimental data used for calculation of autoinduction coefficient of the RC.

With the values of the resistance and autoinduction coefficient calculated above, we can obtain a solution at intervals for equation 2. The number of intervals is determined by the number of sharp changes at dawn-dusk electric field. The function Dst for the interval $t_i < t < t_{i+1}$ can be expressed as follows:

$$Dst = -\frac{\mu_0 \pi}{R} v_x(t) B_z(t) + C_i e^{(t_i-t)\frac{R}{L}} \quad (5)$$

where t_i is the time where the sharp change number i happens, and C_i is a constant for every interval. Figure 4 shows Dst data (solid line) and Dst calculated with our model (dotted line) for a complex event, only using solar wind speed and IMF experimental data and values of R and L , obtained from simpler events. Although the value of C_i coefficients seems to be related to the magnitude of change in dawn-dusk electric field, it also depends of how quick changes. Anyway, a study that includes a great number of events is needed in order to conclude anything about this.

3 The Triggers of Geomagnetic Storms

The objectives of space weather cannot be only modeling the response of the terrestrial environment to solar wind. A special effort should be made in order to know which are the solar phenomena that trigger a geomagnetic storm and the way to forecast its occurrence in advance. Although magnetic storms can be triggered by other solar phenomena, the most intense storms have been associated to coronal mass ejections (CMEs). These solar events are large-scale eruptions of plasma, which are observed with coronagraphs. As these instruments only provide images of the sky plane, it is

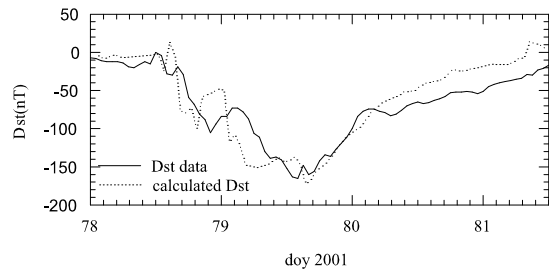


Figure 4: Dst index experimental data and theoretical results for a complex storm event.

difficult to determine if the material ejected from the Sun is directed to Earth. CMEs known as *halo* are those which extend 360° around the disk of the coronagraph. This kind of CMEs are thought to be ejections along the Sun-Earth line [27]. But an event from the visible side of the Sun, seen by a coronagraph, provides the same image as another event on the opposite side. Then, in order to determine if a halo CME goes towards the Earth (front-side event) or goes away from it (back-side event), observations from solar disk are necessary. Front-side halo CMEs are more likely to affect the magnetosphere than other CMEs, but not all of them drive intense geomagnetic storms. As the number of CMEs varies with the solar cycle [28], intense geomagnetic activity triggered by CMEs is expected at solar maximum. A different kind of storms are those recurrent. These storms have been associated to coronal holes (CHs) and it is assumed that they are less intense than those considered before [2]. As the holes are largest and extend toward the helioequator during the declining phase of the solar cycle, at this stage the number of recurrent storms is expected to increase.

Anyway, a geomagnetic storm is the response of the magnetosphere to the interplanetary phenomena, which arises as a consequence of the solar event. Then, it is necessary to identify first the interplanetary event and after relating it to the solar activity. As mentioned above, intense dawn-dusk interplanetary electric field during a long time are the true triggers of geomagnetic storms. There are four kinds of interplanetary events that are associated to these intense electric fields: ejecta, corotating interaction regions (CIRs), alfvenic IMF fluctuations and Russell-McPherron effect [29]. However, the two last events cannot produce any storm if they are not together either to a ejecta or a CIR. Then, ejecta and CIRs are the primary interplanetary triggers of any storm.

The signatures in the solar wind of ejecta and CIRs are reasonably well defined and have been described in a number of previous works (see for example [30] for ejecta

and vol. 89 of *Space Science Reviews* for CIRs). It can be summarized as follows: in an ejecta the magnetic field direction varies slowly, the magnetic field strength increases, and plasma proton temperature and thermal pressure decrease, that is, the ejecta is a low- β plasma. On the other hand, a CIR is a region of compressed plasma formed by the interaction of a high-speed flow with a preceding slow solar wind. Within the boundaries of a CIR, the proton temperature and the magnetic field strength are high.

A common association between solar and interplanetary event guides us to assume as starting point that ejecta are ICMEs (interplanetary CMEs) and CIRs are the result of interaction of a high speed stream from a CH with the slow solar wind. With the exception of some particular events, previous works have studied either the interplanetary or the solar sources of geomagnetic storms, but not the whole solar-terrestrial event. In order to study the solar triggers of geomagnetic storms, we have first identified all geomagnetic storms with an index $Dst < -100$ nT (intense storms) since 1995 to 2001. We have considered this period because it includes minimum and maximum solar activity. Then, we have determined the interplanetary medium event related to every storm. Finally, we have inspected solar data trying to determine the whole solar-terrestrial event.

For the case of a CIR, we inspect sun disk images obtained two or three days before the interplanetary event in order to check if a low latitude CH appears. Then, we associate the fast wind with the wind from that CH. The identification of the solar source of an ejecta requires a more careful analysis. First, we inspect LASCO CME catalog looking for any CME candidate in a time window consistent with the solar wind speed measured for the ejecta. Usually, several CMEs are found and choosing the appropriate candidate for the ejecta is not an easy task. The appearance of a front-side halo CME candidate is widely used as a reliable indicator of the solar source of ejecta [31]. However, a front-side halo CME can be also associated to very bright material ejected far away from the solar central meridian. In this case, the association between the solar ejection and the interplanetary ejecta is far to be sure. Then, we have not considered the angular size of the CME as an indicator for the association of solar and interplanetary events. Instead of that, we take into account the location on the solar disk where the material is ejected. We have checked that this location is near the central solar meridian using Sun disk images, in order to be sure that the ejection reaches the Earth. We have also inspected how the material ejected evolves along the chronograph field of view, and we have tried to relate it with solar wind speed observed at ejecta.

During the period analyzed 48 storm events with Dst less than -100 nT were observed. Our results indicate that the main cause of intense storms are ejecta, but the number of storms related to CIRs is not negligible (29%). Moreover, these storms can be as intense as those from ejecta, as in the case of 22 October 1999. This event was associated previously by Zhang [32] with the CME from S40E05 on October 18,

00:06 UT. By relating interplanetary data and the Dst index, we think that the ejecta related to CME reaches the Earth before starting the storm (at Oct 21, 15:00 UT). In our opinion, the true trigger of this intense storm is the fast wind that appears in interplanetary data after passing the ejecta, that comes from the CH that appears in SXT image on October 20.

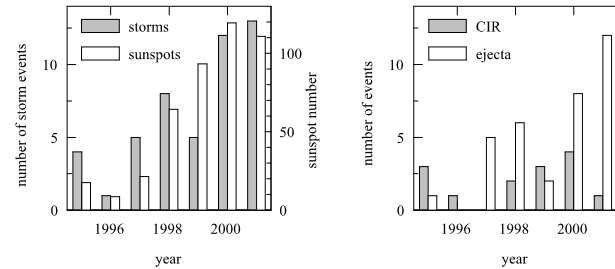


Figure 5: Frecuency histograms along solar cycle.

We have also analyzed if the kind of event that triggers a storm depends on solar cycle. With this aim, we have represented in Figure 5 the yearly sunspot number next to the number of storm events (a) and next to those related to CIRs (b) and ejecta (c). CMEs are considered the origin of intense storms in the increasing side of the solar cycle and coronal holes in the decreasing side [33]. Our results seem to indicate that there is a clear contradiction to those arguments. It can be seen in Figure 5 that the number of storms is closely related to solar cycle, although in year 1999 an anomalous behavior appears. The number of events related to CIRs is almost constant along the solar cycle and those related to ejecta is bigger in years of maximum activity (2000 and 2001) than in those of minimum (1995 and 1996), but the trend does not follow solar cycle.

Several works [32] indicate that most effective CMEs are those full halo and partial halo. Then, trying to check if the angular width of a CME was an indicator of geomagnetic storms, we have make a histogram of the angular width of CMEs related to intense storms (Figure 6a). As figure shows the number of non halo CMEs which trigger an intense storm is not a negligible quantity. Moreover, CMEs with a small angular width can be associated to storms as intense as those halo. Other fact about intense storms is that they are related to fast CMEs. In Figure 6b we show that there is not any relationship, moreover a slower CME can be more geoeffective than a faster one.

Finally, we want to remark that extracting conclusions from the trigger of a storm only from partial information of the whole solar-interplanetary event, can lead us to

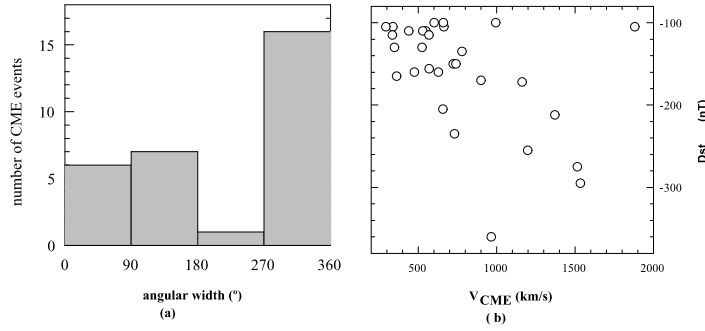


Figure 6: (a) Histogram distribution of the CMEs angular width and (b) the CME speed at $20 R_{SUN}$ as a function of Dst_{peak} .

obtain wrong conclusions. Usually there is only a part of information available, and moreover, it is difficult to be sure that all the pieces of the time-puzzle from the Sun to 1 AU have been settled properly. We think that a great effort should be made in those events that seem to be well identified.

References

- [1] Gonzalez, W. D., Tsurutani, B. T. 1987, *Planet. Space Sci.*, 35, 1101
- [2] Tsurutani B. T. 2001, in *Space Storms and Space Weather Hazard*, I. A. Daglis ed. (Dordrecht: Kluwer)
- [3] Dungey, J. W. 1961, *Phys. Rev. Lett.*, 6, 47
- [4] Tsurutani, B. T., Meng, C.I. 1972, *J. Geophys. Res.*, 77, 2964
- [5] Akasofu, S.-I. 1981, *Space Sci. Rev.*, 28, 111
- [6] Gonzalez, W. D., Mozer, F. S. 1974, *J. Geophys. Res.*, 79, 4186
- [7] Gonzalez, W. D., Tsurutani, B. T., Gonzalez, A. L. C., Smith, E. J., Tang, F., Akasofu, S.-I. 1989, *J. Geophys. Res.*, 94, 8835
- [8] Daglis, I. A., Kozyra, J. U., Kamide, Y., Vassiliadis, D., Sharma, A. S., Liemohn, M. W., Gonzalez, T. W. D., Surutani, B. T., Lu, G. 2003, *J. Geophys. Res.*, 108, 1208
- [9] Gonzalez, W. D., Joselyn, J. A. et al. 1994, *J. Geophys. Res.*, 99, 5771
- [10] Kamide, Y., Baumjohann, W., Daglis, I. A., Gonzalez, W. D., Grande, M., Joselyn, J. A., McPherron, R. L., Phillips, J. L., Reeves, E. G. D., Rostoker, G., Sharma, A. S., Singer, H. J., Tsurutani, B. T., Vasyliunas, V. M. 1998, *J. Geophys. Res.*, 103, 17728

- [11] Daglis, I. A., Thorne, R. M., Baumjohann, W., Orsini, . 1999, Rev. Geophys., 37, 407
- [12] Hamilton, D. C., Gloeckler, Ipavich, F. M., Stdemann, W., Wilken, B., Kremser G. 1988, J. Geophys. Res., 93, 14343
- [13] Jordanova, V. K. , Farrugia, C. J., Quinn, J. M., Ton, R. M., Ogilvie, K. W., Lepping, R. P., Lu, G., Lazarus, A. J., Thomsen, M.F., Belian, R. D. 1998, Geophys. Rev. Lett., 25, 2971
- [14] Greenspan, M. E., Hamilton, D. C. 2000, J. Geophys. Res., 105, 5419
- [15] Akasofu, S.-I., Chapman, S. 1972, Solar Terrestrial Physics (Clarendon, Oxford)
- [16] Rostoker, G., Friedrich, E., Dobbs, M. 1997, in Magnetic Storm, Geophys. Monogr. Ser., 98, B. T. Tsurutani et al. eds (AGU, Washington D. C.)
- [17] Turner, N. E., Baker, D. N., Pulkkinen, T. I., McPherron, R. L. 2000, J. Geophys. Res., 105, 5431
- [18] Jordanova, V. K., Kistler, L. M., Kozyra, J. U., Kharanov, G. V., Nagy, A. F. 1996, J. Geophys. Res., 101, 111
- [19] Kozyra, J. U., Fok, M.-C., Sanchez, E. R., Evans, D. S., Hamilton, D. C., Nagy, A. F. 1998, J. Geophys. Res., 103, 6801
- [20] Kozyra, J. U., Jordanova, V. K., Home, R. B., Thorne, R. M. 1997, in Magnetic Storm, Geophys. Monogr. Ser., 98, B. T. Tsurutani et al. eds (AGU, Washington D. C.)
- [21] McPherron, R. L., Baker, D. N., Bargatze, L. F. 1986, in Solar Wind Magnetosphere Coupling, edited by Y. Kamide and J. A. Slaving
- [22] Lundstedt, H., Gleisner, H., Wintoft, P. 2002, Geophys. Res. Lett., 29
- [23] Burton, R. McPherron, R. L., Russell, C. T. 1975, J. Geophys. Res., 80, 4204
- [24] Fenrich, F. R., Luhmann, J. G. 1998, Geophys. Res. Lett., 25, 2999
- [25] Kamide, Y. 1992, J. Geomagn. Geoelectr., 44, 109
- [26] McPherron, R. L., OBrien, T. P. 2001, in Dobbs in Space Weather, Geophys. Monogr. Ser., 125, P. Song et al. eds (AGU, Washington D. C.)
- [27] Howard, R. A., Michels, D. J., Sheley Jr., N. R., Koomen, M. J. 1982, ApJL, 263, L101-L104
- [28] Webb, D. F., Howard, R. A. 1994, J. Geophys. Res., 99, 4201
- [29] Russell, C. T., McPherron, M. 1973, J. Geophys. Res., 78, 92
- [30] Richardson, I. G., Cane, H. V. 1995, J. Geophys. Res., 100, 23,397
- [31] Gopalswamy, N., Lara, A., Lepping, R. P., Kaise, M. L., Berdichevsky, D., St. Cyr, O. C. 2000, Geophys. Res. Lett., 27, 145
- [32] Zhang, J., Dere, K. P., Howard, R. A., Bothmer, V. 2003, ApJ, 582, 520
- [33] Gonzalez, W. D., Gonzalez, A. L. C. , Tsurutani, B. T. 1990, Planet. Space Sci., 38, 181

DETECTION OF ENERGETIC PARTICLE EVENTS WITH SOHO SPACE OBSERVATORY

*DOLORES RODRÍGUEZ FRÍAS, RAÚL GÓMEZ HERRERO, JULIO GUTIÉRREZ, LUIS DEL PERAL
Departamento de Física, Universidad de Alcalá, E-28871 Alcalá de Henares, SPAIN*

Abstract: An analysis of eighteen solar energetic particle (SEP) events measured with the EPHIN instrument on board the SOHO spacecraft has been performed. Differences among individual events have been shown by the parametrization of temporal profiles. The detected differences are found to depend on the particle acceleration, the magnetic connection with the acceleration zone and the interplanetary physical characteristics transported to the observing point.

1 Introduction

The SOHO spacecraft was launched in December 1995 and it was injected into a halo orbit around the inner Lagrangian point, L1, reaching its final destination, in February 1996. It is observing the Sun continuously from its privileged position outside the Earth magnetosphere. SOHO is a 3-axis stabilized spacecraft where its sensors point to the nominal interplanetary magnetic field direction at 0.99 AU and 45° West of the spacecraft-Sun line. A set of four particle detectors are shipped on board SOHO satellite for detection of suprathermal and energetic particle populations of solar, interplanetary and galactic origin. They are: LION, Low Energy Ion and Electron Instrument; EPHIN, Electron Proton Helium Instrument; LED, Low Energy Detector and HED, High Energy Detector. All of them cover the detection of electrons in the 44 keV - 50 MeV energy range, together with the 44 keV/n - 540 MeV/n energy range for ions.

From its privileged position outside the Earth's magnetosphere SOHO is able to perform direct detections of the heliospheric plasma particles, providing us with particle intensity, anisotropy, composition and energy spectra data.

Detected particles come from different origins: solar energetic particle (SEP) events, interplanetary shock accelerated particles, low energy galactic cosmic radiation modulated by the heliospheric magnetic field, anomalous cosmic radiation, particles accelerated in planetary magnetospheres, etc.

2 Observations

On flight particle identification is obtained from the $\Delta E-E$ technique with the Goulding algorithm. Heavy ion identification is not performed on flight because it requires more exhaustive calculations; a mass resolution as high as 0.15 amu for carbon with the HED detector is obtained. The EPHIN instrument obtains a mass resolution of 0.01 amu for hydrogen, and 0.02 amu for Helium isotopes.

The events analyzed in this work have been selected among more than 60 SEP events registered by SOHO sensors during 1996, 1997 and 1998. The first half of this period showed relatively quiet particle fluxes, corresponding to minimum solar activity. During the second half of this period, solar activity increased gradually, corresponding to the rising phase of the 23rd solar cycle, and extremely large GSEP (Nov 97 and Apr 98) were detected. These events have a wide variety of observational features (composition, spectra, duration, etc), and there is an adequate sample of the differences that can be found studying SEP events. Nevertheless, most of the events may be classified into two broad categories: Impulsive Solar Energetic Particle (ISEP) events and Gradual Solar Energetic Particle (GSEP) events. The observational characteristics of these two categories have been widely described by many authors ([1], [2], [3]). GSEP events show large increases in particle fluxes; they are commonly associated with Coronal Mass Ejections (CMEs) and interplanetary shock waves. They are also long duration (several days) events, and their composition is similar to that of the solar wind and corona. On the other hand, ISEP events are characterized by low particle fluxes, short duration, heavy ions and ^3He enrichment, and for the fact of being commonly associated to impulsive X-ray flares.

The start and end times of individual events have been identified using proton differential fluxes (4.3-7.8 MeV/n). These two times delimit the temporal period analyzed for each SEP event. Particle fluxes, global spectra of ^1H and ^4He , temporal spectral evolution, and isotopic composition have been determined for all the events in order to obtain observational parameters to classify them as ISEP or GSEP events.

3 Gradual Solar Energetic particle events

November 28, 1996. This SEP event presents composition features typical of GSEP events, with coronal abundances of He ($\text{He}/\text{p}=0.023$) and low abundances of ^3He ($^3\text{He}/^4\text{He}<0.01$). This SEP event is dominated by protons. Although some solar flares have been observed, the SEP event seems to be related to a CME observed at 16:50 UT of 970 km/s with a driven shock arriving at Earth at 00:33 UT on December 1, 1996, that should accelerate particles. The proton and Helium energy spectra have a very similar spectral index, that means a common shock acceleration without preferential acceleration. On December 3, at 00:41 UT, a second shock arrived and a

halo CME was detected at 15:35 UT with 613 km/s; this was observed by LASCO, reaching the SOHO position at 12:00 UT on December 5.

December 24, 1996. The SEP event on December 24, 1996, had a very low abundance of Helium and a low e/p ratio with a hard proton spectrum ($\gamma_p = 2.33$) and no ^3He is found (Figure 1). It had not been observed a shock arriving at the SOHO position while a magnetic cloud in coincidence with the SEP event had been detected. This suggests us to classify this event as GSEP.

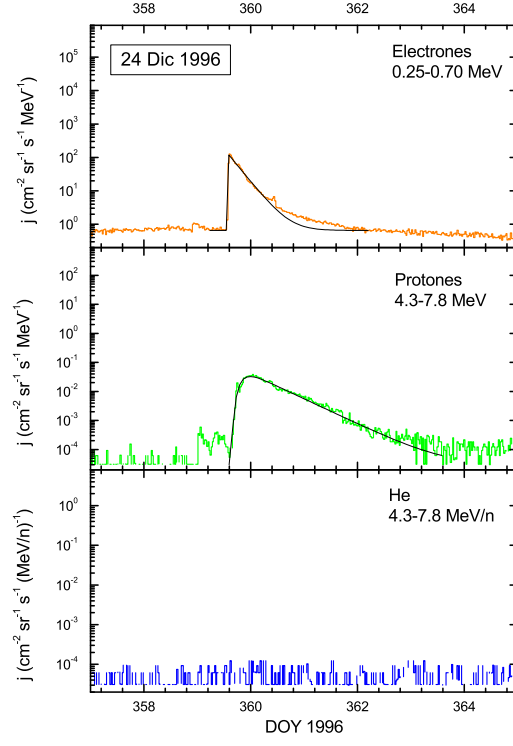


Figure 1: December 24 GSEP event particle temporal profiles.

April 1, 1997. This was another GSEP with low e/p and He/p ratios. It was East connected to the M1.9/1B solar flare on S25E16 location. A hard energy spectra, $\gamma_p = 1.95$ and $\gamma_{He} = 2.46$ was reached with proton acceleration above 25 MeV. No shock was detected and only 296 km/s CME was reported by LASCO. A 3% of Helium was found to be ^3He . Therefore, the event should have been gradual although no shock was observed that produced particle acceleration.

April 7, 1997. This was a typical GSEP event associated with the C6.8/3N solar flare on S30E19, started at 13:50 UT on April 7. A shock, driven a 800 km/s fast CME observed at 14:27 UT by LASCO, arrived at 13:00 UT on November 10 and should have accelerated particles with a very similar spectral index, $\gamma_p = 2.65$ and $\gamma_{He} = 2.85$. Following the shock, the leading edge of the CME happened at 6:00 UT on April 11 up to the trailing edge at 19:00 UT. After the shock passage the spectral index remained constant for protons and Helium. Moreover, low e/p, He/p and $^3He/^4He$ ratios were registered.

September 20, 1997. It was a GSEP event with some features typical of ISEP events. There was a solar flare (0087 B8.01) that may have generated SEP 1 MeV electrons observed at 3:35 UT by EPHIN and 5 MeV protons observed at 13:43 UT. The electron to proton ratios were low. A coronal abundance He/p ratio was found, but more 3He than expected in this kind of events was detected. The passage of a CME with a velocity value between 264.9 km/s and 265.9 km/s was caused by a shock driven at 12:00 UT of DOY264. The spectral index of Helium and protons was very similar. This leads us to the conclusion that the acceleration took place under the same conditions, with no preferential acceleration mechanisms.

September 24, 1997. This was a SEP event with a very hard proton spectra, $\gamma_p = 1.48$. The e/p ratio, low Helium abundances and the absence of 3He lead us to classify this event as GSEP. The problem is that no shock was found that could accelerate SEPs. On September 23 a halo CME could have been the responsible of the SEP generation. The CME had a 760 km/s speed and was observed at 22:02 UT. Thus, when in the NOAA 8088 region a M5.9/1B solar flare started at 2:43 UT on S31E19 location, the CME-driven shock was travelling through the interplanetary medium. This shock should have accelerated particles generating the observed SEP population. The proton spectral index found suggests a very strong shock associated.

November 4, 1997. This GSEP event was related to a X2.1/2B flare on the NOAA 8100 active region at 5:52 UT on S14W33 and a halo CME at 6:10 UT with a driven shock reaching the Earth vicinity. The CME passage occurred during the detection of a SEP on November 6, 1997. The event showed coronal abundances with low e/p=25.9, $^4He/p=0.022$ and $^3He/^4He < 0.01$ ratios, high energy particle generation (i.e. $e^- > 10$ MeV, p and He > 130 MeV/n) (Figure 2). The event was detected at ground level by neutron monitor arrays. The electron, proton and Helium energy spectra showed the same temporal behaviour and values accounting for an unique origin of the SEP. This GSEP event is west correlated showing a fast increase and an exponential decay in the temporal profile. The spectral index $\gamma_p = 2.02$ indicates a strong shock.

November 6, 1997. A second GSEP event was observed in the same NOAA active region, located on S18W63. The event was associated to a new X9.4/2B solar flare started at 11:49 UT on November 6, 1997. A fast CME was detected by LASCO at 12:00 UT on November 6. This CME was very fast and the spectral index of the

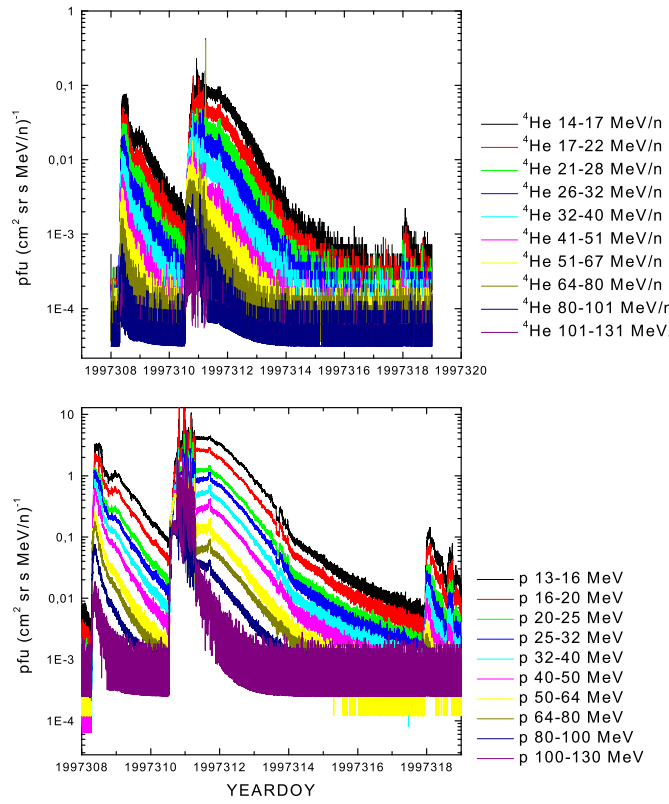


Figure 2: November 1997 LED proton and Helium temporal profiles.

SEP indicates a strong shock associated. Particles of hundredths of MeV/n were observed by LED (Figure 2). The energy spectral indices of protons and Helium are similar indicating, as in the previous event, shock acceleration of coronal material. The temporal profiles corresponded to a well magnetically connected west event. The SEP composition was exactly the same of the previous event; only, it is appreciated more ^3He and electrons than can be explained by a better magnetic connection of the observer that can allow the observation of ^3He and electrons accelerated at the flare region.

April 20, 1998. This was a typical GSEP event with high abundance of electrons and low ^4He and ^3He abundances. The event was associated with a M1.4 solar flare in the NOAA 8194 active region at S43W90 location, detected in X-rays at 9:38 UT

on April 20, 1998. A fast CME was detected by LASCO at 10:07 UT on April 20. The shock arrived at the SOHO position at 16:48 UT of DOY 113. The shock was strong, generating a very hard energy spectrum of SEP ($\gamma_p = 1.16$)

4 Impulsive Solar Energetic particle events

July 9, 1996. This was an ISEP event related to a X2.6/1B flare, the corresponding X-ray emission starting at 09:07 UT on the NOAA active region 7978 located at S10W30 on the solar disk. A CME was observed by LASCO at 12:28 UT with a velocity value of 426 km/s, which did not generate an observable driven shock and it was probably not related to the solar flare because of the temporal separation involved. The SEP event observed was clearly associated with this flare. The SEP event features are clearly from ISEP events, with high abundance of He (He/H=0.139) and electrons (e/H=399.7). No special ^3He acceleration was observed in this event ($^3\text{He}/^4\text{He}=0.01$). The acceleration mechanism was able to accelerate electrons up to 5 MeV and protons and Helium up to 25 MeV/n. From particle transport calculations it arises a path for the particles of 1.16 A.U. into an ambient solar wind of 425 km/s. 1 MeV electrons were observed at 09:21 UT, 44 minutes before expected, and 5 MeV protons arrived at the SOHO position at 10:47 UT, 37 minutes before expectations. This should mean that SEP particles escaped from the flare region about 40 minutes before the X-ray emission that should have been generated by these electrons when they hitted the surrounding plasma.

The differential energy spectra of protons was lightly harder than the transport theoretical predictions, with a 3.13 value and Helium had a harder energy spectrum than protons, showing how the acceleration mechanisms accelerated Helium nuclei more efficiently than protons, and thus energizing Helium easily than protons.

July 12, 1996. The NOAA 7978 active region generated a second flare C4.9/1F at 15:13 UT on July 12, 1996, at S11W72 location on the solar disk. The associated SEP event had similar composition features than that on July 9, although more ^3He was detected in this last event, perhaps because of his better magnetic connection. The energy spectra of protons and electrons were softer than for the July 9 ISEP event. The particles travelled through a 450 km/s solar wind by 1.139 A.U. The arrival time of the 1 MeV electrons is in good correlation with the arrival time but the 5 MeV protons arrived 31 minutes before they were expected.

November 25, 1996. This SEP event was probably associated to a C8.0/1N solar flare starting at 00:19 UT on the SO3E18 position of the NOAA 7999 active region, that was magnetically bad connected with SOHO. This SEP event showed a proton differential energy spectrum as soft as $\gamma = 5.33$, while the Helium spectral index was harder: $\gamma = 3.71$. No ^3He was detected in this SEP event, perhaps because of the very bad magnetic connection involved. Moreover, it was an electron rich

event with an e/p ratio value of 388. From the composition features detected we have classified it as an ISEP event.

There were two correlative SEP events probably related to two solar flares B9.0 in S03E16 and B8.9/SF. The He abundance detected was high, with an energy spectrum becoming harder with time in the first event. Moreover, a low electron to proton ratio was found. No shock or CME was reported.

Although we have classified the first event as an ISEP event, the second one should be a shock accelerated SEP event, that is, a GSEP event.

August 10, 1997. This was the first ^3He -rich event detected by SOHO/EPHIN, with 28% of Helium, that is, with a high He/p=0.284 value. Moreover, a high population of electrons (e/p=658) was detected. The event was associated with a B1.6 solar flare at 17:15 UT on August 10. It was a SEP event with clear features, typical of an ISEP event. 1 MeV electrons began to be detected at 17:45 UT while 5 MeV protons were detected at 20:52 UT.

September 17, 1997. Associated with a M1.0/SF solar flare at the N21W84 location of the NOAA 8084 active region, at 17:45 UT, another ^3He -rich ISEP event was detected by SOHO/EPHIN. It presented a $^3\text{He}/^4\text{He} = 0.18$ ratio and high abundance of electrons, e/p=527, and Helium, He/p=0.155. A halo CME at 20:28 UT was observed by LASCO, driven by a shock. The CME passage seemed not to contribute to the acceleration in the impulsive flare. The SEP travelled through a 350 km/s solar wind plasma, reaching 5 MeV protons to SOHO/EPHIN at 20:52 UT. The event was a joint of two events, and the second one was related to the solar flare on September 8, at 1:39 UT in the 8085 NOAA active region.

November 28, 1997. This event presented the highest ^3He enrichment of all the events analyzed in this work (Figure 4). A 32 % of the Helium population observed was ^3He . This Helium enrichment is also inferred from the He/p=0.144 relative abundance ratio. Neither shock or CME occurrence were associated to the event. The possible source of the SEP was a solar flare X2.6/2B located on the NOAA 8113 active region at N17E63 with a very bad magnetic connection. The observation of an ISEP event with so bad magnetic connection is a rather peculiar fact. It could have been possible that the strength of the flare could have made possible the SEP observation. If this is the situation, probably the $^3\text{He}/^4\text{He}$ ratio should be higher than what has been observed. Another different feature of the ISEP event was the generation of high energy particles, i.e. $e^- > 5$ MeV and proton and He at > 25 MeV/n. Moreover, the energy spectra were harder than usual for ISEP events.

5 Conclusions

Six of the 18 events analyzed have been classified as impulsive: July 9, 1996; July 12, 1996; November 25, 1996; August 10, 1997; September 17, 1997 and November 28,

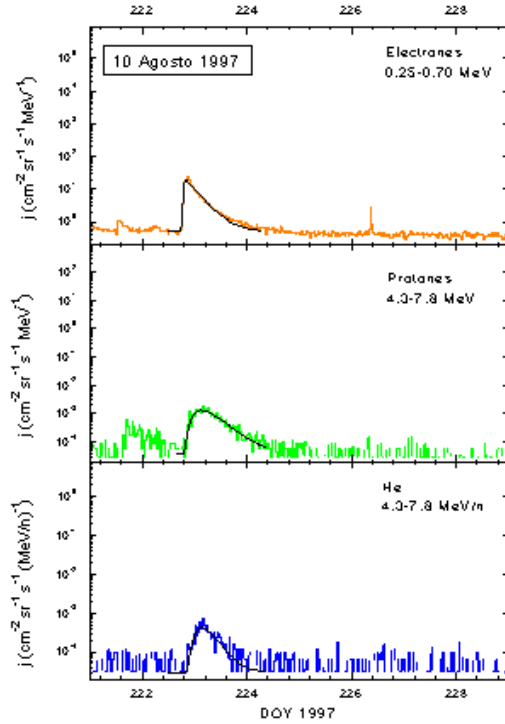


Figure 3: August 10, 1997 ISEP event.

1997. The most relevant observational features found in these events were:

- The event duration is less than 4 days.
- There is no significant proton acceleration beyond 25 MeV.
- High electron contents: in all cases $e(0.25\text{-}4.25 \text{ MeV})/p(4.5\text{-}8.5 \text{ MeV})$ ratio reaches values greater than 100.
- High ${}^4\text{He}$ abundance in all cases ${}^4\text{He}/p(4.5\text{-}8.5 \text{ MeV/n})$ ratio reaches values greater than 0.1.
- Most of the events have ${}^3\text{He}/{}^4\text{He}(4.5\text{-}8.5 \text{ MeV/n})$ ratio greater than 0.01. In some cases this ratio is particularly higher (> 0.1).

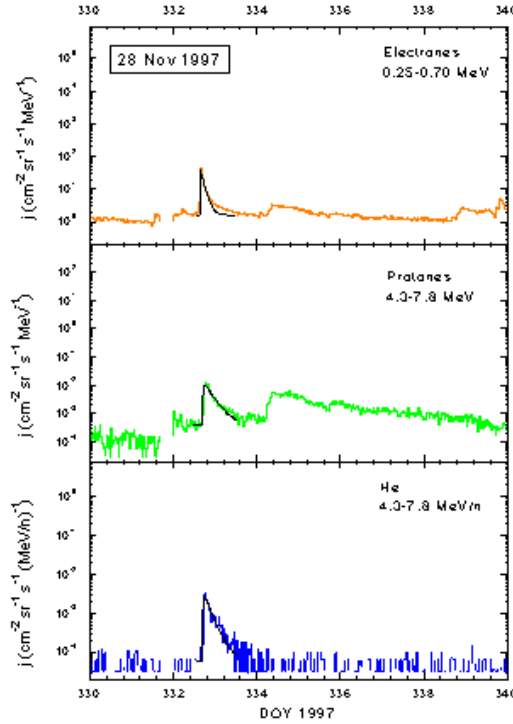


Figure 4: Temporal profiles of the November 28, 1997 ISEP event.

- In general, they have not associated neither CMEs nor interplanetary shock waves.
- Proton and ${}^4\text{He}$ spectra are relatively soft ($\gamma_p < 3.0$), except for the November 28 1997 event.

Seven events have been classified as gradual: November 28 1996, April 1 1997, April 7 1997, September 24 1997, November 4 1997, November 6 1997 and April 20 1998. These events present the following signatures:

- The event duration is greater than five days, exceeding 10 days in many cases.
- Protons are accelerated beyond 25 MeV.
- The electron content is, in general, lower than that of impulsive events. Although, some events have high electron abundance (April 20, 1998).

- ${}^4\text{He}/{}^1\text{H}$ ratio is close to coronal and solar wind abundance (typically between 0.02 and 0.05). In some events slight Helium acceleration is observed and the ratio becomes lower.
- ${}^3\text{He}$ can not be appreciably above background.
- Most of them have associated CMEs, and interplanetary shock waves (although in some cases it has not been possible to find any associated shock). Usually shock passage can be seen as transient hardening of spectral index, followed by long periods of invariant spectrum.
- Proton and ${}^4\text{He}$ spectra are hard ($\gamma_p < 3.0$), except for the November 28 1996 event.

November 25 1996, December 24 1997, and September 20 1997 events have mixed features, although the first one seems to be more impulsive and the last two ones more gradual events. August 13 1996 event shows some peculiarities and it has not been classified.

Acknowledgements: This work has been supported by the Ministerio de Ciencia y Tecnología (MCYT) of Spain, project BXX2000-0784 and the University of Alcalá, project UAH2002/081. SOHO is a project of international cooperation between ESA and NASA.

References

- [1] Mason et al. 1986, ApJ, 303, 849
- [2] Reames, D. V. 1993, Adv. Space Res., 13, 331
- [3] Reames, D. V. et al. 1997, ApJ, 483, 515

THE ROLE OF LABORATORY IN ASTROPHYSICS: LABORATORY EXPERIMENTS ON ICES AND ASTROPHYSICAL APPLICATIONS

MIGUEL ÁNGEL SATORRE, MANUEL DOMINGO, OSCAR GOMIS, RAMÓN LUNA

*Departamento de Física Aplicada, Escuela Politécnica Superior de Alcoy,
Universidad Politécnica de Valencia, E-03801 Alcoy, SPAIN*

M^a ÁNGELES HERNÁNDEZ-FENOLLOSA
*Departamento de Física Aplicada, Universidad Politécnica de Valencia, E-46022
Valencia, SPAIN*

Abstract: Laboratory experiments allow the scientific to simulate some of the conditions where the molecules of astrophysical interest are synthesized, and to study likely mechanisms that could have led to produce them. In a typical astrophysics laboratory many relevant physical properties (optical constants, density, absorbance, etc) can be studied along with their variations induced by temperature changes and UV or ion irradiation. In this work, we want to offer to the reader a general overview of the components of a typical astrophysics laboratory. In addition, we will present some results obtained after carrying out experiments on ion irradiation of ices. These experiments are carbon implantation in water ice and ion irradiation of methane. Finally, some astrophysical applications are shown to highlight the possibilities of this kind of experiments.

1 Introduction

During the last century observational astrophysics has moved from carrying out observations only in the visible region to span a much wider range of the electromagnetic spectrum (from gamma rays to radio). As a matter of fact, infrared (IR) observations have opened the possibility of studying molecules in gas or solid phase [1, 2]. The improvement in the resolution of the instruments and space observatories that avoid the problem of the strong absorption of H₂O and CO₂ present in our atmosphere, have made possible to identify some molecules in solid state phase such as H₂O, CO₂, CO and CH₄. Physical and spectroscopic properties of such molecules have

been studied both by theoretical and experimental ways [3, 4, 5]. In fact, laboratory experiments using in-situ IR spectroscopy are a fundamental tool to understand the space chemistry. In a laboratory, it is possible to simulate adsorption-desorption processes, thermal annealing and UV or ion irradiation [6, 7, 8, 9]. Irradiation plays an important role in the chemical evolution of molecules whose formation reactions demand an energetic contribution [10, 11]. Depending on the scenario of interest a kind or another of radiation becomes relevant. In the inner part of molecular clouds, protected from the external UV field, ion irradiation is supposed to be the dominant mechanism. Our Solar System presents also scenarios where ion irradiation is dominant as the icy Galilean satellites immersed into the intense magnetosphere of Jupiter [12].

In the next sections we will show some results obtained after carrying out experiments on ion irradiation of ices. With this objective in mind, some experiments carried out in the “Laboratorio di Astrofisica Sperimentale di Catania (LAsP)” Italy, will be discussed. In section 2 the experimental setup will be described. Ion irradiation experiments will be presented in section 3 showing that ion irradiation induces the modification of the physical and chemical properties of the ices. Finally, section 4 shows some astrophysical applications based in part on the experiments presented in section 3.

2 Experimental setup

The basic components of an astrophysics laboratory are a vacuum and low temperature system, an analysis technique, and for ion irradiation experiments, an ion gun. Figure 1 shows a block diagram of the experimental apparatus present in the LAsP where all the experiments shown below have been carried out. The main component is a vacuum chamber ($P \sim 10^{-7}$ mbar). Inside the chamber is located a cold finger whose temperature ranges between 10 and 300 K. The working temperature is obtained from the balance of two factors. First of all, there is a closed-cycle He cryostat that is used to cool the substrate down to 10 K. Subsequently, a stationary temperature is kept by mean a resistor. The vacuum chamber has three windows. Two of them are made of KBr and are faced one to each other. This setup allows us to obtain the transmittance spectrum with a FTIR spectrometer Bruker Equinox-55, with a resolution of 1 cm^{-1} . The third window, perpendicular to the previous ones, let us to irradiate the sample. The surface where the ice is deposited onto, forms 45° with both the ion and the infrared beams. In this way the sample can be analyzed before, during and after irradiation. Gases or mixtures of the molecules under study are prepared in a pre-chamber in a proportion estimated from their partial pressures. The gases come into the chamber through a needle valve that regulates the flow of the gas. The molecules accrete onto the substrate (usually a specular monocrystalline

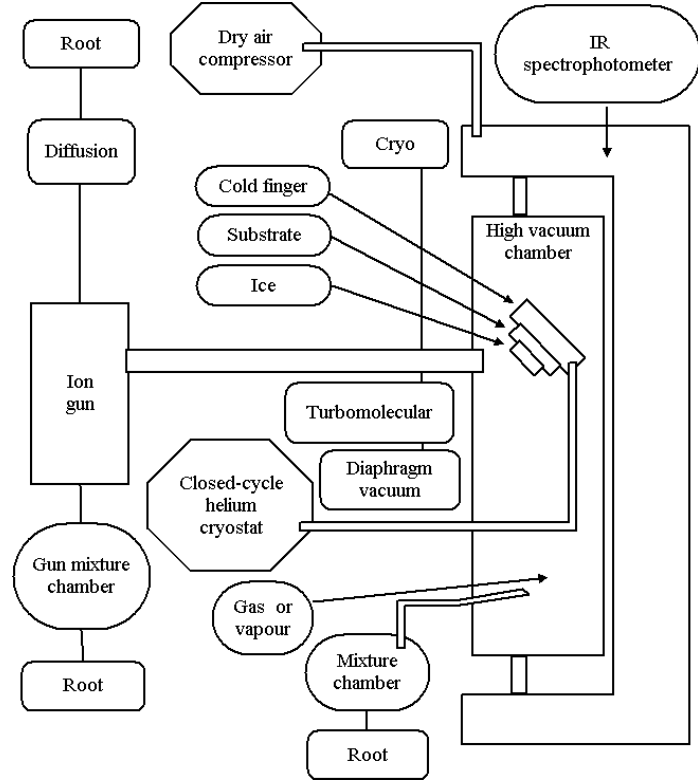


Figure 1: Block diagram of the experimental apparatus present at the Catania Laboratory of Astrophysics.

silicon wafer) put in thermal contact with the cold finger. The thickness of the sample is monitored by interferometry using an He-Ne laser beam. Since not all the molecules have the same sticking coefficient, the final composition of the ice is analyzed by the IR spectrometer. The ice can be irradiated during and/or after deposition, with an ion previously accelerated with a 30 kV potential. Deflection plates placed along the ions path let us irradiate the sample homogeneously. The ion flux is controlled in order to avoid the macroscopic heating of the sample. The effect of the ion beam on the ice is monitored continuously with the spectrometer. It is also possible to carry out Temperature Programmed Desorption (TPD) experiments which let us study the sublimation temperature of the deposited and produced molecules. For further details on the experimental setup see [13, 14].

The experiments here described try to simulate the energetic processes suffered by the ices in different astrophysical scenarios. Depending on the scenario we are interested in, composition, thickness and temperature of the ices, and energy and kind of ion can vary vastly. Let's take as an example the ices present in the dense interstellar medium (ISM) and on the surface of the Jovian satellite Europa. In the first case the thickness of the ice is about tenths of microns while in Europa is more than nine orders of magnitude greater. As far as the ion flux is concerned, in the Jupiter satellite is around six orders of magnitude bigger than in the ISM. On the contrary, the energy of the most abundant ions in Europa is at least one order of magnitude smaller than those in the ISM. The experiments that better reproduce the dense ISM are called *thin film experiments* because the impinging ions have enough energy to pass throughout the sample. On the other hand, experiments that try to reproduce the situation found in a satellite surface or a comet are called *thick film experiments*. In this case, the ion has not enough energy to pass throughout the ice and is implanted into the target [15]. In this situation if the implanted ion is reactive (H^+ , C^+ , O^+ , etc) the new molecules formed could contain the impinging ion [16].

3 Irradiation experiments

In this section some effects of ion irradiation of ices will be shown, in particular the chemical changes induced by ion irradiation.

3.1 Introduction

When a particular ion penetrates inside a material interacts with its atoms loosing energy as it travels through it. The interaction between the ion and the ice can be divided in two different types. The first one is electronic (excitations and ionizations) and the second one is nuclear (breaking of bonds and atomic displacements). These two mechanisms are also called inelastic and elastic respectively. For a detailed description of these processes we refer the reader to Johnson's book [17]. As said above, as the ion passes through the sample several processes are induced such as local increasing of temperature, formation of excited species and ions, etc. Local increasing of temperature is an important effect that must be taking into account when carrying out experiments of astrophysical interest. In space, the number of ions impinging on a surface usually is not enough to produce the macroscopic heating of the same. On the contrary, in laboratory one must be sure that the used ion flux is low enough to avoid heating up macroscopically the sample and therefore to produce some unwanted thermal processes.

The effects induced after ion irradiation of ices can be summarized as follows:

- Physical and chemical modifications of the target are produced including the formation of new species.
- In the case of an implantation experiment (*thick film*), if the used ion is reactive, the possibility exists that the new molecules formed contain the projectile.
- Material is eroded from the target (sputtering).

3.2 Implantation of $^{13}\text{C}^+$ in water ice

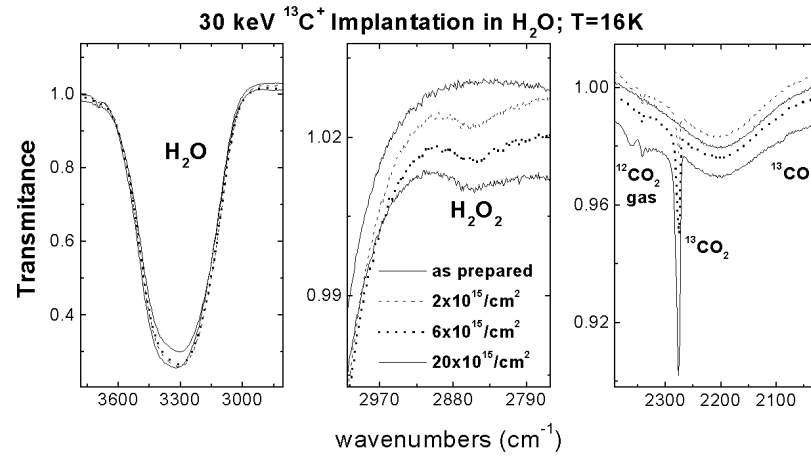


Figure 2: H_2O ice spectra as deposited and after implantation of 30 keV of $^{13}\text{C}^+$. From left to right, the three spectral regions correspond to H_2O , H_2O_2 , and $^{13}\text{CO}_2$ and ^{13}CO bands respectively [10].

Figure 2 shows the results obtained after implantation of $^{13}\text{C}^+$ in water ice at a temperature of 16 K. In the figure are shown three different spectral regions. In the first one it is shown the $3.03 \mu\text{m}$ (3300 cm^{-1}) water ice band and how its area decreases as ion fluence increases. The decreasing in the water ice band intensity is due to two different effects. The first one is the water ice sputtering. The second one is that

part of the radicals produced by ion irradiation can react to produce new molecules. The second region of the spectrum testifies for the appearance of a new species. In this particular case the feature centered at $3.50\ \mu\text{m}$ ($2850\ \text{cm}^{-1}$) is attributed to the hydrogen peroxide molecule. In this way we present a case where ion irradiation has produced a molecule originally not present in the sample. Finally, the third region shows that, after the implantation of $30\ \text{keV}$ of $^{13}\text{C}^+$, $^{13}\text{CO}_2$ is detected. In this particular case, we have found a molecule originally not present that contains the projectile. As can be seen from the figure, we have also detected for the highest ion fluence ^{13}CO . Taking into account the band intensities and the integrated absorbances of both $^{13}\text{CO}_2$ and ^{13}CO , we have deduced that ^{13}CO has not been produced directly by ion implantation of $^{13}\text{C}^+$ but it comes from the destruction of $^{13}\text{CO}_2$. To conclude this section, we would like to point out that ion implantation into an ice not always produces species containing the impinging ion. As an example, oxygen implantation in frozen methane does not produce neither CO_2 nor CO [18].

3.3 Ion Irradiation of CH_4 ice

An important kind of compounds suggested to be present in different astrophysical scenarios are organic molecules. The study of the carbon chemistry has a particular interest because of its possible implication in the origin of life. In fact, the study of the formation of more complex organic compounds such as polymers from elemental molecules for instance CH_4 turns out to be very attractive [19].

Figure 3 shows the results obtained after irradiating with $60\ \text{keV}$ of Ar^{++} ions on pure methane ice at $12\ \text{K}$ [11]. The bottom part of the figure shows the spectrum of CH_4 deposited at $12\ \text{K}$ in two different spectral regions. In the upper part of the figure the same spectral regions are shown after the CH_4 has been irradiated. In this experiment the thickness of the CH_4 ice is about $4\ \mu\text{m}$. The amount of energy deposited in average after irradiation ($7\ \text{eV}/16\ \text{amu}$), has been calculated in eV per 16 atomic mass units ($\text{eV}/16\text{amu}$). This is a convenient way of expressing the dose that allows to compare results obtained by different authors.

From figure 3 can be observed the appearance of many new IR bands after irradiation. These features mainly correspond to new synthesized organic molecules such as acetylene, ethene, ethane and propane. There are also some weak bands that we have not been able to assign to any particular species. These latter bands could be attributed to a carbonaceous residue of unknown composition. In the laboratory, it has been checked that this residue is refractory. In fact, when the temperature of the irradiated sample is increased up to room temperature all the ices sublime and the only compound that remains onto the substrate is the residue. This stability at room temperature allows to analyze it with other techniques such as UV-Vis spectroscopy, Raman spectroscopy and photoluminescence. We have shown a general result that can be summarized as saying that ion irradiation of simple organic molecules produces

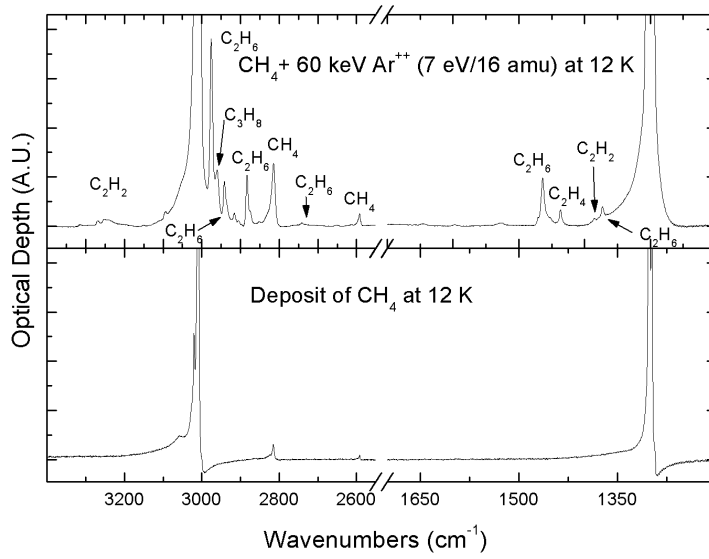


Figure 3: Spectra of methane ice as deposited at 12 K (bottom) and after irradiation with 60 keV Ar⁺⁺ ions (top) in two different spectral regions.

a progressive carbonization (dehydrogenation) on the original ices.

There are some interesting experiments that can be carried out after irradiation of an ice with ions. By using TPD the sublimation dependence of an ice can be studied. It is known that ices sublimate at different temperatures depending on the matrix the molecule is embedded in. In the case the ice or mixture has been previously irradiated the variation of the sublimation temperature can be even greater.

4 Conclusions and astrophysical applications

The effects produced after ion irradiation of ices can be summarized as follows:

- Irradiation destroys sample molecules producing radicals that can then react to form new species.
- In the case a reactive ion is implanted into the ice, the possibility exists that it could form part of the new synthesized molecules.

- Ion irradiation of organic molecules produces a progressive dehydrogenation of the sample. After irradiation a residue is produced. This residue is stable at room temperature.
- Chemical and physical changes due to ion irradiation increase in some cases the sublimation temperature of the ices. These variations depend on the ice mixture, the used ion and on the irradiation dose.

To conclude we would like to give some examples of astrophysical scenarios where ion irradiation experiments have interest.

The first scenario is the Jupiter satellite Europa. NIMS data from the Galileo spacecraft have revealed a feature in the spectrum of Europa's surface that has been attributed to the molecule of H_2O_2 . Recent experiments on ion irradiation of water ice have shown that hydrogen peroxide may be produced by radiolysis even if water ice is the only component found on the surface of satellite Europa [12]. The high efficiency for the production of hydrogen peroxide measured for $^{13}\text{C}^+$ and for other heavy ions, specially for oxygen, opens also the possibility of a patchy distribution on the surface of the satellite [12]. This result could be useful to support the suggested possibility of a radiation-driven ecosystem on Europa based on the availability of organic molecules and oxidants such as hydrogen peroxide [20].

There are several places in the Solar System such as Pluto and Triton where CH_4 ice is present [4] and suffers from ion irradiation. The chemistry induced by low energy ions on the uppermost layers of a surface is considered to be quite equivalent to that induced by more energetic cosmic ions at the end of their travel into thick solid bodies [15]. As an example, it has been evaluated that a fraction of 30 per cent of original ice can be altered at a depth of about 10 m within a cometary surface [15]. Pluto is in fact exposed to cosmic ions [21] and as a consequence its surface is altered to a depth of several meters during its total lifetime. On the other hand, low energy ions, which have higher fluxes, alter the outer surface layers of the planet in a much shorter timescale. On Triton the effects could be even more relevant because the satellite can also be bombarded by ions present in the magnetosphere of Neptune.

Acknowledgements: We thank G. Strazzulla, F. Spinella, G. Baratta, M. E. Palumbo, and G. Leto for their support and help at Catania Astrophysics Laboratory. Without their help this work would have not been possible. This work was partially supported by the “Ministerio de Ciencia y Tecnología, Programa Nacional de Astronomía y Astrofísica AYA2001-2385” and Universidad Politécnica de Valencia under project “Estancias de PDI de la UPV en Centros de Investigación de prestigio”.

References

- [1] Goicoechea, J. R., Cernicharo, J. 2001, The Promise of the Herschel Space Observatory. Eds. G. L. Pilbratt, J. Cernicharo, A. M. Heras, T. Prusti and R. Harris. ESA-SP, 460, 413
- [2] Boogert A. C. A., Ehrenfreund, P. 2004, Insterstellar ices, Astrophysics of dust, ASP Conference Series
- [3] Baratta, G. A., Palumbo, M. E. 1998, J. Optical Society of America A, 15, 3076
- [4] Grundy, W. M. et al. 2002, Icarus, 155, 486
- [5] Baragiola R.A. 2003, Planet. Space Sci., 51, 953
- [6] Kimmel, G. A. et al. 2001, J. Chem. Phys., 114, 5295
- [7] Bahr, D. A. et al. 2003, J. Geophys. Res., 106, 33285
- [8] Leto, G., Baratta, G. A. 2003, A&A, 397, 7 (2003).
- [9] Muñoz-Caro, G. M. et al. 2002, Nature, 416, 403
- [10] Strazzulla, G. et al. 2003, Icarus, 164, 163
- [11] Baratta, G. A. et al. 2003, NIMB, 209, 283
- [12] Gomis, O. et al. 2004, Planet. Space Sci., 52, 371
- [13] Domingo, M. 2003, PhD, Universidad Politécnica de Valencia, Spain
- [14] Gomis, O. 2003, PhD, Universidad Politécnica de Valencia, Spain
- [15] Strazzulla, G., Johnson, R.E. 1991, Comets in the Post-Halley Era, R. Newburn Jr., M. Neugebauer, J. Rahe (Eds.), Kluwer, Dordrecht, 243
- [16] Strazzulla, G. et al. 1996, NIMB, 116, 289
- [17] Johnson, R. E. 1990, Energetic Charged Particle Interactions with Atmospheres and Surfaces. Springer-Verlag, Heidelberg
- [18] Palumbo, M. E. 1997, Adv. Space Res., 20, 1637
- [19] Strazzulla, G. et al. 2002, NIMB, 191, 714
- [20] Chyba, C. F. 2000, Nature, 403, 381
- [21] Johnson R. E. 1989, Geophys. Res. Letters, 16, 1233

ON THE FUTURE OF ULTRAVIOLET (UV) ASTRONOMY

ANA I. GÓMEZ DE CASTRO

*Instituto de Astronomía y Geodesia (Consejo Superior de Investigaciones Científicas
- Universidad Complutense de Madrid)*

*Facultad de Ciencias Matemáticas, Universidad Complutense de Madrid, E-28040
Madrid, SPAIN*

WILLEM WAMSTEKER

VILSPA-European Space Agency, P.O. Box 50727, E-28080 Madrid, SPAIN

Abstract: The situation of UV astronomy: current facilities, future projects and the great science to be done is briefly outlined.

1 Introduction

The UV range supplies a richness of experimental data which is unmatched by any other domain for the study of hot plasma with temperatures in between 10^4 K and 10^5 K; the high excitation lines and the resonance lines of the most abundant species in the Universe are observed in UV. Plasma at these temperatures is observed in all astrophysical environments extending over hot stars, cool stars and planetary atmospheres, gaseous nebulae, the warm and hot components of the ISM, circumstellar material, the close environment of black holes of all masses from X-Ray Binaries to Nuclei of Galaxies, accretion disks, and the intergalactic medium. In addition, the electronic transitions of the most abundant molecules, such as H₂, are observed in this range which is also the most sensitive to the presence of large molecules such as the PAHs. In this brief contribution, the situation of UV astronomy is outlined.

2 The UV facilities

There are three major astronomical facilities working in the UV range: the *Hubble Space Telescope* (HST), the *Galaxy Evolution Explorer* (GALEX) and *Far Ultraviolet Spectroscopic Explorer* (FUSE). HST and FUSE are observatory missions while GALEX is mainly devoted to carry out the first all-sky UV survey. Let us summarize the main characteristics of the UV instrumentation in these missions (see also Table 1 for a summary).

2.1 HST (1990-...)

(URL:www.stsci.edu/hst)

HST is a 2.4 m telescope which was deployed in low-Earth orbit on 1990; it is a cooperative project of ESA and NASA. HST is a general purpose telescope with a core program: the accurate determination of the Hubble constant, through the observations of Cepheid variable stars in the galaxies of the Local Group.

The first generation instruments with UV capabilities were the *High Speed Photometer*, the *Goddard High Resolution Spectrograph* and the *Faint Object Spectrograph*. Currently, the *The Wide Field and Planetary Camera 2* (WFPC2), the *Advanced Camera for Surveys* (ACS) and the *Space Telescope Imaging Spectrograph* (STIS) provide access to the UV range both for imaging and spectroscopic work. The WFPC2 is a 2-dimensional imaging photometer which covers the spectral range between approximately 115 nm and 1050 nm. It simultaneously images a 150" x 150" "L"-shaped region with a spatial sample of 0.1 arcsec per sample and a smaller 34" x 34" square field with 0.046 arcsec per pixel. There are 8 UV filters with central wavelength between 130 nm and 333 nm. However, the presence of significant red leaks in the UV filters, together with the much greater sensitivity and wavelength coverage in the red part of the spectrum for CCD's, makes calibration of the UV observations difficult. As a consequence, the prime instruments for UV astronomers are the ACS and the STIS.

The ACS

The **ACS** is a third generation HST instrument and includes two channels suitable for UV imaging:

- a High Resolution Channel (HRC), with a field of view of 26" x 29" covering the range from 200 to 1100 nm and a plate-scale of 0.027 arcsec/pixel. There are three broad band ($\text{FWHM} \simeq 400 \text{ \AA}$) UV filters available centered at 220 nm, 250 nm and 330 nm.
- a Solar Blind Channel (SBC), with a field of view of 31" x 35", spanning the range from 115 to 170 nm and a plate-scale of 0.032 arcsec/pixel.
- a Solar Blind Channel (SBC), with a field of view of 31" x 35", spanning the range from 115 to 170 nm and a plate-scale of 0.032 arcsec/pixel.

There is also a low resolution (grism) spectroscopic mode available with $R \sim 100$.

The STIS

STIS is the prime ultraviolet instrument on-board the HST. It can be used for imaging, high-spatial resolution long-slit spectroscopy and high spectral resolution (echelle) spectroscopy.

- High resolution, long-slit spectroscopy is available in the 115-310 nm with low and medium spectral resolutions (~ 1000 and $\sim 15,000$, respectively). Slits of 52" length and widths between 0."05 and 2" are available.
- High spectral resolution echelle spectroscopy is available in the 115-315 nm range with resolutions $\sim 50,000$ and $\sim 114,000$.
- When STIS is used in imaging mode in the UV, the field of view is 25"x25" and the plate scale 0.0246 arcsec per pixel. Few filters are available: three narrow band filters with FWHM between 7 nm and 8.5 nm, centered in the L α (121.6 nm), the CIII] (190.9 nm) and the MgII (280 nm) lines, plus some continuum filters with FWHM = 35 nm, centered at 270 nm and 182 nm, and two passband filters.

The wider field of view, the higher sensitivity and the greater selection of filters makes of the ACS the preferred instrument for UV imaging. However, STIS provides higher S/N than the SBC in the far UV and has some narrow band filters which are not available for the ACS.

2.2 FUSE (1999-...)

(URL:fuse.pha.jhu.edu)

FUSE is a NASA-CNES-CSA supported astronomy mission that was launched on June 24, 1999, to explore the Universe using the technique of high-resolution spectroscopy in the far-ultraviolet spectral region. The Johns Hopkins University has the lead role in the mission, in collaboration with the University of Colorado at Boulder and the University of California at Berkeley.

FUSE obtains spectra from about 90.5 nm to 118.7 nm. The true resolution has been difficult to assess on-orbit (see URL: fuse.pha.jhu.edu/support/guide/). The spectral resolving power has been estimated to be $R = 20,000 \pm 2000$, and is nearly flat across the entire bandpass.

FUSE was designed with two primary objectives in mind: to study the physics of the hot component of the Interstellar Medium (ISM) and to estimate how much deuterium has been destroyed since the Big Bang.

2.3 GALEX (2003-2005)

(URL: www.srl.caltech.edu/galextech/)

GALEX is a 50 cm telescope, e.g. a small explorer class mission that is part of NASA's Structure and Evolution of the Universe theme. GALEX will perform both imaging and low resolution spectroscopy, conducting several types of surveys. GALEX will complement the capabilities of space observatories like HST (GALEX has a wide field of view), and the UV spectroscopic capabilities of FUSE, both currently in orbit.

GALEX is the first mission to conduct an all-sky survey in the ultraviolet with a significant sensitivity. Two imaging surveys in a far UV band (135-180 nm) and in a near UV band (180-300 nm) with 3"-5" spatial resolution will be carried out to 20-21 mag (AB). In addition, a spectroscopic survey in the 135 nm-300 nm band, with spectral resolution ~ 100 will be done over 100 square degrees. Detailed information about all GALEX surveys may be found in the GALEX web page (see above).

The scientific objective of GALEX is to characterize the UV properties of the galaxies to study their star formation history over the redshift range $0 < z < 2$.

3 The next generation of UV astronomy

There are two main facilities under study and/or development at this moment: the *International Virtual Observatory* (IVO) and the *World Space Observatory - Ultraviolet* (WSO/UV). In addition to these a limited sky survey specifically oriented to interstellar absorption (TAUVEX) will be launched in 2005 under a collaboration between ISA and ISRO.

3.1 The IVO

(URL:www.ivoa.net)

There are many projects on-going world-wide to create the so-called *Virtual Observatories*, which basically are computational tools that allow consulting, retrieving and processing the information stored in the Astronomical Archives (data from ground-based or space-based observatories, catalogues, etc...) for a given scientific purpose. The IVO alliance tries to coordinate this joint effort world-wide since it is necessary to define common standards for the scientific content of the data (astrometric, photometric, spectrophotometric, polarimetric standards) and for the data format. In addition, communication technologies ought to be common to all the archives to guarantee the required interoperability; a *rigourous* definition of the data is instrumental for the meaningful *scientific* operation of the IVO.

The largest archive of UV data is the Multimission Archive at the Space Telescope (MAST). It provides access to the HST, FUSE and GALEX archives as well as to the

Facility (lifetime)	Type of Instrument	Spectral Range (nm)	Field of view (arcsec)	Spectral Resolution R	Spatial Resolution
HST (1990-...)	Im-ACS(HRC)	200-1100	26x29	Broad band filters (FWHM \sim 40nm)	0. ^{''} 027 pix ⁻¹
	Im-ACS(SBC)	115-170	31x35		0. ^{''} 032 pix ⁻¹
	Im-STIS	115-~350	25x25	Ly α , CIII], MgII Continuum filters	0. ^{''} 0246 pix ⁻¹
	Sp-ACS	115-390	Grism	100	
	Sp-STIS	115-310	Long-Slit (52 $''$)	\sim 15000 \sim 1000	0. ^{''} 03 pix ⁻¹
		115-315	(echelle)	140000 \sim 50000	
FUSE (1999-...)	Sp	90.5-118.7		20000 \pm 2000	
GALEX (2003-2005)	Im	135-300	All-sky	Two broad bands: NUV(180-300) and FUV(135-180)	3 $''$ -5 $''$
	Sp	135-300	(grism)	100	

Table 1: The main UV facilities working in 2003. Im: Imaging; Sp: Spectroscopy

first UV missions: Copernicus and the International Ultraviolet Explorer (IUE). Also, the data from many small missions are included (see Table 2). The MAST provides some tools for cross consultation of all the UV archives. Also cross-consultation with the ROSAT (X-ray) archive and some on-line catalogues is implemented.

IVO will allow the cross-consultation of the UV archives with the rest of the archives spanning the whole spectral range. It will also provide tools to produce directly scientific results as the Spectral Energy Distributions (SED), spectral line identifications and flux determinations or variability studies.

3.2 The WSO/UV

(URL:wso.vilspa.esa.es)

The WSO/UV is a 1.7 m telescope mainly designed to be a spectroscopy mission devoted to high resolution (echelle) spectroscopy (R=50,000) in the 110-340 nm spec-

Mission	Type of Observations	Number of Observations	Spectral Range (nm)	Main Characteristics
IUE	Sp	>10,4000	120-335	Aprox. 10,000 sources
Copernicus	Sp		90-156 & 165-315	551 sources, mostly bright stars
EUVE	Sp		7-76	300 sources, mostly Galactic
HUT	Spphot	491	91.2-185	Aprox 300 sources.
UIT	Im	1579	120-330	259 sources
WUPPE	Sp&Pol	467	140-330	169 sources
BEFS/ORPHEUS	Sp		90-190	75 objects
IMAPS/ORPHEUS	Sp	600	95-115	10 hot stars
TUES/ORPHEUS	Sp	239	90-140	62 targets

Table 2: UV data in the MAST archive (from URL:archive.stsci.edu). Sp: Spectroscopy; Spphot: Spectrophotometry; Im: Imaging; Pol: Polarimetry

tral range. It will also include optical and UV imaging capabilities (see Table 3); long-slit spectroscopic capabilities are under study. The optical design of WSO/UV is optimized to guarantee a maximum light throughput (a high effective area) so, although WSO/UV is slightly smaller than HST, it will be an order of magnitude more sensitive than HST/STIS (at R=50,000). Another important feature for the science to be carried out with WSO/UV is the orbit; it will be placed in the Lagrangian point L2 allowing spectroscopic monitoring which is heavily demanded by the astronomical community and difficult to carry out with the HST due to its low Earth orbit. The mission will have a core program focussed in two key problems for modern astrophysics: the formation of stars and planetary systems and the cosmological and chemical evolution of the interstellar and intergalactic medium up to $z \simeq 2$.

The World Space Observatory Project represents a new space mission concept, since it has grown out directly of the needs of a world wide distributed Astronomical community which demands access to the UV range after the HST era. Basic scientific requirements are improved sensitivity for high spectroscopy and hours-to-days monitoring capabilities. WSO/UV will allow to make full profit of the legacy of the previous UV missions and, especially of the GALEX, first all-sky UV survey.

As WSO/UV has been driven by the needs of scientists from many different countries, a new implementation model was needed to bring the World Space Observatory

Instrument and Type	Spectral Range (nm)	Field of view (arcsec)	Spectral Resolution R	Spatial Resolution
HRI Im	115-310	60	Narrow Band Filters Ly α ,CIV,CIII,MgII (and few more to determine)	0. $''$ 03 pix $^{-1}$
HSI Im	115-310	300	Broad Band Filters for surveys (to determine)	0. $''$ 15
OI Im	360-800	240	(to determine)	0. $''$ 12
HIRDES Sp	102.8-310.0		50,000	

Table 3: The main characteristics of WSO/UV. Im: Imaging; Sp: Spectroscopy

to reality. The developments needed to make the anticipated launch of WSO/UV possible in 2008 are led by an open international committee of scientists the World Space Observatory Implementation Committee (WIC).

4 A science case for the future

The richness of the UV range is instrumental for the study of all the astronomical plasmas from few thousands to several hundred thousand *Kelvin*. As it is not realistic to attempt to cover all the possible astrophysics in this brief contribution, we shall focuss on two key problems: the physics of the formation of stars and planetary systems, and the cosmological and chemical evolution of the intergalactic medium up to $z \simeq 2$, as an example.

4.1 The physics of the formation of stars and planetary systems

The formation of stars is an accretion process; the gravitational energy of the infalling material is stored in accretion disks which transforms it into radiation, thermal energy and mass ejection (winds). The Magneto-Rotational Instability (MRI) is the source of turbulence in the disk leading to accretion and outflow. A new paradigm

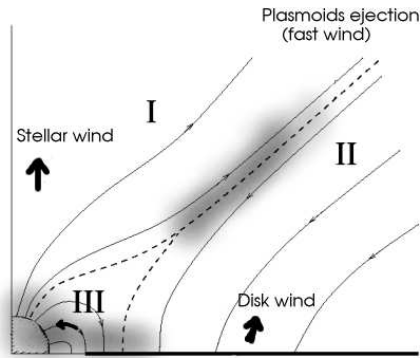
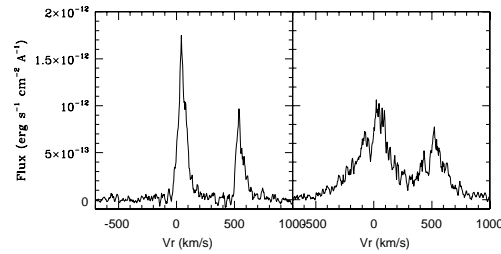


Figure 1:

a) The reference model as described in [9] and adapted from Lovelace et al 1995. Magnetic field lines are represented with the corresponding field orientation.



b) Contribution to the AB Dor C IV[uv1] profile from a normal flare (left) and a transient feature probably associated with a CIR (right). Both events lasted few kiloseconds. The left profile was observed in three events more during the short monitoring time while the last profile was observed only once.

Notice the presence of a narrow absorption and the very broad line wings in the right panel profile (see [3] for more details).

is emerging in the physics of star formation which properly addresses the relevance of the magnetic interaction between the stellar magnetic field and the protoplanetary disk. The interaction disk-magnetosphere basically transforms angular momentum (differential rotation) into toroidal plasmoids which are ejected from the system. Basically all models can be fitted into the basic configuration sketched in Figure 1a; there is a current sheet that separates two distinct regions: an inner *stellar outflow* and an external *disk outflow*. Magnetic flux dissipation is expected to be produced in the current layer leading to plasmoids ejections, as well as to the injection of high energy particles (cosmic rays) in the environment leading to generation of X-rays and ultraviolet radiation. The phenomenon is non-stationary and controlled by two different temporal scales: the rotation period and the magnetic field diffusion time scale. Stellar rotation is a well known parameter which controls the opening of the field lines towards high latitudes however, plasmoids ejection is controlled by *field diffusion* which is poorly determined (see e.g. [7]). In addition, there is direct evidence of infalling gas; the observed velocities are of some few hundredths km s^{-1} , e.g. compatible with free-fall from some few stellar radii. The existence of funnel flows connecting the stellar photosphere with the inner accretion disk has been proposed. The infalling material is expected to release its gravitational energy in the shock at the stellar surface producing hot spots on it.

This outlined paradigm requires to be worked out extensively since many fundamental issues are left opened, for instance,

1. The development of the MRI depends on the effective coupling with the disk, e.g. on the relative density of free charges. The inner region of disks is sufficiently ionized by the stellar X-rays field, but the outer regions are more problematic.
2. There is a timing problem. If we trust that T Tauri systems are alike our early solar system, the meteoric evidence set-up an upper limit of some few 10^7 yr for planetesimal differentiation ([11]). Accretion and outflow are observed in many T Tauri stars 10^7 yr old. How does MRI co-exist with planetesimal formation?.
3. Numerical simulations show that the star-disk-outflow system is self-regulating when various initial disk densities, stellar dipolar field strengths and primordial field associated with the disk are tested ([6]) although strong stellar magnetic fields may disrupt the inner parts of the accretion disk temporarily.
4. The coexistence of several funnel flows is required to explain the correlation between magnetospheric line emission and the accretion rate, however, it is unclear how such a magnetic configuration may be stable and survive in a very active environment.
5. Young stars are very active; rapid variations in the X-ray flux are often detected. However, the source of the X-rays variability is poorly known. In solar and space

plasmas, it is recognized that such rapid variations may be produced by, at least, three very different physical processes: flares, e.g. magnetic reconnection events associated with the solar magnetic activity), corotating interaction regions or CIRs (shock fronts formed in the interaction between the slow and the fast component of the solar wind) and coronal mass ejections. In the star formation context, we often interpret such rapid variations as associated with magnetic reconnection events. However, at least in AB Dor, UV spectroscopy has shown to be able to distinguish between bona-fidae flares and CIRs (see Figure 1b and [3]). The monitoring was done with the *Hubble Space Telescope* and the old Goddard High Resolution Spectrograph. AB Dor is a 30 Myr old star, in many senses fairly similar to some Weak line T-Tauri Stars as HD283572.

The only way to get into the scale of the structures represented in Fig 1a (from a fraction of R_* to some $10 R_*$) is by means of high resolution spectroscopy ($R \geq 30,000$) of warm plasma (from 10,000 to 100,00 K); e.g. high sensitivity, high resolution ultraviolet spectroscopy (see e.g. [4]).

In addition, UV monitorings are instrumental for the study of this highly non-stationary environment phenomena, as well, as to map the structure of the funnel flows. They may also allow us to understand better the physics of cool active stars in connection with the PMS evolution. The existence of large scale magnetic structures, sling-shot prominences, has been proposed to explain the detection of material corotating at some few stellar radii observed in many, rapidly rotating, cool stars (see [2]). In this sense, spectroscopic UV monitorings open the door to the study of the interaction of the stellar wind with protoplanetary disks in the early phases when planetesimals are differentiated and planets form through the formation of corotating interaction regions. Moreover, UV spectroscopy provides fundamental clues on the radiative field in this epoch and its role in the chemical evolution of disk at the time when planets are built. The understanding of PMS stars will allow us to understand better substellar objects.

4.2 The cosmological and chemical evolution of the intergalactic medium up to $z \simeq 2$

Most of the volume of the Universe, and 80% of the cosmic time, is at redshifts less than $z \leq 2$. Studies with 10m class ground-based telescopes have shown that in the first 20% of the Universe metal abundances are of order 1/100th Solar, and suggest a marginally significant- increase of metallicity by a factor of ~ 2 with time, for the redshift range $3.5 < z < 4$ ([8]). There remains however, a factor of at least 50-100 between the observed [Fe/H] at $z = 2$ and the current epoch is of prime importance. The limited information on this, combined with the essentially total absence of reliable information on the metallicity evolution between $0 < z < 2$, leaves a critical gap in the

information needed for the discrimination of the evolutionary models of the Universe (e.g. [1]).

The basic enrichment of the primary material from which the current star formation is drawn is a multifaceted problem in which the IGM plays an essential role. As the formation of heavy elements is, in all current cosmological models, driven solely by processes associated with the life-and-death cycles of stars, and as most star formation takes place in galaxies, the cycling of metals through the Universe must take place on scales which easily exceed the size of galaxies. The IGM contains the material from which the current galaxies have been formed; the recycling of this material after the galaxy and star formation during the period covered by the redshift range from $0 < z < 2$, presents the critical link between our current Universe and the epoch of structure formation.

As the validity of the Hubble classification diagram for galaxies breaks down at $z = 1$ ([10]), it is clear that the answer to the question of the connection between these first epochs of structure formation and the current state of the local Universe can only be addressed in the epochs between $0.2 < z < 1.7$. Only very limited studies have been performed in order to clarify the nature of the metallicity of the IGM at redshifts $z < 3$. [5] (loc.cit.) showed that the ionization distribution in the IGM is an essential parameter in the abundance determination of this diffuse material. The accessibility of observing at high resolution ($R=50,000$) and superior S/N for absorption lines associated with the Ly α forest, and Lyman Limit systems ($15 < \log(N(HI)) < 19$), the lines of e.g. OIII-VI, CII-IV, NeIV-VI etc. will permit the exploration of the full range of ionized and neutral gas out to $z = 2$. The resolution is a critical parameter, since it must be sufficient to assure that no component mixing occurs.

The impact of the determination of abundance evolution of the gaseous baryonic content of the Universe at $z < 2$ is especially important at a time that the problem of Star Formation rate in the same redshift range is being addressed by results expected to be obtained with the GALEX survey. The simultaneous availability of information on the metal enrichment processes between $0 < z < 2$ together with the knowledge of the SFR (from the UV-to-SFR conversion) will allow us to constrain the evolutionary models.

Acknowledgements: We are indebted to all our colleagues in the *World Space Observatory* (WSO) Implementation Committee (WIC) (URL:wso.vilspa.esa.es) and in the *Network for UltraViolet Astronomy* (NUVA) (URL: www.mat.ucm.es/~aig/NUVA/). We all share a common interest in the future of ultraviolet astronomy. Ana I. Gómez de Castro acknowledges the Ministerio of Ciencia y Tecnología of Spain for grants. AYA2000-966 and ESP2001-4637.

References

- [1] Burles, S., Tytler, D., 1998, ApJ, 507, 732
- [2] Collier-Cameron, A., 2001, in “Recent Insights into the Physics of the Sun and Heliosphere: Highlights from SOHO and Other space missions”, IAU Symp. 203, eds P. Brekke, B. Fleck, and J. B. Gurman. ASP, p. 229
- [3] Gómez de Castro, A.I., 2002, MNRAS, 332, 409
- [4] Gómez de Castro, A.I., 2004, Astr. & Sp. Sc., 291, in press.
- [5] Koehler, S., Reimers, D., Wamsteker, W., 1996, A&A, 312, 33
- [6] Matt, S., Goodson, A.P., Winglee, R.M., Bohm, K.-H., 2002, ApJ, 574, 232
- [7] Priest, E., Forbes, T., 2000, “Magnetic reconnection : MHD theory and applications”, New York : Cambridge University Press.
- [8] Prochaska, J.X., Wolfe, A.M., 2002, ApJ, 566, 68
- [9] Uzdenski, D., 2004, Astr. & Sp. Sc., 291, in press.
- [10] van den Bergh, S., 2002, PASP, 114, 797
- [11] Wadhwa, M., Russell, S.S., 2000, in “Protostars and Planets IV”, University of Arizona Press; eds Mannings, V., Boss, A.P., Russell, S. S., p. 995

NEW GENERATION NEAR INFRARED SPECTROGRAPHS IN 3.5 m TO 10 m CLASS TELESCOPES

ARTURO MANCHADO
Instituto de Astrofísica de Canarias, E-38200 La Laguna, SPAIN

Abstract: Here we present a review of the new generation near infrared spectrographs (1 to 5 microns) available in telescopes from 3.5 m to 10 m in diameter. These instruments have in common the new infrared (IR) detectors with a large 1024 x 1024 pixel format, low read-out noise and low dark current both in the 1-2.5 and 1-5 micron range.

1 Introduction

The study of the spectra of astronomical objects in the Near Infrared (NIR) has enormous scientific potential: by using NIR, the composition of the dust can be established, molecular hydrogen can be studied, and high redshift ($z=1$) galaxies, whose main emission lines of Active Galactic Nuclei (AGN) (for example, Halpha) lie in the NIR region, can also be observed. However, working in this spectral region (1-5 microns) is quite a challenge, posing several problems for the astronomer. The first problem is the transmission of the sky: since the earth's atmosphere is dominated by water vapour, only certain spectral regions can be observed, namely, the J, H, K, L and M band. An additional problem is that a black body with a temperature of 300 K will have a very important contribution to the K, L and M band. To avoid this emission, the whole instrument must be cooled to a temperature below 100 K, which results in a myriad of engineering problems to be solved. A third issue is the fact that very fast reads are necessary in order to avoid sky saturation, especially in the L and M band.

During the last 30 years, NIR spectroscopy has been limited by the availability of detectors and cryogenic technology. In the 70s only the Circular Variable Photometers (CVF) were available, with very poor resolution ($R=100$) and very poor throughput. In the 80s, linear arrays and small bidimensional arrays became available, with very high dark current and read-out noise, which limited their use to bright sources and small spectral ranges. In the mid 90s, new large format arrays with very low dark current and read-out noise made NIR spectroscopy more similar to the optical spectroscopy with CCDs in the 80s. NIR spectrographs are very complex

cryogenic machines, and as a result the number of these spectrographs is currently rather scarce. Key points to consider when designing a NIR spectrograph include target acquisition and sky subtraction. Target acquisition is difficult due to the impossibility of using an optical slit view with CCD, since on the one hand differential sky refraction causes the optical and IR image to be shifted by several arcseconds (depending on the airmass), and on the other hand some sources are very red and therefore very weak in the optical image. Another factor to take into account is the strong sky emission in the NIR: for example, the sky emission in the K_s band is 13 magnitude per square arcsecond (3 and -0.5 in the L and M bands). Therefore, most NIR spectrographs have an imaging mode which makes it possible to use in the NIR the usual imaging technique of dithering the telescope around the target position in order to subtract the sky emission. As some of these spectrographs aim at very weak targets, such as $M_K=20$, target acquisition can be a very time-consuming task. Once the target is on the slit, the usual beam-switch technique is used; however, to allow for correct sky subtraction, beam-switching has to be done every 15 minutes. Thus the system (instrument+telescope+autoguider) has to be very stable in order to ensure that the target will be on the slit after several beam-switches (for a 3-hour integration on one target, 12 beam-switches will be necessary). The other key point is sky subtraction, as this spectral range is dominated by strong atmospheric OH emission lines. In order to allow for proper sky subtraction, the design should minimize flexures which will shift the spectral lines. As an example, the user requirement of LIRIS allows maximum flexure of 4-microns between the focal plane and the detector during one hour of integration time. All this makes the optical and mechanical design far more complex than that of an optical spectrograph. Regarding spectral resolution, in order to avoid the atmospheric OH lines, the optimal resolution is between 1000 and 3000. Another important point is the dispersion element. Some spectrographs use reflection gratings which provide high resolution, especially if echelle gratings are used, while for low resolution ($R=1000$) usually grisms (a combination of a prism and a refraction grating) are used.

Array	Pixels	Pixel size	Read out (e ⁻¹)	Dark current (e ⁻¹ s ⁻¹)	Working Temperature (K)
Hawaii	1024 x 1024	18	15	0.01	70
Hawaii-2	2048 x 2048	18.5	15	0.01	70
ALLADIN	1024 x 1024	27	40	0.01	30

Table 1: Characteristics of near-IR arrays

Two different detectors were manufactured in the late 90s, Hg:Cd:Te with a spectral coverage from 0.8 to 2.4 microns (Hawaii 1024 x 1024 and Hawaii-2 2048 x 2048, both manufactured by Rockwell), and InSb with a spectral coverage from 1-5 mi-

crons (ALLADIN 1024 x 1024, manufactured by Raytheon). These detectors require very precise temperature control, as their characteristics (bias, hot pixels, etc) can be altered if there is a difference of even a small fraction of a degree K. For LIRIS it was found that the optimal operation temperature was 70 ± 0.005 K. The spectral dimensions of NIR spectrographs have been divided into two ranges: 0.8 -2.5 microns when using Hawaii arrays, and 1-5 microns when using ALLADIN arrays. The main characteristics of these arrays are listed in Table 1. The spectrographs in the two spectral ranges will be discussed in more detail below.

2 Spectrographs in the 0.8 to 2.4 microns range

Instrument	Telescope	Plate scale "/pixel	Resolution	Polarimetry	MOS	Coronography
IRIS2 [3]	AAT	0.45	2400	no	yes	no
ISSAC [2]	VLT	0.15	500-3000	yes	no	no
LIRIS [4]	WHT	0.25	1000-3000	yes	yes	yes
Omega-Cass [1]	Calar Alto	0.04,0.3	420,1050	yes	no	no
NICS [5]	TNG	0.25,0.13	50-1250	yes	no	no
SOFI [2]	NTT	0.14,0.27,0.29	600-1500	yes	no	no

Table 2: 1-2.5 microns spectrographs

These spectrographs make use of the Hawaii arrays, both the Hawaii and the Hawaii-2 (2048 x 2048). These arrays, which can be seen in Table 1, have very low readout noise and very low dark current, thus the observations are usually limited by background noise for integrations longer than 100 seconds. The low dark current combined with the spectral resolution make long integration times possible. Thus, these spectrographs make observations which are very similar to the observations in the optical wavelength.

All these spectrographs use the Hawaii array and have an imaging mode to allow for target acquisition. They also have full imaging capability with a wide set of astronomical filters. All except for ISSAC use grisms as disperser elements. Spectra resolution ranges from 50 for NICS to 3000 for ISSAC and LIRIS. All except for IRIS2 have polarimetry modes, and only IRIS2 (in the Southern Hemisphere) and LIRIS (in the Northern Hemisphere) have Multi-Objects (MOS) mode. LIRIS is the only spectrograph with coronographic mode, whereas ISSAC is the only spectrograph with two arms, one covering the 1-2.5 micron region and the other covering the 2.5-5 micron region. The diameters of the telescopes range from 3.5m (Calar Alto, NTT and TNG) to 8m (VLT).

Instrument	Telescope	Plate scale "/pixel	Resolution	Pola- rimetry	Corono- graphy
CISCO/OHS [9]	SUBARU	0.105	400	no	no
CONICA [2]	VLT	0.01,0.05	400-1100	yes	yes
GNIRS [7]	Gemini S.	0.15	1000-3000	yes	no
IRCS [9]	SUBARU	0.022,0.058	120-5000	no	no
ISSAC [2]	VLT	0.075	500-3000	yes	no
NIRCSPEC [6]	Keck	0.19	2000-20000	no	no
NIRI [7]	Gemini N.	0.02,0.11	460,1650	no	no
PHOENIX [7]	Gemini S.	0.23	50000	no	no
UIST [8]	UKIRT	0.06,0.12	475-2000	yes	no

Table 3: 1-5 microns spectrographs

3 Spectrographs in the 1 to 5 microns range

All these spectrographs use the ALLADIN detector. CONICA is used in combination with the adaptive optics (AO) system NAOS while NIRI is used with the AO system Altair. IRCS can be also used with the SUBARU AO system. Spectral resolution varies from 120 for IRCS, to 50000 for PHOENIX. CONICA, GNIRS, ISSAC, and UIST all have polarimetry modes, with CONICA being the only spectrograph with coronography mode. UIST is the only one with an Integral Field Unit (IFU). CISCO/OHS has an OH suppressor that removes the OH airglow lines which dominate the broad-band background. This gives a gain in sensitivity in the order of 0.5 magnitude in the J and H band. None of the spectrographs have MOS modes.

4 Future

Here we describe several other instruments which are being developed at present and will be operative in the near future. SINFONI, which will be on the VLT, uses a Hawaii-2 and has an IFU with 32 x 32 spatial pixels and 2048 spectral channels (first light in 2004). CRIRES, which will be on the VLT, will work in the 1-5 micron range with a 1024 x 4096 pixels array, giving a resolution of R=50000 (first light in 2004). LUCIFER, on the BLT, will use the Hawaii-2 array and have a resolution of R=10000-36000, as well as MOS mode (first light 2004). OSIRIS, on the Keck, will use a Hawaii-2 array, and have an IFU (64 x 16 spatial elements) and an OH suppressor with a resolution of R=3800. FLAMINGOS on the 4m Mayal (NOAO), uses a Hawaii-2, and will have R=1800 and a MOS mode. EMIR, which will be on GTC, uses a Hawaii-2 and will have a MOS mode with a FOV of 6 x 6 arcminutes and R=3000 (first light 2008).

Acknowledgements: This work was supported by the Subdirección General de Proyectos de Investigación under grant AYA2001-1658.

References

- [1] <http://www.mpi-a-hd.mpg.de/Public/CAHA/Instruments/index.html>
- [2] <http://www.eso.org/instruments/>
- [3] http://www.ao.gov.au/iris2/iris2_why/
- [4] <http://www.iac.es/proyect/LIRIS>
- [5] <http://www.tng.iac.es/instruments/nics/nics.html>
- [6] <http://www2.keck.hawaii.edu/inst/>
- [7] <http://www.gemini.edu/sciops/instruments/>
- [8] <http://www.jach.hawaii.edu/JACpublic/UKIRT/instruments/uist/uist.html>
- [9] <http://www.naoj.org/Observing/Instruments/index.html>

Author Index

- Arcay, B., 153
Beckman, J. E., 43
Carricajo, I., 153
Cerrato, Y., 165
Cid, C., 165
Cornide, M., 119
Crespo-Chacón, I., 119
Dafonte, C., 153
De Castro, E., 119
Del Peral, L., 177
Domingo, M., 187
Fernández-Figueroa, M.J., 119
Gálvez, M.C., 119
Gómez de Castro, A.I., 197
García-Melendo, E., 63
García-Berro, E., 23
Garrido, R., 133
Gomis, O., 187
Gutiérrez, J., 177
Gómez Herrero, R., 177
Hernán-Obispo, M., 119
Hernández-Fenollosa, M. A., 187
Hidalgo, M. A., 165
Hueso, R., 63
Iglesias Groth, S., 105
Isern, J., 23
López-Santiago, J., 119
Luna, R., 187
MacDonald, J., 133
Manchado, A., 209
Manteiga, M., 133, 153
Montes, D., 119
Moreno, R., 143
Oreiro Rey, R., 133
Pérez Hernández, F., 133
Pérez-Hoyos, S., 63
Rebolo, R., 1
Rodríguez López, C., 133
Rodríguez Espinosa, J.M., 87
Rodríguez, A., 153
Rodríguez Frías, D., 177
Rojas, J. F., 63
Sánchez-Lavega, A., 63
Saiz, E., 165
Satorre, M. A., 187
Ulla, A., 133, 143
Vega Beltrán, J. C., 43
Wamsteker, W., 197
Zurita, A., 43

Subject Index

- 2003aw, 144, 147, 149
2RE J0039+103, 125
2RE J0725-002, 126
2RE J1101+223, 124–126
2RE J0743+224, 125, 127

accretion disks, 197, 203, 205
accretion process, 203, 205
active region, 127, 180–183
active stars, 119, 127
AD Leo, 128, 129
age of the Universe, 23
AM CVn, 143–145, 149
AM CVn system, 143–149
AR Lac, 124
Artificial Intelligence, 153, 154
Astronomical Archives, 200

BK Psc, 125
buckyonions, 105, 107, 111, 113–115
BY Dra binary systems, 120, 123

CABS, 123, 125
CANARICAM, 98
Cassini Orbiter, 68
Castor, 130
Cataclysmic Variable, 143, 148
CE 315, 144–146, 149
CELT, 103
chromosphere, 119, 127, 128
chromospheric lines, 121, 123, 127–129
chromospherically active binaries, 123
CIRs, 171
classical T Tauri stars, 123
CMB anisotropies, 4
CMB data, 1, 4, 8, 10, 11, 14–16, 19, 20
CMB power spectrum, 2, 4, 6, 9, 12, 20
CMB temperature, 2, 8

CMEs, 170
confined flares, 127
convection, 24, 26, 28
convection zone, 119
cool stars, 119
cooling process, 26, 28, 33, 38
corona, 119, 127
coronal abundances, 178, 180
Cosmic Microwave Background (CMB), 1–4, 7, 8, 11, 15, 16, 19, 20
cosmological model, 1, 10, 207
cosmological parameters, 1, 19, 20
CP Eri, 144, 146, 147, 149
CR Boo, 143, 144, 146, 147, 149
critical density, 11
crystallization, 26–30, 32, 33, 38
CTTS, 123

dark matter, 1, 10, 11, 15
database, 153, 155, 161, 163
deep models, 71
density fluctuations, 1, 2, 11
Dst index, 166
dynamo mechanism, 119

EC14026, 135–137
EHB, 134, 137, 138
ejecta, 171
ELMER, 99
EMIR, 101
equivalent width, 128
eruptive flares, 127
ES Cet, 144, 148, 149
EUV, 125
expert systems, 153, 154, 156, 162, 163
EZ Peg, 124

flare, 120, 121, 125–129
foreground emission, 4, 7

fullerenes, 105–110, 112, 113, 115
fuzzy logic, 153, 156, 162

galaxy bar, 43, 44, 50, 51, 53, 57–59
galaxy bulge, 43, 44, 49, 51, 52, 55, 57
galaxy disc, 43–45, 47, 49, 52, 55
Galileo Orbiter, 68
GEMINI, 90
General circulation models, 71
geomagnetic storm, 165
giant planets, 63
Gl 687B, 128
GP Com, 143–146, 149
Gran Telescopio Canarias, 87
GSMT, 103

HD 209458b, 64, 82
HD 95559, 124–126
Helium Cataclysmic Variable, 143
Horizontal Mount, 89
hot Jupiters, 64
hot subdwarfs, 133, 134, 137, 138
HP Lib, 144, 145, 149
HR 1099, 128
Hubble constant, 10
Hyades, 130

IC 2391, 130
ices, 189
II Peg, 127
infrared (IR) detectors, 209
Interacting Binary DB White Dwarf star, 143, 144, 146–148
interferometer, 1, 3, 4, 7
interferometric measurements, 4
interplanetary medium, 180
interstellar medium, 105, 107–109, 111, 113–115
ion irradiation, 190
IR spectroscopy, 188

Jupiter, 63

Keck, 90
KL Dra, 144, 147, 149

large telescopes, 87
late-type stars, 119
Libraries of stellar spectra, 121, 131
lithium abundance, 122
Local Association, 130
LQ Hya, 128
luminosity classes, 156, 159, 160

M dwarfs, 128
magnetic field, 177
magnetic pressure, 127
magnetic reconnection, 119, 127
magnetosphere, 177
microflares, 121
microflaring, 124
MK system, 154
moving group, 130
Mt. Wilson, 87

near infrared (NIR) spectrographs, 209–211
neural networks, 153, 154, 157–163
neutrino mass, 15, 16
NIR spectroscopy, 209

OSIRIS, 97
OWL, 103

Palomar, 88
particle events, 177, 178, 182
photosphere, 119, 126, 128
plages, 121
Pleiades, 130
pre-main sequence stars, 120, 123
primordial anisotropies, 2
prominences, 121
pulsations, 33, 133, 135–139
PW And, 130

radial velocities, 122

radiative levitation, 24, 25
Roche Lobe, 143
ROSAT, 123, 125
rotation curve, 43, 44, 47, 48, 50, 52–
56, 58, 61
rotational velocities, 122
RS CVn binary systems, 120, 123, 127,
128
RX J0806.3+1527, 144, 148, 149

Saturn, 63
sdB, 134–140
sdo, 134, 137–140
sdOB, 134, 139
semiconvection, 27, 28
shallow layer models, 71
SOHO, 177–179, 182, 183, 186
solar flares, 126, 127
space mission, 202
space weather, 165
spectral classification, 154, 156, 157
spectral subtraction technique, 121, 123
spectral types, 153, 156, 159, 160, 163
spectroscopic observations, 120
spectroscopy, 127
spiral arm, 44, 56, 58
star formation rate, 34–36, 38, 43
stellar age, 122
stellar atmosphere, 126
stellar flares, 120, 126–129
stellar kinematic group, 120, 130
stellar population, 44, 45, 49
stellar rotation, 119
structural models, 137, 139, 140
SUBARU, 90
supercluster, 130
surface brightness, 56, 58–60
synthetic spectra, 153, 160, 161, 163

T-Tauri, 206
Taurus-Auriga, 123
Taylor-Proudman theorem, 71

transition region, 119
Ursa Mayor, 130
UV astronomy, 197, 200
UV Cet type stars, 120, 126, 128
UX Ari, 127

V1054 Oph, 128
V407 Vul, 144, 147–149
V789 Mon, 126
V803 Cen, 143, 144, 146, 147, 149
velocity gradient, 43, 58–60
Virtual Observatories, 200
VLT, 90
Voyagers, 66

weak-lined T Tauri stars, 120, 123
White Dwarf, 23–26, 28–34, 36–39
WTTS, 123

X-ray, 125

Astrophysics Symposium Photos